

Equilibrium and non-equilibrium properties of 1d interacting systems

A Thesis

Submitted to the
Tata Institute of Fundamental Research, Mumbai
Subject Board of Physics
for the degree of Doctor of Philosophy

by

Jitendra Kethepalli

International Centre for Theoretical Sciences

Tata Institute of Fundamental Research

August, 2024

Final version submitted on December 2024

DECLARATION

This thesis is a presentation of my original research work. Wherever contributions of others are involved, every effort is made to indicate this clearly, with due reference to the literature, and acknowledgement of collaborative research and discussions.

The work was done under the guidance of Professor Anupam Kundu at the International Centre for Theoretical Sciences, Bengaluru. Professor Manas Kulkarni served as co-supervisor.



Jitendra Kethepalli

In my capacity as the formal supervisor of record of the candidate's thesis, I certify that the above statements are true to the best of my knowledge.



Anupam Kundu

Date: 3/12/2024

Dedicated to my Amma, Nanna and Didi

ACKNOWLEDGMENTS

First and foremost, I would like to express my sincere gratitude to Prof. Anupam Kundu and Prof. Manas Kulkarni. Their supervision has been crucial to the completion of my PhD. Their constant guidance has been invaluable for my growth and development as a researcher. I am deeply grateful for their patience, encouragement, and unwavering support throughout my PhD. Prof. Anupam invested a great deal of time teaching me how to present and solve problems, which has been particularly enriching. He was an ideal supervisor, always available for discussion and guidance. Prof. Manas has always been present for discussions, and his enthusiasm allowed me to work on a variety of problems.

I am also thankful to Prof. Abhishek Dhar, Prof. Satya N. Majumdar, and Prof. Gregory Schehr for their guidance during my PhD. They have been a constant source of inspiration and motivation, teaching me how to effectively approach and think about problems.

I want to thank all my collaborators: Prof. David Huse, Dr. Vir B. Bulchandani, Prof. Herbert Spohn, Prof. Deepak Dhar, Dr. Debarshee Bagchi, Saikat Santra, Prof. David Mukamel, Prof. Gregory Schehr, Prof. Satya N. Majumdar, and Prof. Abhishek Dhar. Working with Prof. Abhishek Dhar has been enlightening, and I find his approach from first principles and his focus on the big picture inspiring. Collaborating with Prof. Satya N. Majumdar was the best experience, some of the confidence I gained was solely due to interaction with him. I particularly, enjoy discussing with Prof. Gregory Sch ehr as he easily simplifies jumbled thoughts and ideas. I would also like to thank Prof. David Mukamel for our short but highly productive interactions, which taught me a lot. Working with Dr. Debarshee Bagchi was both fun and engaging, and our discussions about physics and PhD life greatly helped me grow as a PhD student. I would like to express my heartfelt gratitude to Saikat Santra, who was always willing to discuss various topics related and unrelated to physics.

I must express my gratitude to Prof. Sanjib Sabhapandit and Prof. Abhishek Dhar for providing the platform of the Bangalore School of Statistical Physics (BSSP), which allowed me to interact and learn from some of the best minds in the field of statistical physics. ICTS has been a great place to work and learn, and I am grateful for the opportunity to be part of this vibrant community. Additionally, I would like to thank all the academic and non-academic staff members at ICTS for their help and support.

I am grateful to my batchmates Saikat, Saumav, Devang, Aditya, Divya, Saurav, Srashti, Junaid, Sarthak, Basu, Vijaykumar, Chandra and Omkar. Additionally, I would like to thank Debarshee, Subajit, Soumi, Dipankar, Madhumita, Amit and Argho for their support during my PhD. Without their guidance and encouragement, PhD life would have been much more challenging. I especially appreciate Devang for his friendship and for helping me see the positives in life. I also cherish the memorable late-night group discussions about everything and nothing with Aditya, Saikat, Saurav, Saumav, and Devang.

I am thankful to Panni for our conversations about movies, TV series, and mythology, which provided constant entertainment and helped me through the challenging COVID times. I also want to express my gratitude to Prashant, Tamoghna, Rajarshi, Mrinal, Sparsh, Umesh, Sahil, and Ankush for involving me in discussions about various topics beyond my PhD work, broadening my understanding of physics. I would like to thank Basu and Mahaveer for being consistent partners in all my hiking adventures; their dedication to fitness and hiking is a constant source of inspiration.

My journey to this point has been made possible by the unwavering support and immense sacrifices of my Amma, Nanna, and Didi. Their love and trust have enabled me to reach this milestone in my life. Lastly, I would like to thank my teachers and friends from my schooling and coaching days for their support.

List of Figures

- 1.1 Figure adopted from Fig 1 of Ref. [1]. Classification of the range of interaction based on the additivity of energy. The total energy of the system, $E_{\text{total}} = E_{\text{left}} + E_{\text{right}} + E_{\text{inter}}$, is the sum of the energies of left and right partitions (E_{left} and E_{right}) and the energy corresponding to the inter-specific interactions (E_{inter}). For the short-range system as the energy corresponding to the inter-specific interactions are negligible $E_{\text{inter}} \ll E_{\text{total}}$, the system is additive $E_{\text{total}} \approx E_{\text{left}} + E_{\text{right}}$. While for long-range systems the energy is non-additive $E_{\text{total}} \neq E_{\text{left}} + E_{\text{right}}$ 3
- 1.2 Figure adopted from Fig 2 of Ref. [1]. A schematic plot of the spherical region, of radius R , considered for the computation of energy per particle, ϵ . Here the particles interact via a power-law potential of the form $V_k(\vec{r}) = \frac{J}{|\vec{r}|^k}$ with a cutoff radius a . The energy can be computed by summing the potential energy contributed by $\rho(\vec{r})d^d r$ particles located at position \vec{r} , for all values of \vec{r} . This is formally described in Eq. (1.1). It is shown that the energy per particle diverges with increasing volume V for $k < d$, and remains finite for $k > d$ 4

- 1.3 Figure taken from Ref. [78]. The figure shows the absorption image for the anharmonically trapped Bose-Einstein condensate of Rubidium-87 (^{87}Rb) consisting of 2.5×10^5 atoms. In the experiment, the two clouds of atoms were separated away from the center of the trap. These two clouds oscillate within the trap and meet twice every period. In the plot, note that the progression of time is from right to left. Interestingly the clouds keep oscillating for the large observation times akin to the balls of a Newton's cradle toy where the momentum gets transferred to the other ball upon collision. This oscillatory behavior suggests that the system does not thermalize even after each atom has undergone several thousand collisions. 8
- 2.1 Schematic plot of the particles of the Riesz gas in 1d. The particles of Riesz gas interact via all-to-all repulsive pair-wise potential of the form $V_{ij} = J \text{sgn}(k)|x_i - x_j|^{-k}$ where $x_{i/j}$ represents the position of the i/j -th particle, the interaction strength $J > 0$ and $\text{sgn}(k)$ ensures that the particles repel each other. The external confinement $U(x)$ is represented by the dashed curve and the all-to-all nature of interactions is shown by the double-arrow-headed solid arcs. 13
- 2.2 Figure adopted from Fig. 1 of Ref [45]. Scaled average density of the unconstrained gas $\rho_{\text{uc}}^*(y)$ in Eq. (2.18) vs. y for different values of $k > -2$. The three rows correspond respectively to (i) $k \geq 1$ (third row), (ii) $-1 < k < 1$ (second row), and (iii) $-2 < k \leq -1$ (first row). In (i) the density has a dome shape, in (ii) also has a dome shape, and in (iii) it has a U-shape. At $k = -1$ and $k \rightarrow +\infty$ the density is flat. The blue dashed vertical lines indicate the edges of the support of the density profile. 20
- 2.3 The exponent k characterizes the range of pairwise repulsive interactions between particles. For $k \geq 1$ the interaction is effectively short-ranged. For $-1 < k < 1$, the interaction, though long-ranged, is effectively weak and does not qualitatively change the shape of the density profile compared to the short-ranged case. For $-2 < k \leq -1$, the particles are subjected to strong long-range interactions, that change the shape of the density profile drastically. 21

3.1 Scaled average density of the constrained gas $\rho_k^*(y, w)$ vs. y for different values of $k > -2$. The three rows correspond respectively to (i) $k \geq 1$ (third row), (ii) $-1 < k < 1$ (second row), and (iii) $-2 < k \leq -1$ (first row). The blue dashed vertical lines indicate the edges of the support. In the second and third rows, the right edge of the support coincides with the scaled wall position w . In the third row, the density is a constant at the wall while it diverges in the second row. In both the second and the third row, the density vanishes at the left edge (for $k = 10$ in the third row, the true density at the left edge vanishes, though it is not clearly visible due to the compression of the scale). In the first row, the density has an extended bulk part, sandwiched between the two vertical dashed lines and a delta peak at the wall w (shown by a thick solid vertical line). In between, there is a hole devoid of particles (shaded cyan region) which disappears for $k = -1$ (the third figure in the first row). 26

3.2 *Regime 1* ($k \geq 1$): Comparison between MC simulations (symbols) and the theoretical expression given in Eq. (3.24) (solid line) of the scaled density profile of the Riesz gas in the presence of the hard wall at $w = 1.0$ for $k = 1.5$. The parameters used in this plot are $J = 1$ and $T = 1$. The dashed vertical line on the left marks the left edge $-l_k(w)$ (shown by an arrow) of the density while the wall is located at w (shown also by an arrow). 33

3.3 *Regime 1* ($k \geq 1$): Plot of the support size $L_k(w) = w + l_k(w) = \frac{2m_k w}{2m_k - 1}$ as a function of $w \leq l_{uc}$, obtained by solving Eq. (3.26) for m_k . $L_k(w)$ decreases monotonically with decreasing w , shown for two different values of k . As $w \rightarrow -\infty$, the support size decreases algebraically as $L_k(w) \sim |w|^{-1/(k+1)}$. The vertical dashed lines indicate the positions of the unconstrained right edge l_{uc} for the two values of k 34

- 3.4 *Regime 2* ($-1 < k < 1$): Comparison between MC simulations (symbols) and the theoretical expression given in Eq. (3.38) (solid line) of the scaled density profile of the Riesz gas in the presence of the hard wall at $w = 1.0$ for $k = 0.5$. The parameters used in this plot are $J = 1$ and $T = 1$. The dashed vertical line on the left marks the left edge $-l_k(w)$ (shown by an arrow) of the density while the wall is located at w (shown also by an arrow). The density diverges at the wall as $\sim (w - y)^{(k-1)/2}$ 35
- 3.5 *Regime 2* ($-1 < k < 1$): Plot of the support size $L_k(w) = w + l_k(w) = \frac{2\gamma_k w}{1+\gamma_k - g_k(w)}$ as a function of $w \leq l_{uc}$, obtained by solving Eq. (3.39) for $g_k(w)$. $L_k(w)$ decreases monotonically with decreasing w , shown for two different values of k . As $w \rightarrow -\infty$, the support size decreases algebraically as $L_k(w) \sim |w|^{-1/(k+1)}$. The vertical dashed lines indicate the positions of the unconstrained right edge l_{uc} for the two values of k 36
- 3.6 *Regime 3* ($-2 < k \leq -1$): Scaled density profile for $w = 1$ and $k = -1.5$: Comparison between MC simulations (symbols) and the theoretical expression (solid line) given in Eq. (3.40) with $\rho_b(y, w) = \rho_b^*(y, w)$ in Eq. (3.56) and $D_k(w) = D_k^*(w)$ in Eq. (3.54). The parameters used in this plot are $J = 1$ and $T = 1000$. The dashed vertical line on the left (right) marks the left (right) edge $-l_k(w)$ ($\bar{l}_k(w)$) shown by an arrow. The cyan shaded area is the hole region and the thick black line at $y = w = 1.0$ is the delta function. Note that the theoretical expression has an integrable divergence at the left edge as shown by the solid line. Since the numerical simulations are for finite N , we do not see the divergence very clearly. However, the value of the density at the left edge becomes larger as N increases, which indicates divergence in the limit $N \rightarrow \infty$ 41
- 3.7 *Regime 3* ($-2 < k \leq -1$): Plot of the support size $\tilde{L}_k(w) = \bar{l}_k(w) + l_k(w)$ in Eq. (3.59) (with $g_k(w)$ determined from Eq. (3.57)). $\tilde{L}_k(w)$ decreases monotonically with decreasing w and vanishes at $w = w_c(k)$ given in Eq. (3.61) and marked by the two vertical dashed lines on the left for $k = -1.5$ and $k = -1.1$. The unconstrained right edge l_{uc} , for these two values of k , are also marked by two vertical dashed lines on the right. 42

3.8 *Regime 3*: Simultaneous plots (i) of the amplitude $D_k^*(w)$ of the delta function, associated with the density $\rho^I(y, w)$ in Eq. (3.62) (dashed red line) and (ii) of the order parameter $M_k(w)$ defined in Eq. (3.67) (solid green line), as a function of w for fixed $k = -1.5$. We see that $D_k^*(w)$ increases with decreasing w and approaches to 1 as $w \rightarrow w_c(k)$, while the order parameter $M_k(w)$ coincides with $D_k^*(w)$ for $w > w^*(k)$ but jumps to 1 at $w = w^*(k)$. This jump in $M_k(w)$ at $w = w^*(k)$ demonstrates a first-order phase transition. 43

3.9 Plot of the energy $\mathcal{E}_k^I(w)$ and $\mathcal{E}_k^{II}(w) = w^2/2$ vs. w for two different values of k : for $k = -1.5$ (panel (a)) and $k = -1.8$ (panel (b)). The values of $w^*(k)$ and $w_c(k)$ are marked by vertical dashed lines. In the range $w_c(k) < w < w^*(k)$ the energy $\mathcal{E}_k^I(w) > \mathcal{E}_k^{II}(w)$, showing that the configuration with density $\rho_k^I(y, w)$ is metastable. 45

3.10 The optimal density is one of two different types $\rho_k^I(y, w)$ and $\rho_k^{II}(y, w)$ defined respectively in Eqs. (3.62) and (3.63). For $w > w^*(k)$, $\rho_k^I(y, w)$ is the optimal density. For $w_c(k) < w < w^*(k)$, the density $\rho_k^I(y, w)$ becomes metastable, while $\rho_k^{II}(y, w)$ represents the true minimum. Finally, for $w < w_c(k)$, the solutions $\rho_k^I(y, w)$ and $\rho_k^{II}(y, w)$ merge with each other. 46

3.11 Plot of the critical wall positions $w_c(k)$ and $w^*(k)$ as functions of k in regime 3 $-2 < k \leq -1$. $w_c(k)$ (black solid line) is given by Eq. (3.61) and $w^*(k)$ (blue dots) is found numerically from the crossover location between the energies $\mathcal{E}_k^I(w)$ and $\mathcal{E}_k^{II}(w)$ as shown in Fig 3.9. We find that $w_c(k) \leq w^*(k)$ for all $-2 < k \leq -1$ with $w_c(k) = w^*(k)$ only for $k = -1$. 47

3.12 In this figure we study the metastability of the extended profile in the region $w_c(k) < w < w^*(k)$ for $k = -1.5$. For this value of k , $w_c(k) = -0.563$ and $w^*(k) = -0.441$. The figure is divided into three columns corresponding to the three regimes (a) $w = -0.6 < w_c(k)$, (b) $w_c(k) < w = -0.5 < w^*(k)$ and (c) $w = -0.2 > w^*(k)$. For each column, the insets of the top row and the bottom row indicate two different initial conditions (a delta peak and a flat density) while the main figures show the final configuration after a large number of MC steps. In columns (a) and (c) we see that the final configurations in the top row and in the bottom row are qualitatively similar, indicating the irrelevance of the initial conditions. In contrast, in column (b) the final configurations in the top and in the bottom row corresponding to two different initial conditions seem to lead to different final configurations, within the time scale of the simulation. This dependence on the initial condition is a signature of metastability in the region (b). 49

4.1 Schematic plot of the observable $x_{\max} = \max(x_1, x_2, x_3, \dots, x_N)$, the position of the rightmost particle, where x_i is the position of i -th particle. In this chapter, We study the fluctuations of x_{\max} for the harmonically confined Riesz gas with the energy function given in Eq. (2.1). 54

4.2 Schematic plot of the probability density function (PDF) of (a) the largest eigenvalue in RMT (Dyson's log-gas) and (b) the position of the rightmost particle in the 1dOCP, along with the respective density profiles. The PDF of the position of the edge particle in these cases is divided into three parts – typical (black) in the central part and, left (red) and right (green) large deviations. We show in this chapter that such representative pictures also hold for the harmonically confined Riesz gas with $-2 < k < \infty$ 56

4.3 Behavior of η_k [Eq. (4.20), disks] and the exponent $a_k^{(e)}$ of the mean gap at the edge [Eq. (4.22), squares], as a function of k is plotted here. The exponent η_k for different values of k are obtained by fitting the data for $\sigma_{y_{\max}}^2$ with N [See Fig. A.1 and A.2] obtained numerically (MC) for the confined Riesz gas [Eq. (2.1)]. The exponent $a_k^{(e)}$ is obtained similarly. We notice that $a_k^{(e)}$ obtained from numerics agrees with the one obtained from the Lifshitz argument (dashed red line) given in Eq. (4.21). Green stars represent the exponent η_k^{hess} obtained by numerically inverting the Hessian matrix [see Eq. (4.26) and Eq. (4.27)]. We also find the exponent $\eta_k^{\text{(hMC)}}$ [See Fig. A.2 and A.2] from the MC simulations of the Hessian hamiltonian [Eq. (4.24)]. It is interesting to note that the value of the exponent extracted from the three different approaches is in excellent agreement with each other ($\eta_k = \eta_k^{(\text{hess})} = \eta_k^{(\text{hMC})}$). The solid blue line represents the conjecture for η_k for $-2 < k < 0$ given in Eq. (4.30) (where the superscript “c” indicates our conjecture). The agreement between this conjecture and the MC simulation results is excellent. The parameters used in these simulations are $T = 1$ and $J = 1$ 59

4.4 Typical distribution of y_{\max} for various values of k . We notice excellent data collapse, when we plotted $\sigma_{y_{\max}} \mathcal{P}_k(y_{\max})$ versus the scaling variable $(y_{\max} - \langle y_{\max} \rangle) / \sigma_{y_{\max}}$. Here the values of $\sigma_{y_{\max}}$ and $\langle y_{\max} \rangle$ were extracted from the data (therefore no fitting parameter was used). 60

4.5 (a) Plot of the exponent e_k^- , that governs the asymptotic behavior of the left large deviation function given in Eq. (4.50) for $k \geq 1$, Eq. (4.60) for $-1 < k < 1$ and Eq. (4.73) for $-2 < k \leq -1$. (b) Plot of the exponent e_k^+ characterising the asymptotic behavior of the right LDF which is 1 for $k \geq 1$, and is given in Eq. (4.61) for $-1 < k < 1$ and Eq. (4.74) for $-2 < k \leq -1$ 61

- 4.6 The schematic plot shows the distribution of y_{\max} which is centred around $y_{\max} = l_{\text{uc}}$. The typical part of the distribution is represented in solid blue color and is the region where $|w - l_{\text{uc}}| \lesssim O(N^{-\eta_k})$. These fluctuations are quantified by $\sigma_{y_{\max}} \sim O(N^{-\eta_k})$, the standard deviation of y_{\max} . The atypical part of the distribution is described by the left and the right LDF $\Phi_{-}(w, k)$ and $\Phi_{+}(w, k)$ represented by red and green solid lines, respectively. We identify the length scales ℓ_l and ℓ_r where the typical distribution starts having an exponential form described by the LDFs while still being of $O(N^0)$ 66
- 4.7 A plot of the scaled average density in the presence of wall $\rho_k^*(y, w)$ versus y for the three regimes (a) $k \geq 1$, (b) $-1 < k < 1$ and (c) $-2 < k \leq -1$. The blue dashed vertical line indicates the left edge $[-l_k(w)]$ of the support and the black solid line represents the wall position w . In regime 1 the density is constant at the wall while it diverges in regime 2. In both of these regimes, the density vanishes at the left edge. In regime 3 the density has two disjoint regions, an extended bulk part $[-l_k(w) < y < \bar{l}_k(w)]$ and a delta function at the wall position (shown by a thick solid vertical line). They are separated by a hole region $[\bar{l}_k(w) < y < w]$ devoid of particles (shaded cyan region). 72
- 4.8 *Regime 1* ($k \geq 1$): The numerical verification of the LDF $\Phi_{\pm}(w, k)$ given in Eq. (4.47) and Eq. (4.48), respectively in panels (a) and (b). The rare events such that $|y_{\max} - l_{\text{uc}}| \sim O(1)$ are generated using the importance sampling method [141, 142] and the associated probabilities are computed from which the large deviation functions are calculated numerically. The parameters used in the simulations are $J = 1$ and $\beta = 1$ 73
- 4.9 *Regime 2* ($-1 < k < 1$): The numerical verification of the LDF $\Phi_{\pm}(w, k)$ given in Eq. (4.55) and Eq. (4.56), respectively in panels (a) and (b). The probabilities of rare events such that $|y_{\max} - l_{\text{uc}}| \sim O(1)$ are computed numerically from which the large deviation functions are extracted. The parameters used in the simulations are $J = 1$ and $\beta = 1$ 74

4.10 *Regime 3* ($-2 < k < -1$): The numerical verification of the LDF $\Phi_{\pm}(w, k)$ given in Eq. (4.69) and Eq. (4.71), respectively in panels (a) and (b). The probabilities of rare events such that $|y_{\max} - l_{\text{uc}}| \sim O(1)$ are computed from which the large deviation functions are calculated numerically. In the simulation, we use the parameters $J = 1$ and $\beta = 10^{-3}$. It is easy to show that our field theory calculation remains valid at this temperature since it satisfies the condition $\beta L_N^2 > 1$ 77

5.1 Schematic representation of the domain $[-W, W]$ (shaded region) studied in this chapter. The blue dots are the positions of the particles. The number of particles in the region $[-W, W]$ is defined as $\mathcal{N}(W, N)$. The black solid line is indicative of the harmonic confinement. 85

5.2 Phase diagram in the (w, c) plane showing three different regimes: (I) low, (II) moderate and (III) high fraction of particles in the box $[-W, W]$, where the saddle point density profiles given in Eq. (5.21) exhibit distinctly different shapes (see inset). The critical fraction line $c = \bar{c}(w)$ [Eq. (5.23)] separates the phases (I) and (II). Below this fraction, we observe a disjoint density profile in the phase (I) and above this concentration the two disjoint parts join and we observe a density profile as shown in the inset of the regime (II). Around this line, the LDF behaves non-analytically which leads to a third-order phase transition [see Appendix. A.5]. On the other hand, the crossover line $c = c^*(w)$ [Eq. (5.2)] separates the phases (II) and (III) and the LDF shows analytic behavior around it [see Eq. (5.33)]. This plot is generated for $k = 1.25$, however, such a plot is expected to be qualitatively the same for all $k > 1$. Note that the x -axis is in the units of l_{uc} 87

5.3 Plots of the equilibrium density profiles for different fractions of particles c confined inside the box $[-w, w]$ with $w = 0.75$, $k = 1.5$ and $J = 1$. The boundaries of the box at $y = \pm w$ are shown by the blue vertical dashed lines. We consider three values of c , (a) 0.08 (b) 0.4 and (c) 0.8 which are representative of the three regimes: (I) $c < \bar{c}(w)$, (II) $\bar{c}(w) < c < c^*(w)$ and (III) $c^*(w) < c$, respectively, where $c^*(w)$ is given in Eq. (5.3) and $\bar{c}(w)$ is given in Eq. (5.23). For $w = 0.75$ and $k = 1.5$ one finds that $\bar{c}(w) = 0.136$ and $c^*(w) = 0.552$. The symbols in all the plots are obtained using MC simulation for $N = 256$ and $N = 512$ whereas the solid lines represent the theoretical results given Eq. (5.21). The dotted line in each plot represents the density profiles $\rho_0(y)$ [see Eq. (2.18)] in the unconstrained case *i.e.*, without any wall, from which one can compute the fraction $c^*(w)$ of particles within the region $[-w, w]$. Here we have taken an average of over 10^6 samples for all the plots. 94

5.4 The plot displays the large deviation function $\Phi(c, w)$, given in Eq. (5.30), for $k = 1.5$ and $J = 1$. In (a) we show a plot of $\Phi(c, w)$ as a function of w for $c = 0.552$ and in (b) we plot $\Phi(c, w)$ as a function of c for $w = 0.75$. In both plots, we have demarcated three regions (I, II and III) based on the three types of saddle point density profiles (as shown in Fig. 5.3) that create the large deviations in those three different regions. Schematic plots of such density profiles are provided in the insets. 97

5.5 Numerical verification of the mean and variance of the number distribution problem. The plot displays the W dependence of (a) the mean fraction of particles and (b) the scaled variance of the number of particles in the box $[-W, W]$ for $N = 128, 256, 512$ with parameters $k = 1.5$, $T = 10$ and $J = 1$. The vertical blue dashed line represents the box with $W = l_{uc}N^{\alpha_k}$. The symbols indicate the results obtained from the Monte Carlo simulations and they are compared with our theoretical predictions (solid lines) given by Eqs. (5.2) and (5.34) for the mean and the variance, respectively. . . . 98

5.6	The plot displays the derivatives of the LDF $\Phi(c, w)$ [Eq. (5.30)]. Specifically, it shows the first (red dashed line), second (green dotted line) and third (blue dash-dotted line) derivatives: (a) w.r.t. c for $w = 0.75$ and (b) w.r.t. w for $c = 0.552$. Notably, we observe a pronounced discontinuity in the third derivative of $\Phi(c, w)$ in (a) at $c = \bar{c}(w)$ [see Eq. (5.23)] and in (b) at $w = \bar{w}(c) = l_{uc}c^{\alpha_k}$, establishing the presence of third order phase transitions.	99
6.1	A schematic representation for partitioning the system into N_b subsystems, each of size Δ . Here $s = 1, 2, \dots, N_b$ denotes the subsystem index. Note that the particles are represented by orange circles. In the s^{th} subsystem there are n_s particles. The double arrow indicates the extent of each subsystem. While analyzing each subsystem we take large- n_s and then for the complete system, we finally take the small- Δ limit.	113
6.2	Comparison of scaled equilibrium density profiles $\rho_R(y, c)$, obtained from Monte-Carlo simulations with field theory [Eq. (6.30)] denoted by ‘FT’, for the HR model with [(a)-(c)] harmonic trap ($\delta = 2$) and [(d)-(f)] quartic trap ($\delta = 4$). We show Monte-Carlo data for three values of c : $c = 0.1$, $c = 1.0$ and $c = 10.0$, for $N = 32, 64, 128$. Here the scaled variables are related to the unscaled variables as $y = x/N$ and $c = T/N^\delta$ as given in Eq. (6.28).	118
6.3	A comparison of the asymptotic densities up to the third iteration (see Appendix. A.9.1) with the densities obtained from the numerical solution of Eq. (6.30), denoted by ‘FT’, at low temperature $c = 0.01$ for the HR model in [(a)-(c)] harmonic trap ($\delta = 2$) and [(d)-(f)] quartic trap ($\delta = 4$) shows the densities for hard rods confined to harmonic trap ($\delta = 2$). Here [(a),(d)] show the bulk ($ y < y_c - O(c)$), [(b),(e)] edge ($ y - y_c \lesssim O(c)$) and [(c),(f)] tail ($ y > y_c + O(c)$) regions. The vertical dotted line represents the position $y = y_c$ given in Eq. (6.35) and this determines these three regions.	119

6.4	Chemical potential, $\mu_R(c)$, for the HR model obtained using Eq. (6.30) and Eq. (6.31), plotted as a function of the rescaled temperature c for harmonic trap with $\delta = 2$ (blue) and quartic trap with $\delta = 4$ (red). At large values of c the chemical potential is negative and diverges.	120
6.5	Comparison of the asymptotic densities up to third order (see Appendix. A.9.1) with the numerical solution of Eq. (6.30), denoted by ‘FT’, at high temperature $c = 10.0$ for the HR model confined to (a) harmonic trap ($\delta = 2$) and (b) quartic trap ($\delta = 4$).	121
6.6	Comparison of scaled equilibrium density profiles $\rho_C(y, c)$, obtained from Monte-Carlo simulations with field theory [Eq. (6.45)], denoted by ‘FT’, for the HC model with [(a)-(c)] harmonic trap ($\delta = 2$) and [(d)-(f)] quartic trap ($\delta = 4$). We show MC data for three values of c : $c = 0.1$, $c = 1.0$ and $c = 10.0$, for $N = 32, 64, 128$. Here the scaled variables are related to the unscaled variables as $y = x/N^{\alpha_C}$ and $c = T/N^{\gamma_C}$, where α_C and γ_C are given in Eq. (6.44).	124
6.7	Chemical potential $\mu_C(c)$ for HC model, computed by using Eq. (6.45) along with the normalization condition Eq. (6.46), plotted as a function of the rescaled temperature c for harmonic trap with $\delta = 2$ (blue) and quartic trap with $\delta = 4$ (red). At large values of c the chemical potential is negative and diverges.	125
6.8	A comparison of the asymptotic densities up to third order (see Appendix. A.9.2) with the densities obtained from the numerical solution of Eq. (6.45), denoted by ‘FT’, at low temperature $c = 0.01$ for the HC model. Here we show the densities for HC model confined to [(a)-(c)] harmonic trap ($\delta = 2$) and [(d)-(f)] quartic trap ($\delta = 4$). Here [(a),(d)] show the bulk ($ y < y_c$), [(b),(e)] edge ($ y - y_c \lesssim O(c)$) and [(c),(f)] tail ($ y > y_c$) regions. The dotted vertical line represents the position $y = y_c$ which determines the three regions. In (c) and (f), as $y = y_c$ falls outside of the domain of the x -axis, for the sake of presentation, we do not show the dotted line.	126

6.9	Comparison of the asymptotic densities up to third order (see Appendix. A.9.2) with the numerical solution of Eq. (6.45), denoted by ‘FT’, at high temperature $c = 10.0$ for the HC model confined to (a) harmonic trap ($\delta = 2$) and (b) quartic trap ($\delta = 4$).	127
7.1	Plots of (a) time-dependent Lyapunov exponent $\lambda(t)$, and (b) Poincaré section for $N = 3$ rods in the harmonic trap for 10 and 6 different initial conditions, respectively, with $E = 6$ and $E_{\text{cm}} = 0$. Figures (c,d) show plots of $\lambda(t)$ and the Poincaré section for $N = 2$ rods in the quartic potential for 5 and 2 initial conditions, respectively, with energy $E = 3.2$. To compute $\lambda(t)$, we used linearized dynamics for (a) and two trajectories with $\epsilon = 10^{-10}$ for (c). The $\log t/t$ behavior in (a) and the regular sections in (b) are consistent with the integrability of $N = 3$ rods in the harmonic trap. Interestingly, figure (c) reveals the existence of both chaotic and non-chaotic trajectories for the quartic case. This is also reflected in (d) where we observe two types of patterns, namely scattered (black) and regular (red).	137
7.2	Time evolution of $\lambda(t)$ and $c_1(t)$ for $N = 4$, starting from 40 different initial conditions (each color denotes one initial condition) generated using the SMED protocol, for (a,c,e) $e = 0.5$ and (b,d,f) $e = 5.0$. This shows the strong dependence on initial conditions of the late-time values of $\lambda(t)$ and $c_1(t)$ for $N = 4$ hard rods in a harmonic trap. In (e) and (f) we show the evolution of the time-averaged values of $c_i = T_i/N^2$ of $N = 4$ hard-rods for $e = 0.5$ and $e = 5.0$ respectively, for one realization. In the long time limit, c_1 and c_4 are equal but have a value that is significantly different from c_2 and c_3 , indicating a lack of energy equipartition.	139
7.3	(a,b,c,d) Distribution of the maximal Lyapunov exponent λ and rescaled temperature c_1 of the left-most rod, for $4 \leq N \leq 32$, computed at time $t = 10^5$. The system sizes corresponding to different plots are provided in subplot (c). We find a significant breakdown of ergodicity for hard rods in this harmonic trap. (e,f) Distribution of λ for $N = 8$ at different times, $10^3 \leq t \leq 10^6$, which shows that $P(\lambda, t)$ approaches a steady limiting distribution at late times. The initial conditions for all the plots are generated using the SMED: (a,c,e) for $e = 0.5$ and (b,d,f) for $e = 5.0$	140

7.4	Probability distribution of (a) maximum Lyapunov exponents λ and (b) c_1 for $N = 4$ rods in a quartic trap. We observe that both distributions collapse at different times after shifting by their respective means and scaling by \sqrt{t} . This indicates that the width of these two distributions decreases with time and becomes increasingly sharp, in contrast to our findings for the harmonic trap depicted in Fig. 7.3. In the insets, we show the time evolution of λ and c_1 for 20 different realizations (each color denotes one initial condition), all of which converge to a unique value at late times, regardless of the initial conditions.	141
7.5	Plot of average maximal Lyapunov exponent ($\langle\lambda\rangle$) with rescaled energy e for (a) harmonic and (b) quartic trap. The average number of collisions per unit time $\langle n_{\text{coll}} \rangle$ as a function of total energy e for $N = 8$ for (c) harmonic trap and (d) quartic trap.	142
7.6	(a) Density profiles $\rho(x)$ and (b) velocity distributions $P(v)$ in the harmonic trap, with $e = 0.5$ and $N = 128$, that appear at different times within one time-cycle of the trap, $0 < t \lesssim \tau = 2\pi$. These profiles are obtained starting at $t = 0$ from a two-blob density profile and Gaussian velocity distribution (<i>i.e.</i> Nc-Mx) of the hard rods. For all the figures in (a) and (b), the abscissa runs from -400 to 400 . For (a) and (b), the ordinate scale ranges are $0 - 0.007$ and $0 - 0.01$ respectively. As can be observed, the hard-rod system in a harmonic trap has an initial ‘breathing-mode’ dynamics and exhibits oscillations in the distributions, somewhat resembling Newton’s cradle. For our parameters, these oscillations damp out in $O(20)$ cycles.	144
7.7	Time evolution of density and velocity profiles: (a,c) for $e = 0.5$ and (b,d) $e = 5.0$ for $N = 128$ hard rods in a harmonic trap, starting from Newton’s cradle initial condition (<i>i.e.</i> two spatially separated blobs of rods) with Maxwellian velocities (Nc-Mx, in the notation of Sec. 7.3). The times simulated are indicated by the legend in (b). These plots illustrate that at late times ($t = 10^4\tau$) the density profiles and velocity distributions obtained from EDMD converge to forms that differ from those obtained from SMED.	145

7.8 In this figure, we investigate the initial condition dependence of the late time ($t = 10^4\tau$) distributions obtained from EDMD of hard rods in a harmonic potential. These are compared with thermal predictions obtained from SMED. We compare the density and velocity profiles of 128 rods at two energies (and : (a-c) $e = 0.5$ and (b-d) $e = 5.0$. We use four different initial conditions: (i) uniform density and uniform velocity distribution (blue dashed line), (ii) uniform density and Gaussian velocity distribution (red dotted line), (iii) Newton’s cradle density and uniform velocity distribution (yellow dashed-dotted line), and (iv) Newton’s cradle density and Gaussian velocity distribution (magenta dashed-double-dotted line). We find that neither the density profile nor the velocity distribution agrees between EDMD and SMED (black solid line), even at long times $t = 10^4\tau$. We also observe that late-time density profiles depend on the choice of initial condition for both temperatures. 146

7.9 Time evolution of (a-c) MD density and (b-d) velocity distribution for hard rods in a quartic trap, starting from (a-b) Nc-Mx and (c-d) U-MX initial condition, compared with Monte-Carlo profiles for $N = 16$ and $e = 0.10$. In this case, the MD profile converges to the Monte Carlo (MC) result appreciably fast, and the velocity distribution approaches a Gaussian at late times, as expected for a non-integrable system. 147

7.10 Time evolution of the distance measure, D_{L1} [defined in Eq. (7.12)], between $\rho(x)$ and $\rho_{\text{SMED}}(x)$ for $e = 0.5$ and $e = 5.0$ in a harmonic trap. For both EDMD and SMED, the system is initially prepared in the Nc-Mx initial condition. The oscillations at small times are consistent with the oscillations observed in Fig. 7.6. The saturation of D_{L1} to non-zero values at large times indicates a lack of thermalization to a Gibbs state. 148

- A.1 Plots of the logarithm of the variance of the position of the rightmost particle obtained using the MC simulations of the confined Riesz gas Hamiltonian [Eq. (2.1)] versus the logarithm (base-2) of system size N (disks) for (a) $k = -1.5$, (b) $k = -1.25$, (c) $k = -0.75$, (d) $k = -0.5$, (e) $k = -0.25$, (f) $k \rightarrow 0$, (g) $k = 0.25$, (h) $k = 0.5$, (i) $k = 0.75$, (j) $k = 1.0$, (l) $k = 1.25$, (n) $k = 1.5$, (m) $k = 1.75$, (n) $k = 2.25$, (o) $k = 2.5$. Here we use a linear fit (solid lines) of the data to extract the slope $-2\eta_k$ 162
- A.2 Plots of the logarithm of the variance of the position of the rightmost particle obtained using the MC simulations for the Hessian Hamiltonian [Eq. (4.24)] versus the logarithm (base-2) of system size N (disks) for (a) $k = -1.5$, (b) $k = -1.25$, (c) $k = -0.75$, (d) $k = -0.5$, (e) $k = -0.25$, (f) $k \rightarrow 0$, (g) $k = 0.25$, (h) $k = 0.5$, (i) $k = 0.75$, (j) $k = 1.0$, (l) $k = 1.25$, (n) $k = 1.5$, (m) $k = 1.75$, (n) $k = 2.25$, (o) $k = 2.5$. Here we use a linear fit (solid lines) of the data to extract the slope $-2\eta_k^{(\text{hMC})}$ 163
- A.3 *Regime 2* ($-1 < k < 1$): For $k = 0.5$, the plot of chemical potential as a function of the wall position, computed from numerical integration (circles) of Eq. (A.38) for $z = 0$. This evaluation is compared with the simplified expression given in Eq. (A.45) (solid lines). The parameter used for the computations is $J = 1$ 167
- A.4 *Regime 3* ($-2 < k < -1$): For $k = -1.5$, the plot of chemical potential as a function of wall position, computed from numerical integration (circle) given in Eq. (4.62) and the simplified expression (solid lines) given in Eq. (A.62). Here we considered $J = 1$ 172
- A.5 (a) We join the $P_\theta(y_{\max})e^{\theta y_{\max}}$ for different values of θ by multiplying them by the appropriate normalization constant considering there is a small overlap in the argument of the distribution for two successive values of θ . (b) This stitching procedure gives the distribution of y_{\max} in the unbiased problem for rare fluctuations. 174

A.6 In (a) we plot the scaling function of the thermodynamic pressure [Eq. (A.91)], $\mathbf{P}(w)$, as depicted by the dashed line and the scaled average mechanical pressure [Eq. (A.92)], $\mathbf{P}_M(wN^{\alpha_k}, N)/N^{\frac{2(k+1)}{k+2}}$, as indicated by symbols. The average in Eq. (A.92) is computed using the MC simulations. In plot (b), the scaling function of the bulk modulus [Eq. (A.100)], $\mathbf{K}(w)$, as depicted by the dashed line is compared with \mathbb{K}_m/N [Eq. (A.94)] where $m = c^*(w)N$ and is shown by symbols. In Eq. (A.94), the variance of the position of the m^{th} particle is computed using the MC simulations. We use $k = 1.5$, $T = 1$, and $J = 1$ for performing the MC simulations of the unconstrained gas consisting of $N = 128, 256$ and 512 particles and the averages are computed using 10^6 samples. 182

List of Tables

4.1	The table summarizes the exponents e_k^\mp that characterize the asymptotic behavior of left and right LDF respectively. The reference to the expressions together with the corresponding plot of the LDF in various regimes of k are also provided.	61
6.1	A summary of the scaling behavior of the densities for the hard rods (HR) and the hyperbolic Calogero (HC) model in harmonic and quartic traps.	127
7.1	The table provides a summary of our findings for $N > 3$ hard rods confined to harmonic and quartic traps. The case of $N = 3$ rods in a harmonic trap is special (Fig. 7.1a,b) because it is characterized by vanishing Lyapunov exponents although its quartic counterpart, even for $N = 2$, has non-zero Lyapunov exponents (Fig. 7.1c,d).	149

Contents

Abstract	1
1 Introduction	3
1.1 Overview of the thesis	10
2 Riesz gas in one-dimension	13
2.1 Properties of 1d Riesz gas	16
2.1.1 Field theory for the Riesz gas	16
2.1.2 Average Density profiles of the Riesz gas	19
3 Average density profile in the presence of a hard wall	23
3.1 Introduction	23
3.2 Summary of the results	25
3.3 Derivation	29
3.3.1 Regime 1 ($k \geq 1$): short-ranged interactions	31
3.3.2 Regime 2 ($-1 < k < 1$): Weakly long-ranged interactions	34
3.3.3 Regime 3 ($-2 < k \leq -1$): Strongly long-ranged interactions	38
3.4 Conclusions	49
4 Edge fluctuations and third-order phase transition	53
4.1 Introduction	53
4.2 Summary of the results	58
4.3 Distribution of x_{\max}	63
4.3.1 Distribution in the typical region	63
4.3.2 Distribution in the atypical region	68
4.4 Discussions and Conclusions	80

5	Full counting statistics of 1d short-range Riesz gases in confinement	83
5.1	Introduction	83
5.2	Summary of the main results	86
5.3	Derivation of the number distribution	90
5.4	Index distribution	100
5.5	Linear statistics	103
5.6	Conclusions	105
6	Finite temperature equilibrium density profiles of integrable systems in confining potentials	109
6.1	Introduction	109
6.2	Models and definitions	111
6.3	Field theory formalism	112
6.4	Results from field theory and comparison with Monte-Carlo simulations .	115
6.4.1	Hard rods model	116
6.4.2	Hyperbolic Calogero model	121
6.5	Conclusion	127
7	Unusual ergodic and chaotic properties of trapped hard rods	129
7.1	Introduction	129
7.2	Models and definitions	133
7.3	Numerical methods	135
7.4	Results on Chaos, ergodicity and thermalization	136
7.4.1	Chaos and ergodicity	137
7.4.2	Energy dependence of chaos	142
7.4.3	Thermalization in macroscopic systems	143
7.5	Conclusions	147
8	Conclusions and Outlook	151
A	Appendix	157
A.1	Constrained density profiles	157
A.1.1	Regime 2 : $-1 < k < 1$	157
A.1.2	Regime 3 : $-2 < k \leq -1$	158

A.2	System size dependence of $\sigma_{y_{\max}}$	161
A.3	Large deviation functions	161
A.3.1	Regime 1 : $k > 1$	162
A.3.2	Regime 2 : $-1 < k < 1$	165
A.3.3	Regime 3 : $-2 < k \leq -1$	169
A.4	Importance sampling method	173
A.5	Non-analytic properties of LDF $\Phi(c, w)$	175
A.5.1	$\Phi(c, w)$ for $c \sim \bar{c}(w)$ for a fixed w	176
A.5.2	$\Phi(c, w)$ for $w \sim \bar{w}(c)$ for a fixed c	178
A.6	Pressure and Bulk modulus	179
A.7	Variance of linear statistics	182
A.8	Derivation of the free energy	184
A.8.1	Free energy for hard rods	185
A.8.2	Free energy for hyperbolic Calogero model	186
A.9	Analytical forms of density profiles for hard rods and hyperbolic Calogero model at low and high rescaled temperatures c	188
A.9.1	Analytical forms of the density profiles for hard rods	189
A.9.2	Asymptotic densities for hyperbolic Calogero model	194
	Bibliography	199
	Publication list	231

Abstract

In this thesis, we investigate the equilibrium and non-equilibrium properties of strongly interacting confined systems. We first study the classical 1d Riesz gas model consisting of N particles and confined to an external harmonic potential. These particles interact pair-wise via the repulsive power-law potential of the form: $V(r) \sim J \text{sgn}(k)r^{-k}$ where r represents the interparticle distance and the exponent k ranges from -2 to ∞ . The Riesz gas is an all-to-all interacting model and by tuning the exponent k , we can modify the interactions from short-range (when $k \geq 1$) to long-range (when $-2 < k < 1$).

We consider the Riesz gas in Gibbs equilibrium at $T \sim O(1)$. Initially, we introduce some of the equilibrium properties of the Riesz gas. We use these properties to analyze the behavior of the typical and the atypical fluctuations of different observables in the large- N limit. First, we obtain the large-deviation form for the distribution of the position of the rightmost particle. We also analyze the distribution of the number of particles in a symmetric interval around the origin. This analysis involves the computation of the density profiles in the presence of barriers, which we study in detail.

Next, we focus on the Riesz gas with exponent $k \rightarrow \infty$, this model is equivalent to a system of hard rods of unit length. The hard-rods system is integrable in the absence of external confinement. However, the presence of external confinement breaks the integrability. In the second part of this thesis, we study the density profile of the hard rods when confined to external harmonic and quartic traps at high temperatures. Furthermore, we investigate the chaos, and ergodicity of the trapped hard rod system, to understand its thermalization properties.

Chapter 1

Introduction

Statistical physics has emerged as a powerful tool for investigating many-particle interacting systems. These systems are important for understanding many natural phenomena, like how magnets work, why water freezes, how stars collapse, and even how living things function. To understand them, we generally model the systems such that particles have certain interactions with each other. These interactions can be mainly categorized into two types: short-range (SR) and long-range (LR) interactions. This classification is based on the additivity of energy, which states that the total energy of a combined system is equal to the sum of the energies of its subsystems. For instance, consider a system partitioned into two subsystems as shown in Fig. 1.1. The energy of the left and right

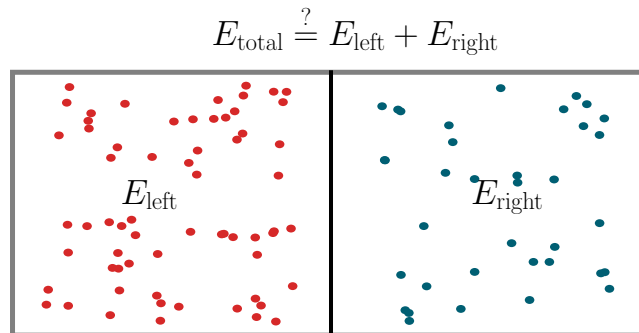


Figure 1.1: Figure adopted from Fig 1 of Ref. [1]. Classification of the range of interaction based on the additivity of energy. The total energy of the system, $E_{\text{total}} = E_{\text{left}} + E_{\text{right}} + E_{\text{inter}}$, is the sum of the energies of left and right partitions (E_{left} and E_{right}) and the energy corresponding to the inter-specific interactions (E_{inter}). For the short-range system as the energy corresponding to the inter-specific interactions are negligible $E_{\text{inter}} \ll E_{\text{total}}$, the system is additive $E_{\text{total}} \approx E_{\text{left}} + E_{\text{right}}$. While for long-range systems the energy is non-additive $E_{\text{total}} \neq E_{\text{left}} + E_{\text{right}}$.

partitions, E_{left} and E_{right} , depends solely on the degrees of freedom (DOF) of the par-

ticles in their respective partitions. In contrast, the total energy of the system depends on the DOF of all particles and is given by $E_{\text{total}} = E_{\text{left}} + E_{\text{right}} + E_{\text{inter}}$ which is the sum of the energies of left and right partitions and the energy corresponding to the inter-specific interactions (E_{inter}). Here the inter-specific interactions stand for the interaction between the particles of different partitions. When the system's energy is non-additive, $E_{\text{total}} \neq E_{\text{left}} + E_{\text{right}}$, it is classified as long-range [1]. Conversely, when the energy is additive, $E_{\text{total}} \approx E_{\text{left}} + E_{\text{right}}$, the system is short-ranged as the inter-specific energy is very small, $E_{\text{inter}}/E_{\text{total}} \ll 1$. For short-range systems, the additivity of energy implies that the total energy is extensive, i.e. it is proportional to the number of particles or the volume of the system. For example, doubling the number of particles or volume would double the energy. Extensivity also implies that the energy per particle (ϵ) is finite and independent of the system size. On the other hand, in long-range systems, the energy per particle diverges with system size. This can be understood by considering a system as shown in Fig. 1.2 with volume V and density ρ of particles interacting via a power-law potential of the form $V_k(\vec{r}) = J/r^k$, where $r = |\vec{r}|$ is the distance between the particles, J is the strength of the interaction and k is the exponent of the power-law potential. The energy per particle (ϵ) can be obtained by integrating the potential energy over the

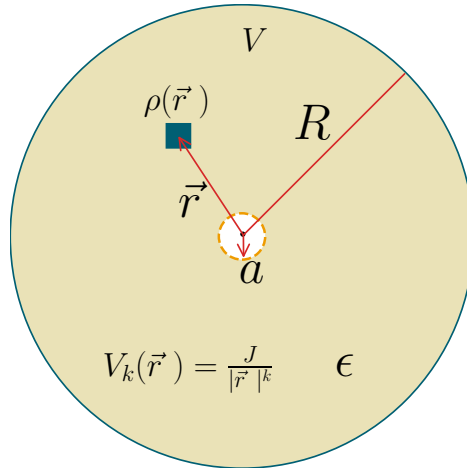


Figure 1.2: Figure adopted from Fig 2 of Ref. [1]. A schematic plot of the spherical region, of radius R , considered for the computation of energy per particle, ϵ . Here the particles interact via a power-law potential of the form $V_k(\vec{r}) = \frac{J}{|\vec{r}|^k}$ with a cutoff radius a . The energy can be computed by summing the potential energy contributed by $\rho(\vec{r})d^d r$ particles located at position \vec{r} , for all values of \vec{r} . This is formally described in Eq. (1.1). It is shown that the energy per particle diverges with increasing volume V for $k < d$, and remains finite for $k > d$.

volume of the system. For the system of radius R and a cutoff radius a for the interaction

potential, the energy per particle is given by:

$$\epsilon = \int_a^R d^d r V_k(\vec{r}) \rho = \frac{J\rho V_d}{(d-k)} (R^{d-k} - a^{d-k}) \sim \frac{J\rho V_d}{(d-k)} \begin{cases} O(V^{1-\frac{k}{d}}) & \text{for } k < d \\ O(V^0) & \text{for } k > d \end{cases}, \quad (1.1)$$

where V_d is the volume of a d dimensional sphere with unit radius. In the thermodynamic limit, the energy of the system is then given by

$$E = \rho V \epsilon = \begin{cases} J\rho O(V^{2-\frac{k}{d}}) & \text{for } k < d \\ J\rho O(V^1) & \text{for } k > d \end{cases}. \quad (1.2)$$

Here, we observe that the energy of the system grows super-extensively with volume for $k < d$ and is extensive for $k > d$. In principle, by rescaling the interaction strength J appropriately with system size, we can restore the extensivity of energy. For example, the energy for a system with $k < d$ can be made extensive if we scale the interaction strength as $J = J_0 V^{\frac{k}{d}-1}$. This procedure of rescaling interaction is called the Kac scaling prescription [2]. While this restores extensivity it does not imply that the energy of the system is additive. Consequently, the system with $k < d$ is called the long-range system and the system with $k > d$ is called the short-range system.

The equilibrium properties of SR systems are well-established and extensively studied using the principles of thermodynamics and statistical mechanics. However, the LR systems are less understood but have also garnered significant interest across various scientific communities, including astrophysics [3–5], plasma physics [6], free electron lasers [7], hydrodynamics [8, 9] and cold atomic physics [10–13]. While the range of interaction provides some classification of systems the possibility of analytical solvability also classifies systems as integrable and non-integrable. Integrable systems [14, 15] are fine-tuned models that have an extensive number of conserved quantities. These models show different properties compared to those of the non-integrable systems with only a few conserved quantities. For example, an isolated non-integrable system with SR interactions, where the energy is conserved, is typically expected to thermalize to the Gibbs ensemble. This ensemble is determined only by the temperature of the system, a conjugate to the energy. In contrast, an isolated integrable system is expected to equilibrate to a statistical state known as the Generalized Gibbs ensemble (GGE) [16]. The GGE differs from the

Gibbs ensemble as it accounts for all the conserved quantities and correspondingly the state is determined by an extensive number of chemical potentials, each conjugate to the respective conserved quantities. While the integrable models and LR systems are areas of active research, there remains much to be understood about their equilibrium and non-equilibrium properties. In this thesis, we investigate how the equilibrium property of a given LR system in thermal equilibrium (Gibbs state) differs from those of the SR system. Next, we investigate if and how an integrable system thermalizes when confined to integrability-breaking traps.

A natural platform to study macroscopic properties of the LR and SR systems is the family of one-dimensional (1d) Riesz gas [17]. It is a classical system of particles interacting via the repulsive potential, of the form $\text{sgn}(k)r^{-k}$, which varies with the interparticle distance (r) as a power-law with an exponent k . By changing the exponent k , we can modify the nature of the interactions from SR when $k > 1$ to LR when $k < 1$. This effectively allows us to systematically study the role of LR and SR interactions. For the Riesz gas, some values of k are well studied such as Dyson's log-gas [18–25] ($k \rightarrow 0$) which is the 2d Coulomb gas and the Calogero-Moser system [15, 26, 27] ($k = 2$) which is an integrable model. Other special values include $k = -1$ and $k \rightarrow \infty$ which are known as the 1d one-component plasma (1dOCP) [28–32] and the hard rods gas [33], respectively. Dyson's log-gas ($k \rightarrow 0$) and 1dOCP ($k = -1$) are LR systems that have been studied theoretically extensively. For example, the edge particle statistics [22, 23, 25, 31, 32], linear statistics [34, 35], truncated linear statistics [36, 37], full counting statistics [31, 32, 38–42], Gap distribution [42, 43] and equilibrium correlations [19, 44] have been computed. Furthermore, the theoretical study of Riesz gas for general k has attracted significant interest not only from the physics communities [45–49] but also is an active area of research in mathematics [50–54].

In experiments of ultra-cold atoms, the particles can now be engineered to have specific interactions [11–13]. For example, using a strong electromagnetic field, a dipole-dipole-like interaction gets induced between the atoms of Strontium-84 (^{84}Sr). These interactions can be effectively modelled as a long-range power-law potential with exponent $k \sim -1$ [12]. Quantum simulators have been developed [55] which are a type of quantum computer where the interaction between the qubits can be controlled. In such simulators, the laser-driven interactions can be tuned, and the system can be well described by an interacting

spin system where the coupling strength between spins is a power-law with an exponent that can be adjusted between $k = 0.0$ to 3.0 . Moreover, recent experimental techniques have made it possible to probe physics at a microscopic scale as demonstrated in cold atoms [56–58] and ions [13]. Given the experimental feasibility of studying the 1d systems with power-law interaction and the versatility of Riesz gas, it is a natural model to theoretically study the equilibrium and non-equilibrium properties of LR and SR systems. One of the aims of this thesis is to study some of the equilibrium properties of the Riesz gas for general k . In particular, we focus on local observables like the position of the rightmost particle [59] and the global observables like the average thermal density profile in the presence of barriers [60], the full counting statistics of the number of particles in a symmetric domain $[-W, W]$ and the index distribution for the semi-infinite domain $(-\infty, W]$ [61]. In the above mentioned studies, we consider Riesz gas in equilibrium at $T \sim O(1)$. At higher temperatures the properties of these system for general k are not well understood. Consequently, we further study the average density profile at all temperatures for a special case of $k \rightarrow \infty$ of the Riesz gas known as the hard rod gas. This average density profile can be used to benchmark the thermalization behaviour of hard rods confined to external trap.

To study the equilibrium properties of an isolated system, we generally expect that all the microscopic configurations with fixed energy are equally probable [62–64]. This is based on the assumption of ergodicity and molecular chaos. While ergodicity implies that the time average of any observable is equal to its ensemble average, chaos in a system quantifies or indicates the loss of information about the initial conditions. Similarly, when the SR system is in contact with the environment, where only energy exchange is allowed, it is expected that the probability of any microscopic configuration is given by the Gibbs-Boltzmann distribution [62–64]. However, a natural question arises: what properties should a system possess such that it reaches a Gibbs state or other equilibrated states? Are chaos and ergodicity really necessary? These questions have puzzled physicists for a long time, and the well-known attempt to answer them was the famous Fermi-Pasta-Ulam-Tsingou (FPUT) problem [65].

In the FPUT problem, the particles interact via non-linear springs with small non-linearity and evolve based on Newton’s equations of motion. Starting from a specific class of initial configurations they found that the system at long times did not reach

equilibrium. To understand this behavior many mechanisms have been proposed [66–73]. One of the main reasons could be its proximity to an integrable model as it can be described by a perturbation of an integrable model [74–77]. More recently, in the first-of-its-kind experiment, an anharmonically trapped Bose-Einstein condensate of ultra-cold Rubidium atoms was investigated [78]. This gas can be modeled up to a good approximation [79] by the well-known Lieb-Liniger model, where the identical Bosons have contact repulsion formally expressed by a delta function interaction. The Lieb-Liniger gas is an integrable model when it is not trapped. However, the trap breaks its integrability. In the experiment, Newton’s-cradle-like oscillatory dynamics was observed as shown in Fig. 1.3. To understand this peculiar oscillatory dynamics, the theory of

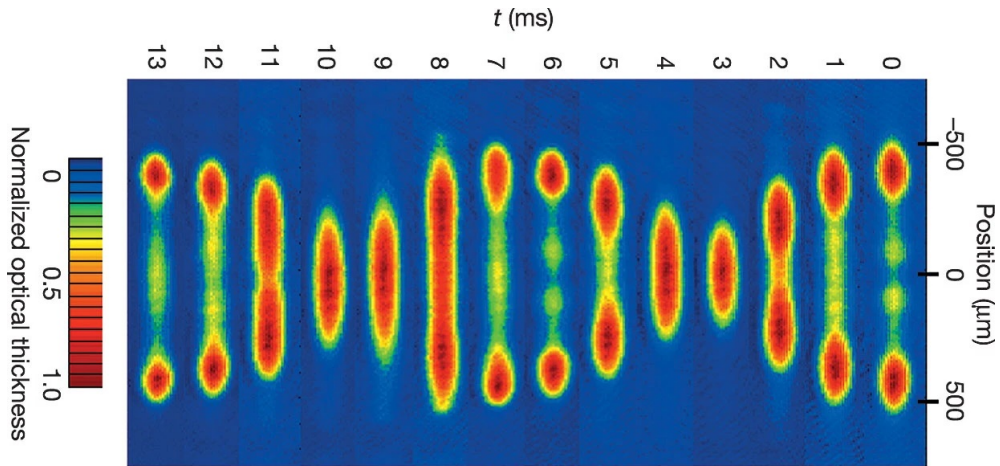


Figure 1.3: Figure taken from Ref. [78]. The figure shows the absorption image for the anharmonically trapped Bose-Einstein condensate of Rubidium-87 (^{87}Rb) consisting of 2.5×10^5 atoms. In the experiment, the two clouds of atoms were separated away from the center of the trap. These two clouds oscillate within the trap and meet twice every period. In the plot, note that the progression of time is from right to left. Interestingly the clouds keep oscillating for the large observation times akin to the balls of a Newton’s cradle toy where the momentum gets transferred to the other ball upon collision. This oscillatory behavior suggests that the system does not thermalize even after each atom has undergone several thousand collisions.

generalized hydrodynamics (GHD) [80,81] was used. The GHD equation at Euler’s scale are useful to describe the hydrodynamic evolution of conserved quantities for integrable systems. A key assumption to obtain the hydrodynamic evolution is the notion of local equilibrium [82]. While the presence of an external trap breaks integrability, the local dynamics remain similar to those of a homogeneous evolution governed by an integrable Hamiltonian. Consequently, the approximation of local GGE stays valid under time evolution. As a result, a modified GHD was proposed [83] which incorporates the effects

of external trapping in the form of an additional force-like term. This is similar to the case of conventional hydrodynamics like the Navier-Stokes equation where a force term is used to represent the effect of the external field even though the momentum is no longer a conserved quantity. This modified GHD proved to be effective in modeling such short-time oscillatory dynamics [84–86]. However, the fate of these systems at long times remains inconclusive. In the experiment, it was found that the system did not thermalize even after each atom had undergone several thousand collisions. This is in contrast to generic ultra-cold atomic gases where only a few collisions typically lead to thermalization [87].

To theoretically understand the long-time behavior of integrability-broken systems, a classical model of hard rods confined to a harmonic trap in 1d was investigated in Ref. [84]. The hard rod system in 1d is an integrable model where the rods undergo elastic collisions and they only exchange momenta. Consequently, the momenta of all the particles only get permuted under the dynamics and are conserved, which suggests the model is integrable. When these hard rods are confined to an external harmonic potential, integrability is broken. The time evolution of the confined rods was numerically studied in Ref. [84] using molecular dynamics simulation. It was observed that the system is chaotic but did not thermalize to the Gibbs state at the longest accessible simulation times (around 10,000 periods of trapping potential), instead reaches a non-Gibbsian stationary state. It was also shown [84], that this non-thermal state is well described by the modified GHD at Euler scale (no dissipation). It is important to note that the Euler GHD does not lead to the entropy production expected of systems that are equilibrating and hence an appropriate diffusive correction needs to be incorporated [88]. Interestingly, it was proposed that the diffusive correction in the modified GHD could thermalize the system [86]. However, this proposal starkly contrasts the observation of the non-thermal steady state at long times for the harmonically confined hard rods studied in Ref. [84]. This raises a natural question: even if the system goes to a thermal state, due to diffusive correction to the modified GHD, why is the time scale so long *i.e.* longer than the numerically accessed times in Ref. [84]? It is important to recognize that the modified GHD is a phenomenological theory and the true evolution of these systems could be very different, governed by the microscopic dynamics of positions and momenta of the particles. Therefore, studying the microscopic dynamics of the hard rods in the presence of

the external trap is crucial, which we undertake in the later part of the thesis. Moreover, several fundamental questions concerning the thermalization of trapped integrable particles remain unresolved, including whether or not these systems are truly ergodic, whether they can support additional microscopic conservation laws, and how far these properties coexist with chaos. In the second part of this thesis, we aim to address some of these questions using molecular dynamics simulations in the context of 1d hard rods confined to harmonic and quartic traps.

1.1 Overview of the thesis

This thesis is structured as follows. In Chapter 2, we define the Riesz gas in 1d and summarize the well-known equilibrium properties of the Riesz gas. Chapters 3, 4, 5, 6 and 7 are based on five different articles provided at the end of each chapter. In Chapter 8, we provide a conclusion.

In Chapter 3, we study the density profiles of the constrained Riesz gas at $T \sim O(1)$. Using the saddle point method, we compute the equilibrium density profile of the particles in the presence of a hard wall such that all the particles are always to the left of the wall. We find that the density profiles show three different behaviors depending on the exponent k . Furthermore, by analyzing the behavior of the density profiles as the position w of the hard wall is changed, we find that the system undergoes a first-order phase transition for all k s with value $-2 < k < -1$.

In Chapter 4, we focus on the probability distribution of the position of the rightmost particle. Using the Coulomb gas method we compute the distribution of the atypical fluctuations. The atypical fluctuations have a large deviation form with appropriate large-deviation functions which we analytically compute and verify using numerical simulations. By studying the asymptotic behavior of the large-deviation functions, we find that the system undergoes a pulled to pushed third-order phase transition for all $k > -2$. Furthermore, we numerically study the distribution of the typical fluctuations which shows non-Gaussian behavior different from the Tracy-Widom distribution that appears in Random matrix theory or Dyson's Log-gas [89,90]. Using the asymptotic behavior of the large deviation function we conjecture the system size dependence of the variance of the position of the rightmost particle. It works well for k values $-2 < k < 0$.

In Chapter 5, we investigate the full counting statistics (FCS) of a harmonically confined 1d short-range Riesz gas. We examine the probability distribution of the number of particles in a finite domain $[-W, W]$ called number distribution. Using the Coulomb gas method, we find that the probability distribution possesses a large deviation form and the large deviation function depends on the the fraction c of the particles inside the domain and W . We show that the density profiles that create the large deviations display interesting shape transitions as one varies c and W . This is manifested by a third-order phase transition exhibited by the large deviation function that has discontinuous third derivatives. Monte Carlo (MC) simulations show good agreement with our analytical expressions for the corresponding density profiles. By analyzing the large deviation function around its minimum we find that the typical fluctuations are Gaussian distributed and we compute its variance. Additionally, we adapt our formalism to study the index distribution (where the domain is semi-infinite $(-\infty, W]$), thermodynamic pressure, and bulk modulus. In the previous three chapters, we focused on the low-temperature or $T \sim O(1)$ properties of the Riesz gas when the entropy was subdominant. One naturally wonders about their high-temperature properties when the entropy is of a similar magnitude as the energy. In the next chapter 6, we investigate this regime for the hard rods which is $k \rightarrow \infty$ of the Riesz gas.

In Chapter 6, we focus on the equilibrium density profile of the one-dimensional classical integrable models, namely the hard rods placed in confining potentials at very high temperatures. Using a field-theoretic technique, we compute the density profile and their scaling with system size and temperature. We further compare the average density profiles with results from Monte-Carlo simulations and find good agreement between the field theory and simulations.

In chapter 7, we move away from equilibrium and study the equilibration properties of the hard rods. We investigate ergodicity, chaos, and thermalization for the hard rods confined to an external (harmonic or quartic) trap, which breaks integrability. We find that harmonically trapped hard rods are highly non-ergodic and do not resemble a Gibbs state even at extremely long times, despite compelling evidence of chaos for four or more rods. On the other hand, our numerical results reveal that hard rods in a quartic trap exhibit both chaos and thermalization and eventually equilibrate to a Gibbs state as expected for a nonintegrable many-body system.

Chapter 2

Riesz gas in one-dimension

In this chapter, we introduce the classical Riesz gas [17] in one dimension (1d), a central theme of this thesis, and discuss the equilibrium properties originally derived in Ref. [45] which are important for our work. The Riesz gas is composed of N particles confined to an external trap and interacting via repulsive pair-wise potential which varies with distance as a power-law. When these particles are confined to harmonic trap $U(x) = x^2/2$, the

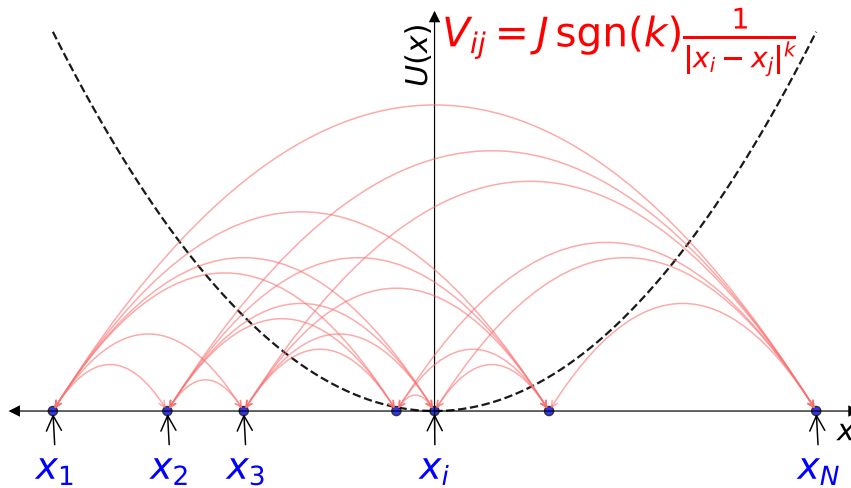


Figure 2.1: Schematic plot of the particles of the Riesz gas in 1d. The particles of Riesz gas interact via all-to-all repulsive pair-wise potential of the form $V_{ij} = J \operatorname{sgn}(k) |x_i - x_j|^{-k}$ where $x_{i/j}$ represents the position of the i/j -th particle, the interaction strength $J > 0$ and $\operatorname{sgn}(k)$ ensures that the particles repel each other. The external confinement $U(x)$ is represented by the dashed curve and the all-to-all nature of interactions is shown by the double-arrow-headed solid arcs.

energy function of the system is given by

$$\tilde{E}_k(\{x_i\}) = \sum_{i=1}^N \frac{x_i^2}{2} + \frac{J \operatorname{sgn}(k)}{2} \sum_{i=1}^N \sum_{\substack{j=1 \\ j \neq i}}^N |x_i - x_j|^{-k}, \quad (2.1)$$

where $\{x_i\}$ denotes the positions of the particles on a line and the exponent k characterizes the range of the interaction, it is LR for $-2 < k < 1$ and SR for $k \geq 1$. The interaction strength J is positive and $\operatorname{sgn}(k)$ in Eq. (2.1) ensures that the pair-wise interaction is always repulsive. In Fig. 2.1 we show a schematic demonstration of these particles. We confine our study to the range $k > -2$. For $k < -2$, the repulsive interaction term $|x_i - x_j|^{-k}$ is stronger than the confining potential x_i^2 and the configuration is unstable and the particles fly away to $\pm\infty$ to minimize energy.

For this system, the external potential ($U(x) = x^2/2$) tries to confine all the particles to the bottom of the trap, and the repulsive interactions ($V(r) \sim \operatorname{sgn}(k)r^{-k}$) tries to push the particles apart. As a result, one expects that in the large- N limit, the positions of the particles in the minimum energy configuration are supported over a length scale L_N such that both the terms in the energy function in Eq. (2.1) are balanced. Consequently, the length scale L_N depends on the exponent k and also on the number of particles N . For the notational simplicity, we drop the explicit k dependence. To estimate L_N , we first compute the approximate N dependence of the interaction and external potential energy in the limit of large- N as follows. We introduce a scaled variable y_i for $i = 1, 2, 3, \dots, N$ such that

$$y_i = \frac{x_i}{L_N}, \quad \text{with } y_i \sim O(1), \quad (2.2)$$

where $x_i \sim O(L_N)$ is the position of the i -th particle. For large- N , the N dependence of the harmonic potential energy is approximately given by

$$\sum_{i=1}^N x_i^2 = NL_N^2 \frac{\sum_{i=1}^N y_i^2}{N} \sim O(NL_N^2). \quad (2.3)$$

Similarly, the interaction energy can be estimated as follows

$$\sum_{i=1}^N \sum_{\substack{j=1 \\ j \neq i}}^N |x_i - x_j|^{-k} = L_N^{-k} \sum_{i=1}^N \sum_{\substack{j=1 \\ j \neq i}}^N |y_i - y_j|^{-k}. \quad (2.4)$$

To estimate the double sum we note that the typical distance between adjacent particles is $\sim O(N^{-1})$ and consequently one expects $|y_i - y_j| \sim O(N^{-1}|i - j|)$. Therefore, the interaction energy scales as

$$\sum_{i=1}^N \sum_{\substack{j=1 \\ j \neq i}}^N |x_i - x_j|^{-k} \sim \begin{cases} O(N^{k+1} L_N^{-k}) & \text{for } k > 1 \\ O(N^2 \ln N L_N^{-1}) & \text{for } k = 1 \\ O(N^2 L_N^{-k}) & \text{for } -2 < k < 1 \end{cases}. \quad (2.5)$$

Here, the differences arise due to the convergence behavior of the series $\sum_{n=1}^N n^{-k}$, in the thermodynamic limit, for different values of k . In particular, the series is convergent *i.e.* takes a finite value for $k > 1$ and diverges Logarithmically as $\sim O(\ln N)$ for $k = 1$ and as a power-law N^{1-k} for $k < 1$ in the large- N limit. By balancing the energy contribution due to the external potential given in Eq. (2.3) and the interaction potential given in Eq. (2.4), one finds

$$L_N = \begin{cases} N^{\alpha_k} & \text{for } -2 < k \neq 1 \\ (N \ln N)^{1/3} & \text{for } k = 1 \end{cases}, \quad \text{where } \alpha_k = \begin{cases} \frac{k}{k+2} & \text{for } k > 1 \\ \frac{1}{k+2} & \text{for } -2 < k < 1 \end{cases}. \quad (2.6)$$

In terms of the scaled variables $\{y_i\}$, many computations and results are more convenient and revealing and we use them frequently. For example, the energy function in Eq. (2.1) can now be expressed in terms of the scaled variables $\{y_i\}$ as

$$\begin{aligned} \tilde{E}_k(\{x_i\}) &= N L_N^2 E_k(\{y_i\}), \quad \text{where, } y_i = \frac{x_i}{L_N} \text{ and,} \\ E_k(\{y_i\}) &= \frac{1}{N} \sum_{i=1}^N \frac{y_i^2}{2} + \frac{J \operatorname{sgn}(k)}{2} \frac{1}{N L_N^{k+2}} \sum_{i=1}^N \sum_{\substack{j=1 \\ j \neq i}}^N |y_i - y_j|^{-k}. \end{aligned} \quad (2.7)$$

Here L_N is given in Eq. (2.6) and the energy function scales super extensively with system size as $\tilde{E}_k(\{x_i\}) \sim O(N L_N^2)$ as the scaled energy is $E_k(\{y_i\}) \sim O(1)$ and $L_N > O(1)$ for

all k . The super extensive scaling of the energy function is due to the external potential and the all-to-all nature of the interactions in the Riesz gas.

For the Riesz gas in thermal equilibrium at temperature $T = \beta^{-1}$, the joint probability distribution function (jpdf) of the positions of the particles is described by the Gibbs-Boltzmann distribution given by

$$P_k(\{x_i\}) = \frac{1}{Z_k} \exp(-\beta \tilde{E}_k(\{x_i\})), \quad (2.8)$$

where $\tilde{E}_k(\{x_i\})$ is given in Eq. (2.1) and the partition function is given by

$$Z_k = \int_{-\infty}^{\infty} dx_1 \int_{-\infty}^{\infty} dx_2 \cdots \int_{-\infty}^{\infty} dx_N \exp(-\beta \tilde{E}_k(\{x_i\})), \quad (2.9)$$

which normalizes this probability distribution. To keep our notation light, the temperature ($T = \beta^{-1}$) and system size N dependence of the partition function, $Z_k \equiv Z_k(N, \beta)$, and the jpdf, $P_k(\{x_i\}) \equiv P_k(\{x_i\}, N, \beta)$, is assumed to be present implicitly and is stated otherwise. For the Riesz gas, some of the equilibrium properties have been studied in Ref. [45] and discussed in the following sections.

2.1 Properites of 1d Riesz gas

In this section, we provide an overview of some of the known results for the harmonically confined Riesz gas in 1d. We first discuss the field-theoretic energy functional which was derived in Ref. [45] and then discuss the average density profiles of the Riesz gas in Gibbs equilibrium. These results are used extensively in Chapters 3,4 and 5.

2.1.1 Field theory for the Riesz gas

To study the equilibrium properties, generally one has to compute the partition function given in Eq. (2.9), and performing this N -fold integral is hard for general k . However, one can compute it in the large- N limit by coarse-graining the system in terms of the empirical density profile, $\rho_N(x) = \frac{1}{N} \sum_{i=1}^N \delta(x - x_i)$ which is normalized to unity. The main difficulty in this coarse-graining procedure is going from the microscopic configuration of the positions of particles to the macroscopic density profile, $\{x_i\} \rightarrow \rho_N(x)$. More specifically, expressing the energy function $\tilde{E}_k(\{x_i\})$ given in Eq. (2.1) as a functional of

the density profile $\rho_N(x)$. This was achieved in Ref. [45] where expressed the energy due to harmonic confinement in Eq. (2.1) was expressed in terms of the density profiles as

$$\sum_{i=1}^N \frac{x_i^2}{2} = \frac{N}{2} \int_{-\infty}^{\infty} dx x^2 \rho_N(x). \quad (2.10)$$

Similarly, the double summation in the interaction term given in Eq. (2.1) can be expressed as a functional of the density profile $\rho_N(x)$ as

$$\sum_{i=1}^N \sum_{\substack{j=1 \\ j \neq i}}^N |x_i - x_j|^{-k} \approx \frac{N^2}{2} \int_{-\infty}^{\infty} \int_{-\infty}^{\infty} dx' dx \frac{\rho_N(x') \rho_N(x)}{|x - x'|^k} \quad \text{for } -2 < k < 1. \quad (2.11)$$

Here, the self energy corrections are subleading to this $O(N^2)$ term in the large- N limit and the integral $\int_{-\infty}^{\infty} dx' \rho_N(x') \rho_N(x) |x - x'|^{-k}$ refers to the principal value integral for $0 < k < 1$ due to the integrable singularity at $x = x'$. For $k \geq 1$, the coarse-graining turns out to be harder due to the non-integrable singularity of the potential $|x_i - x_j|^{-k}$ at $x_i = x_j$. Consequently, the double sum cannot be expressed as a double integral and instead has to be evaluated more carefully and the following different approach is used. By ordering the position of the particles $x_1 < x_2 < \dots < x_N$, x_i can be approximated by a smooth function $x(i)$ of the index i in the large- N limit. Next, using the Taylor series expansion of $x(j) \approx x(i) + (j - i)x'(i)$ in the interaction term of Eq. (2.1) one obtains

$$\sum_{i=1}^N \sum_{\substack{j=1 \\ j \neq i}}^N |x_i - x_j|^{-k} \approx \sum_{i=1}^N \sum_{\substack{j=1 \\ j \neq i}}^N |i - j|^{-k} (x'(i))^{-k}, \quad (2.12)$$

where $x'(i) = dx(i)/di$ is the gap between the i -th and $(i+1)$ -th particle and only the first term of the series expansion is considered. The gap $x'(i) = x_{i+1} - x_i$ can be expressed as the inverse of the density at x_i *i.e.*, $x'(i) = 1/N\rho_N(x_i)$. The interaction term then can be expressed as a functional of the density profile $\rho_N(x)$ as

$$\sum_{i=1}^N \sum_{\substack{j=1 \\ j \neq i}}^N |x_i - x_j|^{-k} \approx \begin{cases} \zeta(k) N^{k+1} \int_{-\infty}^{\infty} dx [\rho_N(x)]^{k+1}, & \text{for } k > 1 \\ N^2 \ln N \int_{-\infty}^{\infty} dx [\rho_N(x)]^{k+1}, & \text{for } k = 1 \end{cases}, \quad (2.13)$$

where $\zeta(k) = \lim_{N \rightarrow \infty} \sum_{n=1}^N n^{-k}$ is the Riemann zeta function and appears due to the all-to-all nature of the interaction. For $k = 1$, the sum $\sum_{n=1}^N n^{-k}$ diverges Logarithmically

with N and consequently the interaction term is modified. In Eq. (2.13) the next-order terms are subleading in the thermodynamic limit. Using the expressions for the external potential energy and interaction energy from Eqs. (2.10), (2.11) and (2.13) in Eq. (2.1), we find that the coarse-grained energy functional $\tilde{\mathcal{E}}_k[\rho_N]$ in the large- N limit can be expressed in the following concise form

$$\tilde{\mathcal{E}}_k[\rho_N] = \frac{N}{2} \int_{-\infty}^{\infty} dx x^2 \rho_N(x) + J \begin{cases} \zeta(k) N^{k+1} \int_{-\infty}^{\infty} dx [\rho_N(x)]^{k+1}, & \text{for } k > 1 \\ N^2 \ln N \int_{-\infty}^{\infty} dx [\rho_N(x)]^2, & \text{for } k = 1 \\ \frac{\text{sgn}(k) N^2}{2} \int_{-\infty}^{\infty} \int_{-\infty}^{\infty} dx' dx \frac{\rho_N(x') \rho_N(x)}{|x-x'|^k} & \text{for } -2 < k < 1. \end{cases} \quad (2.14)$$

For $k \geq 1$, the interaction term is a local functional of the density profile $\rho_N(x)$, indicating that the interactions are SR. In contrast, for $-2 < k < 1$, the interaction term is non-local, effectively capturing the LR nature in this case. It turns out that for large- N the density profile possesses the following scaling relation

$$\rho_N(x) = \frac{1}{L_N} \rho \left(\frac{x}{L_N} \right). \quad (2.15)$$

Using this form, the energy functional in Eq. (2.14) can be expressed in terms of the scaled density function $\rho(y)$ as

$$\tilde{\mathcal{E}}_k[\rho_N(yL_N)] = \mathcal{B}_N \mathcal{E}_k[\rho(y)], \quad \text{where } \mathcal{B}_N = NL_N^2, \quad \text{and}, \quad (2.16)$$

$$\mathcal{E}_k[\rho(y)] = \frac{1}{2} \int_{-\infty}^{\infty} dy y^2 \rho(y) + J \begin{cases} \zeta(k) \int_{-\infty}^{\infty} dy \rho(y)^{k+1}, & \text{for } k > 1 \\ \int_{-\infty}^{\infty} dy \rho(y)^2, & \text{for } k = 1 \\ \frac{\text{sgn}(k)}{2} \int_{-\infty}^{\infty} \int_{-\infty}^{\infty} dy' dy \frac{\rho(y) \rho(y')}{|y-y'|^k}, & \text{for } -2 < k < 1. \end{cases}$$

Clearly, the energy $\tilde{\mathcal{E}}_k[\rho_N]$ in Eq. (2.14) is superextensive and scales with system size as $\tilde{\mathcal{E}}_k[\rho_N] \sim O(NL_N^2)$. This field theoretic free energy was used in Ref. [45] to compute the average density profiles of the Riesz gas in Gibbs equilibrium at temperature $T \sim O(1)$. We discuss these results next.

2.1.2 Average Density profiles of the Riesz gas

The average density profile $\langle \rho_N(x) \rangle$ in the large- N limit minimizes the free energy of the Riesz gas [45]. The free energy $\tilde{F}_k[\rho_N]$ has contributions from the energy of the system and the configurational entropy $\tilde{S}[\rho_N]$ as $\tilde{F}_k[\rho_N] = \tilde{\mathcal{E}}_k[\rho_N] - T\tilde{S}[\rho_N]$. The configurational entropy is the entropy due to the number of ways the particles can be arranged in the system such that the density profile is given by ρ_N . In the large- N limit, the entropy functional can be expressed as $\tilde{S}[\rho_N] = -N \int_{-\infty}^{\infty} dx \rho_N(x) \ln \rho_N(x) \sim O(N)$. At $T \sim O(1)$, the contribution of the extensive configurational entropy $\tilde{S}[\rho_N] \sim O(N)$ to the free energy $\tilde{F}_k[\rho_N]$ is negligible when compared to the super-extensive energy function $\tilde{\mathcal{E}}_k[\rho_N] \sim O(NL_N^2)$. Hence the free energy gets dominated by the energy only. Consequently, the average density profile $\langle \rho_N(x) \rangle$ is the one which minimizes the energy functional $\tilde{\mathcal{E}}_k[\rho_N]$ given in Eq. (2.14) with the constraint that the density profile is normalized $\int_{-\infty}^{\infty} dx \rho_N(x) = 1$. In Ref. [45], the average density profile in the large- N limit was formally obtained using the saddle point method. It was shown that the shape and the scale of the average density profile crucially depend on the exponent k . For any k , it has finite support and is described by the following scaling form

$$\langle \rho_N(x) \rangle = \frac{1}{L_N} \rho_{\text{uc}}^* \left(\frac{x}{L_N} \right), \quad (2.17)$$

where the scaling function $\rho_{\text{uc}}^*(y)$ is given by

$$\rho_{\text{uc}}^*(y) \equiv \rho_{\text{uc}}^*(y, k) = A_k (l_{\text{uc}}^2 - y^2)^{\gamma_k}, \quad \text{for } -l_{\text{uc}} < y < l_{\text{uc}}, \quad \text{with} \quad (2.18)$$

$$\gamma_k = \begin{cases} \frac{1}{k} & \text{for } k \geq 1 \\ \frac{k+1}{2} & \text{for } -2 < k < 1 \end{cases}, \quad \text{and } l_{\text{uc}} \equiv l_{\text{uc}}(k) = \frac{1}{2} (A_k B(\gamma_k + 1, \gamma_k + 1))^{-\alpha_k}. \quad (2.19)$$

Here, $B(a, b) = \int_0^1 dx x^{a-1} (1-x)^{b-1}$ is the Beta function and the constant A_k is given by

$$A_k = \begin{cases} [2J(k+1)\zeta(k)]^{-\gamma_k} & \text{for } k > 1 \\ \frac{1}{4J} & \text{for } k = 1 \\ \frac{\sin(\pi\gamma_k)}{2\pi J|k|^{\gamma_k}} & \text{for } -2 < k < 1 \end{cases}, \quad (2.20)$$

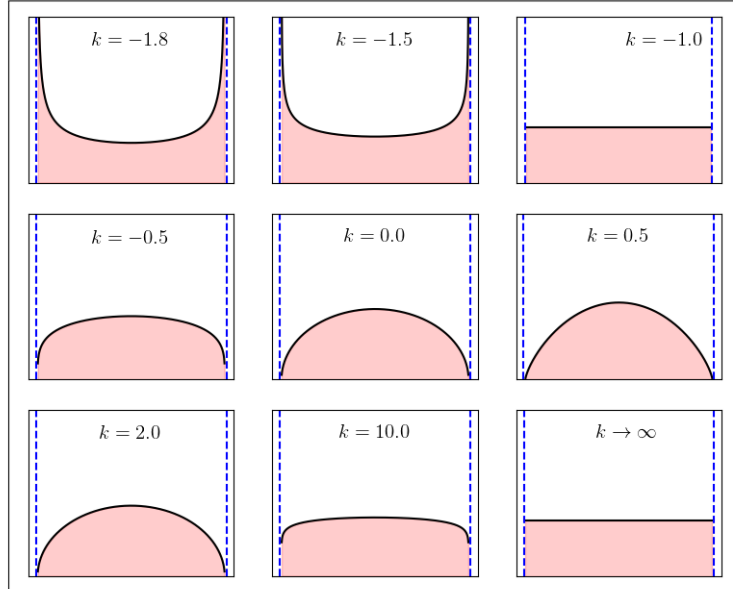


Figure 2.2: Figure adopted from Fig. 1 of Ref [45]. Scaled average density of the unconstrained gas $\rho_{\text{uc}}^*(y)$ in Eq. (2.18) vs. y for different values of $k > -2$. The three rows correspond respectively to (i) $k \geq 1$ (third row), (ii) $-1 < k < 1$ (second row), and (iii) $-2 < k \leq -1$ (first row). In (i) the density has a dome shape, in (ii) also has a dome shape, and in (iii) it has a U-shape. At $k = -1$ and $k \rightarrow +\infty$ the density is flat. The blue dashed vertical lines indicate the edges of the support of the density profile.

The formulae Eq. (2.20) are true for $k \neq 0$. However for $k \rightarrow 0$, as described in the introduction one has to assume $J = J_0/k$ to get a meaningful limit. In this limit $l_{\text{uc}} = \sqrt{2}$ and $A_0 = 1/\pi$. The superscript ‘uc’ in $\rho_{\text{uc}}^*(y)$ and l_{uc} refers to the Riesz gas in the unconstrained setup where no physical constraint other than harmonic confinement is present. Note that for notational simplicity, the k dependence of $\rho_{\text{uc}}^*(y)$ and l_{uc} are assumed to be present implicitly.

The Fig. 2.2 is taken from Fig. 1 of Ref. [45], it shows the shapes of the scaling form for the average density profile given in Eq. (2.18) for different values of k . The density profile changes shape as k is modified and its behaviour can be described separately in three regimes of k depending on the range of the pairwise interactions (see Fig. 2.3):

- (i) *Regime 1 ($k \geq 1$): short-ranged interactions.* In this range, the interaction falls off rather rapidly, as a function of the separation between two particles. Consequently, one can replace the pairwise long-ranged interaction with an effective short-ranged one. In this regime, the average density is dome-shaped with a maximum at the center and the density vanishes at the two edges of the support (see the third row of Fig. 2.2).

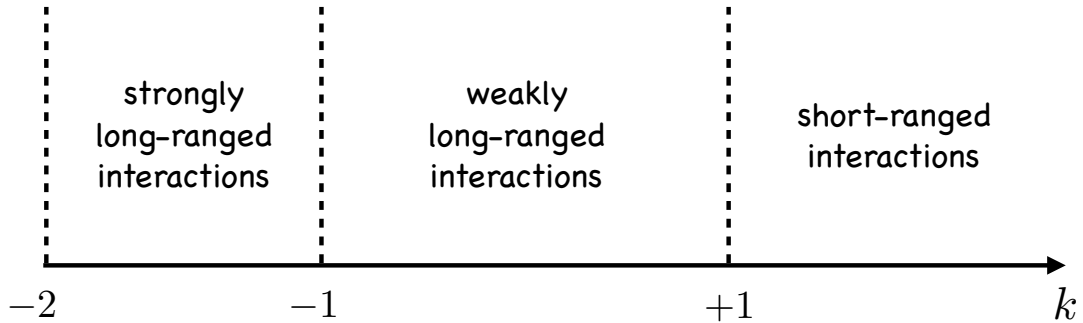


Figure 2.3: The exponent k characterizes the range of pairwise repulsive interactions between particles. For $k \geq 1$ the interaction is effectively short-ranged. For $-1 < k < 1$, the interaction, though long-ranged, is effectively weak and does not qualitatively change the shape of the density profile compared to the short-ranged case. For $-2 < k \leq -1$, the particles are subjected to strong long-range interactions, that change the shape of the density profile drastically.

- (ii) *Regime 2* ($-1 < k < 1$): *weakly long-ranged interactions*. In this case, the long-ranged interaction can not be replaced by an effective short-ranged one as in the regime 1 above. Nevertheless, the average density remains dome-shaped, as in regime 1 (see the second row of Fig. 2.2). Hence we call this regime “weakly long-ranged”.
- (iii) *Regime 3* ($-2 < k \leq -1$): *strongly long-ranged interactions*. In this regime, the repulsive force between two particles (i.e., the derivative of the pairwise interaction potential) vanishes when they get closer to each other. However, at large distances, the force increases with separation $|r|$ as a power law $\sim |r|^{|k|-1}$, making this a “strongly long-ranged” system. This affects rather strongly the shape of the average density profile. In fact, the density profile is now ‘U-shaped’ where it diverges at the two edges (but still integrable) and has a minimum at the center of the support (see the first row of Fig. 2.2).

The density profile is completely flat exactly at $k = -1$. Furthermore, the system undergoes a change of behavior at $k = 1$. This is also manifest in the k -dependence of the exponents α_k and γ_k in Eqs. (2.6) and (2.19) where one sees a drastic change of behavior as k crosses the value $k = 1$. Note that the classification of the three regimes above is based on the shape of the density profile. This is somewhat different from the nomenclature (short-ranged/weakly long-ranged and strongly long-ranged) typically used in the literature on long-ranged interacting particle systems, where the classification is

based on the thermodynamic behavior of the free energy [91].

The study of the average density profile is one of the most basic questions as it can be used to compute the free energy of the system— essential for studying equilibrium properties. Consequently, this calculation was extended for a finite-range (not all-to-all coupled) Riesz gas [92, 93]. In a similar spirit, a natural question arises: how do the average density profiles get modified for all values of k when the system is subjected to barriers that restrict the particles to a particular side? This modified density profile, as we will see later, is an important ingredient for studying various quantities of the Riesz gas. This is the subject of the next Chapter.

Chapter 3

Average density profile in the presence of a hard wall

3.1 Introduction

The main goal of this Chapter is to study how the average density profile in the unconstrained Riesz gas gets modified in the presence of a wall at position W , such that the particles are constrained to stay to the left of the wall. This is a naturally interesting question in any interacting particle system: how does the presence of a hard wall affect the collective properties of the system, such as the average density? Recent experimental progress has made ultra-cold gases an ideal platform to explore such collective behavior. In many experiments involving ultra-cold gases, appropriate barriers are introduced to create desired non-trivial density profiles in a controllable/tunable manner [10, 94–97]. It is also an important intermediate step in the computations of extreme value statistics (EVS) in a strongly interacting system [98]. In EVS, one is interested in the distribution of the position of the rightmost particle, x_{\max} . Using the Boltzmann distribution in Eq. (2.8), the cumulative distribution of x_{\max} , in thermal equilibrium at inverse temperature β , is given by [25]

$$\text{Prob.}(x_{\max} \leq W) = \frac{1}{Z_k} \int_{-\infty}^W dx_1 \dots \int_{-\infty}^W dx_N e^{-\beta \tilde{E}_k[\{x_i\}]}, \quad (3.1)$$

where Z_k is the partition function of the Riesz gas given in Eq. (2.9) and $\tilde{E}_k[\{x_i\}]$ is its energy defined in Eq. (2.1). To evaluate this restricted partition function in the large N

limit using the saddle-point method, one needs to compute the density that optimizes the multiple integrals in Eq. (3.1). This optimal density, in the large N limit, also coincides with the average density in the presence of a wall. Hence, computing the average density in the presence of a wall is the first step towards calculating the EVS in this strongly interacting system.

The average density profile of the constrained Riesz gas (i.e., in the presence of a wall at W) has been computed, for large N , for two special values of k : namely $k \rightarrow 0$ limit (Dyson's log gas) and $k = -1$ (1dOCP). For the $k \rightarrow 0$ case, it was shown in Refs. [22,23] that the constrained density profile satisfies the scaling form as given in Eq. (2.17) and the scaling function is given by

$$\rho_0^*(y, w) = \begin{cases} \frac{1}{\pi} \sqrt{2 - y^2}, & \text{with } -\sqrt{2} \leq y \leq \sqrt{2} \quad \text{for } w > \sqrt{2}, \\ \frac{1}{2\pi} \sqrt{\frac{y+l_0(w)}{w-y}} [w + l_0(w) - 2y], & \text{with } -l_0(w) \leq y \leq w \quad \text{for } w < \sqrt{2}, \end{cases} \quad (3.2)$$

where $w = W/\sqrt{N}$, and $l_0(w) = \frac{2\sqrt{w^2+6}-w}{3}$. For $w > \sqrt{2}$, the gas does not feel the presence of the wall at w and the density is the same as that of the unconstrained gas, i.e., the Wigner semi-circular form, as given in the first line of Eq. (3.2). In contrast, when $w < \sqrt{2}$, the gas gets pushed by the wall. This leads to a complete re-organization of the charges and the density gets drastically modified from the Wigner semi-circular law, as given in the second line of Eq. (3.2), where the density vanishes at the left edge of the support $l_0(w)$, while it diverges as a square-root singularity $\sim \frac{1}{\sqrt{w-y}}$ at the right edge of the support located at w . This integrable divergence indicates an accumulation of charges at the wall when the gas is pushed [25].

However, the presence of the pushing wall affects the density for the 1dOCP ($k = -1$) differently. It has been shown in Refs. [31,32] that in this case the constrained density profile is given by

$$\rho_{-1}^*(y, w) = \begin{cases} \frac{1}{2J}, & \text{with } -J \leq y \leq J \quad \text{for } w > J \\ \frac{1}{2J} + \frac{J-w}{2J} \delta(y-w), & \text{with } -J \leq y \leq w \quad \text{for } -J < w < J \\ \delta(w-y), & \text{with } y \leq w \quad \text{for } w < -J \end{cases} \quad (3.3)$$

As in the log gas, for $w > J$, the gas does not feel the presence of the wall and the average density has the same flat profile as in the unconstrained case. When $w < J$, the particles feel the presence of the wall, leading to a re-organization of the particles, as in the log gas. However, how they get reorganized for $k = -1$ is drastically different from the $k \rightarrow 0$ case. For $k = -1$, the particles that get displaced by the wall get fully absorbed inside the wall, leading to a delta-function peak at $y = w$, that coexists with an undisturbed flat bulk to the left of w . This leads to the density in the second line of Eq. (3.3). Finally, when $w < -J$, all the particles get absorbed in the wall, leading to a single delta-peak, as given in the third line of Eq. (3.3).

These two specific cases of k suggest that the shape of the density profile gets affected dramatically due to the presence of the wall. In this chapter, we compute exactly, for all $k > -2$, the density profile of the constrained gas in the presence of a wall. In the next section, we summarise our main results. The derivations of our results are provided in Section 3.3. Section 3.4 contains a summary and conclusions. Some details are relegated to the Appendix.

3.2 Summary of the results

Our main result is the exact computation of the average density of the Riesz gas (characterized by the exponent $k > -2$) in thermal equilibrium in the presence of a wall at position W . The effect of the wall is to constrain the particles to stay on the semi-infinite line to the left of the wall. Consider first the unconstrained gas, i.e., without the wall. This is equivalent to placing the wall at $W = +\infty$. The scaled density of the unconstrained gas is supported over $[-l_{\text{uc}}, l_{\text{uc}}]$ (see Fig. 2.2 where l_{uc} is given in Eq. (2.18)). Now imagine bringing the wall from infinity to a finite position W . For all $k > -2$, we find that the scaled density of the unconstrained gas remains unchanged as long as the (scaled) position of the wall $w = W/N^{\alpha_k}$ [with α_k given in Eq. (2.6)] is larger than l_{uc} . In this regime, the particles do not feel the presence of the wall. However, when $w < l_{\text{uc}}$, the particles feel the presence of the wall and reorganize themselves. This leads to a modification of the mean density and the nature of the modifications depends on the exponent k characterizing the range of the interactions. We again find three principal regimes of k (see Fig. 2.3): (1) $k \geq 1$ (where the interaction is effectively short-ranged),

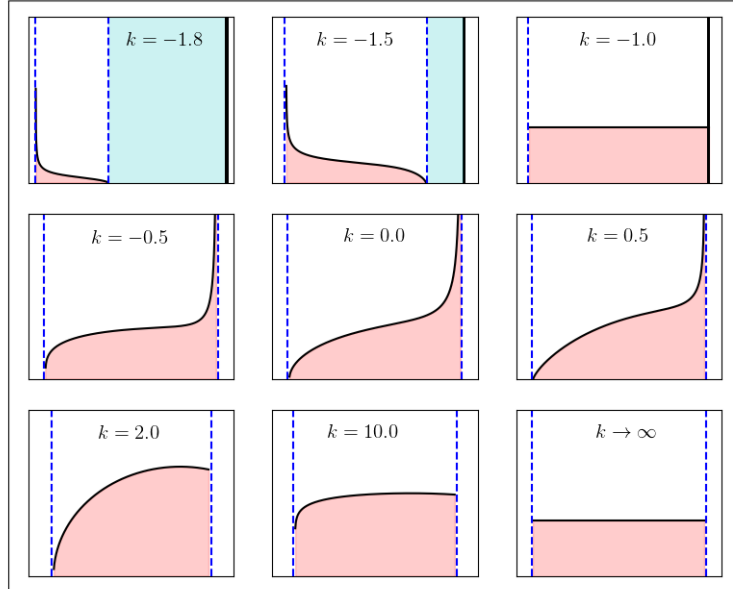


Figure 3.1: Scaled average density of the constrained gas $\rho_k^*(y, w)$ vs. y for different values of $k > -2$. The three rows correspond respectively to (i) $k \geq 1$ (third row), (ii) $-1 < k < 1$ (second row), and (iii) $-2 < k \leq -1$ (first row). The blue dashed vertical lines indicate the edges of the support. In the second and third rows, the right edge of the support coincides with the scaled wall position w . In the third row, the density is a constant at the wall while it diverges in the second row. In both the second and the third row, the density vanishes at the left edge (for $k = 10$ in the third row, the true density at the left edge vanishes, though it is not clearly visible due to the compression of the scale). In the first row, the density has an extended bulk part, sandwiched between the two vertical dashed lines and a delta peak at the wall w (shown by a thick solid vertical line). In between, there is a hole devoid of particles (shaded cyan region) which disappears for $k = -1$ (the third figure in the first row).

(2) $-1 < k < 1$ (weakly long-ranged interaction), and (3) $-2 < k \leq -1$ (strongly long-ranged interaction). The exact form of the modified density in these three regimes is summarised below (see also Fig. 3.1). We obtain these results by employing a saddle-point method in the large- N limit. Finding the analytical solution of this saddle-point equation is the main technical achievement of this chapter.

Regime 1 ($k \geq 1$): short-ranged interactions. In this regime, the interaction is extremely short-ranged and the effective field theory becomes local and simple [45]. Solving the associated saddle-point equation in the presence of a wall at the scaled position $w = W/N^{\alpha_k}$ with $\alpha_k = k/(k+2)$, we find that, for $w < l_{\text{uc}}$, the mean density, supported over

the finite interval $[-l_k(w), w]$, is given by

$$\rho_k^*(y, w) = A_k (l_k(w)^2 - y^2)^{\frac{1}{k}} \quad , \quad \text{for } -l_k(w) \leq y \leq w, \quad w < l_{\text{uc}} \quad , \quad (3.4)$$

where A_k is given in Eq. (2.20) and the location $-l_k(w)$ of the left edge of the support is determined from the normalization condition $\int_{-l_k(w)}^w \rho_k^*(y, w) dy = 1$. This analytical result is verified through Monte-Carlo (MC) simulation in Fig. 3.2. The density vanishes at the left edge $-l_k(w)$ while it approaches a finite value at the right edge, i.e., at the location of the wall (see Fig. 3.1). In addition, as $w \rightarrow -\infty$, the size of the support in scaled units

$$L_k(w) = w + l_k(w) \quad , \quad (3.5)$$

decreases as $L_k(w) \sim |w|^{-\frac{1}{k+2}}$ for a fixed $k \geq 1$ (see Fig. 3.3).

Regime 2 ($-1 < k < 1$): *weakly long-ranged interactions*. In this regime the interaction between two particles at small separation is weaker compared to the previous case ($k > 1$), however, it is relatively more long-ranged. As a result, the action in the large- N field theory becomes non-local. This modifies the density in a slightly different way compared to the regime 1. We find that the density is still supported on a finite interval $[-l_k(w), w]$ and it vanishes at the left edge $-l_k(w)$. However, at the right edge, i.e., at the wall, the density diverges, though it remains integrable. This is different from regime 1 where the density approaches a nonzero constant at the wall. We find that the density profile in this regime is explicitly given by

$$\rho_k^*(y, w) = A_k \frac{(\tilde{l}_k(w) - y)(l_k(w) + y)^{\frac{k+1}{2}}}{(w - y)^{\frac{1-k}{2}}} \quad , \quad \text{for } -l_k(w) \leq y \leq w \quad , \quad w < l_{\text{uc}} \quad (3.6)$$

$$\text{where } \tilde{l}_k(w) = \frac{1}{2}((k+1)l_k(w) + (1-k)w) \quad . \quad (3.7)$$

Here, A_k is given by Eq. (2.20), and $l_k(w)$ is found from the normalization of the density. A plot of this expression of the profile is given in Fig. 3.4 where it is also compared with numerical results. As in the case of regime 1, we have studied the support size $L_k(w) = w + l_k(w)$ as a function of w , shown in Fig. 3.5. As $w \rightarrow -\infty$, the support size

decays algebraically as $L_k(w) \sim |w|^{-\frac{1}{k+2}}$.

Regime 3 ($-2 < k \leq -1$): *strongly long-ranged interactions*. In this regime, the force between two particles vanishes when two particles get closer to each other. However, at long separation, the repulsive force increases as a power law $\sim |r|^{|k|-1}$ of the inter-particle distance $|r|$. As a consequence, the associated field theory is strongly non-local. In the presence of the wall, this leads to a rather exotic scaled density profile consisting of two disjoint pieces separated by a hole: a bulk part, supported over $[-l_k(w), \bar{l}_k(w)]$ and a delta peak with weight $D_k^*(w)$ located at $w > \bar{l}_k(w)$ (see the top row of Fig. 3.1). Thus the hole extends over $[\bar{l}_k(w), w]$ which is devoid of any particle. Moreover, unlike in regimes 1 and 2, where the density vanishes at the left edge $-l_k(w)$, in regime 3, the density diverges in an integrable fashion. The presence of the wall is felt over a much wider region in this case, due to the strong non-local nature of the interaction. As the wall is pushed further to the left side, at some critical position $w_c(k) < l_{uc}$ the support of the bulk part shrinks to zero and all the particles accumulate at the wall, leading to a single delta function at the wall for $w < w_c(k)$. We find the following explicit expression for the density profile

$$\rho_k^*(y, w) = \begin{cases} A_k \frac{(l_k(w)+y)^{\frac{k+1}{2}} (\bar{l}_k(w)-y)^{\frac{k+3}{2}}}{(w-y)} \mathbb{I}[-l_k(w) < y \leq \bar{l}_k(w)] + D_k^*(w) \delta(w-y), & \text{for } w > w_c(k) \\ \delta(w-y), & \text{for } w < w_c(k) \end{cases} \quad (3.8)$$

where \mathbb{I} represents the indicator function, A_k is given by Eq. (2.20) and the other constants are given by

$$\bar{l}_k(w) = \frac{2w + (k+1)l_k(w)}{k+3}, \quad (3.9)$$

$$D_k^*(w) = \frac{(l_k(w) - w)(w + l_k(w))^{\frac{k+1}{2}}}{|k|(k+3)} \left(\frac{(k+1)(w - l_k(w))}{k+3} \right)^{\frac{k+1}{2}}, \quad (3.10)$$

$$w_c(k) = \frac{(k+2)|k(k+1)|^{\frac{1}{k+2}}}{k+1}. \quad (3.11)$$

The value of $l_k(w)$ is again determined from the normalization condition. The analytical expression in the first line of Eq. (3.8) is plotted in Fig. 3.6 where it is also compared to

MC simulations. In this regime 3 of k , the support length of the extended part decays as the wall is pushed to the left and goes to zero at a critical wall position $w = w_c(k)$. This can be seen in Fig. 3.7.

Furthermore, in this regime 3 of k , we find an interesting first-order phase transition in the density profile as the scaled wall position decreases below a critical value $w^*(k) > w_c(k)$. We find that the actual density profile is a pure delta function for all $w < w^*(k)$. Thus the solution in the first line of Eq. (3.8) is actually metastable in the intermediate region $w_c(k) < w < w^*(k)$. This is discussed in Section 3.3.3.

3.3 Derivation

For a given configuration of the positions (x_1, x_2, \dots, x_N) of the particles, we define the empirical density as

$$\rho_N(x) = \frac{1}{N} \sum_{i=1}^N \delta(x - x_i) . \quad (3.12)$$

We are interested in computing the thermal average of this empirical density for large N which we denote by $\langle \rho_N(x) \rangle$. To proceed, we first look at the partition function of the Riesz gas in the presence of a wall given by

$$Z_k(W) = \int_{-\infty}^W dx_1 \dots \int_{-\infty}^W dx_N e^{-\beta \tilde{E}_k(\{x_i\})} . \quad (3.13)$$

For large N the multiple integrals in the partition function can in principle be done in two steps.

1. Integrate over the microscopic configurations corresponding to a given macroscopic density profile $\rho_N(x)$. This introduces an entropy contribution corresponding to this density profile. Also, this stage involves converting the energy function $\tilde{E}_k(\{x_i\})$ in Eq. (2.1) to an energy functional $\tilde{\mathcal{E}}_k[\rho_N(x)]$ [45, 92]. This yields

$$Z_k(W) \approx \int D[\rho_N] e^{-\beta \mathcal{E}_k[\rho_N(x)] - N \int dx \rho_N(x) \ln(\rho_N(x))} \delta \left(\int_{-\infty}^W dx \rho_N(x) - 1 \right) , \quad (3.14)$$

where the delta function ensures that the functional integrals are performed only over normalized density profiles. For large N , the energy functional $\tilde{\mathcal{E}}_k[\rho_N]$ takes

the following form, depending on the value of k

$$\tilde{\mathcal{E}}_k[\rho_N(x)] \approx \frac{N}{2} \int_{-\infty}^W dx x^2 \rho_N(x) + J \begin{cases} \zeta(k) N^{k+1} \int_{-\infty}^W dx [\rho_N(x)]^{k+1}, & \text{for } k > 1 \\ N^2 \ln N \int_{-\infty}^W dx [\rho_N(x)]^2, & \text{for } k = 1 \\ \frac{\text{sgn}(k) N^2}{2} \int_{-\infty}^W dx' dx \frac{\rho_N(x') \rho_N(x)}{|x-x'|^k} & \text{for } -2 < k < 1. \end{cases} \quad (3.15)$$

2. We perform the functional integral in Eq. (3.14) using the saddle point method.

We further find the saddle point density by extremizing the action which finally provides $Z_k(W)$ in the exponential form, as will be shown later.

To proceed, it is convenient to use the scaled variables $y_i = x_i/L_N$ with L_N given in Eq. (2.6). In these variables, the density profile has a scaling form $\rho_N(y) = L_N^{-1} \rho(y L_N^{-1})$ [see Eq. (2.15)]. Substituting this scaling form in Eq. (3.15), we find that the energy functional

$$\tilde{\mathcal{E}}_k[\rho_N] = \mathcal{B}_N \mathcal{E}_k[\rho] \quad \text{where} \quad \mathcal{B}_N = N L_N^2, \quad (3.16)$$

and the scaled energy functional $\mathcal{E}_k[\rho]$ takes the following forms

$$\mathcal{E}_k[\rho(y)] \approx \frac{1}{2} \int_{-\infty}^w dy y^2 \rho(y) + J \begin{cases} \zeta(k) \int_{-\infty}^w dy \rho(y)^{k+1} & k > 1 \\ \int_{-\infty}^w dy \rho(y)^2 & k = 1 \\ \frac{\text{sgn}(k)}{2} \int_{-\infty}^w \int_{-\infty}^w dy' dy \frac{\rho(y) \rho(y')}{|y'-y|^k} & -2 < k < 1, \end{cases} \quad (3.17)$$

with $w = W/L_N$. Substituting (3.16) in the expression (3.14) for the partition function, one finds that the energy scale \mathcal{B}_N is much bigger than the scale of the entropy, since $\mathcal{B}_N \gg N$ for large N and fixed β . Hence, neglecting the entropy term and using the integral representation of the delta function $\delta(x) = \int_{\Gamma} \frac{d\mu}{2\pi i} e^{\mu x}$ where Γ runs along the imaginary axis in the complex μ -plane, we rewrite the partition function in Eq. (3.14) as

$$Z_k(W) = C_N \int d\mu \int \mathcal{D}[\rho] \exp[-\beta \mathcal{B}_N \Sigma_k[\rho(y), \mu] + o(\mathcal{B}_N)], \quad (3.18)$$

where $o(\mathcal{B}_N)$ represents terms of order smaller than \mathcal{B}_N (subdominant) which is composed of the self-energy term and the entropy term. The action $\Sigma_k[\rho(y), \mu]$ is given by

$$\Sigma_k[\rho(y), \mu] = \left(\mathcal{E}_k[\rho(y)] - \mu \left(\int_{-\infty}^w dy \rho(y) - 1 \right) \right), \quad (3.19)$$

with $\mathcal{E}_k[\rho_k(y)]$ given in Eq. (3.17). Note that a Jacobian C_N appears in Eq. (3.18) when the positions are rescaled from $\{x_i\} \rightarrow \{y_i\}$ in Eq. (3.13) where $y_i = x_i/L_N$. This multiplicative factor is given by

$$C_N = \begin{cases} (L_N)^N & \text{for } k \neq 0, \\ N^{\frac{N}{2} + \beta \frac{N(N-1)}{4}} & \text{for } k \rightarrow 0 \end{cases}. \quad (3.20)$$

The Jacobian C_N is a multiplicative factor in Eq. (3.18) which does not affect the equilibrium properties.

The integrals in Eq. (3.18) can be performed using the saddle point method in which one is required to minimize the action $\Sigma_k[\rho(y), \mu]$ in Eq. (3.19) to find the saddle point density $\rho_k^*(y, w)$ and the chemical potential μ_k^* . The saddle point equations read

$$\left. \frac{\delta \Sigma_k[\rho(y), \mu]}{\delta \rho(y)} \right|_{\substack{\rho(y) = \rho_k^*(y, w) \\ \mu = \mu_k^*}} = 0 \quad (3.21)$$

$$\left. \frac{\partial \Sigma_k[\rho(y), \mu]}{\partial \mu} \right|_{\substack{\rho(y) = \rho_k^*(y, w) \\ \mu = \mu_k^*}} = 0. \quad (3.22)$$

Note that the second equation above is equivalent to the normalization condition $\int_{-\infty}^w dy \rho(y) = 1$. In the limit $N \rightarrow \infty$, the saddle point density coincides with the average density.

3.3.1 Regime 1 ($k \geq 1$): short-ranged interactions

In this regime, the interaction energy falls so quickly with increasing separation that it effectively acts as short-ranged and consequently the energy functional $\mathcal{E}_k[\rho_k(y)]$ becomes local in the leading order for large N (see Eq. (3.17)). The saddle point equation (3.21) becomes

$$\mu_k^* = \frac{y^2}{2} + (k+1)\zeta(k) [\rho_k^*(y, w)]^k, \quad (3.23)$$

for $k > 1$ (the case $k = 1$ is treated separately below). This equation of course is valid for y belonging to the support of the density. To determine the support, we solve Eq. (3.23) explicitly, giving

$$\rho_k^*(y, w) = A_k (2\mu_k^* - y^2)^{\frac{1}{k}}, \quad (3.24)$$

where A_k is given in the first line of Eq. (2.20). This density is real and nonzero for $-\sqrt{2\mu_k^*} < y < +\sqrt{2\mu_k^*}$. Now there are two possible situations: (i) when $w > \sqrt{2\mu_k^*}$ and (ii) when $w < \sqrt{2\mu_k^*}$. Consider the situation (i) first. In this case, the density is given by Eq. (3.24) and is supported over $[-\sqrt{2\mu_k^*}, +\sqrt{2\mu_k^*}]$. The only unknown is μ_k^* which is fixed by the normalization condition $\int_{-\sqrt{2\mu_k^*}}^{\sqrt{2\mu_k^*}} \rho_k^*(y, w) dy = 1$. It is easy to show that it gives $\sqrt{2\mu_k^*} = l_{uc}$ where l_{uc} is given in Eq. ((2.19)). In this case, the density in Eq. (3.24) is precisely the unconstrained density given in Eq. (2.18). Thus we conclude that for $w > l_{uc}$ the unconstrained density is not affected by the presence of the wall.

We next consider the case (ii) above, i.e., when $w < \sqrt{2\mu_k^*}$. In this case, the support of the density in Eq. (3.24) is over $[-\sqrt{2\mu_k^*}, w]$. Thus, unlike in case (i) above, the density does not vanish at the upper edge w of the support (see Fig. 3.2) and it reads

$$\rho_k^*(y, w) = A_k (2\mu_k^* - y^2)^{\frac{1}{k}}, \quad -\sqrt{2\mu_k^*} \leq y \leq w. \quad (3.25)$$

Setting $\sqrt{2\mu_k^*} = l_k(w)$, the density is then supported over $[-l_k(w), w]$. The only unknown $l_k(w)$ is then fixed by the normalization condition $\int_{-l_k(w)}^w \rho_k^*(y, w) dy = 1$. Substituting the density from Eq. (3.25), the normalization condition can be expressed in terms of an auxiliary variable $m_k = \frac{w+l_k(w)}{2l_k(w)}$

$$(2m_k - 1) \left(\frac{B(\gamma_k + 1, \gamma_k + 1)}{B(m_k; \gamma_k + 1, \gamma_k + 1)} \right)^{\alpha_k} = \frac{w}{l_{uc}} \quad (3.26)$$

where $B(m_k; a, b) = \int_0^{m_k} u^{a-1} (1-u)^{b-1} du$ is the incomplete Beta function and we recall that $\gamma_k = 1/k$ and $\alpha_k = k/(k+2)$. The variable m_k lies in the range $[0, 1]$. Solving Eq. (3.26) gives m_k , which in turn fixes the unknown constant $l_k(w)$. Let us investigate two limiting cases. First, consider the limit $w \rightarrow l_{uc}$ from the left. In this case the right hand side of Eq. (3.26) approaches 1 and therefore $m_k \rightarrow 1$ in this limit, i.e., $l_k(w) \rightarrow l_{uc}$ as expected. In the opposite limit where $w \rightarrow -l_k(w)$ (i.e., in the limit of vanishing support size $L_k(w) = w + l_k(w) \rightarrow 0$, which happens when $w \rightarrow -\infty$), the variable $m_k \rightarrow 0$.

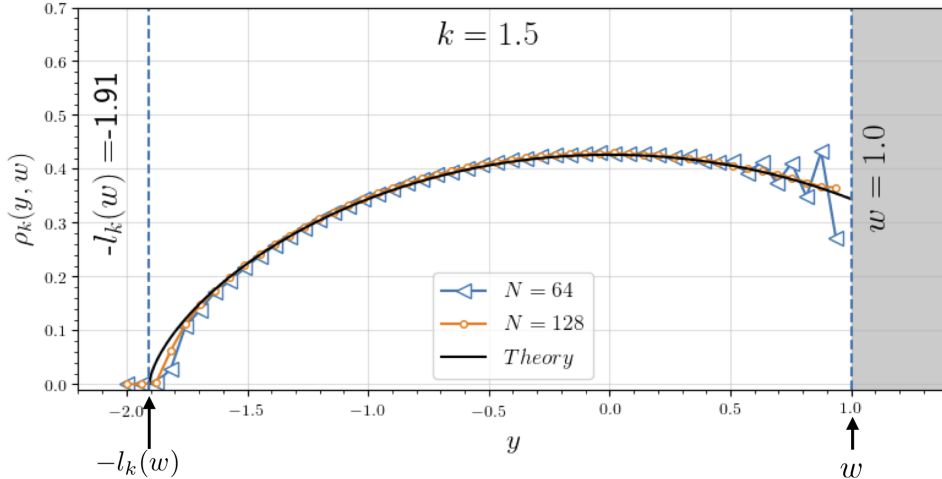


Figure 3.2: *Regime 1* ($k \geq 1$): Comparison between MC simulations (symbols) and the theoretical expression given in Eq. (3.24) (solid line) of the scaled density profile of the Riesz gas in the presence of the hard wall at $w = 1.0$ for $k = 1.5$. The parameters used in this plot are $J = 1$ and $T = 1$. The dashed vertical line on the left marks the left edge $-l_k(w)$ (shown by an arrow) of the density while the wall is located at w (shown also by an arrow).

Using the small m_k behavior of $B(m_k; a, b) \sim m_k^a$ in Eq. (3.26), it is easy to verify that the support length $L_k(w) = w + l_k(w) \sim |w|^{-1/(k+1)}$, as $w \rightarrow -\infty$.

The density profile of the constrained gas in Eq. (3.25) is plotted (solid line) in Fig. 3.2 where it is compared with numerical simulations (symbols) for different values of N . We observe that for increasing N the numerical density profile converges to the analytical expression. Clearly, the density is nonzero at the wall while it vanishes at the left edge as $\sim (l_k(w) - |y|)^{\gamma_k}$ with $\gamma_k = 1/k$, as in the unconstrained case. As w decreases below l_k^{uc} , the gas is pushed to the left and, as argued above, the support size $L_k(w) = w + l_k(w)$ shrinks algebraically $L_k(w) \sim |w|^{-\frac{1}{1+k}}$ as $w \rightarrow -\infty$. This result is verified in simulations in Fig. 3.3 where we plot the support length $L_k(w)$ as a function of w for given k . Following the same procedure for $k = 1$, we find that the density profile is given by the same form as for $k > 1$

$$\rho_1^*(y, w) = A_1 (l_1(w)^2 - y^2), \quad \text{for } -l_1(w) \leq y \leq w, \quad w < l_1^{\text{uc}}, \quad (3.27)$$

with the prefactor $A_1 = 1/4J$ (see the second line of Eq. (2.20)) and $l_1(w)$ is determined for the normalization condition.

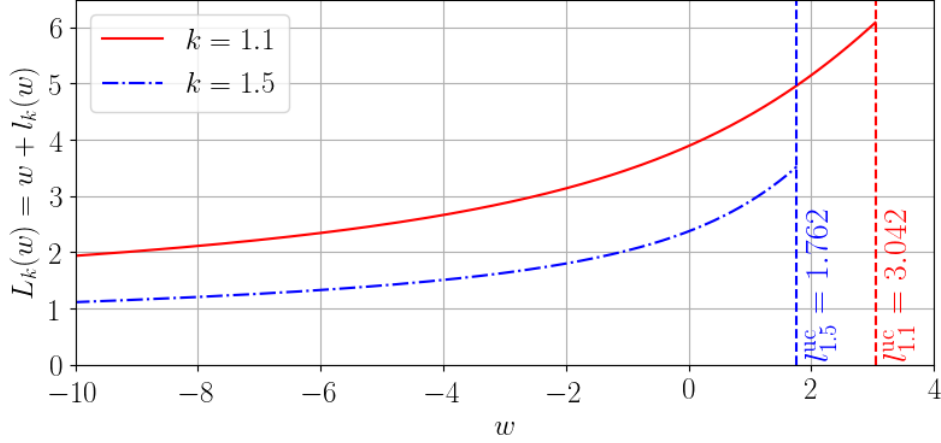


Figure 3.3: *Regime 1* ($k \geq 1$): Plot of the support size $L_k(w) = w + l_k(w) = \frac{2m_k w}{2m_k - 1}$ as a function of $w \leq l_{uc}$, obtained by solving Eq. (3.26) for m_k . $L_k(w)$ decreases monotonically with decreasing w , shown for two different values of k . As $w \rightarrow -\infty$, the support size decreases algebraically as $L_k(w) \sim |w|^{-1/(k+1)}$. The vertical dashed lines indicate the positions of the unconstrained right edge l_{uc} for the two values of k .

3.3.2 Regime 2 ($-1 < k < 1$): Weakly long-ranged interactions

In this regime of k , the interaction forces decay slower with increasing inter-particle separation compared to the previous short-ranged regime. The energy functional in this regime is given by the third line in Eq. (3.17). Using this in the saddle point equation (3.21) we get

$$\mu_k^* = \frac{y^2}{2} + \text{sgn}(k) \int_{-\infty}^w dy' \frac{\rho_k^*(y', w)}{|y' - y|^k}. \quad (3.28)$$

To solve this equation, we note that the first term on the right-hand side grows arbitrarily for large negative y whereas the second term can at maximum grow as $y^{1+|k|}$ (for $k < 0$). Since μ_k^* is a constant the Eq. (3.28) can be valid only for density profiles with finite support $(-l_k(w), w)$. Taking a derivative with respect to y on both sides of Eq. (3.28) we get

$$P.V. \int_{-l_k(w)}^w \frac{\rho_k^*(y', w) \text{sgn}(y' - y)}{|y - y'|^{k+1}} dy' = -\frac{y}{|k|}, \quad -l_k(w) \leq y \leq w, \quad (3.29)$$

where *P.V.* represents the principal value. Note that this integral is interpreted in principal value sense only for $0 \leq k < 1$, but for $-2 < k < 0$ it is considered a normal integral. The principal value for $0 \leq k < 1$ appears because the second term in Eq. (3.28) is not

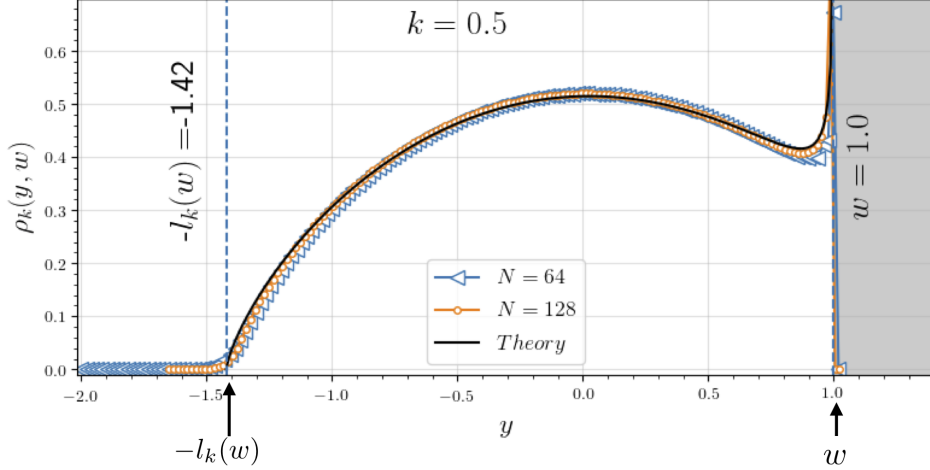


Figure 3.4: *Regime 2* ($-1 < k < 1$): Comparison between MC simulations (symbols) and the theoretical expression given in Eq. (3.38) (solid line) of the scaled density profile of the Riesz gas in the presence of the hard wall at $w = 1.0$ for $k = 0.5$. The parameters used in this plot are $J = 1$ and $T = 1$. The dashed vertical line on the left marks the left edge $-l_k(w)$ (shown by an arrow) of the density while the wall is located at w (shown also by an arrow). The density diverges at the wall as $\sim (w - y)^{(k-1)/2}$.

differentiable at $y = y'$ and we consider a weak derivative with respect to y (as discussed in Ref. [99]). We need to solve the integral equation (3.29) to obtain the desired density. We can simplify the calculations by shifting the coordinates to the left edge and scaling with the length of the support $L_k(w) = w + l_k(w)$, i.e., by making the transformation $z = \frac{y+l_k(w)}{L_k(w)}$. Since the density is normalized it is expected to take the scaling form

$$\rho_k^*(y, w) = \frac{1}{L_k(w)} \phi_k \left(\frac{y + l_k(w)}{L_k(w)}, w \right), \quad (3.30)$$

where $\phi(z, w)$ is now supported over $z \in [0, 1]$ and satisfies the Sonin equation

$$P.V. \int_0^1 \frac{\phi_k(z', w) \text{sgn}(z' - z)}{|z - z'|^{k+1}} dz' = h_k(z) \quad , \quad 0 \leq z \leq 1, \quad (3.31)$$

with $h_k(z) = \mathcal{A}_k(z - q_k(w))$, $\mathcal{A}_k = -\frac{[L_k(w)]^{k+2}}{|k|}$ and $q_k(w) = \frac{l_k(w)}{L_k(w)}$. The only unknown so far is $l_k(w)$. Fortunately, the Sonin equation can be inverted for arbitrary source function $h_k(z)$ and the general solution is given by [100]

$$\phi_k(z, w) = C_0(z(1 - z))^{\frac{k-1}{2}} + u_k(z), \quad \text{with} \quad (3.32)$$

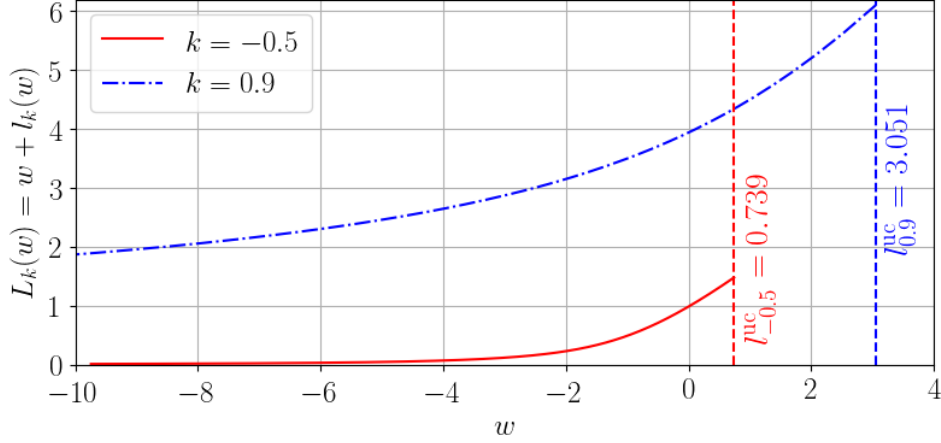


Figure 3.5: *Regime 2* ($-1 < k < 1$): Plot of the support size $L_k(w) = w + l_k(w) = \frac{2\gamma_k w}{1+\gamma_k - g_k(w)}$ as a function of $w \leq l_{\text{uc}}$, obtained by solving Eq. (3.39) for $g_k(w)$. $L_k(w)$ decreases monotonically with decreasing w , shown for two different values of k . As $w \rightarrow -\infty$, the support size decreases algebraically as $L_k(w) \sim |w|^{-1/(k+1)}$. The vertical dashed lines indicate the positions of the unconstrained right edge l_{uc} for the two values of k .

$$u_k(z) = \frac{2A_k|k|}{B\left(\frac{k+1}{2}, \frac{k+1}{2}\right)} z^{\frac{k-1}{2}} \frac{\partial}{\partial z} \left(\int_z^1 t^{-k} (t-z)^{\frac{k+1}{2}} \frac{\partial}{\partial t} \int_0^t h_k(y) y^{\frac{k+1}{2}} (t-y)^{\frac{k-1}{2}} dy dt \right), \quad (3.33)$$

where C_0 is an arbitrary constant and A_k is given in Eq. (2.20). In Eq. (3.32), the first term represents the general solution of the homogenous part of the equation (with $h_k(z) = 0$), while the second term $u_k(z)$, given explicitly in Eq. (3.33), represents a particular solution of the full inhomogeneous equation (3.31). Inserting the explicit form of $h_k(z)$ [given after Eq. (3.31)] in Eq. (3.33) and performing the integral (detailed in A.1.1), we obtain the full general solution

$$\phi_k(z, w) = (z(1-z))^{\gamma_k-1} \left[C_0 - A_k|k| \mathcal{A}_k(1-z)(z - \gamma_k(2q_k(w) - 1)) \right], \quad (3.34)$$

where $\gamma_k = (k+1)/2$. The only unknown parameters so far are C_0 and $l_k(w)$.

As in regime 1, there are two possible scenarios, depending on the value of w compared to the unconstrained right edge l_{uc} . Let us consider $w < l_{\text{uc}}$. In this case, it turns out that the constant C_0 is nonzero and is determined as follows. To fix C_0 in this case, we need to use some information about the density profile from numerical simulations (see Fig. 3.4). From the simulations, we see that the density vanishes at the left edge (corresponding to $z = 0$ in the shifted coordinate), while it diverges at the right edge at w (corresponding

to $z = 1$ in the shifted coordinate). From Eq. (3.34), since $\gamma_k - 1 = (k - 1)/2 < 0$ here for $k < 1$, it follows that if the density has to vanish at $z = 0$, the term in the square bracket must vanish at $z = 0$. This fixes the constant $C_0 = -A_k |k| \mathcal{A}_k \gamma_k (2q_k(w) - 1)$. Hence $\phi_k(z, w)$ becomes

$$\phi_k(z, w) = -A_k |k| \mathcal{A}_k z^{\gamma_k} (1 - z)^{\gamma_k - 1} (g_k(w) - z) \mathbb{I}[0 < z < 1] \quad (3.35)$$

where $\mathcal{A}_k = -\frac{[L_k(w)]^{k+2}}{|k|}$,

$$g_k(w) = \gamma_k (2q_k(w) - 1) + 1 = \frac{(k + 3)l_k(w) + (1 - k)w}{2(w + l_k(w))}, \quad (3.36)$$

and we used $q_k(w) = l_k(w)/(w + l_k(w))$. Note that when $w \rightarrow l_k^{\text{uc}-}$, $q_k \rightarrow \frac{1}{2}^+$, which suggests that $C_0 \rightarrow 0$ in this limit. As a result, we get the unconstrained density profile given in Eq. (2.18). Now if w is increased further to the right of l_{uc} , as discussed before (Section 3.2, the particles do not feel the presence of the wall and the density remains unconstrained. Hence, we expect $C_0 = 0$ for $w > l_{\text{uc}}$. Note that $g_k(w)$ in Eq. (3.36) can also be expressed in terms of the support length $L_k(w) = w + l_k(w)$ as

$$g_k(w) = \frac{k + 3}{2} - \frac{(k + 1)w}{L_k(w)}. \quad (3.37)$$

Thus, finally, the density in terms of the original coordinate y reads

$$\rho_k^*(y, w) = A_k (l_k(w) + y)^{\frac{k+1}{2}} (w - y)^{\frac{k-1}{2}} \left(\tilde{l}_k(w) - y \right), \quad \text{for } -l_k(w) \leq y \leq w, \quad w < l_{\text{uc}} \quad (3.38)$$

where $\tilde{l}_k(w) = \frac{1}{2}((k + 1)l_k(w) + (1 - k)w)$ as given in Eq. (3.7). The only remaining unknown $l_k(w)$ is then determined from the normalization condition $\int_{-l_k(w)}^w \rho_k^*(y, w) dy = 1$. The normalization condition can be conveniently expressed in terms of $g_k(w)$ defined in Eq. (3.36) as

$$\left(\frac{\gamma_k + 1 - g_k(w)}{\gamma_k} \right) \left(g_k(w) \left(2 + \frac{1}{\gamma_k} \right) - \left(1 + \frac{1}{\gamma_k} \right) \right)^{-\alpha_k} = \frac{w}{l_{\text{uc}}}, \quad (3.39)$$

where we recall that $\alpha_k = 1/(k + 2)$ and $\gamma_k = (k + 1)/2$. This equation is the analog of Eq. (3.26) in regime 1. For a given w and k , we solve this equation numerically to get $g_k(w)$

which, via Eq. (3.36), in turn fixes the only remaining unknown constant $l_k(w)$. Once $l_k(w)$ is fixed, Eq. (3.38) then provides the exact density profile of the constrained gas. We verify that in the limit $k \rightarrow 0$ our results recover the known results for the Dyson's log gas in the presence of a wall [22, 23]. The numerical results from MC simulation for the density profile are in perfect agreement with our analytical predictions, as shown in Fig. 3.4 for a representative value $k = -0.5$ in this regime.

One can show that the solution for $g_k(w)$ in Eq. (3.39) lies in the range $[1, +\infty)$. It is easy to see that when w approaches l_{uc} , the right hand side of Eq. (3.39) approaches 1 and consequently $g_k(w) \rightarrow 1$. From Eq. (3.36), we see that $l_k(w) \rightarrow w$ and since $w \rightarrow l_{\text{uc}}$ it follows that $l_k(w) \rightarrow l_{\text{uc}}$, i.e., to the right edge of the unconstrained gas. In contrast, when $w \rightarrow -\infty$, it is easy to check from Eq. (3.39) that $g_k(w)$ diverges as $g_k(w) \sim |w|^{\frac{k+2}{k+1}}$. Substituting this behavior in Eq. (3.37), we see that $L_k(w) \sim |w|^{-\frac{1}{k+1}}$ as $w \rightarrow -\infty$. In Fig. 3.5, we plot the support size $L_k(w)$ as a function of w for $k = -0.5$ and $k = 0.9$.

We see from Eq. (3.38) that the density at the wall diverges as $\rho_k^*(y, w) \sim (w-y)^{(k-1)/2}$ (since $k < 1$). Thus the divergence becomes stronger as k decreases and at $k = -1$ it becomes non-integrable, signaling a breakdown of the validity of the solution in Eq. (3.38). This calls for a different analysis for $-2 < k \leq -1$, which we carry out in the next subsection.

3.3.3 Regime 3 ($-2 < k \leq -1$): Strongly long-ranged interactions

In this regime not only the interaction energy but also the interaction force is zero at vanishingly small separation. As a consequence of this the density in this regime, in the presence of a wall, displays interesting features as seen in Fig. 3.6 where we plot constrained density profile $\rho_k^*(y, w)$ as a function of y obtained from numerical simulations. Interestingly, in this case, for $k < -1$, the average density profile, supported over a finite range, consists of two disjoint parts with a region devoid of the particles (hole) in between them. One part corresponds to a very high density (a delta peak) at the position of the wall (see the inset in Fig. 3.6). The other part has an extended profile which vanishes at the right edge bordering the hole and has an integrable divergence at the left edge (see Fig. 3.6). Strictly for $k = -1$ (1dOCP), the hole disappears, and the extended bulk merges with the delta-peak [32]. These observations suggest an ansatz for the scaled

density profile of the form

$$\rho_k(y, w) = \rho_b(y, w)\mathbb{I}[-l_k(w) \leq y \leq \bar{l}_k(w)] + D_k(w)\delta(w - y), \quad (3.40)$$

where $-l_k(w) < \bar{l}_k(w) < w$. The extended part of the density $\rho_b(y, w)$ (where the subscript b refers to the bulk density) is assumed to be supported over $(-l_k(w), \bar{l}_k(w))$. Here $\bar{l}_k(w)$ denotes the right edge of the extended density profile, or equivalently the left edge of the hole. Hence the hole is over the region $y \in (\bar{l}_k(w), w)$. The amplitude $D_k(w)$ of the delta function just denotes the fraction of particles in the delta peak. In fact, with this ansatz (3.40) the normalisation condition reads

$$\int_{-l_k(w)}^{\bar{l}_k(w)} \rho_b(y, w) dy + D_k(w) = 1. \quad (3.41)$$

The next step is to substitute this ansatz (3.40) in the expression for the scaled energy function in the third line of Eq. (3.17). It reads

$$\begin{aligned} \mathcal{E}_k[\rho_k(y)] \approx & \frac{1}{2} \int_{-l_k(w)}^{\bar{l}_k(w)} dy y^2 \rho_b(y, w) - \frac{1}{2} \int_{-l_k(w)}^{\bar{l}_k(w)} \int_{-l_k(w)}^{\bar{l}_k(w)} dy' dy \frac{\rho_b(y, w)\rho_b(y', w)}{|y' - y|^k} \\ & + D_k(w) \left[\frac{w^2}{2} - \int_{-l_k(w)}^{\bar{l}_k(w)} \frac{\rho_b(y, w)}{|w - y|^k} dy \right]. \end{aligned} \quad (3.42)$$

The first two terms represent the energy of the particles in the extended part with density $\rho_b(y, w)$. The third term represents the energy of the particles localized in the delta-function – it has two parts: the first part $D_k(w) w^2/2$ represents the potential energy of these particles while the second part represents the long-ranged interaction energy between these particles and the extended bulk with density $\rho_b(y, w)$, separated by the hole. Note that the interaction energy between the particles localized at w does not contribute as it vanishes identically for $k < 0$, which is the case in this regime 3.

The goal is now to minimize this scaled energy functional in (3.42) by varying $\rho_b(y, w)$. Note that the amplitude of the delta-peak $D_k(w)$ is automatically fixed by the normalization condition (3.41). Hence the optimization will be only with respect to $\rho_b(y, w)$, and not $D_k(w)$ independently. Taking a functional derivative with respect to $\rho_b(y, w)$ subject

to the constraint (3.41) enforced by a Lagrange multiplier μ_k , we get

$$\mu_k^* = \frac{y^2}{2} - \int_{-l_k(w)}^{\bar{l}_k(w)} \frac{\rho_b^*(y', w)}{|y - y'|^k} dy' - D_k^*(w)(w - y)^{-k}, \quad (3.43)$$

where the subscript ‘*’ indicates the optimal value of the parameters and the density. The optimal density $\rho_b^*(y, w)$ has thus two unknown parameters $-l_k(w)$ and $\bar{l}_k(w)$ and we recall that the constant $D_k(w)$ is fixed from the normalization condition (3.41).

To proceed further we take a derivative of Eq. (3.43) with respect to y and get

$$\int_{-l_k(w)}^{\bar{l}_k(w)} \frac{\rho_b^*(y', w) \operatorname{sgn}(y' - y)}{|y - y'|^{k+1}} dy' = -\frac{y}{|k|} - D_k^*(w)(w - y)^{-(k+1)}. \quad (3.44)$$

This can be simplified after a change of variable $z = \frac{y + l_k(w)}{\tilde{L}_k(w)}$ where $\tilde{L}_k(w) = \bar{l}_k(w) + l_k(w)$ is the size of the support. In this shifted and scaled coordinate the density takes the scaling form

$$\rho_b^*(y, w) = \frac{1}{\tilde{L}_k(w)} \phi_k \left(\frac{y + l_k(w)}{\tilde{L}_k(w)}, w \right), \quad (3.45)$$

where $\phi_k(z, w)$ satisfies the following equation

$$\int_0^1 dz' \frac{\operatorname{sgn}(z' - z)}{|z' - z|^{k+1}} \phi_k(z', w) = h_k(z) \quad , \quad 0 \leq z \leq 1, \quad (3.46)$$

with $h_k(z) = \mathcal{A}_k(z - q_k) + \mathcal{B}_k(g_k - z)^{-(k+1)}$. The constants are

$$\mathcal{A}_k = -\frac{[\tilde{L}_k(w)]^{k+2}}{|k|}, \quad g_k(w) = \frac{w + l_k(w)}{\tilde{L}_k}, \quad q_k(w) = \frac{l_k(w)}{\tilde{L}_k(w)}, \quad \mathcal{B}_k = -D_k^*(w), \quad (3.47)$$

where we recall that $\tilde{L}_k(w) = \bar{l}_k(w) + l_k(w)$. This equation (3.46) looks similar to (3.31) in regime 2. However, there is no principal value (*P.V.*) in Eq. (3.46). This is due to the fact that for $k \leq -1$ the integrand is not singular inside the support.

The integral equation (3.46) can be solved exactly using the Sonin inversion formula given in Eq. (3.32). After a long calculation presented in A.1.2, we find

$$\begin{aligned} \phi_k(z, w) = (z(1 - z))^{\gamma_k - 1} & \left[C_0 - A_k |k| (1 - z) \mathcal{A}_k (\gamma_k (1 - 2q_k(w)) + z) \right. \\ & \left. - A_k |k| \frac{1 - z}{g_k(w) - z} \mathcal{B}_k \frac{2\gamma_k g_k(w)}{(g_k(w)(g_k(w) - 1))^{\gamma_k}} \right], \end{aligned} \quad (3.48)$$

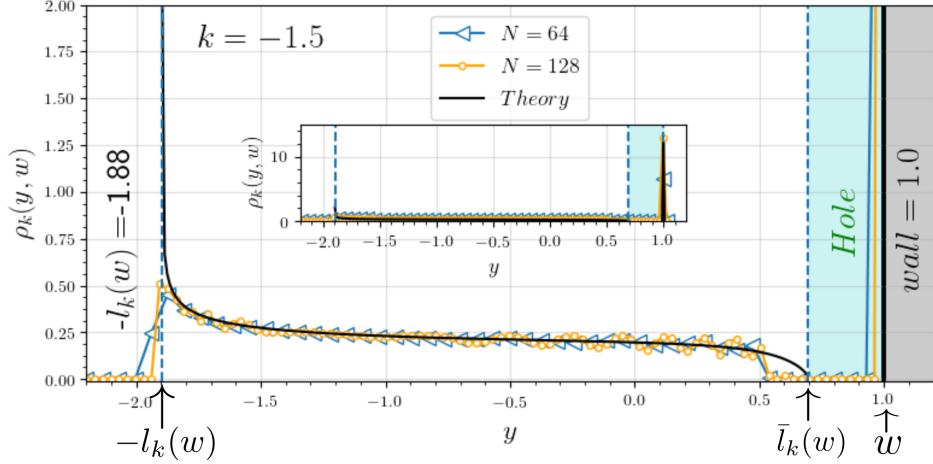


Figure 3.6: *Regime 3* ($-2 < k \leq -1$): Scaled density profile for $w = 1$ and $k = -1.5$: Comparison between MC simulations (symbols) and the theoretical expression (solid line) given in Eq. (3.40) with $\rho_b(y, w) = \rho_b^*(y, w)$ in Eq. (3.56) and $D_k(w) = D_k^*(w)$ in Eq. (3.54). The parameters used in this plot are $J = 1$ and $T = 1000$. The dashed vertical line on the left (right) marks the left (right) edge $-l_k(w)$ ($\bar{l}_k(w)$) shown by an arrow. The cyan shaded area is the hole region and the thick black line at $y = w = 1.0$ is the delta function. Note that the theoretical expression has an integrable divergence at the left edge as shown by the solid line. Since the numerical simulations are for finite N , we do not see the divergence very clearly. However, the value of the density at the left edge becomes larger as N increases, which indicates divergence in the limit $N \rightarrow \infty$.

where C_0 is an arbitrary constant and $\gamma_k = (k+1)/2$. Thus so far, we have three unknown constants characterizing the optimal density: $l_k(w)$, $\bar{l}_k(w)$, and C_0 . To fix these three unknowns we proceed as follows.

We start by fixing C_0 . As $z \rightarrow 1$ in Eq. (3.48), the density $\phi_k(z, w) \sim C_0(1-z)^{(k-1)/2}$. Since $k \leq -1$ we see that the density has a non-integrable divergence at $z = 1$ unless $C_0 = 0$. Since the density is normalizable, $C_0 = 0$ is the only possible choice. Setting $C_0 = 0$ in Eq. (3.48), we get

$$\begin{aligned} \phi_k(z, w) &= -A_k |k| \mathcal{A}_k \frac{z^{\gamma_k-1} (1-z)^{\gamma_k}}{g_k(w) - z} \\ &\times \left[(\gamma_k(1-2q_k(w)) + z)(g_k(w) - z) + \frac{\mathcal{B}_k}{\mathcal{A}_k} \frac{2\gamma_k g_k(w)}{(g_k(w)(g_k(w) - 1))^{\gamma_k}} \right], \end{aligned} \quad (3.49)$$

where we recall again that $\gamma_k = (k+1)/2 < 0$ in this regime 3. Let us first look at the edge at $z = 1$. The term $(1-z)^{\gamma_k}$ clearly diverges at the right edge, where $z \rightarrow 1$. On the other hand, from MC simulations, we see the density always vanishes at this edge. This means that the term inside the square bracket in the second line of Eq. (3.49) must vanish as $z \rightarrow 1$. Secondly, investigating the $z \rightarrow 0$ limit in Eq. (3.49), we see that the

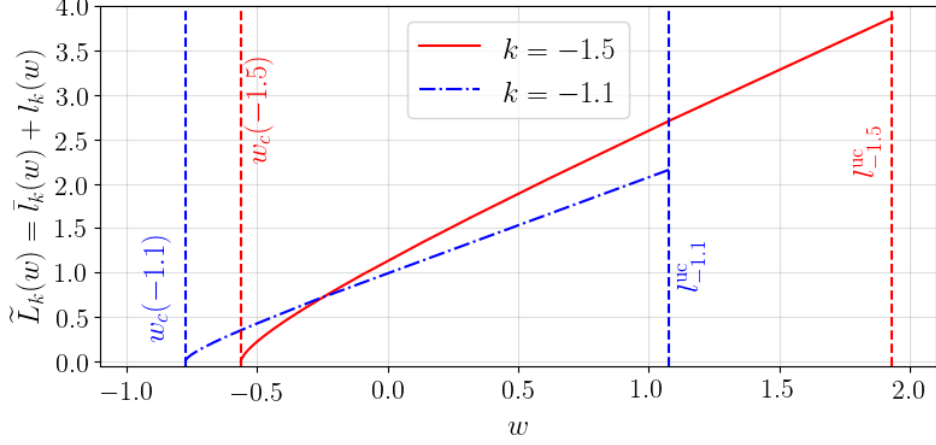


Figure 3.7: *Regime 3* ($-2 < k \leq -1$): Plot of the support size $\tilde{L}_k(w) = \bar{l}_k(w) + l_k(w)$ in Eq. (3.59) (with $g_k(w)$ determined from Eq. (3.57)). $\tilde{L}_k(w)$ decreases monotonically with decreasing w and vanishes at $w = w_c(k)$ given in Eq. (3.61) and marked by the two vertical dashed lines on the left for $k = -1.5$ and $k = -1.1$. The unconstrained right edge l_{uc} , for these two values of k , are also marked by two vertical dashed lines on the right.

amplitude diverges as $z^{(k-1)/2}$ which leads to a non-integrable divergence. Hence the term inside the square bracket in the second line of Eq. (3.49) must also vanish as $z \rightarrow 0$. Note that the square bracket on the second line of Eq. (3.49) is a polynomial in z of degree 2, and hence it must be of the form $z(1-z)$ in order to satisfy the behavior at both edges $z = 0$ and $z = 1$. This implies

$$\left[(\gamma_k(1 - 2q_k(w)) + z)(g_k(w) - z) + \frac{\mathcal{B}_k}{\mathcal{A}_k} \frac{2\gamma_k g_k(w)}{(g_k(w)(g_k(w) - 1))^{\gamma_k}} \right] = z(1 - z). \quad (3.50)$$

Matching the powers of z on both sides gives two relations

$$q_k(w) = \frac{\gamma_k + 1 - g_k(w)}{2\gamma_k}, \quad (3.51)$$

and

$$\frac{\mathcal{B}_k}{\mathcal{A}_k} = -\frac{D_k^*(w)}{\mathcal{A}_k} = \frac{g_k(w)^{\gamma_k} (g_k(w) - 1)^{\gamma_k + 1}}{|1 + k|}, \quad (3.52)$$

where we used $\mathcal{B}_k = -D_k^*(w)$ from Eq. (3.47). Solving these Eqs. (3.51) and (3.52) one can get D_k^* and $\bar{l}_k(w)$ in terms of $l_k(w)$

$$\bar{l}_k(w) = \frac{2w + (k + 1)l_k(w)}{k + 3}, \quad (3.53)$$

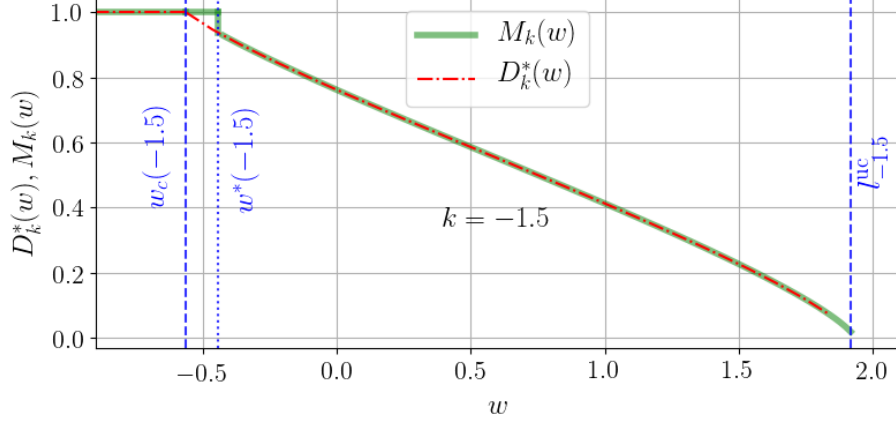


Figure 3.8: *Regime 3*: Simultaneous plots (i) of the amplitude $D_k^*(w)$ of the delta function, associated with the density $\rho^I(y, w)$ in Eq. (3.62) (dashed red line) and (ii) of the order parameter $M_k(w)$ defined in Eq. (3.67) (solid green line), as a function of w for fixed $k = -1.5$. We see that $D_k^*(w)$ increases with decreasing w and approaches to 1 as $w \rightarrow w_c(k)$, while the order parameter $M_k(w)$ coincides with $D_k^*(w)$ for $w > w^*(k)$ but jumps to 1 at $w = w^*(k)$. This jump in $M_k(w)$ at $w = w^*(k)$ demonstrates a first-order phase transition.

$$D_k^*(w) = \frac{(l_k(w) - w)(w + l_k(w))^{\frac{k+1}{2}}}{|k|(k+3)} \left(\frac{(k+1)(w - l_k(w))}{k+3} \right)^{\frac{k+1}{2}}. \quad (3.54)$$

The only remaining constant $l_k(w)$ is finally determined from the normalization condition Eq. (3.41). The scaled bulk density is then given by

$$\phi_k(z, w) = -A_k |k| \mathcal{A}_k \frac{z^{\gamma_k} (1-z)^{\gamma_k+1}}{g_k(w) - z}, \quad (3.55)$$

which in terms of the original coordinates reads

$$\rho_b^*(y, w) = A_k (l_k(w) + y)^{\gamma_k} \frac{(\bar{l}_k(w) - y)^{\gamma_k+1}}{(w - y)} \quad \text{where} \quad \gamma_k = \frac{k+1}{2}, \quad (3.56)$$

and the constant A_k is given in Eq. (2.20). Inserting this density (3.56) in the normalization condition Eq. (3.41) and using the expression for $D_k^*(w)$ in (3.54) we find that $l_k(w)$ satisfies the equation

$$\frac{g_k(w)(2\gamma_k + 1) - (\gamma_k + 1)}{\gamma_k B(\gamma_k + 1, \gamma_k + 1)^{-\alpha_k}} \left(I(g_k(w), \gamma_k, \gamma_k + 1) + \frac{d_k(w)}{A_k} \right)^{-\alpha_k} = \frac{w}{l_{uc}}, \quad (3.57)$$

where we recall that $g_k(w) = L_k(w)/\tilde{L}_k(w)$ with $L_k(w) = w + l_k(w)$ and $\tilde{L}_k(w) = \bar{l}_l(w) +$

$l_k(w)$. Here

$$I(g_k(w), \gamma_k, \gamma_k + 1) = \int_0^1 \frac{z^{\gamma_k} (1-z)^{\gamma_k+1}}{g_k(w) - z} dz \quad \text{and} \quad d_k(w) = \frac{g_k(w)^{\gamma_k} (g_k(w) - 1)^{\gamma_k+1}}{k(k+1)}. \quad (3.58)$$

For a given w and k , we solve this equation numerically to get $g_k(w)$. Using $g_k(w) = (w + l_k(w))/\tilde{L}_k(w)$ where

$$\tilde{L}_k(w) = \bar{l}_k(w) + l_k(w) = \frac{2\gamma_k w}{(2\gamma_k + 1)g_k(w) - (1 + \gamma_k)}, \quad (3.59)$$

we then finally fix the only unknown $l_k(w)$. We then have the full analytical expression of the bulk density $\rho_b^*(y, w)$ in Eq. (3.56) and the weight of the delta function $D_k^*(w)$ in Eq. (3.54). The numerical results from MC simulation for the density shown in Fig. 3.6 are in good agreement with these analytical predictions. A slight complication arises in the MC simulation as it turns out that the particles have extremely small fluctuations and hence are confined to a small region around their mean position. So to get a better thermal average of density we need to go to larger N which is computationally costly. We bypassed this issue by considering comparatively high temperature $T = 1000$ but still satisfying the constraint $\beta N^{2\alpha_k} \gg 1$. At such high temperatures, particles fluctuate more leading to a smoother density profile for the chosen values of N . We notice that the numerical densities match better with the expression Eq. (3.56) for larger values of N .

Let us first analyze the limit $w \rightarrow l_{uc}$ from the left. In this limit, the right-hand side of Eq. (3.57) approaches 1. Consequently, one can show, by analyzing the left-hand side of Eq. (3.57) that $g_k(w) = L_k(w)/\tilde{L}_k(w) \rightarrow 1$ in that limit. Consequently, $L_k(w) = w + l_k(w)$ approaches $\tilde{L}_k(w) = l_k(w) + \bar{l}_k(w)$. Hence, $\bar{l}_k(w) \rightarrow w$ indicates that the hole disappears in this limit. In addition, from Eq. (3.59), it follows that $l_k(w) \rightarrow w$ and the support length $\tilde{L}_k(w) \rightarrow 2l_{uc}$. In addition, the weight of the delta-peak in Eq. (3.54) vanishes in this limit. We thus fully recover the 'U-shaped' unconstrained density, as in the first row of Fig. 2.2.

Now consider pushing the position of the wall w further to the left. As w decreases, more and more particles get transferred from the extended bulk to the delta peak. As a result, the support of the bulk density $\tilde{L}_k(w)$ reduces monotonically with decreasing w (see Fig. 3.7 and the weight of the delta-peak $D_k^*(w)$ increases monotonically with

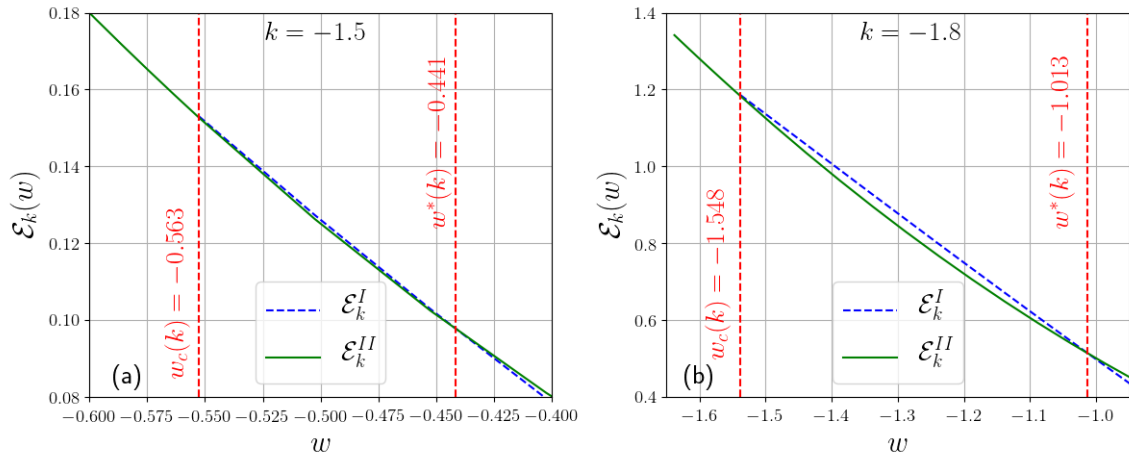


Figure 3.9: Plot of the energy $\mathcal{E}_k^I(w)$ and $\mathcal{E}_k^{II}(w) = w^2/2$ vs. w for two different values of k : for $k = -1.5$ (panel (a)) and $k = -1.8$ (panel (b)). The values of $w^*(k)$ and $w_c(k)$ are marked by vertical dashed lines. In the range $w_c(k) < w < w^*(k)$ the energy $\mathcal{E}_k^I(w) > \mathcal{E}_k^{II}(w)$, showing that the configuration with density $\rho_k^I(y, w)$ is metastable.

decreasing w (see Fig. 3.8). It turns out that there is a critical value $w_c(k)$ at which $D_k^*(w)$ hits 1 and simultaneously $\tilde{L}_k(w)$ hits 0. At $w = w_c(k)$, there are no particles left in the extended bulk and the wall absorbs all the particles. If w is decreased below $w_c(k)$, all the particles are still at the wall and the density remains a delta function at the wall, i.e.,

$$\rho_k^*(y, w) = \delta(w - y) \quad \text{for } w \leq w_c(k). \quad (3.60)$$

To determine the critical value $w_c(k)$, we first note that the support length $\tilde{L}_k(w) = l_k(w) + \bar{l}_k(w) = 0$ at $w = w_c(k)$. Using $\bar{l}_k(w_c) = -l_k(w_c)$ in Eq. (3.53) gives $l_k(w_c) = -w_c/(k+2)$. Substituting this value in the expression of $D_k^*(w)$ in Eq. (3.54) and setting $D_k^*(w_c) = 1$ gives

$$w_c(k) = \frac{(k+2) |k(k+1)|^{\frac{1}{k+2}}}{k+1}. \quad (3.61)$$

Since $-2 < k < -1$, $w_c(k) < 0$. Note that in the limit $k \rightarrow -1$, $w_c(k) \rightarrow -1$, which is indeed the left edge of the unconstrained scaled density [31, 32].

Metastability and first-order phase transition. So far, we have assumed that the optimal density profile for $-2 < k < -1$ is given by the ansatz in Eq. (3.40) which consists of a disjoint bulk part and a delta-peak at the wall, separated by a hole in between. We will

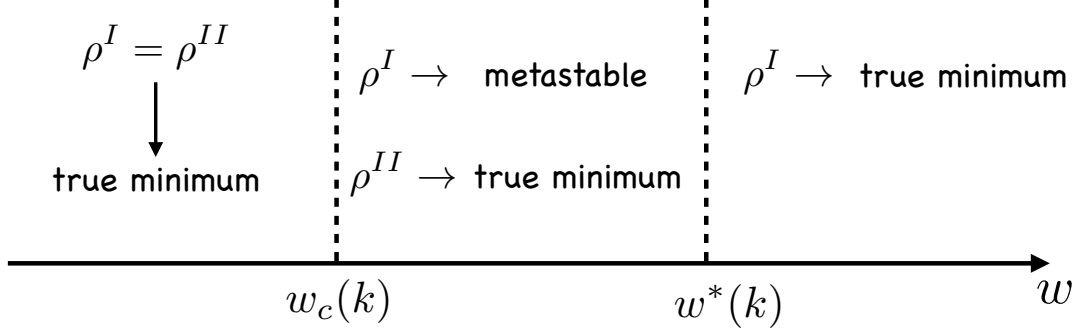


Figure 3.10: The optimal density is one of two different types $\rho_k^I(y, w)$ and $\rho_k^{II}(y, w)$ defined respectively in Eqs. (3.62) and (3.63). For $w > w^*(k)$, $\rho_k^I(y, w)$ is the optimal density. For $w_c(k) < w < w^*(k)$, the density $\rho_k^I(y, w)$ becomes metastable, while $\rho_k^{II}(y, w)$ represents the true minimum. Finally, for $w < w_c(k)$, the solutions $\rho_k^I(y, w)$ and $\rho_k^{II}(y, w)$ merge with each other.

denote this solution by the superscript I and it reads

$$\rho_k^I(y, w) = \rho_b^*(y, w)\mathbb{I}[-l_k(w) \leq y \leq \bar{l}_k(w)] + D_k^*(w)\delta(w - y). \quad (3.62)$$

We have seen that for $w \leq w_c(k)$ this density becomes a pure delta-peak located at w , with $w_c(k)$ given in Eq. (3.61). This suggests that there could be a candidate configuration for a minimum energy, denoted by a superscript II , which consists of a pure delta-function at w for any w , and not just for $w \leq w_c(k)$. It reads

$$\rho_k^{II}(y, w) = \delta(y - w). \quad (3.63)$$

These two candidate configurations $\rho_k^I(y, w)$ and $\rho_k^{II}(y, w)$ merge for $w \leq w_c(k)$. Hence for $w > w_c(k)$, one naturally wonders which one of these two configurations $\rho_k^I(y, w)$ and $\rho_k^{II}(y, w)$ has the lower energy. To answer this question, we need to evaluate the energy in Eq. (3.17) associated with these two density profiles and compare them for $w > w_c(k)$. Let us denote the two energies by $\mathcal{E}_k^I(w)$ and $\mathcal{E}_k^{II}(w)$ respectively. The energy $\mathcal{E}_k^{II}(w)$ is very simple and is given by just $\mathcal{E}_k^{II}(w) = w^2/2$. In contrast, the energy $\mathcal{E}_k^I(w)$ has to be evaluated from Eq. (3.42) with the substitution $\rho_b(y, w) = \rho_b^*(y, w)$ as given explicitly in Eq. (3.56) and $D_k(w) = D_k^*(w)$ as given in Eq. (3.54). It is a bit hard to obtain an explicit formula for $\mathcal{E}_k^I(w)$ but it can be evaluated numerically very accurately. The results are shown in Fig. 3.9 for two different values of k . Surprisingly, it turns out that

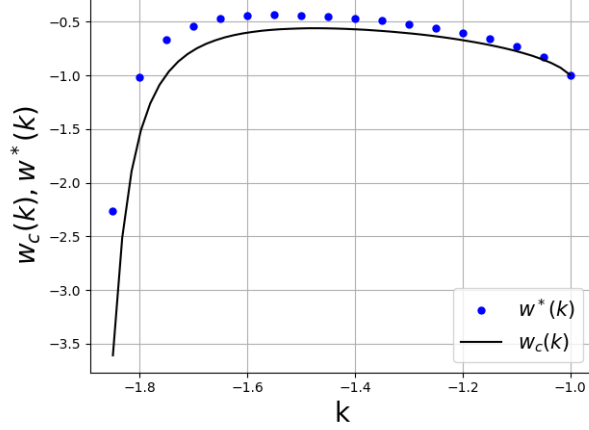


Figure 3.11: Plot of the critical wall positions $w_c(k)$ and $w^*(k)$ as functions of k in regime 3 $-2 < k \leq -1$. $w_c(k)$ (black solid line) is given by Eq. (3.61) and $w^*(k)$ (blue dots) is found numerically from the crossover location between the energies $\mathcal{E}_k^I(w)$ and $\mathcal{E}_k^{II}(w)$ as shown in Fig 3.9. We find that $w_c(k) \leq w^*(k)$ for all $-2 < k \leq -1$ with $w_c(k) = w^*(k)$ only for $k = -1$.

there is yet another critical value $w^*(k) > w_c(k)$ such that

$$\mathcal{E}_k^I(w) < \mathcal{E}_k^{II}(w) = \frac{w^2}{2} \quad \text{when} \quad w > w^*(k) \quad (3.64)$$

$$\mathcal{E}_k^I(w) > \mathcal{E}_k^{II}(w) = \frac{w^2}{2} \quad \text{when} \quad w_c(k) < w < w^*(k). \quad (3.65)$$

Thus for $w > w^*(k)$, the density $\rho_k^I(y, w)$ is the true optimal solution, while in the intermediate range $w_c(k) < w < w^*(k)$ the solution $\rho_k^{II}(y, w)$ (pure delta peak) turns out to be the true minimum. Thus for $w_c(k) < w < w^*(k)$ the solution $\rho_k^I(y, w)$ corresponds to a “metastable” minimum. Numerically we find that, in this intermediate region, the two energies $\mathcal{E}_k^I(w)$ and $\mathcal{E}_k^{II}(w)$ are very close to each other (see Fig. 3.9. Hence to summarise, the true optimal density profile is given by

$$\rho_k^*(y, w) = \begin{cases} \rho_k^I(y, w) & \text{for } w > w^*(k), \\ \rho_k^{II}(y, w) & \text{for } w < w^*(k). \end{cases} \quad (3.66)$$

These behaviors are summarised in Fig. 3.10. Thus we see that the system undergoes a first-order phase transition at $w = w^*(k)$ where the true minimum density changes abruptly from ρ^I to ρ^{II} as w crosses $w^*(k)$ from above. A manifestation of this first-order

phase transition can be observed in the order parameter defined as the amplitude of the delta peak in the true optimal solution $\rho_k^*(y, w)$

$$M_k(w) = \begin{cases} D_k^*(w) & , \quad w > w^*(k) \\ 1 & , \quad w < w^*(k) . \end{cases} \quad (3.67)$$

For $w > w^*(k)$ it is given by $D_k^*(w)$ in Eq. (3.54) associated with the density ρ^I . When w goes below $w^*(k)$ this amplitude undergoes a jump to 1 corresponding to the full delta function ρ^{II} in Eq. (3.63). In Fig. 3.8 we have plotted both $D_k^*(w)$ associated with the density ρ^I and the true order parameter $M_k(w)$ given in Eq. (3.67). Thus $M_k(w)$ undergoes a jump at $w = w^*(k)$, demonstrating a first-order phase transition.

In order to check this scenario numerically, we have performed MC simulations. We have first determined $w^*(k)$ numerically by evaluating the energy of the solutions ρ^I and ρ^{II} . In Fig. 3.11 we plot $w^*(k)$ (numerical) and $w_c(k)$ (analytical from Eq. (3.61)) as a function of k for $-2 < k \leq -1$. We observe that the difference between the two is rather small but clearly $w_c(k) < w^*(k)$. In fact, the difference between them vanishes as $k \rightarrow -1$ (see Fig. 3.11). This is expected because we know from the exact solution of the case $k = -1$ (1dOCP) that $\rho_k^I(y, w)$ is the exact optimal solution for all w [31, 32]. To test the metastability in the intermediate regime $w_c(k) < w < w^*(k)$, we consider three different wall positions (a) $w < w_c(k)$, (b) $w_c(k) < w < w^*(k)$ and (c) $w > w^*(k)$ for $k = -1.5$. For each wall position, we study two distinct initial conditions: (i) delta function and (ii) a uniform density profile, and observe the steady-state profiles. In Fig. 3.12, we find that for cases (a) and (c) the steady state profile is independent of the initial conditions and converges respectively to $\rho_k^{II}(y, w)$ and $\rho_k^I(y, w)$. On the other hand in case (b) the late time profile (within the time scale of the simulation) depends on the initial conditions – a typical hallmark of metastability. More precisely, if one starts with a delta function profile, the late time configuration remains a delta function whereas if the initial profile is uniform then the late time profile seems to stay closer to $\rho_k^I(y, w)$, within the time scale of the simulation. This picture is thus fully consistent with our discussion that for $w_c(k) < w < w^*(k)$ the density profile $\rho_k^I(y, w)$ is metastable and the true minimum is given by $\rho_k^{II}(y, w)$.

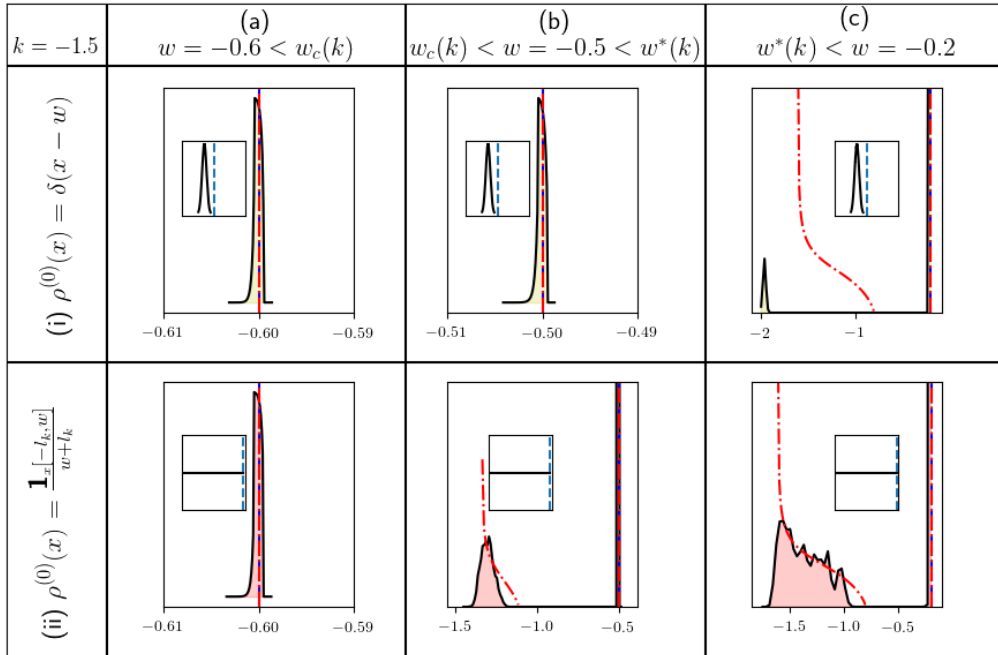


Figure 3.12: In this figure we study the metastability of the extended profile in the region $w_c(k) < w < w^*(k)$ for $k = -1.5$. For this value of k , $w_c(k) = -0.563$ and $w^*(k) = -0.441$. The figure is divided into three columns corresponding to the three regimes (a) $w = -0.6 < w_c(k)$, (b) $w_c(k) < w = -0.5 < w^*(k)$ and (c) $w = -0.2 > w^*(k)$. For each column, the insets of the top row and the bottom row indicate two different initial conditions (a delta peak and a flat density) while the main figures show the final configuration after a large number of MC steps. In columns (a) and (c) we see that the final configurations in the top row and in the bottom row are qualitatively similar, indicating the irrelevance of the initial conditions. In contrast, in column (b) the final configurations in the top and in the bottom row corresponding to two different initial conditions seem to lead to different final configurations, within the time scale of the simulation. This dependence on the initial condition is a signature of metastability in the region (b).

3.4 Conclusions

In this chapter, we have studied the average density of a harmonically confined Riesz gas [see Eq. (2.1)] of N particles for large N in the presence of a hard wall located at W . We have computed exactly this average density in the limit of large N . This density can be classified into three different regimes of k , as depicted in Figs. 2.3 and 3.1. For $k \geq 1$, where the interactions are effectively short-ranged, the appropriately scaled density has finite support over $[-l_k(w), w]$ where w is the scaled position of the wall. While the density vanishes at the left edge of the support, it approaches a nonzero constant at the right edge w . For $-1 < k < 1$, where the interactions are weakly long-ranged, we find that

the scaled density is again supported over $[-l_k(w), w]$. While it vanishes at the left edge of the support, it diverges at the right edge w algebraically with an exponent $(k - 1)/2$. For $-2 < k \leq -1$, the interactions are strongly long-ranged, leading to a rather exotic density profile: here the density has an extended bulk part and a delta-peak at the wall and they are separated by a hole for $-2 < k < -1$. Interestingly, we find that there is a first-order phase transition at a critical value $w = w^*(k)$ such that for $w < w^*(k)$ the optimal solution changes its nature. It consists only of a delta peak at the wall, i.e., the wall essentially absorbs all the particles and there is no extended part. The amplitude of the delta-peak $M_k(w)$ plays the role of an order parameter that undergoes a jump to a value 1 as w is decreased through $w^*(k)$.

Our derivation can be straightforwardly generalized to other forms of external confining potential, for e.g. $|x|^\delta$ with any positive and real δ . Note that our study corresponds to $\delta = 2$. In this case, depending on the value of δ , we expect the system to have: (1) short-ranged interacting, (2) weakly long-ranged interacting and (3) strongly long-ranged interacting regimes as mentioned in the introduction. It would be interesting to study how the transitions in the shape of the density profile appear as one goes from one regime to another and also how these density profiles get modified in the presence of a wall. Note that for a potential $|x|^\delta$, to confine the particles, we must have $k > -\delta$. Now, by definition, the strongly long-ranged interaction exists in the range $-\delta < k < -1$. Hence, the strongly long-ranged phase exists only for $\delta > 1$ where the range $k \in [-\delta, -1]$ is non-empty.

As mentioned in the introduction, the cumulative distribution of the position of the right-most particle x_{\max} is closely related to this density profile in the presence of a wall in the large N limit [see Eq. (3.1)]. Therefore the results obtained here will be an essential ingredient to compute the probability of large deviations of x_{\max} for any $k > -2$. Indeed, this large deviation behavior of x_{\max} has so far been computed only for two specific values of k , namely $k \rightarrow 0$ limit [22, 23] and $k = -1$ [31, 32]. The $k \rightarrow 0$ limit, also describes the large deviation behaviour of the largest eigenvalue of random matrix from the Gaussian ensemble. In this case, it is known that when the wall hits the right edge l_{uc} of the unconstrained density ($\rho_{\text{uc}}^*(y)$), it is accompanied by a third-order phase transition, where the third derivative of the large deviation function has a discontinuity [25]. Interestingly, a similar third-order phase transition occurs also for $k = -1$ [31, 32]. It will be interesting

to investigate whether this transition remains third-order for other values of k [59]. We study this problem in the next chapter.

This chapter describes the study from the following published work, Ref. [60]:

J. Kethepalli, M. Kulkarni, A. Kundu, S. N. Majumdar, D. Mukamel, G. Schehr, “Harmonically confined long-ranged interacting gas in the presence of a hard wall”, [Journal of Statistical Mechanics: Theory and Experiment 2021 \(10\), 103209](#)

Remark: In the following published article Ref. [60], we have expressed the scaled variables with a tilde and unscaled variables without a tilde. However, to make notations consistent throughout the thesis all the scaled variables are without tilde and the unscaled variables are with tilde.

Chapter 4

Edge fluctuations and third-order phase transition

4.1 Introduction

Understanding the properties of interacting many-particle systems has been a subject of immense interest in both physics and mathematics. Examples of such systems range from sand-pile [101] to neural networks [102], electrons in metal and quantum liquids [103] to finance [104], Big-data [105], charged particles [11] and gravitational systems [3] to name a few. While collective phenomena are widely studied in many of these systems, recently there has been a growing interest in investigating the local properties such as fluctuations, correlations, and extreme value statistics (EVS). With recent developments in experimental techniques, it has become possible to probe the physics at a microscopic scale such as in cold atoms [56–58] and ions [13]. Often the physics becomes even more interesting and exotic when the interactions become long-ranged in such systems. Therefore, there is a growing need to study the properties of long-range interacting systems. A suitable and promising platform for such a study is the family of confined Riesz gas [17] models with the energy function given in Eq. (2.1).

In the previous Chapters, we discussed the density profile of these particles in thermal equilibrium has a finite support [45, 60]. In this chapter, we study the fluctuations of the position x_{\max} of the rightmost particle. In Fig. 4.1, a schematic plot of the observable x_{\max} is shown. This question falls under the paradigm of EVS of correlated variables [98]. Such questions have been studied in several contexts, for example, random matrix theory

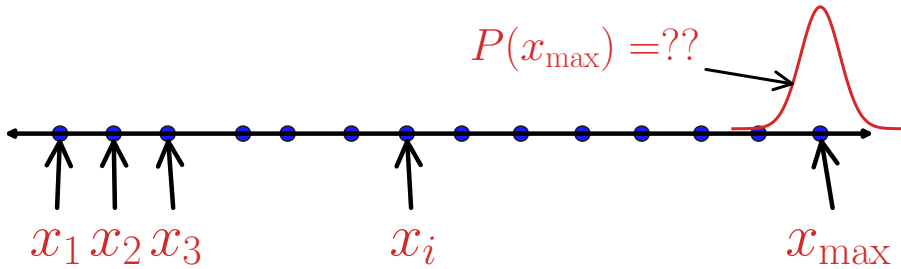


Figure 4.1: Schematic plot of the observable $x_{\max} = \max(x_1, x_2, x_3, \dots, x_N)$, the position of the rightmost particle, where x_i is the position of i -th particle. In this chapter, We study the fluctuations of x_{\max} for the harmonically confined Riesz gas with the energy function given in Eq. (2.1).

(RMT) [25, 89, 90, 106], the lowest energy modes in ultracold gas [107], highest energy barrier in disordered systems [108], height fluctuations in interface problems [109–111] and binary search problems [112] to name a few.

In the context of RMT, the position x_{\max} of the rightmost particle corresponds to the largest eigenvalue λ_{\max} of a $N \times N$ random matrix. For random matrices chosen from Gaussian ensembles characterized by the symmetry class parameter $\beta = 1, 2, 4$, the joint distribution of the real eigenvalues $\{\lambda_1, \lambda_2, \dots, \lambda_N\}$ is given by [19, 20, 23, 25]

$$P_0[\{\lambda_i\}] = \frac{1}{Z_0} \exp \left(-\frac{\beta}{2} \left(\sum_i \lambda_i^2 - \sum_{i \neq j} \ln |\lambda_i - \lambda_j| \right) \right), \quad (4.1)$$

where Z_0 is a normalization constant. This distribution can be interpreted as the Boltzmann weight of N particles with positions $x_i \equiv \lambda_i$ interacting via logarithmic potential. This system of particles is known in the literature as Dyson’s log-gas [20]. Note that this system corresponds to taking $k \rightarrow 0$ limit of the Riesz gas [Eq. (2.1)] after the substitution $J \rightarrow J_0/k$. Hence, we use subscript “0” in Eq. (4.1) and set $J_0 = 1$. It is well known that for large N the particle (or eigenvalue) density is given by Wigner semi-circle law i.e.

$$\rho_N^*(\lambda) = \frac{1}{\sqrt{N}} f_0 \left(\frac{\lambda}{\sqrt{N}} \right) \quad \text{with} \quad f_0(y) = \frac{1}{\pi} \sqrt{2 - y^2}. \quad (4.2)$$

with the support $\lambda \in [-\sqrt{2N}, \sqrt{2N}]$ [18, 21]. The largest eigenvalue $\lambda_{\max} = \max_{1 \leq i \leq N} \{\lambda_i\}$ represents the position of the rightmost particle of the log-gas. The statistics of λ_{\max} is well understood [22, 23, 25, 89, 90]. In particular, the average of λ_{\max} is given by the

upper edge of the Wigner semi-circle $\langle \lambda_{\max} \rangle = \sqrt{2N}$. The typical fluctuations around this mean are known to scale as $\sigma_{\lambda_{\max}} = \sqrt{\langle \lambda_{\max}^2 \rangle - \langle \lambda_{\max} \rangle^2} \sim N^{-\frac{1}{6}}$ and are described by the Tracy-Widom distribution $\mathcal{F}'_{\beta}(y) = \mathcal{F}_{\beta}^{(0)'}$, where the superscript '(0)' refers to the limit $k \rightarrow 0$ [89, 90]. The distribution of atypically large fluctuations of λ_{\max} of $O(\sqrt{N})$ on both sides of the mean (left and right) are described by appropriate large deviation functions (LDF). A schematic plot of this distribution is shown in Fig. 4.2a. The cumulative distribution function (CDF) of the scaled variable $\tilde{\lambda}_{\max} = \lambda_{\max}/\sqrt{N}$ is given by [22, 23, 25, 89, 90, 113]

$$\text{Prob.}[\tilde{\lambda}_{\max} < w, N] \approx \begin{cases} e^{-\beta N^2 \Phi_{-}(w,0)} & \sqrt{2} - w \sim O(1) \\ \mathcal{F}_{\beta}^{(0)}\left(\sqrt{2}N^{\frac{2}{3}}(w - \sqrt{2})\right) & |\sqrt{2} - w| \sim O(N^{-\frac{2}{3}}) \\ e^{-\beta N \Phi_{+}(w,0)} & w - \sqrt{2} \sim O(1), \end{cases} \quad (4.3)$$

where $\Phi_{-}(w, 0)$ and $\Phi_{+}(w, 0)$ are, respectively, the left and the right LDF. The 0 in the argument of the LDF indicates that the log-gas corresponds to Riesz gas in Eq. (2.1) in the limit $k \rightarrow 0$. These functions have been explicitly computed and are given by [22, 23]

$$\Phi_{-}(w, 0) = \frac{1}{108} \left[36w^2 - w^4 - (15w + w^3)\sqrt{w^2 + 6} + 27 \left(\ln 18 - 2 \ln[w + \sqrt{w^2 + 6}] \right) \right], \quad (4.4)$$

for $w < \sqrt{2}$ and [113]

$$\Phi_{+}(w, 0) = \frac{1}{2}w\sqrt{w^2 - 2} + \ln \frac{w - \sqrt{w^2 - 2}}{\sqrt{2}}, \quad \text{for } w > \sqrt{2}. \quad (4.5)$$

The large deviation behavior is different for $w > \sqrt{2}$ and $w < \sqrt{2}$. This difference is manifested as a thermodynamic phase transition if one considers the free energy density given by

$$\lim_{N \rightarrow \infty} -\frac{1}{N^2} \log \left(\text{Prob.}[\tilde{\lambda}_{\max} < w, N] \right) = \begin{cases} \Phi_{-}(w, 0), & w < \sqrt{2} \\ 0 & w > \sqrt{2}. \end{cases} \quad (4.6)$$

Since $\Phi_{-}(w, 0) \sim (\sqrt{2} - w)^3$ as $w \rightarrow \sqrt{2}$ from Eq. (4.4), the third derivative of the free energy with respect to w is discontinuous at $w = \sqrt{2}$. This implies that the system

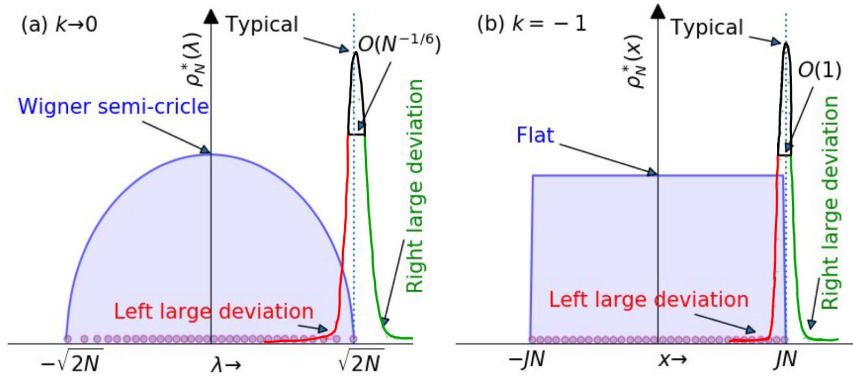


Figure 4.2: Schematic plot of the probability density function (PDF) of (a) the largest eigenvalue in RMT (Dyson’s log-gas) and (b) the position of the rightmost particle in the 1dOCP, along with the respective density profiles. The PDF of the position of the edge particle in these cases is divided into three parts – typical (black) in the central part and, left (red) and right (green) large deviations. We show in this chapter that such representative pictures also hold for the harmonically confined Riesz gas with $-2 < k < \infty$.

undergoes a 3rd order phase transition, from a phase ($w > \sqrt{2}$) in which the rightmost particle is pulled out from the bulk to the right of $w = \sqrt{2}$ (pulled phase) to a phase ($w < \sqrt{2}$) in which all the particles are pushed to the left of $w = \sqrt{2}$ (pushed phase) [25]. Recall that $w = \sqrt{2}$ is the right edge of the scaled density of the particles.

A similar transition has also been observed in the 1d one component plasma (1dOCP) confined by a harmonic potential. The energy function in this case is given by

$$\tilde{E}_k(\{x_i\}) = \sum_i^N \frac{x_i^2}{2} - \frac{J}{2} \sum_{i \neq j}^N |x_i - x_j|, \quad (4.7)$$

where x_i ’s are the particle positions and J is the strength of the repulsive interaction. Note that this corresponds to $k = -1$ of the Riesz gas model Eq. (2.1). Here the average thermal density profile is flat and is given by

$$\rho_N^*(x) = \frac{1}{N} f_{-1} \left(\frac{x}{N} \right) \text{ where } f_{-1}(y) = \frac{1}{2J}, \quad (4.8)$$

with the support $x \in [-NJ, NJ]$. The statistics of the position of the rightmost particle x_{\max} has been studied recently [31, 32, 37, 114]. Its average is $\langle x_{\max} \rangle = NJ$ and its typical fluctuations are $O(1)$ and are governed by the CDF $\mathcal{F}_\beta^{(-1)}(x)$ which is a solution to a

non-local eigenvalue equation

$$\frac{d}{dx} \mathcal{F}_\beta^{(-1)}(x) = A(J) e^{-\frac{x^2}{2}} \mathcal{F}_\beta^{(-1)}(x + 2J), \quad (4.9)$$

where the eigenvalue $A(J)$ is determined by satisfying the boundary conditions $\mathcal{F}_\beta^{(-1)}(-\infty) = 0$, $\mathcal{F}_\beta^{(-1)}(\infty) = 1$ and $0 \leq \mathcal{F}_\beta^{(-1)}(x) \leq 1$ for $x \in (-\infty, \infty)$. The distribution of atypical fluctuations (of $O(N)$ from the mean) governed by the LDF $\Phi_\pm(w, -1)$ are also well understood. A schematic plot of the PDF is shown in Fig. 4.2b. The CDF of the scaled variable $y_{\max} = x_{\max}/N$ is given by

$$\text{Prob.}[y_{\max} < w] \approx \begin{cases} e^{-\beta N^3 \Phi_-(w, -1)} & J - w \sim O(1) \\ \mathcal{F}_\beta^{(-1)}(N(w - J) + J) & |w - J| \sim O(N^{-1}) \\ e^{-\beta N^2 \Phi_+(w, -1)} & w - J \sim O(1). \end{cases} \quad (4.10)$$

The LDF are given by [31, 32]

$$\Phi_-(w, -1) = \begin{cases} \frac{w^2}{2} + \frac{J^2}{6} & \text{for } w < -J \\ \frac{(J-w)^3}{12J} & \text{for } -J < w < J, \end{cases} \quad (4.11)$$

$$\Phi_+(w, -1) = \frac{(w - J)^2}{2}. \quad (4.12)$$

Analogous to the log-gas case [Eq. (4.3)], for the 1dOCP also the large deviation functions exhibit different behaviors to the left and right of the mean position $\langle y_{\max} \rangle = J$. Once again this difference gets manifested as a pulled-to-pushed phase transition at $w = J$. Interestingly the order of the phase transition is also 3 because $\Phi_-(w, -1) \sim (J - w)^3$ as $w \rightarrow J$ from Eq. (4.11) [32].

There are many physical problems where these pulled-to-pushed types of phase transitions have been investigated. For example, such transitions have been observed in spin-glass [115], wireless telecommunication [116], chaotic cavities [117–120], entanglement in bipartite quantum systems [121–123], random tilings [124] and non intersecting Brownian excursions [125, 126] to name a few (a review can be found in Ref. [25]). Since these systems are often related to RMT, the third-order transition is attributed to Dyson’s log-gas and its variants. Another family of models different from log-gas which also exhibit such

third-order phase transitions are confined particles in d dimensions interacting via d dimensional Coulomb interaction potentials ($V(r)$ is $|r|, \log(r)$ for $d = 1, 2$ respectively and $V(r) = 1/r^{d-2}$ for $d > 2$) [127, 128] and Yukawa potentials [129]. In fact, similar phase transitions were already identified in the context of large- N gauge theories and are well known as Gross-Witten-Wadia [130, 131] or Douglas-Kazakov [132] phase transitions.

The third-order phase transitions in all the above studies are either rooted in RMT or Coulomb interaction. In this chapter, we investigate the extent of this universality in models that do not fall in either of the above two classes and focus on the Riesz gas family of models which has repulsive interactions of the form $V(r) \propto |r|^{-k}$.

We study the large-deviation properties of the distribution of the position of the rightmost particle of the harmonically confined Riesz gas model with general $k > -2$. We obtain the explicit expressions for the left and the right LDF $\Phi_-(w, k)$ and $\Phi_+(w, k)$, respectively. We find that for these models also the properties of large deviations get manifested as a pulled-to-pushed phase transition. Remarkably, we show that the third-order phase transition persists $\forall k > -2$, thereby demonstrating the universality even beyond RMT and Coulomb class of models. We also study the system size scaling of the typical fluctuations numerically and we find that the commonly used ‘‘Lifshitz argument’’ is valid only for special values $k = -1$ and $k \rightarrow 0$. In addition, we also show that the appropriate Hessian theory predicts the scale of the typical fluctuations remarkably well.

The rest of the chapter is organized as follows. In Section. 4.2 we provide a summary of our results. The derivation of results is given in Section. 4.3. We conclude our findings along with an outlook in Section. 4.4. Additional details of our analytical and numerical results are relegated to A.2, A.3 and A.4.

4.2 Summary of the results

We study the distribution of the typical and the atypical fluctuations of the scaled position y_{\max} of the rightmost particle for different k . The typical part of the distribution is studied numerically and the atypical part is studied both analytically and numerically. We show that the atypical fluctuations are described by the appropriate LDF. The mean of the rightmost particle is given by the upper edge of the support of unconstrained density [Eq. (2.20)], which in scaled variable $y_{\max} = x_{\max}/L_N$ is given by $\langle y_{\max} \rangle = l_{\text{uc}}$ where l_{uc} is

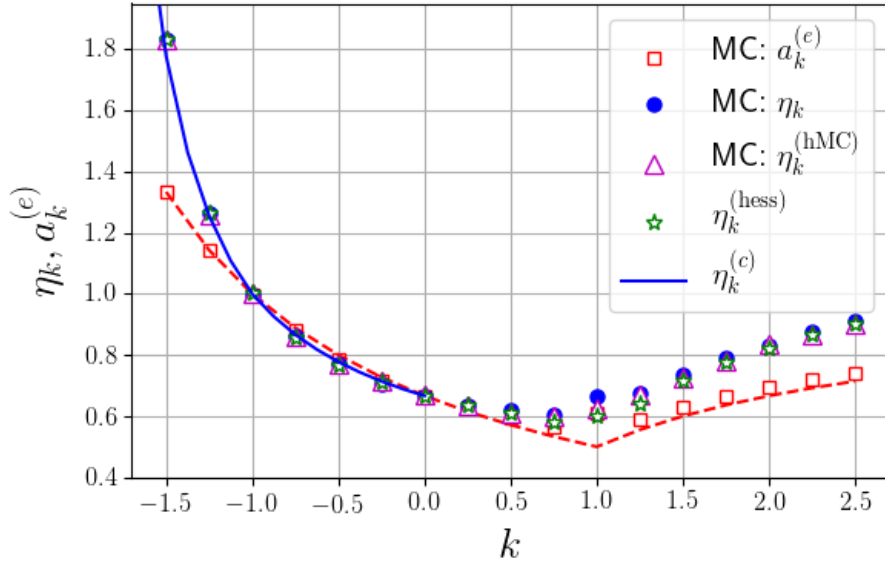


Figure 4.3: Behavior of η_k [Eq. (4.20), disks] and the exponent $a_k^{(e)}$ of the mean gap at the edge [Eq. (4.22), squares], as a function of k is plotted here. The exponent η_k for different values of k are obtained by fitting the data for $\sigma_{y_{\max}}^2$ with N [See Fig. A.1 and A.2] obtained numerically (MC) for the confined Riesz gas [Eq. (2.1)]. The exponent $a_k^{(e)}$ is obtained similarly. We notice that $a_k^{(e)}$ obtained from numerics agrees with the one obtained from the Lifshitz argument (dashed red line) given in Eq. (4.21). Green stars represent the exponent η_k^{hess} obtained by numerically inverting the Hessian matrix [see Eq. (4.26) and Eq. (4.27)]. We also find the exponent $\eta_k^{(\text{hMC})}$ [See Fig. A.2 and A.2] from the MC simulations of the Hessian hamiltonian [Eq. (4.24)]. It is interesting to note that the value of the exponent extracted from the three different approaches is in excellent agreement with each other ($\eta_k = \eta_k^{(\text{hess})} = \eta_k^{(\text{hMC})}$). The solid blue line represents the conjecture for η_k for $-2 < k < 0$ given in Eq. (4.30) (where the superscript “c” indicates our conjecture). The agreement between this conjecture and the MC simulation results is excellent. The parameters used in these simulations are $T = 1$ and $J = 1$.

given in Eq. (2.19). For large but finite N , y_{\max} fluctuates from sample to sample and we numerically observe that the standard deviation $\sigma_{y_{\max}} = \sqrt{\langle y_{\max}^2 \rangle - \langle y_{\max} \rangle^2}$ describing the typical fluctuation is of order $N^{-\eta_k}$. It is known that, for inverse temperature $\beta = O(1)$, for the Dyson’s log-gas $\eta_0 = 2/3$ [20, 25], for the 1dOCP $\eta_{-1} = 1$ [31, 32] while for the Calogero-Moser system $\eta_2 = 5/6$ ¹ [133]. We have computed η_k numerically for different values of k via Monte-Carlo (MC) simulation using the Metropolis-Hastings algorithm and the results are shown in Fig. 4.3. By expanding the energy around the ground state and truncating it at bilinear order, as is done within the Hessian theory, we find that the resulting exponent of the variance fits the numerically obtained exponent remarkably

¹The values of η_0 [20, 25] and η_{-1} [31, 32] are analytically established whereas that of η_2 is numerically established [133].

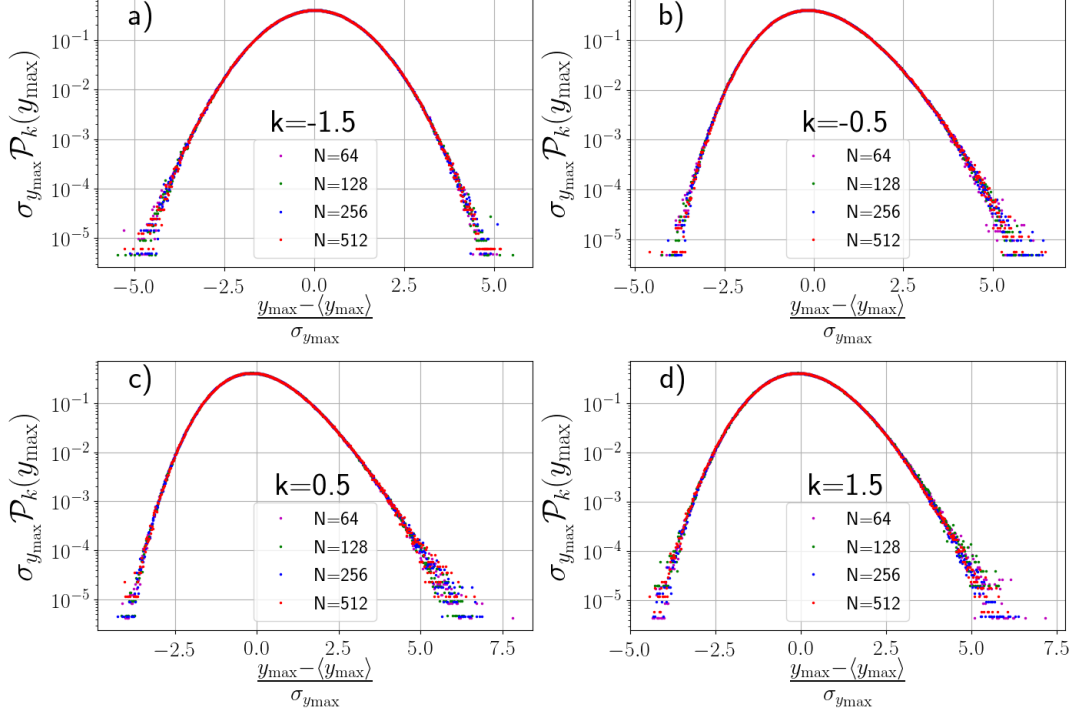


Figure 4.4: Typical distribution of y_{\max} for various values of k . We notice excellent data collapse, when we plotted $\sigma_{y_{\max}} \mathcal{P}_k(y_{\max})$ versus the scaling variable $(y_{\max} - \langle y_{\max} \rangle) / \sigma_{y_{\max}}$. Here the values of $\sigma_{y_{\max}}$ and $\langle y_{\max} \rangle$ were extracted from the data (therefore no fitting parameter was used).

well. Further, we provide a conjecture [Eq. (4.30)] for the explicit k dependence of η_k for $k < 0$ based on scaling arguments. Fig. 4.3 demonstrates an excellent agreement between our conjecture and numerical data. We observe an excellent collapse for the typical part of the distribution in terms of the scaling variable $\tilde{y}_{\max} = (y_{\max} - \langle y_{\max} \rangle) / \sigma_{y_{\max}}$ (see Fig. 4.4). This implies that the CDF has scaling form $\text{Prob.}[y_{\max} < w] = \mathcal{F}_{\beta}^{(k)}(N^{\eta_k}(w - l_{\text{uc}}))$ for large N in the typical part of the distribution i.e. $|w - l_{\text{uc}}| \lesssim O(N^{-\eta_k})$. The fluctuations larger than this scale i.e. $|w - l_{\text{uc}}| \sim O(1)$ are atypical fluctuations which are described by the left and the right LDF $\Phi_{-}(w, k)$ and $\Phi_{+}(w, k)$ respectively. The CDF has the form

$$\text{Prob.}[y_{\max} < w] \approx \begin{cases} e^{-\beta N^{2\alpha_k+1} \Phi_{-}(w, k)} & l_{\text{uc}} - w \gtrsim O(1) \\ \mathcal{F}_{\beta}^{(k)}(N^{\eta_k}(w - l_{\text{uc}})) & |w - l_{\text{uc}}| \lesssim O(N^{-\eta_k}) \\ 1 - e^{-\beta N^{2\alpha_k} \Phi_{+}(w, k)} & w - l_{\text{uc}} \gtrsim O(1), \end{cases} \quad (4.13)$$

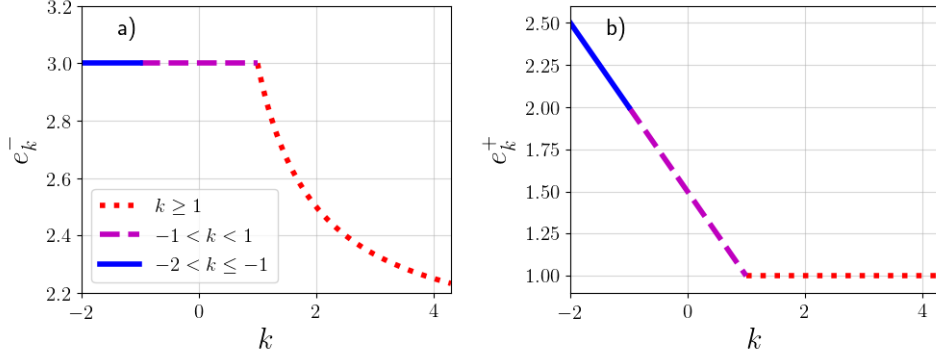


Figure 4.5: (a) Plot of the exponent e_k^- , that governs the asymptotic behavior of the left large deviation function given in Eq. (4.50) for $k \geq 1$, Eq. (4.60) for $-1 < k < 1$ and Eq. (4.73) for $-2 < k \leq -1$. (b) Plot of the exponent e_k^+ characterising the asymptotic behavior of the right LDF which is 1 for $k \geq 1$, and is given in Eq. (4.61) for $-1 < k < 1$ and Eq. (4.74) for $-2 < k \leq -1$.

Regimes	e_k^-	e_k^+	$\Phi_-(w, k)$	$\Phi_+(w, k)$
$k > 1$	$2 + \frac{1}{k}$	1	Eq. (4.47), Fig. 4.8a	Eq. (4.48), Fig. 4.8b
$-1 < k < 1$	3	$\frac{3-k}{2}$	Eq. (4.55), Fig. 4.9a	Eq. (4.56), Fig. 4.9b
$-2 < k < -1$	3	$\frac{3-k}{2}$	Eq. (4.69), Fig. 4.10a	Eq. (4.71), Fig. 4.10b

Table 4.1: The table summarizes the exponents e_k^\mp that characterize the asymptotic behavior of left and right LDF respectively. The reference to the expressions together with the corresponding plot of the LDF in various regimes of k are also provided.

where α_k is given in Eq. (2.6) and equivalently the PDF is given by

$$\mathcal{P}_k[y_{\max} = w] \approx \begin{cases} e^{-\beta N^{2\alpha_k+1} \Phi_-(w, k)} & l_{\text{uc}} - w \gtrsim O(1) \\ N^{\eta_k} \mathcal{F}_\beta^{(k)'}(N^{\eta_k}(w - l_{\text{uc}})) & |w - l_{\text{uc}}| \lesssim O(N^{-\eta_k}) \\ e^{-\beta N^{2\alpha_k} \Phi_+(w, k)} & w - l_{\text{uc}} \gtrsim O(1). \end{cases} \quad (4.14)$$

It is worth reminding that for $k \rightarrow 0$, $\mathcal{F}_\beta^{(0)'}$ (z) is the Tracy-Widom distribution while for $k = -1$, $\mathcal{F}_\beta^{(-1)}$ (z) is the solution of Eq. (4.9). As mentioned above for general k , we provide numerical evidence supporting the existence of the scaling distributions $\mathcal{F}_\beta^{(k)}$ (z) for other values of k (see Fig. 4.4).

We have analytically studied the probability of the atypical fluctuations characterized by the LDF $\Phi_\pm(w, k)$. We have obtained explicit expressions of these functions given in Eq. (4.47) and (4.48) for $k \geq 1$, Eq. (4.55) and (4.56) for $-1 < k < 1$ and Eq. (4.69) and (4.71) for $-2 < k < -1$. These explicit expressions are one of our main results.

Another important result of our study is the observation that for general k also, the PDF behaves differently for $w > l_{\text{uc}}$ and $w < l_{\text{uc}}$ (as seen in Dyson's log-gas and the 1dOCP) which again leads to a phase transition at the $w = l_{\text{uc}}$. This transition can be seen from the behavior of the free energy (discussed later in the Section. 4.3.2), namely

$$\lim_{N \rightarrow \infty} -\frac{1}{N^{2\alpha_k+1}} \log(\text{Prob.}[y_{\text{max}} < w]) = \begin{cases} \Phi_-(w, k), & w < l_{\text{uc}} \\ 0 & w > l_{\text{uc}}, \end{cases} \quad (4.15)$$

across $w = l_{\text{uc}}$. The nature of the transition is determined by the asymptotic behavior of the left large deviation function as $w \rightarrow l_k^{\text{uc}-}$,

$$\Phi_-(w, k) \sim (l_{\text{uc}} - w)^{e_k^-}, \quad (4.16)$$

where the exponent e_k^- determines the order of the transition. The asymptotic behavior of the right large deviation function as $w \rightarrow l_k^{\text{uc}+}$ is given by

$$\Phi_+(w, k) \sim (w - l_{\text{uc}})^{e_k^+}. \quad (4.17)$$

In Section. 4.3 we compute the exponents e_k^\mp , $\forall k > -2$ analytically. The values of these exponents are presented in Table 4.1 and a representative plot is given in Fig 4.5. In the regime $-2 < k < 1$, we find that the order of phase transition is 3, since $e_k^- = 3$. In the regime $k > 1$, $e_k^- = (2 + 1/k)$, which implies that the third derivative of $\Phi_-(w, k)$ is discontinuous and hence the system undergoes a third-order phase transition (because $[2 + 1/k] = 3$, for $k > 1$ where $[\cdot]$ represents the ceiling function) according to the Ehrenfest classification [134, 135]. This leads to the remarkable finding that $\forall k > -2$ the system exhibits a third-order phase transition ².

²Alternatively, the Ehrenfest classification [134, 135] can be generalized by extending the notion of normal derivatives to fractional derivatives [136–138] $\frac{d^a}{dw^a} w^b = \frac{\Gamma[b+1]}{\Gamma[b+1-a]} w^{b-a}$, with $a, b > 0$. If one goes by this classification the order of phase transition is $(2 + 1/k)$ for $k > 1$.

4.3 Distribution of x_{\max}

We start with the CDF of $x_{\max} = \max_{1 \leq i \leq N} x_i$, namely

$$\text{Prob.}[x_{\max} < W] = \text{Prob.}[\{x_i < W\}_{i=1}^N, \beta, N] = \frac{Z_k(W)}{Z_k(W \rightarrow \infty)}, \quad (4.18)$$

where, the partition function $Z_k(W)$ is given by

$$Z_k(W) = \int_{-\infty}^W dx_1 \dots \int_{-\infty}^W dx_N \exp\left(-\beta \tilde{E}_k(\{x_i\})\right), \quad (4.19)$$

with $\tilde{E}_k(\{x_i\})$ given in Eq. (2.1). This partition function can be interpreted as the partition function of the original Riesz gas in the presence of a hard wall at $x = W$. Recall that we studied this partition function in the previous chapter 3. For $k \rightarrow 0$ and $k = -1$, these multiple integrals can be computed in the large N limit. It has been shown that this integral is related to the solution of Painlevé equation for $k \rightarrow 0$ [89, 90] and a non-local eigenvalue equation for $k = -1$ [31, 32]. For other values of k , performing these multiple integrals analytically remains an open and challenging problem. We therefore resort here to direct numerical simulations to compute the typical part of the distribution.

4.3.1 Distribution in the typical region

In this section, we discuss the distribution of $y_{\max} = x_{\max}/L_N$. To compute this distribution numerically we perform conventional MC simulations using the Metropolis-Hastings algorithm for different values of k from the three regimes mentioned previously ($k \geq 1$, $-1 < k < 1$ and $-2 < k \leq -1$). For each value of k , we perform simulations for $N = 64, 128, 256, 512$ and also compute the $\langle y_{\max} \rangle$ and the variance $\sigma_{y_{\max}}^2 = \langle y_{\max}^2 \rangle - \langle y_{\max} \rangle^2$. As argued before, we expect $\langle y_{\max} \rangle = l_{\text{uc}}$, for large- N , which is indeed corroborated by our simulations. Furthermore, we find that for large N , $\sigma_{y_{\max}}$ scales as

$$\sigma_{y_{\max}} \sim N^{-\eta_k}, \quad \text{with } \eta_k > 0, \quad (4.20)$$

as shown in Fig. A.1 in A.2. In Fig. 4.3 we plot η_k as a function of k where we observe that η_k is interestingly non-monotonic.

One naturally wonders how this fluctuation of y_{\max} compares with the mean of the separation between the scaled positions of the rightmost and the second rightmost particles denoted as $\langle \Delta_{\text{edge}} \rangle$. The N dependence of this average separation at the edge can be obtained using the ‘‘Lifshitz argument’’, which is frequently used in extreme value statistics [25, 98]. According to this argument

$$N \int_{l_{\text{uc}} - \langle \Delta_{\text{edge}} \rangle}^{l_{\text{uc}}} dy \rho_{\text{uc}}^*(y) = 1, \quad (4.21)$$

which essentially says that there is only one particle between the positions $l_{\text{uc}} - \langle \Delta_{\text{edge}} \rangle$ and l_{uc} . This equation implies

$$\langle \Delta_{\text{edge}} \rangle \sim N^{-a_k^{(e)}} \quad \text{with} \quad a_k^{(e)} = \frac{1}{1 + \gamma_k}, \quad (4.22)$$

where γ_k is given in Eq. (2.19). Our numerical data (squares) for $\langle \Delta_{\text{edge}} \rangle$ verifies this result in Eq. (4.22) as shown in Fig. 4.3. It is usually assumed that the average edge gap provides the scale for the fluctuations of y_{\max} . This has been confirmed for Dyson’s log-gas ($k \rightarrow 0$) and the 1dOCP ($k = -1$). Interestingly, our numerical results in Fig. 4.3 show that this assumption $\eta_k = a_k^{(e)}$ is not true for other values of k .

We now look at the distribution of the typical fluctuations (of order $\sim \sigma_{y_{\max}}$) for different values of k . In Fig. 4.4 we plot $\sigma_{y_{\max}} P_{\text{num}}(y_{\max})$ obtained numerically as functions of $\frac{y_{\max} - \langle y_{\max} \rangle}{\sigma_{y_{\max}}}$ (where the subscript ‘‘num’’ represents the distribution obtained from numerics). The excellent data collapse for different values of N indicates the following scaling behavior for the typical part of the distribution

$$\mathcal{P}_k [y_{\max} = w] \approx N^{\eta_k} \mathcal{F}_\beta^{(k)'} (N^{\eta_k} (w - l_{\text{uc}})), \quad \text{for } |w - l_{\text{uc}}| \lesssim O(N^{-\eta_k}), \quad (4.23)$$

as announced in Eq. (4.14). However, this scaling form is not expected to be valid for larger fluctuations of y_{\max} of $O(1)$ around its mean. For this one needs to study the atypical fluctuations which is done in Section 4.3.2. Below we first provide some understanding of the exponent η_k using a Hessian theory and a scaling argument.

Estimating the exponent η_k

Hessian Approach: Since the inverse temperature $\beta \sim O(1)$, one would expect that

the small fluctuations of y_{\max} around its mean can be described by making a quadratic approximation of the Hamiltonian characterized by a Hessian evaluated around the minimum energy position configuration $y_i^* = x_i^*/L_N$ for $i = 1, 2, \dots, N$. This configuration $\{x_i^*\}$ can be obtained by minimizing the energy function in Eq. (2.1) numerically using the Broyden-Fletcher-Goldfarb-Shanno (BFGS) algorithm [139, 140]. Under the Hessian approximation, the Hamiltonian takes the form

$$\tilde{E}_k(\{x_i\}) \approx \tilde{E}_k(\{x_i^*\}) + \frac{1}{2} \sum_{i,j=1}^N H_{ij}(x_i - x_i^*)(x_j - x_j^*), \quad (4.24)$$

where the Hessian matrix is given by

$$H_{ij} = \left[\frac{\partial^2 \tilde{E}_k(\{x_i\})}{\partial x_i \partial x_j} \right]_{\{x_i^*\}} = \delta_{ij} \left[1 + \sum_{n \neq i}^N \frac{J \operatorname{sgn}(k) k(k+1)}{(x_i^* - x_n^*)^{k+2}} \right] - (1 - \delta_{ij}) \frac{J \operatorname{sgn}(k) k(k+1)}{(x_i^* - x_j^*)^{k+2}}. \quad (4.25)$$

The above Hessian approximation is justified when the standard deviation (σ_{Δ_i} where $\Delta_i = x_{i+1} - x_i$) of the i^{th} bond is smaller than the mean length of the bond ($\langle \Delta_i \rangle$) i.e. the relative fluctuations are very small ($\sigma_{\Delta_i}/\Delta_i \ll 1$) at a given temperature and system size N . We can investigate the properties of interest using the Hessian Hamiltonian [Eq. (4.24)] as a starting point. In other words, one can perform MC simulations for the Hessian Hamiltonian [Eq. (4.24)], which in principle allows for crossing. However, in the temperature regime considered here, such events are very rare. Thus, assuming that the particles stay ordered, the variance of $y_{\max} = x_N/L_N$ is given by

$$\sigma_{y_{\max}}^2 = \frac{[H^{-1}]_{NN}}{L_N^2}, \quad (4.26)$$

where H^{-1} is the inverse of the matrix H . We numerically perform this inversion and find that $\sigma_{y_{\max}}$ has the following N scaling:

$$\sigma_{y_{\max}} \sim N^{-\eta_k^{(\text{hess})}}. \quad (4.27)$$

We compare this exponent $\eta_k^{(\text{hess})}$ (obtained by inversion of the Hessian matrix) with the exponent obtained using MC simulations of both the original confined Riesz gas [Eq. (2.1)] denoted by η_k [Eq. (4.20)] and the Hessian Hamiltonian [Eq. (4.24)] denoted by $\eta_k^{(\text{hMC})}$

in Fig. 4.3. We observe an excellent agreement suggesting $\eta_k = \eta_k^{(\text{hess})} = \eta_k^{(\text{hMC})}$. The fact that $\eta_k^{(\text{hess})} = \eta_k^{(\text{hMC})}$ justifies the above assumption of almost non-crossing trajectories of particles at $O(1)$ temperature. While the Hessian theory along with the assumption of an order implies the Gaussian form for the scaling distribution $\mathcal{F}_\beta^{(k)}(z)$, the actual MC simulation gives a non-Gaussian form as shown in Fig. 4.4, even though the scale $\sigma_{y_{\max}} \sim N^{-\eta_k^{(\text{hess})}}$ of the data collapse is provided by the Hessian theory. Our findings therefore indicate that the Hessian theory (albeit an approximation) encodes some non-trivial features of the underlying confined Riesz gas.

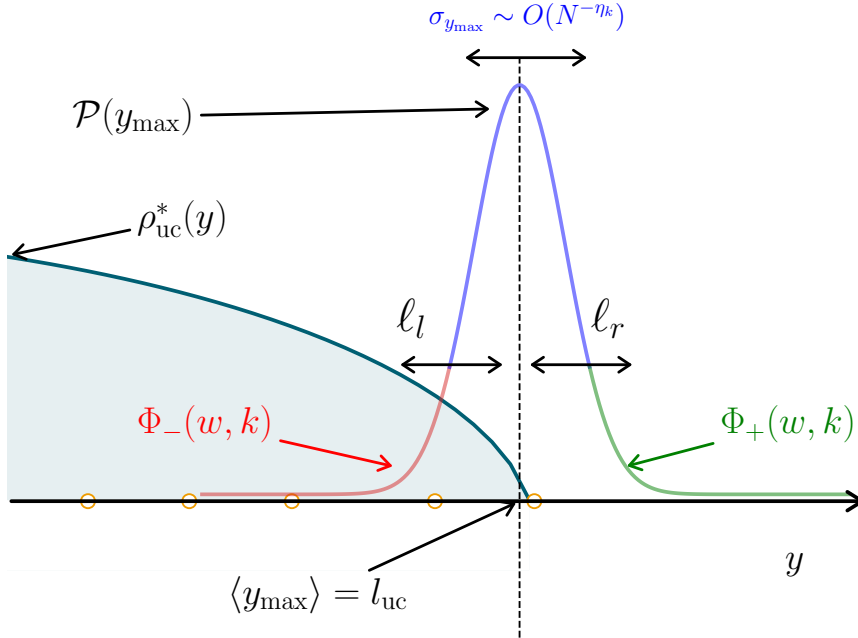


Figure 4.6: The schematic plot shows the distribution of y_{\max} which is centred around $y_{\max} = l_{\text{uc}}$. The typical part of the distribution is represented in solid blue color and is the region where $|w - l_{\text{uc}}| \lesssim O(N^{-\eta_k})$. These fluctuations are quantified by $\sigma_{y_{\max}} \sim O(N^{-\eta_k})$, the standard deviation of y_{\max} . The atypical part of the distribution is described by the left and the right LDF $\Phi_-(w, k)$ and $\Phi_+(w, k)$ represented by red and green solid lines, respectively. We identify the length scales l_l and l_r where the typical distribution starts having an exponential form described by the LDFs while still being of $O(N^0)$.

Analytical estimate of η_k for $-2 < k < 0$: To find an analytical estimate of η_k , we look at the relevant length scales present in the system. Two length scales l_l and l_r can be identified by estimating the distance (measured from $w = l_{\text{uc}}$ on the left and right, respectively) at which the PDF starts having the exponential form while still being of $O(N^0)$. In Fig. 4.6, we show a schematic of the two length scales. At these length

scales the large deviation behavior characterized by LDF $\Phi_-(w, k)$ and $\Phi_+(w, k)$ start becoming valid. To identify ℓ_l we rewrite the probability in the left large deviation part in Eq. (4.14) as

$$\mathcal{P}_k [y_{\max} = w] \approx \exp \left[-\beta \left(\frac{l_{\text{uc}} - w}{\ell_l} \right)^{e_k^-} \right], \text{ for } w \rightarrow l_k^{\text{uc}-} \text{ where } \ell_l \sim N^{-\frac{2\alpha_k+1}{e_k^-}}. \quad (4.28)$$

In Eq. (4.28), we have used the asymptotic form of $\Phi_-(w, k)$ from Eq. (4.16). Note that when we approach l_{uc} from $w \ll l_{\text{uc}}$, ℓ_l is the length scale at which the PDF in the left large deviation regime becomes $O(1)$ i.e $\mathcal{P}_k [w = l_{\text{uc}} - \ell_l, N] \sim e^{-\beta N L_N^2 \Phi_-(w, k)} \sim O(1)$, where $L_N = N^{\alpha_k}$ for $k \neq 1$ and α_k is given in Eq. (2.6). Using a similar argument one can estimate

$$\ell_r \sim N^{-\frac{2\alpha_k}{e_k^+}}. \quad (4.29)$$

For $-2 < k < -1$ and $k > 0$ we find that $\ell_r < \ell_l$ while for $-1 < k < 0$ we find that $\ell_l < \ell_r$. Notice that at the smallest length scale, the PDF described by the left and right LDF is $O(N^0)$. If this length scale is required to describe the typical fluctuation of y_{\max} , the LDF form of the PDF should smoothly match the tails of the distribution in the typical regime. Assuming that such smooth matching occurs at this scale, we arrive at the conjecture of the exponent

$$\eta_k^{(c)} = \begin{cases} \frac{2\alpha_k}{e_k^+} = \frac{4}{(k+2)(3-k)} & \text{for } -2 < k < -1 \\ \frac{2\alpha_k+1}{e_k^-} = \frac{4+k}{3(k+2)} & \text{for } -1 < k < 0. \end{cases} \quad (4.30)$$

where we have used the values of e_k^+ and e_k^- which are calculated in Section. 4.3 and summarized in Table 4.1. This conjecture in Eq. (4.30) (solid line) agrees remarkably well with our numerical data as shown in Fig. 4.3. This excellent agreement (for $k < 0$) verifies the presence of a single scale that smoothly connects the large deviation and the typical fluctuation regimes. The existence of a single scale is consistent with the fact that the field theory for $k < 0$ is exact (in the sense that there are no subleading corrections in N) and there is just a single term of $O(N^2)$ (the double sum in Eq. (2.1) can be replaced by a double integral without invoking the notion of principal value).

For $k > 0$, the argument based on the existence of a single scale connecting the

large deviation and the typical regimes gives $\eta_k^{(c)} = 4/(k+2)(3-k)$ for $0 < k < 1$ and $\eta_k^{(c)} = 2k/(k+2)$ for $k > 1$. We find that these values of the exponent for $k > 0$ fail to describe the typical fluctuations. This is probably because the field theory for $k > 0$ has the subleading corrections (higher order derivatives in density) in N , including the correction due to entropy. This could lead to multiple intermediate scales.

4.3.2 Distribution in the atypical region

The formal expression for the distribution of y_{\max} is given in Eq. (4.18), where the partition function $Z_k(W)$ is a N -fold multiple integral in terms of the microscopic variables x_i s. One can compute this integral using the coarse-graining approach—by converting it to a problem of functional integration over the density profiles as described in the previous chapter 3, see Eq. (3.14). We find that the partition function is given by [see Eq. (3.18)]

$$Z_k(wL_N) = C_N \int d\mu \int \mathcal{D}[\rho] \exp[-\beta \mathcal{B}_N \Sigma_k[\rho(y), \mu] + o(\mathcal{B}_N)], \quad (4.31)$$

where C_N is given in Eq. (3.20) and the action $\Sigma_k[\rho(y), \mu]$ is given by

$$\Sigma_k[\rho(y), \mu] = \left(\mathcal{E}_k[\rho(y)] - \mu \left(\int_{-\infty}^w dy \rho(y) - 1 \right) \right), \quad (4.32)$$

with $\mathcal{E}_k[\rho(y)]$ given in Eq. (3.17). Note that, we have considered $T \sim O(1)$, but at high temperatures $T \sim O(N^{2\alpha_k})$, the energy and entropy terms become comparable and the free energy controls the value of the partition function in Eq. (4.31). The integral in Eq. (4.31) can be performed using the saddle point method in which one requires to minimize the action $\Sigma_k[\rho(y), \mu]$ in Eq. (4.32) to find the saddle point density $\rho_k^*(y, w)$ and the chemical potential $\mu_k^*(w)$. The saddle point equations then read

$$\left. \frac{\delta \Sigma_k[\rho(y), \mu]}{\delta \rho(y)} \right|_{\substack{\rho(y)=\rho_k^*(y,w) \\ \mu=\mu_k^*(w)}} = 0, \quad (4.33)$$

$$\left. \frac{\partial \Sigma_k[\rho(y), \mu]}{\partial \mu} \right|_{\substack{\rho(y)=\rho_k^*(y,w) \\ \mu=\mu_k^*(w)}} = 0. \quad (4.34)$$

Note that the second equation above is precisely the normalization condition

$$\int_{-\infty}^w dy \rho_k^*(y, w) = 1.$$

Solving the above two equations (4.33) and (4.34) satisfying the normalization condition, one finds $\rho_k^*(y, w)$. In the limit $N \rightarrow \infty$, the saddle point density $\rho_k^*(y, w)$ is the average density of the particles of the Riesz gas in the presence of a hard wall at $W = wL_N$. In the previous chapter 3, explicit expressions for the saddle point density $\rho_k^*(y, w)$ (hereafter called constrained densities) have been obtained for all values of $k > -2$ [60].

Substituting this saddle point density in Eqs. (4.31) and (4.32), one finds the partition function $Z_k(W)$ in Eq. (4.19) as $Z_k(W) \approx \exp[-\beta\mathcal{B}_N \mathcal{E}_k[\rho_k^*(y, w)]]$ where the (scaled) energy functional is given in Eq. (3.17). Hence, using Eq. (4.18), the CDF of the position of the rightmost particle is given by

$$\text{Prob.}[x_{\max} < wL_N, N] \approx \exp[-\beta\mathcal{B}_N (\mathcal{E}_k[\rho_k^*(y, w)] - \mathcal{E}_k[\rho_k^*(y, w \rightarrow \infty)])], \quad (4.35)$$

where $w = W/L_N$ represents the scaled position of the wall. Notice that in the limit $w \rightarrow \infty$, the saddle point density $\rho_k^*(y, w)$ corresponds to the density of the unconstrained gas i.e. in the absence of any wall. As mentioned earlier, this unconstrained density $\rho_{\text{uc}}^*(y) = \rho_k^*(y, w \rightarrow \infty)$ was computed in Ref. [45] where it was shown to be given by Eq. (2.18).

Note that if the wall is placed outside the support of the unconstrained density (i.e. $w > l_{\text{uc}}$) the density profile remains unchanged because $\rho_{\text{uc}}^*(y)$ has finite support $[-l_{\text{uc}}, l_{\text{uc}}]$. In other words, $\rho_k^*(y, w) = \rho_{\text{uc}}^*(y)$ for $w \geq l_{\text{uc}}$ since the effect of the hard wall is noticeable only when $w < l_{\text{uc}}$. Consequently, the right-hand side of Eq. (4.35) can not describe the probability distribution of y_{\max} for $y_{\max} > l_{\text{uc}}$. In this case, one needs to employ a different method to find the CDF of y_{\max} . This is expected since, intuitively, one would anticipate different energy costs for creating a fluctuation with $y_{\max} < l_{\text{uc}}$ and $y_{\max} > l_{\text{uc}}$.

To compute the PDF for $y_{\max} > l_{\text{uc}}$, we follow the procedure described in Ref. [113]. In Ref. [113] it was argued for Dyson's log-gas that for large N the dominant contribution to the PDF for $y_{\max} > l_{\text{uc}}$ would come from the energy cost required to pull the rightmost particle to the right of the right edge of the unconstrained density. Assuming the same mechanism to hold for all values of $k > -2$ (which will be verified numerically later), we

write

$$\text{Prob.}[x_{\max} = W, N] = \frac{1}{Z_k} \int_{-\infty}^W dx_{N-1} \dots \int_{-\infty}^{x_2} dx_1 \exp(-\beta \tilde{E}_k(x_1, x_2, \dots, x_{N-1})) \quad (4.36)$$

$$\begin{aligned} & \times \exp \left[-\beta \left(\frac{W^2}{2} + \text{sgn}(k) \sum_{i=1}^{N-1} |W - x_i|^{-k} \right) \right] \\ & = \left\langle \exp \left[-\beta \left(\frac{W^2}{2} + \text{sgn}(k) N \int dx \frac{\rho_{N-1}(x)}{|W-x|^k} \right) \right] \right\rangle_{N-1}, \end{aligned} \quad (4.37)$$

where $\tilde{E}_k(x_1, x_2, \dots, x_{N-1})$ is given in Eq. (2.1) with $N - 1$ particles and it represents the energy of the gas in the absence of the rightmost particle and the angular brackets $\langle \cdot \rangle_{N-1}$ denotes the average with respect to $N - 1$ particle distribution. This average can be computed as follows

$$\begin{aligned} \text{Prob.}[x_{\max} = W, N] &= \int \mathcal{D}[\rho_{N-1}(x)] P[\rho_{N-1}(x)] \times \\ & \exp \left[-\beta \left(\frac{W^2}{2} + \text{sgn}(k) N \int dx \frac{\rho_{N-1}(x)}{|W-x|^k} \right) \right], \end{aligned} \quad (4.38)$$

where the probability distribution functional of the density profile $\rho_{N-1}(x)$ for $N - 1$ particles is

$$P[\rho_{N-1}(x)] \approx \frac{\exp \left(-\beta \tilde{\mathcal{E}}[\rho_{N-1}(x)] \right)}{Z_k}. \quad (4.39)$$

In the large- N limit, Eq. (4.38) can be expressed in terms of the scaled variables as

$$\begin{aligned} \text{Prob.}[x_{\max} = W, N] &= \int \mathcal{D}[\rho(y)] \frac{\exp(-\beta N L_N^2 \mathcal{E}[\rho(y)])}{Z_k} \times \\ & \exp \left[-\beta \left(\frac{L_N^2 w^2}{2} + \text{sgn}(k) N L_N^{-k} \int dy \frac{\rho(y)}{|w-y|^k} \right) \right]. \end{aligned} \quad (4.40)$$

The integral in Eq. (4.40) is computed using the saddle point method. Extremizing the exponent in Eq. (4.40) gives the saddle point density as $\rho^*(y) = \rho_{\text{uc}}^*(y)$. Note that this is the unconstrained density given in Eq. (2.18) and is obtained as the contribution of exponent in the square bracket of Eq. (4.40) is subleading $\sim O(L_N^2)$ compared to the

energy which is $\sim O(NL_N^2)$. Using this saddle point density in Eq. (4.40), we get

$$\text{Prob.}[x_{\max} = wL_N, N] \approx \exp \left[-\beta L_N^2 \left(\frac{w^2 - l_{\text{uc}}^2}{2} + \frac{\text{sgn}(k)N}{L_N^{k+2}} \int_{-l_{\text{uc}}}^{l_{\text{uc}}} dy \rho_{\text{uc}}^*(y) \left(\frac{1}{|w-y|^k} - \frac{1}{|l_{\text{uc}}-y|^k} \right) \right) \right]. \quad (4.41)$$

The expressions in Eqs. (4.35) and (4.41) suggest the following large deviation form of the CDF of $y_{\max} = x_{\max}/L_N$

$$\text{Prob.}[y_{\max} < w] \approx \begin{cases} \exp(-\beta \mathcal{B}_N \Phi_-(w, k)), & \text{for } l_{\text{uc}} - w \geq O(1) \\ 1 - \exp(-\beta L_N^2 \Phi_+(w, k)), & \text{for } w - l_{\text{uc}} \geq O(1), \end{cases} \quad (4.42)$$

in the large N limit, where \mathcal{B}_N and L_N are given in Eqs. (3.16) and (2.6), respectively.

The LDF is given by

$$\begin{aligned} \Phi_-(w, k) &= \mathcal{E}_k[\rho_k^*(y, w)] - \mathcal{E}_k[\rho_{\text{uc}}^*(y)], \\ \Phi_+(w, k) &= \left(\frac{w^2 - l_{\text{uc}}^2}{2} \right) + \text{sgn}(k) \Theta(1-k) \int_{-l_{\text{uc}}}^{l_{\text{uc}}} dy \rho_{\text{uc}}^*(y) \left(\frac{1}{|w-y|^k} - \frac{1}{|l_{\text{uc}}-y|^k} \right). \end{aligned} \quad (4.43)$$

Here the scaled energy functional is given in Eq. (3.17). The form of the saddle point densities $\rho_k^*(y, w)$ and $\rho_{\text{uc}}^*(y)$, in the presence and the absence of the wall, respectively, depends explicitly on k . Therefore the form of the LDF as well as the exponents e_k^\mp characterizing their asymptotic behaviors near the wall, would also depend on k . In the following, we compute the explicit form of the LDF and the exponents in the following regimes (1) $k \geq 1$, (2) $-1 < k < 1$ and (3) $-2 < k < -1$, separately.

Regime 1 ($k \geq 1$): Short-ranged interactions -

In this regime the interaction energy falls relatively fast with increasing separation, i.e. it effectively acts as short-ranged. Consequently, the energy functional, given in Eq. (3.17), is local in the leading order for large N . Using this functional in the saddle point equation in Eq. (4.33), one finds that the density is given by [60] [see Fig. 4.7a and Eq. (3.24)]

$$\rho_k^*(y, w) = A_k (l_k(w)^2 - y^2)^{\frac{1}{k}}, \quad -l_k(w) \leq y \leq w. \quad (4.44)$$

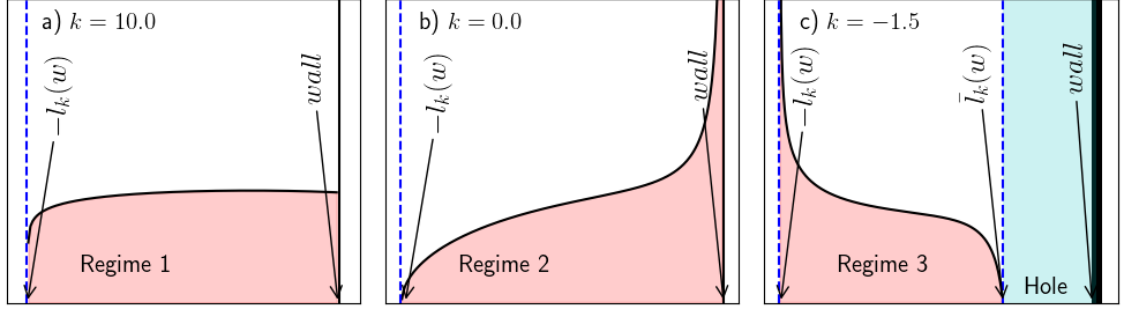


Figure 4.7: A plot of the scaled average density in the presence of wall $\rho_k^*(y, w)$ versus y for the three regimes (a) $k \geq 1$, (b) $-1 < k < 1$ and (c) $-2 < k \leq -1$. The blue dashed vertical line indicates the left edge $[-l_k(w)]$ of the support and the black solid line represents the wall position w . In regime 1 the density is constant at the wall while it diverges in regime 2. In both of these regimes, the density vanishes at the left edge. In regime 3 the density has two disjoint regions, an extended bulk part $[-l_k(w) < y < \bar{l}_k(w)]$ and a delta function at the wall position (shown by a thick solid vertical line). They are separated by a hole region $[\bar{l}_k(w) < y < w]$ devoid of particles (shaded cyan region).

Substituting this form of the density profile in the normalization condition gives us an equation for $l_k(w)$ expressed in terms of an auxiliary variable

$$m_k(w) = \frac{w + l_k(w)}{2l_k(w)}, \text{ for } k \geq 1 \text{ and } w \leq l_{\text{uc}}, \quad (4.45)$$

as

$$(2m_k(w) - 1) \left(\frac{B(\gamma_k + 1, \gamma_k + 1)}{B(m_k(w); \gamma_k + 1, \gamma_k + 1)} \right)^{\alpha_k} = \frac{w}{l_{\text{uc}}}. \quad (4.46)$$

We recall that in this regime $\gamma_k = 1/k$ and $\alpha_k = k/(k + 2)$. The variable $m_k(w)$ lies in the range $[0, 1]$. Solving Eq. (4.46) gives $m_k(w)$, which in turn fixes the left edge of the support $l_k(w)$ through Eq. (4.45). Note that in this regime the density at the wall is finite.

Finally by substituting the density profile $\rho_k^*(y, w)$ in Eq. (3.17) we get the scaled energy functional $\mathcal{E}_k[\rho_k^*]$, which together with Eq. (4.43) allows to compute the LDF

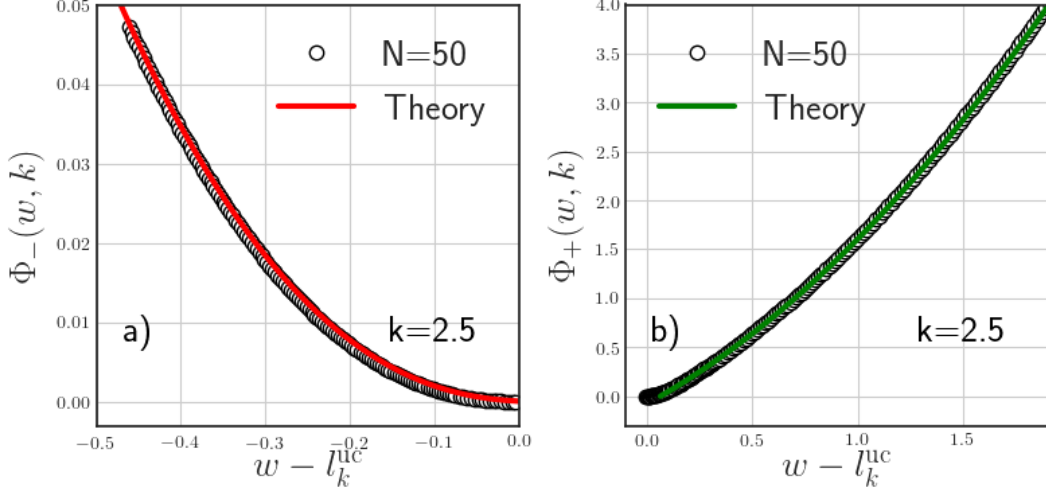


Figure 4.8: *Regime 1* ($k \geq 1$): The numerical verification of the LDF $\Phi_{\pm}(w, k)$ given in Eq. (4.47) and Eq. (4.48), respectively in panels (a) and (b). The rare events such that $|y_{\max} - l_{\text{uc}}| \sim O(1)$ are generated using the importance sampling method [141, 142] and the associated probabilities are computed from which the large deviation functions are calculated numerically. The parameters used in the simulations are $J = 1$ and $\beta = 1$.

$\Phi_{\pm}(w, k)$. We find the following explicit expressions (see A.3.1 for details)

$$\Phi_-(w, k) = \frac{l_k(w)^2}{2(k+1)} \left[1 + \frac{4k}{B(m_k(w), \gamma_k + 1, \gamma_k + 1)} \left(B(m_k(w), \gamma_k + 3, \gamma_k + 1) - B(m_k(w), \gamma_k + 2, \gamma_k + 1) + \frac{B(m_k(w), \gamma_k + 1, \gamma_k + 1)}{4} \right) \right] - \frac{(l_{\text{uc}})^2(k+2)}{2(3k+2)}, \quad (4.47)$$

$$\Phi_+(w, k) = \frac{w^2 - (l_{\text{uc}})^2}{2}. \quad (4.48)$$

Here $B(x, a, b) = \int_0^x s^{a-1}(1-s)^{b-1}$ is the incomplete Beta function.

Using an importance sampling method described in the A.4, we compute the probability distribution $P_{\text{num}}(y_{\max})$ which includes the atypical part also. To extract the left large deviation function we plot $-\log(P_{\text{num}}(y_{\max}))/\mathcal{B}_N$ as a function of $y_{\max} - \langle y_{\max} \rangle$. Similarly the right large deviation function is extracted by plotting $-\log(P_{\text{num}}(y_{\max}))/L_N^2$ as a function of $y_{\max} - \langle y_{\max} \rangle$. In Fig. 4.8, we compare the LDF obtained numerically with our analytical expression given in Eqs. (4.47) and (4.48) and observe remarkable agreement up to an overall translation on the x axis. This translation is an artifact of

finite size effect, due to which $\langle y_{\max} \rangle$ is slightly different from its theoretical value l_{uc} in the thermodynamic limit.

We study the asymptotic behavior of $\Phi_-(w, k)$ as $w \rightarrow l_k^{\text{uc}-}$. From Eq. (4.46) we obtain the asymptotic behaviour of $m_k(w)$ as $w \rightarrow l_k^{\text{uc}-}$ as

$$m_k(w) \approx 1 - \frac{l_{\text{uc}} - w}{2l_{\text{uc}}} + o(l_{\text{uc}} - w). \quad (4.49)$$

Performing the series expansion about $m_k(w) = 1$ and using the approximation of $m_k(w)$ [Eq. (4.49)] we get from Eq. (4.47)

$$\Phi_-(w, k) \approx \frac{k^2(2l_{\text{uc}})^{-\frac{1}{k}} B(1 + \gamma_k, 1 + \gamma_k)}{2(2k + 1)(k + 1)} (l_{\text{uc}} - w)^{e_k^-} \quad \text{with } e_k^- = 2 + \frac{1}{k}. \quad (4.50)$$

Hence the system undergoes a 3rd order phase transition based on Ehrenfest classification. The asymptotic behavior of $\Phi_+(w, k)$ can be obtained by taking the limit $w \rightarrow l_k^{\text{uc}+}$ in Eq. (4.48) and is given by

$$\Phi_+(w, k) \approx l_{\text{uc}} (w - l_{\text{uc}})^{e_k^+} \quad \text{with } e_k^+ = 1. \quad (4.51)$$

Regime 2 ($-1 < k < 1$): Weakly long-ranged interactions -

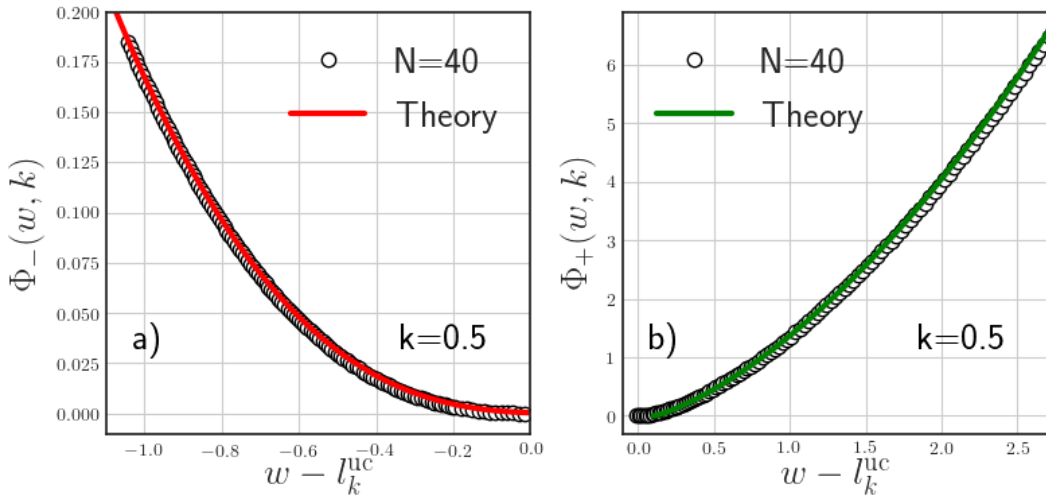


Figure 4.9: *Regime 2* ($-1 < k < 1$): The numerical verification of the LDF $\Phi_{\pm}(w, k)$ given in Eq. (4.55) and Eq. (4.56), respectively in panels (a) and (b). The probabilities of rare events such that $|y_{\max} - l_{\text{uc}}| \sim O(1)$ are computed numerically from which the large deviation functions are extracted. The parameters used in the simulations are $J = 1$ and $\beta = 1$.

In this regime of k , the interaction forces decay slower with increasing inter-particle separation compared to the previous short-ranged regime. The energy functional in this regime is given in Eq. (3.17) and is non-local in leading order for large N . Using this energy functional in Eq. (4.33), we obtain the saddle point equation given in Eq. (3.28). This Eq. (3.28) has been solved in the last chapter [see Eq. (3.38) and Ref. [60]] using the Sonin inversion formula [100] and is given by [see Fig. 4.7b]

$$\rho_k^*(y, w) = A_k(l_k(w) + y)^{\frac{k+1}{2}}(w - y)^{\frac{k-1}{2}} \left(\tilde{l}_k(w) - y \right), \quad \text{for } -l_k(w) \leq y \leq w, \quad (4.52)$$

where $\tilde{l}_k(w) = \frac{1}{2}((k+1)l_k(w) + (1-k)w)$. Here, it is worth noting that the density at the wall has an integrable divergence while it vanishes on the left edge $-l_k(w)$ of the support. The quantity $l_k(w)$ is determined from the normalization condition $\int_{-l_k(w)}^w \rho_k^*(y, w) dy = 1$ which leads to [60]

$$\left(\frac{k+3-2g_k(w)}{k+1} \right) \left(\frac{2g_k(w)(2+k) - (k+3)}{k+1} \right)^{-\alpha_k} = \frac{w}{l_{\text{uc}}}, \quad (4.53)$$

where the auxiliary variable is

$$g_k(w) = \frac{l_k(w) + \tilde{l}_k(w)}{w + l_k(w)}, \quad \text{for } -1 < k < 1 \text{ and } w < l_{\text{uc}}. \quad (4.54)$$

We recall that $\alpha_k = 1/(k+2)$ [see Eq. (2.6)]. This equation is the analog of Eq. (4.46) in the regime 1. This equation gives $g_k(w)$ for a fixed w , which is used to find the left edge of the support $l_k(w)$ using Eq. (4.54). We use this saddle point density to find the large deviation function given in Eq. (4.43). To do so we first need to calculate the scaled energy functional $\mathcal{E}_k[\rho_k^*]$ given in Eq. (3.17). We relegate some details of this computation in the A.3.2. Here we present only the final expressions namely

$$\begin{aligned} \Phi_-(w, k) = & (k+2)(l_{\text{uc}})^2 \left[\left(1 + \frac{2(k+2)}{k+1}(g_k(w) - 1) \right)^{-\frac{k+4}{k+2}} \left[\frac{1}{2k(k+4)} \right. \right. \\ & \left. \left. + \frac{(g_k(w) - 1)}{k(k+1)} + \frac{2(g_k(w) - 1)^2}{k(k+1)^2} + \frac{4(g_k(w) - 1)^3}{(1+k)^3} \right] - \frac{1}{2k(k+4)} \right], \end{aligned} \quad (4.55)$$

$$\Phi_+(w, k) = (l_{\text{uc}})^2 \frac{32(g_{\text{uc}}(w)^{-1} - 1)^{\frac{3-k}{2}} B(2+k, \frac{5-k}{2})}{(k+3)(k+5)(k+7)} \times {}_2F_1\left[-\frac{k+1}{2}, \frac{k+3}{2}, \frac{5-k}{2}, 1 - g_{\text{uc}}(w)^{-1}\right], \quad (4.56)$$

where $g_{\text{uc}}(w) = 2l_{\text{uc}}/(w + l_{\text{uc}})$ and

$${}_2F_1[a, b, c, u] = B(b, c-b)^{-1} \int_0^1 ds \frac{s^{b-1}(1-s)^{c-1-b}}{(1-us)^a} \quad (4.57)$$

$$= \sum_{n=0}^{\infty} \frac{(a)_n (b)_n}{(c)_n} \frac{z^n}{n!} \quad (4.58)$$

is the hypergeometric function with $(a)_n = a(a+1)(a+2)\dots(a+n)$ being the Pochhammer symbol. Note that $g_{\text{uc}}(w)$ is the ratio of the size of the unconstrained gas to that of the constrained gas. These expressions of LDF are in excellent agreement with our numerical results obtained using the importance sampling method [see A.4] as can be seen in Fig. 4.9. As mentioned earlier the LDF describes the pulled-to-pushed type phase transition and its nature is determined by the asymptotic behavior of LDF near the right edge of the support of the unconstrained density.

To characterize this asymptotic behavior of LDF for $w \rightarrow l_k^{\text{uc}-}$ we need to expand $g_k(w)$ around $w = l_{\text{uc}}$. From the Eq. (3.39) we observe that

$$g_k(w) \approx 1 + \frac{k+1}{4l_{\text{uc}}}(l_{\text{uc}} - w) + o(l_{\text{uc}} - w), \quad (4.59)$$

$$g_{\text{uc}}(w) = 1 + \frac{w - l_{\text{uc}}}{2l_{\text{uc}}}.$$

We expand $\Phi_-(w, k)$ and $\Phi_+(w, k)$ in powers of $g_k(w) - 1$ and $g_{\text{uc}}(w)^{-1} - 1$, respectively and then use these expansions Eq. (4.59) which give

$$\Phi_-(w, k) \approx \frac{(k+2)}{12l_{\text{uc}}} (l_{\text{uc}} - w)^{e_k^-} \quad \text{with } e_k^- = 3, \quad (4.60)$$

$$\Phi_+(w, k) \approx \frac{2(1-k)B(k+2, \frac{5-k}{2}) (l_{\text{uc}})^{-e_k^+}}{3A_k(k+5)(k+7) |k| B(\frac{k+3}{2}, 1-k)} (w - l_{\text{uc}})^{e_k^+} \quad \text{with } e_k^+ = \frac{3-k}{2}. \quad (4.61)$$

The exponent $e_k^- = 3$ suggests that the system undergoes a 3rd order phase transition.

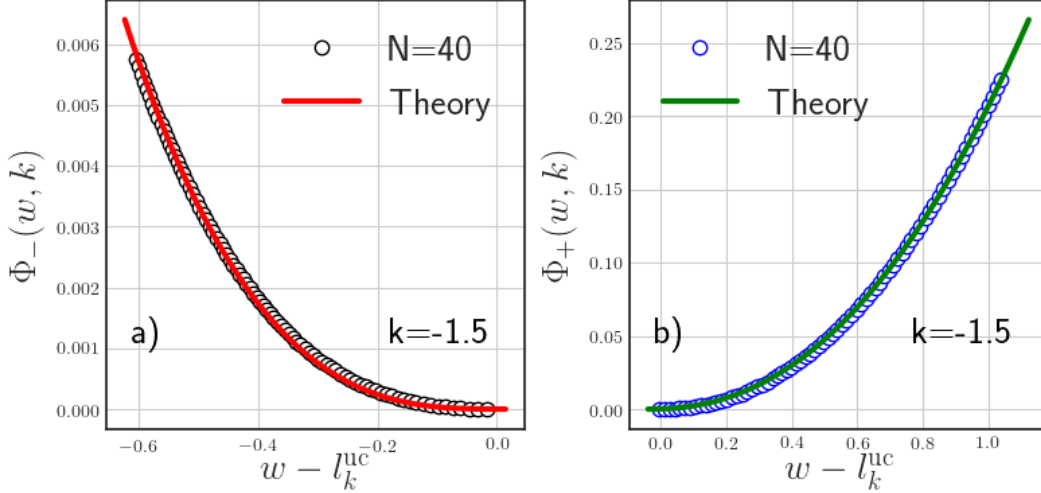


Figure 4.10: *Regime 3* ($-2 < k < -1$): The numerical verification of the LDF $\Phi_{\pm}(w, k)$ given in Eq. (4.69) and Eq. (4.71), respectively in panels (a) and (b). The probabilities of rare events such that $|y_{\max} - l_{\text{uc}}| \sim O(1)$ are computed from which the large deviation functions are calculated numerically. In the simulation, we use the parameters $J = 1$ and $\beta = 10^{-3}$. It is easy to show that our field theory calculation remains valid at this temperature since it satisfies the condition $\beta L_N^2 > 1$.

Regime 3 ($-2 < k \leq -1$): Strongly long-ranged interactions -

This regime is a bit more complicated since the constrained density has disjoint parts namely a delta function at the wall and an extended part separated by a region devoid of particles [60]. The divergence of the density at the wall seen in the previous regime (see Section. 4.3.2) becomes a delta function. This is rooted in the fact that the particles are allowed to sit in the same position. It turns out that due to the intricate interplay between the repulsive interaction and the confining harmonic potential the fraction of the particles tries to sit together at the wall. The rest of the particles then get pushed away from the wall by “supercharge” resulting from the delta function. This creates a hole between the delta function and the extended region [60]. This density profile is obtained by solving the saddle point equations (4.33), which in this regime takes the form

$$\mu_k^*(w) = \frac{y^2}{2} + \text{sgn}(k) \int_{-\infty}^w dy' \frac{\rho_k^*(y', w)}{|y' - y|^k}. \quad (4.62)$$

This equation is solved in detail in the previous chapter 3 [see Eq. (3.8) and Ref. [60]] leading to the result [see Fig. 4.7c]

$$\rho_k^*(y, w) = \begin{cases} \underbrace{A_k \frac{(l_k(w) + y)^{\frac{k+1}{2}} (\bar{l}_k(w) - y)^{\frac{k+3}{2}}}{(w - y)} \mathbb{I}[-l_k(w) < y \leq \bar{l}_k(w)]}_{\text{extended}} + \underbrace{D_k^*(w) \delta(w - y)}_{\text{“super charge”}}, & \text{for } w > w_c(k) \\ \delta(w - y), & \text{for } w < w_c(k), \end{cases} \quad (4.63)$$

where $\mathbb{I}[a < z \leq b]$ represents the indicator function of the interval $[a, b]$. The amplitude A_k is given in Eq. (2.20) and

$$w_c(k) = \frac{(k+2) |k(k+1)|^{\frac{1}{k+2}}}{k+1}. \quad (4.64)$$

The other constants in Eq. (4.63) are expressed in terms of the position $-l_k(w)$ of the left edge of the extended part of the density and are given by

$$\bar{l}_k(w) = \frac{2w + (k+1)l_k(w)}{k+3}, \quad (4.65)$$

$$D_k^*(w) = \frac{(l_k(w) - w)(w + l_k(w))^{\frac{k+1}{2}}}{|k|(k+3)} \left(\frac{(k+1)(w - l_k(w))}{k+3} \right)^{\frac{k+1}{2}}. \quad (4.66)$$

The constant $D_k^*(w)$ represents the strength of the “supercharge” in the saddle point density expression in Eq. (4.63). Note from Eq. (4.63) that $\bar{l}_k(w)$ is the position of the right edge of the extended part of the density. Since $\bar{l}_k(w) < w$, as can be seen from Eq. (4.65), there is a region $\bar{l}_k(w) < y < w$ devoid of particles. A schematic representation of the density is given in Fig. 4.7c. The value of $l_k(w)$ is determined from the normalization condition which can be expressed in terms of the auxiliary function

$$h_k(w) = \frac{w + l_k(w)}{\bar{l}_k(w) + l_k(w)}, \quad \text{for } -2 < k < -1, \quad (4.67)$$

as

$$\left(1 + (h_k(w) - 1) \frac{2(k+2)}{(k+1)} \right) {}_2F_1\left[1, -(k+2), -\frac{k+1}{2}, 1 - h_k(w)\right]^{-\frac{1}{k+2}} = \frac{w}{l_{\text{uc}}}. \quad (4.68)$$

The details of the computation leading to Eqs. (4.67) and (4.68) are given in A.3.3.

The scaled energy functional $\mathfrak{E}_k[\rho_k^*]$ is obtained by substituting the density profile $\rho_k^*(y, w)$ in Eq. (3.17). Using this energy functional in Eq. (4.43), we compute the LDF $\Phi_{\pm}(w, k)$ which is given by (see A.3.3 for details)

$$\begin{aligned} \Phi_-(w, k) = & (l_{\text{uc}})^2 {}_2F_1\left[1, -(k+2), -\frac{k+1}{2}, 1 - h_k(w)\right]^{-\frac{2}{k+2}} \left[\frac{1}{4k} - \frac{(h_k(w) - 1)}{k(k+1)} \right. \\ & - (k+2) \frac{(h_k(w) - 1)^2}{k(k+1)^2} + n_k(w)^2 \\ & - n_k(w) \frac{{}_2F_1\left[1, -(k+3), -\frac{k+1}{2}, 1 - h_k(w)\right]}{{}_2F_1\left[1, -(k+2), -\frac{k+1}{2}, 1 - h_k(w)\right]} \\ & \left. + \frac{k+5}{4(k+4)} \frac{{}_2F_1\left[1, -(k+4), -\frac{k+1}{2}, 1 - h_k(w)\right]}{{}_2F_1\left[1, -(k+2), -\frac{k+1}{2}, 1 - h_k(w)\right]} \right] - (l_{\text{uc}})^2 \frac{k+2}{2k(k+4)}, \end{aligned} \quad (4.69)$$

where,

$$n_k(w) = \frac{l_k(w)}{\tilde{L}_k(w)} = \frac{1}{2} + \frac{1 - h_k(w)}{k+1}. \quad (4.70)$$

The calculation for the right LDF is the same as in Section. 4.3.2, hence the expression is the same as Eq. (4.56) i.e.

$$\begin{aligned} \Phi_+(w, k) = & (l_{\text{uc}})^2 \frac{32(h_k^{\text{uc}}(w)^{-1} - 1)^{\frac{3-k}{2}} B\left(2+k, \frac{5-k}{2}\right)}{(k+3)(k+5)(k+7)} \\ & \times {}_2F_1\left[-\frac{k+1}{2}, \frac{k+3}{2}, \frac{5-k}{2}, 1 - h_k^{\text{uc}}(w)^{-1}\right], \end{aligned} \quad (4.71)$$

where $h_k^{\text{uc}}(w) = g_{\text{uc}}(w) = 2l_{\text{uc}}/(w + l_{\text{uc}})$. Once again these LDFs are verified numerically using the importance sampling method in Fig. 4.10 which demonstrates an excellent agreement.

The asymptotic behavior of $\Phi_-(w, k)$ is obtained by performing the series expansion about $h_k(w) = 1$, namely

$$h_k(w) = 1 - \frac{k+1}{k+3} \frac{l_{\text{uc}} - w}{2l_{\text{uc}}} + o(l_{\text{uc}} - w). \quad (4.72)$$

Substituting this asymptotic behavior in Eq. (4.69) one finds

$$\Phi_-(w, k) \approx \frac{2(k+2)(k+5)}{3(3+k)^2(k-1)(k-3)l_{\text{uc}}} (l_{\text{uc}} - w)^{e_k^-} \quad \text{with } e_k^- = 3. \quad (4.73)$$

Hence in this regime also the system undergoes a 3rd order pulled-to-pushed phase transition. Finally, the asymptotic behavior of the right LDF is given by Eq. (4.61) namely

$$\Phi_+(w, k) \approx \frac{2(1-k)B(k+2, \frac{5-k}{2}) (l_{\text{uc}})^{-e_k^+}}{3A_k(k+5)(k+7)|k|B(\frac{k+3}{2}, 1-k)} (w - l_{\text{uc}})^{e_k^+} \quad \text{with } e_k^+ = \frac{3-k}{2}. \quad (4.74)$$

4.4 Discussions and Conclusions

In this chapter, we investigated the fluctuations of the position of the rightmost (edge) particle $y_{\text{max}} = x_{\text{max}}/L_N$ of harmonically confined Riesz gas [Eq. (2.1)]. We studied both typical and the atypical fluctuations of y_{max} separately. From numerical analysis, we found that the typical fluctuations characterized by the variance scales as $N^{-2\eta_k}$ with N . Similar to the scaling of the support, the exponent η_k associated with the variance of y_{max} , also depends on k non-monotonically as shown in Fig. 4.3. We have provided a physical understanding of the k dependence of η_k based on Hessian theory and a scaling argument. For $-2 < k < 0$, the assumption that the full distribution of y_{max} has a single length scale led us to conjecture an explicit expression of η_k given in Eq. (4.30). This conjecture was tested against the MC simulations in Fig. 4.3 and we found remarkable agreement. For $k > 0$, we found that the exponent η_k matches extremely well with the one computed from the Hessian theory [see Fig. 4.3]. For all k , we found that the distribution of y_{max} when shifted by mean and scaled by the $\sigma_{y_{\text{max}}} \sim N^{-\eta_k}$, exhibits a remarkable data collapse leading to a scaling distribution which is non-Gaussian in general.

The atypical fluctuations to the left and right of the mean are described by the left and the right LDF. We computed the explicit expressions for these LDFs in different regimes of k . We found that their asymptotic behavior near the edge of the unconstrained density is k dependent and shown in Table. 4.1 and Fig. 4.5. This difference is a consequence of the different mechanisms by which the saddle point density of the gas gets modified in the presence of a wall. A manifestation of this difference in the asymptotic behavior of the LDF is demonstrated in terms of the analytic properties of appropriately defined free energies which exhibit the third-order pulled-to-pushed phase transition $\forall k > -2$.

Therefore our results reveal a striking universality of the third-order phase transition in a family of models that fall outside the paradigm of Coulomb systems and RMT. All our results hold for temperature $T < L_N^2$.

The extreme value statistics is an example of local observable as it studies the distribution of the rightmost particle. While it can be studied in experiments, global observables are more robust. In the next chapter, we discuss the Full Counting statistics (FCS) which is a global observable and study the fluctuations of the total number of particles in a certain domain.

This chapter describes the study from the following published work, Ref. [59]:

J. Kethepalli, M. Kulkarni, A. Kundu, S. N. Majumdar, D. Mukamel, G. Schehr, “Edge fluctuations and third-order phase transition in harmonically confined long-range systems”, [Journal of Statistical Mechanics: Theory and Experiment 2022 \(3\), 033203](#)

Chapter 5

Full counting statistics of 1d short-range Riesz gases in confinement

5.1 Introduction

The study of many-particle low-dimensional quantum and classical systems has been a subject of great theoretical and experimental interest. A very interesting observable that unravels the equilibrium and non-equilibrium properties of low-dimensional systems is the distribution of the number of particles in a given domain. This is often referred to as full counting statistics (FCS). FCS is a global quantity and hence it is experimentally more accessible [143, 144].

In the context of quantum systems, FCS has been studied in various physical setups, including non-equilibrium Luttinger liquids [145], quantum transport [146–148], shot noise [149–151], quantum dots [152, 153] as well as in quantum spin chains and fermionic chains [154, 155]. Furthermore, the entanglement entropy of a subsystem with its remaining part is studied extensively in the context of the free Fermi gas and is intricately connected to FCS [156–161]. This connection holds true, particularly in regimes where the particle number fluctuations exhibit Gaussian behavior. The study of FCS for interacting systems has also gained considerable interest [162–165] as FCS can now be measured in cold atom experiments [143, 144]. This connection emphasizes the wide-ranging applications of FCS, particularly in understanding the relationship between in-

interactions and correlations in the system.

In the context of classical systems, the FCS has also been widely investigated. For instance, in many ecological settings, it has been observed that the distribution of the number of species and the average number of species in a given domain exhibit universal features [166–168]. The statistics of the number of particles in specific domains for different point processes have also been investigated [169, 170]. Such point processes can be classified based on the system size dependence of the Fano factor $\mathbb{V}(\mathcal{D}) = \text{Var}(\mathcal{N}(\mathcal{D})) / \langle \mathcal{N}(\mathcal{D}) \rangle$ where $\mathcal{N}(\mathcal{D})$ is the number of particles in a given domain \mathcal{D} . This ratio of the variance and the mean measures the strength of the relative fluctuations of $\mathcal{N}(\mathcal{D})$. In the large N limit, typical systems such as Poissonian point processes are characterized by $\mathbb{V}(\mathcal{D}) \sim O(1)$. Interestingly there are some systems for which $\mathbb{V}(\mathcal{D}) \rightarrow 0$, in the large N limit, and they are generically called hyperuniform [171, 172].

While FCS is an interesting quantity both in classical and quantum systems the role of interactions is not well understood. This chapter investigates FCS in a one-dimensional system of classical Riesz gas [17, 52]. We consider a harmonically confined Riesz gas composed of N particles in thermal equilibrium described by the Boltzmann distribution $P(\{x_i\}) = \exp[-\beta \tilde{E}_k(\{x_i\})] / Z_k$ where β^{-1} is temperature and Z_k is the partition function. The energy function of the gas is given by [see Eq. (2.1)]

$$\tilde{E}_k(\{x_i\}) = \sum_i^N \frac{x_i^2}{2} + \frac{J \text{sgn}(k)}{2} \sum_{i=1}^N \sum_{j \neq i}^N |x_i - x_j|^{-k}, \quad (5.1)$$

where x_i is the position of i^{th} particle with $i = 1, 2, \dots, N$ and $\text{sgn}(k)$ is the sign function. The strength of the repulsive interaction is controlled by $J > 0$ and the exponent k of the power law determines the nature of interactions; in particular, for $k > 1$ the system is short-ranged and for $k < 1$ it is long-ranged. In this chapter, we study FCS of the Riesz gas defined in Eq. (2.1) and we restrict ourselves to the short-range interactions, *i.e.*, $k > 1$ where the associated field theory is local [45]. It is to be noted that for the Riesz gas, the exact results on FCS are only known for $k \rightarrow 0$ [40, 41, 173–176] and $k = -1$ [32, 42], both of which are long-range models.

Our aim in this chapter is to study the statistical properties of $\mathcal{N}(W, N)$ which represents the number of particles in domain $[-W, W]$. As will be discussed later, in the large- N limit, the problem of finding the distribution of $\mathcal{N}(W, N)$ at $O(1)$ temperature

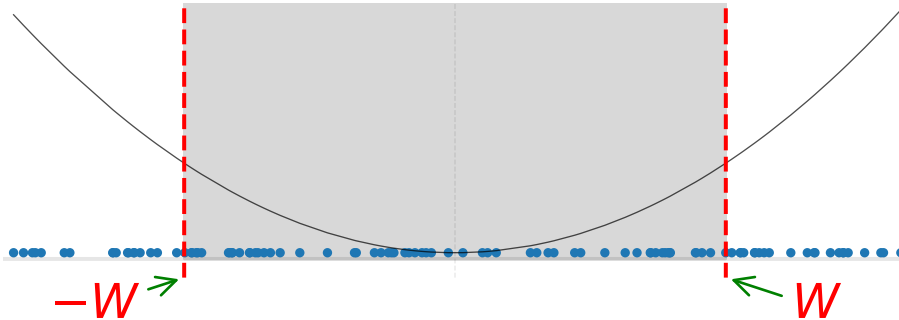


Figure 5.1: Schematic representation of the domain $[-W, W]$ (shaded region) studied in this chapter. The blue dots are the positions of the particles. The number of particles in the region $[-W, W]$ is defined as $\mathcal{N}(W, N)$. The black solid line is indicative of the harmonic confinement.

gets effectively converted to an optimization problem. This problem tries to find the most probable density profile satisfying the constraint of fixed $\mathcal{N}(W, N)$. Note that, under the transformation to the rescaled variables in Eq. (2.2), the wall position W gets transformed to $w = W/N^{\alpha_k}$. It is evident that if $w > l_{uc}$ then the density profile does not get affected by the presence of the hard walls and it remains the unconstrained density profile given in Eq. (2.18). On the other hand for $w < l_{uc}$ the most probable density profile will be drastically different from the one given in Eq. (2.18). This modified density profile, as we will see later, is an important ingredient for the study of FCS. We compute the constrained density profile and use it to study the probability distribution (more precisely the associated LDF) of $\mathcal{N}(W, N)$. Before going into the details of the computation, we summarize our main findings in the next section.

The rest of the chapter is organized as follows. In Section 5.2, we summarize our main results on the FCS of the Riesz gas. In Section 5.3, we explain the derivation of the large deviation function, which characterizes the probability distribution of the number of particles in the domain $[-W, W]$. The corresponding average density profiles are also calculated. These profiles are used to study the variance along with asymptotic behaviors, and non-analytic properties of the associated large deviation function (LDF). Our formalism has been adapted to study the index distribution which corresponds to the semi-infinite domain $(-\infty, W]$ in Section 5.4. In Section 5.5, we study the linear statistics of the Riesz gas. We conclude and provide some future directions in Section 5.6.

5.2 Summary of the main results

In this section, we present the main results related to the statistics of $\mathcal{n}(W, N)$, the number of particles in a finite box $[-W, W]$ which is schematically shown in Fig. 5.1. It is easy to show that the mean number of particles in the box increases linearly with the system size (i.e., number of particles N) and is given by

$$\langle \mathcal{n}(W, N) \rangle \simeq N c^* \left(\frac{W}{N^{\alpha_k}} \right) \quad (5.2)$$

$$\text{with } c^*(w) = \int_{-w}^w dy \rho_{\text{uc}}^*(y), \quad (5.3)$$

where the unconstrained density profile $\rho_{\text{uc}}^*(y)$ is given in Eq. (2.18). We denote the probability distribution of $\mathcal{n}(W, N)$ as

$$\mathcal{P}(\mathcal{n} = cN) = \text{Prob.}[\mathcal{n}(W, N) = cN, W]. \quad (5.4)$$

We find that in the large- N limit, the probability distribution takes the large deviation form given by

$$\mathcal{P}(\mathcal{n} = cN) \asymp \exp \left(-\beta N^{1+2\alpha_k} \Phi(c, W/N^{\alpha_k}) \right), \quad (5.5)$$

valid when $W \rightarrow \infty$, $N \rightarrow \infty$ keeping the ratio $w = W/N^{\alpha_k}$ fixed. Here we recall that $\alpha_k = k/(k+2)$ as given in Eq. (2.6). To calculate the LDF $\Phi(c, W/N^{\alpha_k})$, we use the Coulomb gas method [22, 23]. A crucial ingredient in this method is the saddle point density profiles that satisfy the constraint of having cN particles in the box $[-W, W]$. We find that these constrained density profiles are also dome-shaped similar to the unconstrained density profiles. However, their support is parameterized by the box size controlled by $w = W/N^{\alpha_k}$ and the fraction of particles c inside it. As w and c are varied, the shape of the constrained density profile undergoes interesting shape transitions in the $(w - c)$ plane, as indicated in Fig. 5.2 by shaded regions separated by the two curves $c = \bar{c}(w)$ and $c = c^*(w)$. The loci of these two curves are calculated analytically in Eq. (5.23) and Eq (5.3) respectively. In Fig. 5.3 we compare our analytical results for the saddle point density with the MC simulations and observe a very good agreement.

The LDF and its properties: Using these saddle point densities, we have obtained explicit

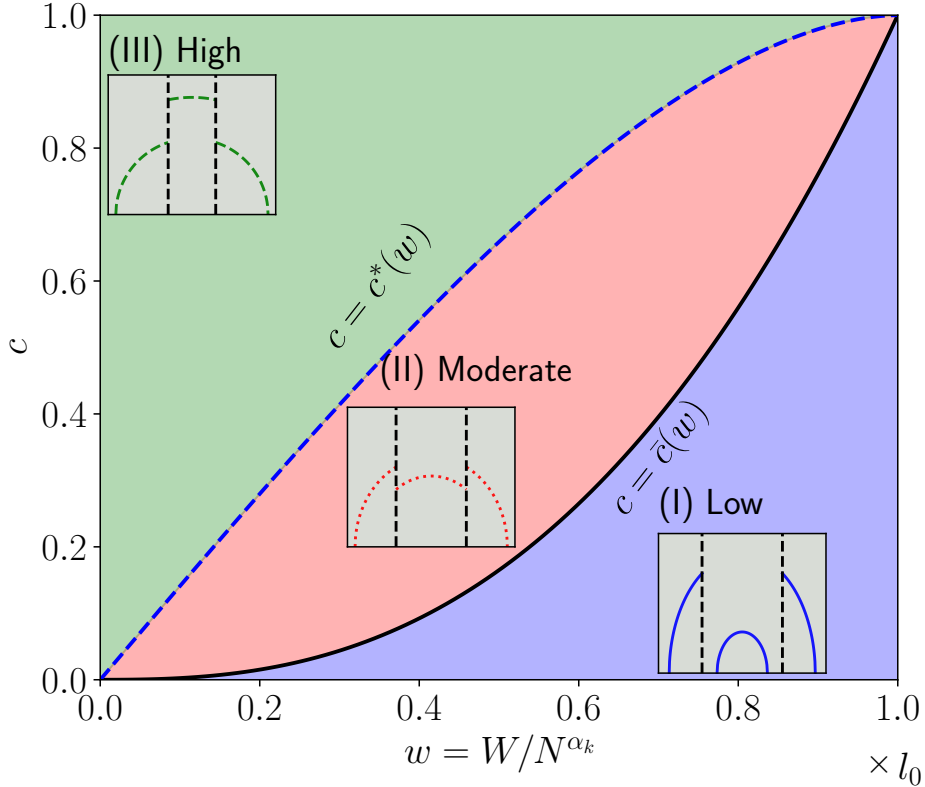


Figure 5.2: Phase diagram in the (w, c) plane showing three different regimes: (I) low, (II) moderate and (III) high fraction of particles in the box $[-W, W]$, where the saddle point density profiles given in Eq. (5.21) exhibit distinctly different shapes (see inset). The critical fraction line $c = \bar{c}(w)$ [Eq. (5.23)] separates the phases (I) and (II). Below this fraction, we observe a disjoint density profile in the phase (I) and above this concentration the two disjoint parts join and we observe a density profile as shown in the inset of the regime (II). Around this line, the LDF behaves non-analytically which leads to a third-order phase transition [see Appendix. A.5]. On the other hand, the crossover line $c = c^*(w)$ [Eq. (5.2)] separates the phases (II) and (III) and the LDF shows analytic behavior around it [see Eq. (5.33)]. This plot is generated for $k = 1.25$, however, such a plot is expected to be qualitatively the same for all $k > 1$. Note that the x -axis is in the units of l_{uc} .

analytical expression of the LDF $\Phi(c, w)$ which is given in Eq. (5.30) and plotted in Fig. 5.4. The behavior of the LDF is similarly governed by two parameters c and $w = W/N^{\alpha_k}$. We note that, for a fixed box $[-W, W]$, as the fraction of particles is increased from below $\bar{c}(w)$ [regime (I)] to above it [regime (II)], the hole region in the density profile vanishes (see Fig. 5.2). This gap closing transition at $c = \bar{c}(w)$ with a fixed w gives rise to a non-analytic behavior of the LDF characterized by a discontinuous third-order derivative of the LDF $\Phi(c, w)$ w.r.t. c for $|c - \bar{c}(w)| \ll 1$ as can be seen from

$$\frac{\partial^3 \Phi(c, w)}{\partial c^3} = \begin{cases} \frac{(1+2k)(1+k)}{\bar{c}(w)^3 k^3} \tilde{\mathcal{C}}_+ \left(\frac{c - \bar{c}(w)}{\bar{c}(w)} \right)^{\frac{1}{k} - 1}, & \text{for } c > \bar{c}(w) \\ \frac{6}{\bar{c}(w)^3} \tilde{\mathcal{C}}_-, & \text{for } c < \bar{c}(w) \end{cases}, \quad (5.6)$$

where $\tilde{\mathcal{C}}_{\pm}$ are constants [see Appendix A.5 for details]. This discontinuity in the third derivative implies a third-order phase transition according to Ehrenfest classification [137]. By the same mechanism, a similar gap-closing transition occurs but now with a decreasing box size for a fixed c (along a horizontal line in Fig. 5.2). Such third-order phase transitions via gap-closing mechanisms have been found in numerous examples [25].

Similar non-analytic behavior of the LDF associated to $\mathcal{N}(W, N)$ has also been observed in long-range interacting models such as the Dyson's log-gas [40, 41] and the 1dOCP [42]. Interestingly, the non-analyticity of LDF in our short-range case ($k > 1$) of Riesz gas, appears at $c = \bar{c}(w)$ unlike these long-range models ($k \rightarrow 0$ and $k = -1$) for which it appears at $c = c^*(w)$. For our short-range case, the LDF $\Phi(c, w)$ is analytic at $c = c^*(w)$ and shows quadratic behavior, i.e., $\Phi(c = c^*(w) + \kappa, w) \sim O(\kappa^2)$. This quadratic behavior of the LDF $\Phi(c, w)$ around $c = c^*(w)$ suggests that the typical fluctuations in the number of particles in the box are described by a Gaussian probability distribution given by

$$\mathcal{P}(\mathcal{N} = cN) \asymp \exp\left(\frac{-N^2(c - c^*(w))^2}{2 \text{Var}(\mathcal{N})}\right), \quad (5.7)$$

for $|c - c^*(w)| \lesssim O\left(\sqrt{\text{Var}(\mathcal{N})}\right)$.

Here the variance is given by

$$\text{Var}(\mathcal{N}) = \frac{N^{\nu_k}}{\beta l_{\text{uc}}^2 \alpha_k} \mathcal{V} \left(\frac{W}{N^{\alpha_k} l_{\text{uc}}} \right) \text{ with } \nu_k = \frac{2-k}{2+k}, \quad (5.8)$$

and the function $\mathcal{V}(h)$ is given in Eq. (5.35). The analytical result in Eq. (5.2) for the mean and in Eq. (5.8) for the variance is verified with MC simulations in Fig 5.5a,b, respectively for $k = 1.5$. We note that the variance scales with system size as N^{ν_k} with $\nu_k = (2-k)/(k+2)$. This implies that for $1 < k < 2$ the variance increases with increasing system size. For $k \rightarrow 2$ we see $\nu_k \rightarrow 0$ as a result $N^{\nu_k} \rightarrow \log(N)$, hence one generally expects that the variance grows logarithmically with N similar to the case of the Dyson's log-gas ($k \rightarrow 0$). For $k > 2$, $\nu_k < 0$ and the variance decreases with system size which suggests that the system becomes very rigid in the thermodynamic limit and possibly the typical fluctuations are dominated by microscopic fluctuations at the edges of the box. This is not captured by the present scaling analysis.

Generalization to other quantities: Using the same approach, we also study a more general quantity known as linear statistics defined as $S_N = \sum_{i=1}^N r(y_i)$, where $y_i = x_i/N^{\alpha_k}$ and $r(y)$ is an arbitrary function. The mean of this quantity scales linearly with system size as expected, whereas the variance scales as a power-law $\sim O(N^{\nu_k})$ with $\nu_k = (2-k)/(k+2)$ as described in Section. 5.5. Note that the number distribution $\mathcal{N}(W, N)$ is also a linear statistic with the choice $r(y) = \Theta(w-y)\Theta(w+y)$, where $\Theta(x)$ is the Heavyside Theta function. Another interesting and well-studied quantity is the index defined as the number of particles, denoted by $\mathcal{G}(W, N)$, in the semi-infinite box $(-\infty, W]$ which corresponds to the choice $r(y) = \Theta(w-y)$ in the linear statistics. This quantity appears naturally in the study of the stability of complex systems [177, 178]. It has been well studied in the context of the random matrix theory [38, 179], Dyson's log-gas [39] and the 1dOCP model [32, 114]. We find that the properties of the saddle point density profiles and the LDF corresponding to the index distributions are qualitatively similar to the number statistics problem summarized above. It is important to note that, in general, FCS behaves differently from the linear statistics with a smooth function $r(y)$ [40–42, 180, 181]. However, for the short-range case, this distinction does not seem to occur at least for the variance.

5.3 Derivation of the number distribution

In this section, we outline the derivation of the distribution of $\mathcal{n}(W, N)$, which quantifies the number of particles in the box $[-W, W]$, as defined by

$$\mathcal{n}(W, N) = \sum_{i=1}^N \Theta(W - x_i) \Theta(W + x_i). \quad (5.9)$$

Here $\Theta(x)$ is the Heaviside theta function. We start by writing the Gibbs-Boltzmann probability distribution of the position configuration in terms of the scaled variables $\{y_i = x_i/N^{\alpha_k}\}$ for $i = 1, 2, \dots, N$ [see Eq. (2.2)]:

$$P(y_1, y_2, \dots, y_N) = \frac{1}{Z_k} \exp\left(-\beta N^{1+2\alpha_k} E_k(\{y_i\})\right), \quad (5.10)$$

where $E_k(\{y_i\})$ is the energy function in Eq. (2.7) and Z_k is the partition function, given by

$$Z_k = \int_{-\infty}^{\infty} dy_1 \int_{-\infty}^{\infty} dy_2 \dots \int_{-\infty}^{\infty} dy_N \exp\left(-\beta N^{1+2\alpha_k} E_k(\{y_i\})\right). \quad (5.11)$$

The mean of the number of particles can be easily computed as $\langle \mathcal{n}(W, N) \rangle = \sum_i \langle \Theta(w - y_i) \Theta(y_i + w) \rangle$, where $w = W/N^{\alpha_k}$ and $y_i = x_i/N^{\alpha_k}$. Simplifying further, we get $\langle \mathcal{n}(W, N) \rangle \simeq c^*(w) N$ where $c^*(w)$ is given in Eq. (5.3).

The distribution of $\mathcal{n}(W, N)$ can be obtained by integrating the microscopic configurations with the constraint of having cN particles inside the box and it is given by

$$\mathcal{P}(\mathcal{n} = cN) = \int_{-\infty}^{\infty} dy_1 \dots \int_{-\infty}^{\infty} dy_N \frac{\exp(-\beta N^{1+2\alpha_k} E_k(\{y_i\}))}{Z_k} \times \delta\left(cN - \sum_{i=1}^N \Theta(w + y_i) \Theta(w - y_i)\right), \quad (5.12)$$

where recall that $w = W/N^{\alpha_k}$. For the sake of brevity W and N in the argument of $\mathcal{n}(W, N)$ are suppressed. For finite N , the integrals over the microscopic positions in Eqs. (5.11) and (5.12) are difficult to carry out for arbitrary k with the only notable exceptions for $k \rightarrow 0$ [19] and $k = -1$ [31, 42, 180]. However, in the large N limit and for $\beta \sim O(1)$, the multiple integrals can be computed approximately using the Laplace method in which one first rewrites the microscopic integral as a path integral

over density field configurations and then performs the saddle point calculation. Such a method in the literature is known as the Coulomb gas method [22, 23], which has been used recently in the context of Riesz gases [45]. To adopt this field-theoretic method, we first rewrite the integral in Eq. (5.12) as a path integral over the empirical density field $\rho(y) = \frac{1}{N} \sum_{i=1}^N \delta(y - y_i)$. More precisely, we compute the integral in Eq. (5.12) in two steps: (i) we integrate over the microscopic positions corresponding to a density field $\rho(y)$ (which one could assume to be a smooth function in the large N limit) and (ii) perform the integration over these density profiles. After the first step, one generates an entropy term $\mathcal{S}[\rho(y)]$ in the exponential in addition to the energy functional $\mathcal{E}_k[\rho(y)]$ to arrive at [45]

$$\mathcal{P}(n = cN) = \int \mathcal{D}[\rho(y)] \frac{\exp(-\beta N^{1+2\alpha_k} \mathcal{E}_k[\rho(y)] + N\mathcal{S}[\rho(y)])}{Z_k} \times \delta\left(cN - N \int_{-\infty}^{\infty} dy \rho(y) \Theta(w+y) \Theta(w-y)\right) \delta\left(\int_{-\infty}^{\infty} dy \rho(y) - 1\right), \quad (5.13)$$

where the energy functional $\mathcal{E}_k[\rho(y)]$ is given in Eq. (2.16) and the entropy functional is given by [22, 23]

$$\mathcal{S}[\rho(y)] = \left(-\int_{-\infty}^{\infty} dy \rho(y) \log \rho(y)\right). \quad (5.14)$$

Using the integral representation of the delta function on the complex plane, one can express $\mathcal{P}(n, W)$ in Eq. (5.13) as

$$\mathcal{P}(n = cN) = \int d\mu \int d\bar{\mu} \int \mathcal{D}[\rho(y)] \frac{\exp(-\beta N^{1+2\alpha_k} G[\rho(y)])}{Z_k}, \quad (5.15)$$

with the action given by

$$\begin{aligned} G[\rho(y)] &= \mathcal{E}_k[\rho(y)] - \frac{T}{N^{2\alpha_k}} \mathcal{S}[\rho(y)] \\ &\quad - \mu \left(\int_{-\infty}^{\infty} dy \rho(y) (1 - \Theta(w+y) \Theta(w-y)) - 1 + c \right) \\ &\quad - \bar{\mu} \left(\int_{-\infty}^{\infty} dy \rho(y) \Theta(w+y) \Theta(w-y) - c \right), \end{aligned} \quad (5.16)$$

where $w = W/N^{\alpha_k}$. The functional $G[\rho(y)]$ in the above equation is essentially the free

energy required to create a particular density profile with the chemical potentials $\bar{\mu}$ and μ ensuring that the fraction of particles inside and outside of the box $[-w, w]$ is c and $1 - c$ respectively.

Note that the factor $N^{1+2\alpha_k}$ in the exponent of Eq. (5.15) diverges for $N \rightarrow \infty$, since $1 + 2\alpha_k > 0$ [see Eq. (2.6)]. Therefore, the integral can be evaluated by a saddle point technique in which one needs to minimize the action in Eq. (5.16) w.r.t. the density field $\rho(y)$ as well as the chemical potentials $\bar{\mu}$ and μ . Moreover, for large N and $T \sim O(1)$ one can neglect the contribution from the entropy term in the saddle point calculation. We find the following equations

$$\bar{\mu}^* = \frac{y^2}{2} + J\zeta(k)(k+1)(\varrho^*(y))^k \quad \text{for } |y| < w, \quad (5.17)$$

$$\mu^* = \frac{y^2}{2} + J\zeta(k)(k+1)(\varrho^*(y))^k \quad \text{for } |y| > w, \quad (5.18)$$

along with the normalization constraints

$$\int_{-\infty}^{\infty} dy \varrho^*(y) \Theta(w+y) \Theta(w-y) = c, \quad (5.19)$$

$$\int_{-\infty}^{\infty} dy \varrho^*(y) (1 - \Theta(w+y) \Theta(w-y)) = 1 - c. \quad (5.20)$$

Here the * represents the saddle point values. Note that the saddle point equations in Eqs. (5.17) and (5.18) are valid when the size ($2w$) of the box $[-w, w]$ is much larger than the (typical) mean inter-particle scaled distance *i.e.*, $w \gg O(1/N)$.

Note that the chemical potentials $\bar{\mu}^*$ and μ^* in Eqs. (5.17) and (5.18) are independent of the position y . On the other hand, the right-hand sides of Eqs. (5.17) and (5.18) diverge in the limit $y \rightarrow \infty$. This suggests that the saddle point density has a finite support. The density profile takes the form

$$\varrho^*(y) = \begin{cases} A_k (\bar{l}^2 - y^2)^{\frac{1}{k}} & \text{for } |y| \leq \min(w, \bar{l}) \\ A_k (l^2 - y^2)^{\frac{1}{k}} & \text{for } w \leq |y| \leq l \\ 0 & \text{otherwise} \end{cases}, \quad \text{where } \bar{l} = \sqrt{2\bar{\mu}^*}, \quad l = \sqrt{2\mu^*}, \quad (5.21)$$

and the constant A_k is given in Eq. (2.20). The length scales $\bar{l} \equiv \bar{l}(c, w)$ and $l \equiv l(c, w)$ are functions of the two parameters c and w and are obtained from the normalization

conditions Eqs. (5.19) and (5.20), respectively. We find

$$\bar{l} = \begin{cases} c^{\alpha_k} l_{\text{uc}} & \text{for } c \leq \bar{c}(w), \\ c^{\alpha_k} l_{\text{uc}} I\left(\left(\frac{w}{\bar{l}}\right)^2, \frac{1}{2}, \frac{1}{k} + 1\right)^{-\alpha_k} & \text{for } c \geq \bar{c}(w) \end{cases}, \quad (5.22)$$

where $\bar{c}(w)$ is the fraction for which $\bar{l} = w$ which is given by

$$\bar{c}(w) = \left(\frac{w}{l_{\text{uc}}}\right)^{\frac{1}{\alpha_k}}. \quad (5.23)$$

In Eq. (5.22) we have introduced the function $I(h, a, b)$ which is defined as

$$I(h, a, b) = \frac{B(h, a, b)}{B(1, a, b)} \text{ with } B(h, a, b) = \int_0^h ds s^{a-1} (1-s)^{b-1}. \quad (5.24)$$

For the edge l of the density profile outside the box, we find

$$l = (1-c)^{\alpha_k} l_{\text{uc}} \left(1 - I\left(\left(\frac{w}{\bar{l}}\right)^2, \frac{1}{2}, \frac{1}{k} + 1\right)\right)^{-\alpha_k}. \quad (5.25)$$

We can now numerically compute the lengths l and \bar{l} for any c and w by solving the transcendental Eqs. (5.22) and (5.25). Note that the edge of the support of the density profile inside the box is $\min(w, \bar{l})$. The extent of this support depends on the fraction of particles c in the box $[-w, w]$. For c less than a certain value $\bar{c}(w)$ we find $\bar{l} < w$ while for $c > \bar{c}(w)$ we get $\bar{l} > w$. As c is changed the shape of the density profile changes and we obtain three distinct regimes (as depicted in Fig. 5.2) namely: (I) low (II) moderate and (III) high fraction regimes. We further elaborate on these regimes below.

(I) *Low fraction* $[0 \leq c < \bar{c}(w)]$: As shown in Fig. 5.3a, in this regime, due to the low fraction of the particles c within the box, the density profile inside forms a small droplet at the minimum of the harmonic trap. It does not spread over the full extent of the box $[-w, w]$ and is only supported over the region $[-\bar{l}, \bar{l}]$. This leads to the appearance of two holes with no particles between the droplet and the edges of the box. Outside of the box, the remaining particles form truncated domes on both sides. The support of the left dome is $[-l, -w]$ while for the right dome, it is $[w, l]$. As we further increase the fraction c , the edge of the support of the droplet \bar{l} increases and eventually touches the edges of the box located at $\pm w$ when $c = \bar{c}(w)$. For the sake of brevity, we sometimes suppress

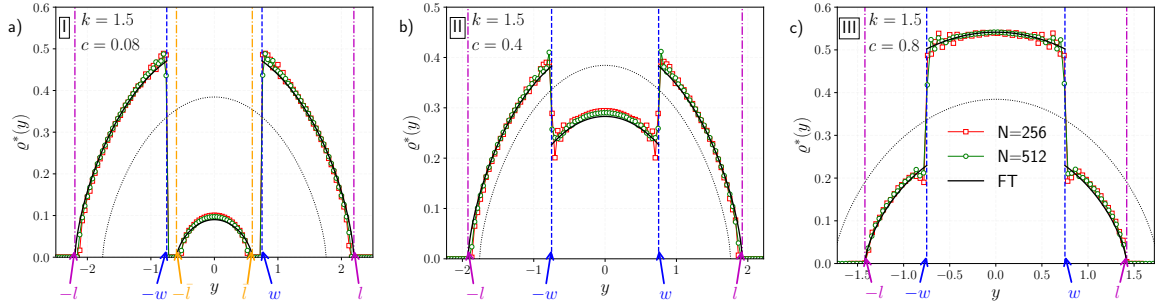


Figure 5.3: Plots of the equilibrium density profiles for different fractions of particles c confined inside the box $[-w, w]$ with $w = 0.75$, $k = 1.5$ and $J = 1$. The boundaries of the box at $y = \pm w$ are shown by the blue vertical dashed lines. We consider three values of c , (a) 0.08 (b) 0.4 and (c) 0.8 which are representative of the three regimes: (I) $c < \bar{c}(w)$, (II) $\bar{c}(w) < c < c^*(w)$ and (III) $c^*(w) < c$, respectively, where $c^*(w)$ is given in Eq. (5.3) and $\bar{c}(w)$ is given in Eq. (5.23). For $w = 0.75$ and $k = 1.5$ one finds that $\bar{c}(w) = 0.136$ and $c^*(w) = 0.552$. The symbols in all the plots are obtained using MC simulation for $N = 256$ and $N = 512$ whereas the solid lines represent the theoretical results given Eq. (5.21). The dotted line in each plot represents the density profiles $\rho_0(y)$ [see Eq. (2.18)] in the unconstrained case *i.e.*, without any wall, from which one can compute the fraction $c^*(w)$ of particles within the region $[-w, w]$. Here we have taken an average of over 10^6 samples for all the plots.

the w dependence in $\bar{c}(w)$.

(II) *Moderate fraction* [$\bar{c}(w) < c \leq c^*(w)$]: As shown in Fig. 5.3b, as the fraction c is increased above $\bar{c}(w)$, the droplet grows but its support does not expand. As a consequence, the density near the walls just inside the box increases and this droplet becomes a truncated dome. Outside the box, the support of the left and right truncated domes shrink. The value of the density just outside the box decreases. Therefore the density profile is discontinuous at the locations of the wall ($\pm w$) [see Fig. 5.3b and Fig. 5.2 (inset)]. As the fraction c inside the box is further increased, the jump in the value of the density at the location of the wall is reduced. This jump eventually disappears when the fraction inside the box becomes the same as the fraction $c^*(w)$ [see Eq. (5.3)]. Hence in this regime with $\bar{c}(w) < c < c^*(w)$, the density profile has three parts: two truncated domes on either side of the box and another truncated dome inside the box.

(III) *High fraction* [$c^*(w) < c < 1$]: When $c > c^*(w)$, we find that the density at the wall just inside the box, increases further and becomes higher than that of the density at the wall just outside the box [see Fig. 5.3c and Fig. 5.2 (inset)]. Therefore the density profile in this regime, with $c > c^*(w)$, comprises three truncated domes.

In Fig. 5.3a,b,c, we plot the density profiles given in Eq. (5.21) for the three regimes

along with the same obtained from MC simulation and we observe an excellent agreement. The above discussion was based on varying c with the wall position w fixed. Similarly, one could obtain these three regimes by varying the wall position w by keeping the fraction c fixed [see Fig. 5.2].

As a next step in computing the integral in Eq. (5.15), we substitute the saddle point density profile from Eq. (5.21) in the expression of the action, $G[\varrho^*(y)]$, in Eq. (5.16), we find the following large deviation form for the probability distribution

$$\mathcal{P}(N = cN) \asymp \exp\left(-\beta N^{1+2\alpha_k} \Phi(c, w)\right), \text{ with } w = \frac{W}{N^{\alpha_k}} \quad (5.26)$$

where the large deviation function is given by

$$\Phi(c, w) = G[\varrho^*(y)] - G_{\text{uc}}. \quad (5.27)$$

Here the unconstrained action, G_{uc} , is given by the logarithm of the partition function in Eq. (5.11). For large N it reads [59]

$$G_{\text{uc}} \approx -\frac{\log Z_k}{\beta N^{1+2\alpha_k}} = \frac{l_{\text{uc}}^2(k+2)}{2(3k+2)}, \quad (5.28)$$

where l_{uc} is the edge of the support of the unconstrained density profile $\rho_0(y)$ [see Eq. (2.20)]. By neglecting the contribution from the entropy term in Eq. (5.16), we approximate the action by

$$G[\varrho^*(y)] = \mathcal{E}_k[\varrho^*(y)] \quad (5.29)$$

where the energy functional is given in Eq. (2.16). After simplifying Eq. (5.27) we obtain the LDF as

$$\Phi(c, w) = \begin{cases} G_{\text{uc}} \left((1-c)^{\frac{3k+2}{k+2}} \mathcal{H}\left(\frac{w}{l}\right) + (c)^{\frac{3k+2}{k+2}} - 1 \right), & \text{for } c \leq \bar{c}(w), \\ G_{\text{uc}} \left((1-c)^{\frac{3k+2}{k+2}} \mathcal{H}\left(\frac{w}{l}\right) + (c)^{\frac{3k+2}{k+2}} \mathcal{J}\left(\frac{w}{\bar{l}}\right) - 1 \right), & \text{for } c \geq \bar{c}(w). \end{cases} \quad (5.30)$$

The length scales \bar{l} and l are given in Eqs. (5.22) and (5.25). The functions $\mathcal{H}(h)$ and

$\mathcal{J}(h)$ in Eq. (5.30) are simple and given by

$$\begin{aligned} \mathcal{H}(h) &= \left(1 - I\left(h^2, \frac{1}{2}, 1 + \frac{1}{k}\right)\right)^{-\frac{2k}{k+2}} \\ &\quad + \frac{h(1-h^2)^{\frac{1}{k}+1}(2k^2)}{(k+1)(k+2)B\left(\frac{1}{2}, 1 + \frac{1}{k}\right)} \left(1 - I\left(h^2, \frac{1}{2}, 1 + \frac{1}{k}\right)\right)^{-\frac{3k+2}{k+2}}, \end{aligned} \quad (5.31)$$

$$\begin{aligned} \mathcal{J}(h) &= \left(I\left(h^2, \frac{1}{2}, 1 + \frac{1}{k}\right)\right)^{-\frac{2k}{k+2}} \\ &\quad - \frac{h(1-h^2)^{\frac{1}{k}+1}(2k^2)}{(k+1)(k+2)B\left(\frac{1}{2}, 1 + \frac{1}{k}\right)} \left(I\left(h^2, \frac{1}{2}, 1 + \frac{1}{k}\right)\right)^{-\frac{3k+2}{k+2}}, \end{aligned} \quad (5.32)$$

where $I(h, a, b)$ is given in Eq. (5.24). In Fig. 5.4a. we show the LDF $\Phi(c, w)$ given in Eq. (5.30) as a function of w (for fixed c) and in Fig. 5.4b we show the variation of LDF with c (for fixed w). The three types of saddle point density profiles corresponding to the three regions I, II, and III, shown in Fig. 5.3, determine the form of the LDF as shown in Fig. 5.4a,b. Next, we discuss the asymptotic behavior of $\Phi(c, w)$ in different limits.

Behaviour around $c^(w)$:* We start with the behaviour of $\Phi(c, w)$ near $c^*(w)$ which describes the probability of typical fluctuations of c around $c^*(w)$. Recall from Eq. (5.3) that c represents the mean fraction of particles inside a box of size w . Setting $c = c^*(w) + \kappa$ in Eq. (5.30) and expanding to leading order in κ we find $\Phi(c^*(w) + \kappa, w) \propto \kappa^2$. A slightly different derivation of this expansion is given in Appendix. A.7. The quadratic behavior of $\Phi(c^*(w) + \kappa, w)$ with κ in the leading order implies a Gaussian distribution for the typical fluctuations given by

$$\mathcal{P}(\mathcal{N} = (c^*(w) + \kappa)N, W) \asymp \exp\left(-\frac{N^2\kappa^2}{2 \text{Var}(\mathcal{N})}\right), \quad (5.33)$$

with the variance of the number of particles given by

$$\text{Var}(\mathcal{N}) = \frac{N^{\nu_k}}{\beta l_{\text{uc}}^2 \alpha_k} \mathcal{V}\left(\frac{W}{N^{\alpha_k} l_{\text{uc}}}\right), \quad \text{with } \nu_k = 1 - 2\alpha_k = \frac{2-k}{k+2}, \quad (5.34)$$

$$\text{and } \mathcal{V}(h) = I\left(h^2, \frac{1}{2}, \frac{1}{k}\right) \left(1 - I\left(h^2, \frac{1}{2}, \frac{1}{k}\right)\right), \quad (5.35)$$

where the function $I(h, a, b)$ is given in Eq. (5.24). For small h , the function $\mathcal{V}(h) \propto h$ whereas for $h \rightarrow 1$, $\mathcal{V}(h) \propto (1-h)^{1/k}$. In Fig. 5.5a,b, we compare our theoretical results for the mean [see Eq. (5.3)] and variance [see Eq. (5.34)] of \mathcal{N} with the same measured

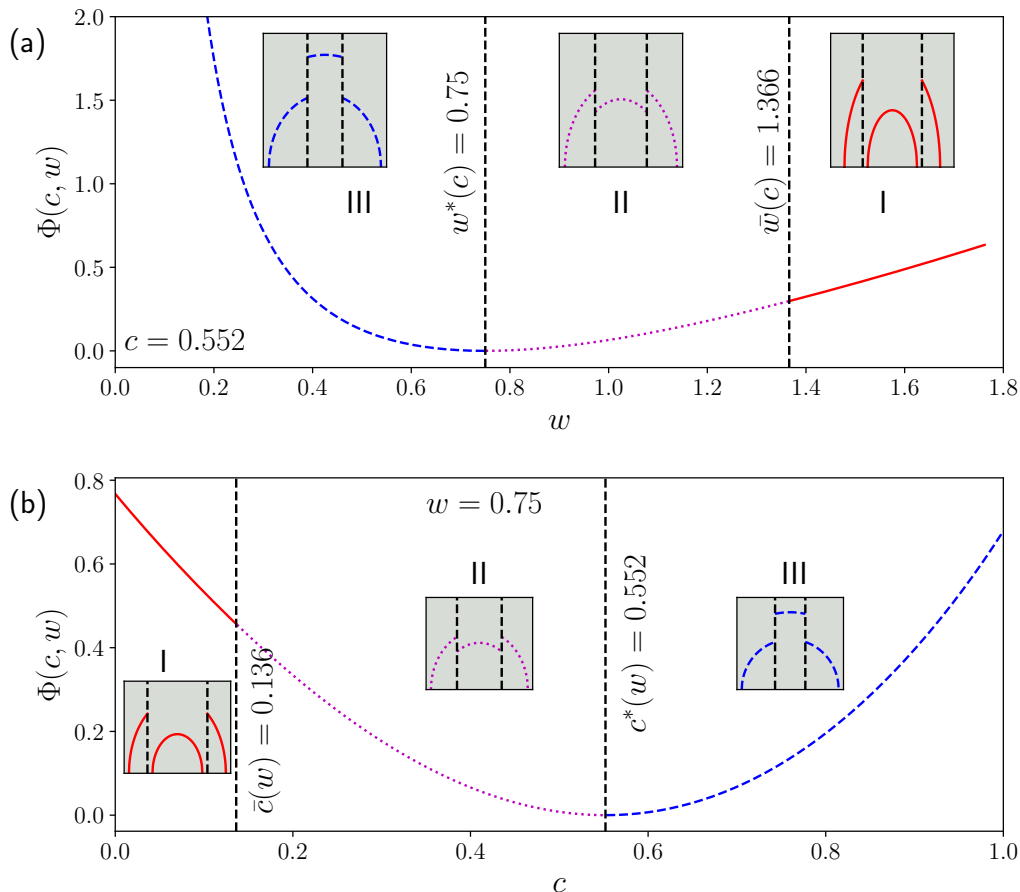


Figure 5.4: The plot displays the large deviation function $\Phi(c, w)$, given in Eq. (5.30), for $k = 1.5$ and $J = 1$. In (a) we show a plot of $\Phi(c, w)$ as a function of w for $c = 0.552$ and in (b) we plot $\Phi(c, w)$ as a function of c for $w = 0.75$. In both plots, we have demarcated three regions (I, II and III) based on the three types of saddle point density profiles (as shown in Fig. 5.3) that create the large deviations in those three different regions. Schematic plots of such density profiles are provided in the insets.

in MC simulations and observe good agreement everywhere except the edges where it matches better for large- N . This is due to finite- N corrections. Note that for $k > 2$ the exponent ν_k , given in Eq. (5.34), is negative implying that the variance decreases with increasing system size. This suggests that the contribution to the typical fluctuations for large- N are primarily due to the microscopic fluctuation at the edges of the box. Such fluctuations do not cause changes in the density profile and are thereby missed in the field theory description. In the marginal case of $k = 2$, as mentioned earlier, the exponent $\nu_k = 0$ possibly suggests $\log(N)$ growth of the variance.

Non-analytic behavior and phase transitions: We recall that $\bar{c}(w)$ given in Eq. (5.23) represents the fraction at which the hole in the density profile inside the box vanishes. We find that this hole-closing phenomenon gives rise to non-analytic properties of $\Phi(c, w)$

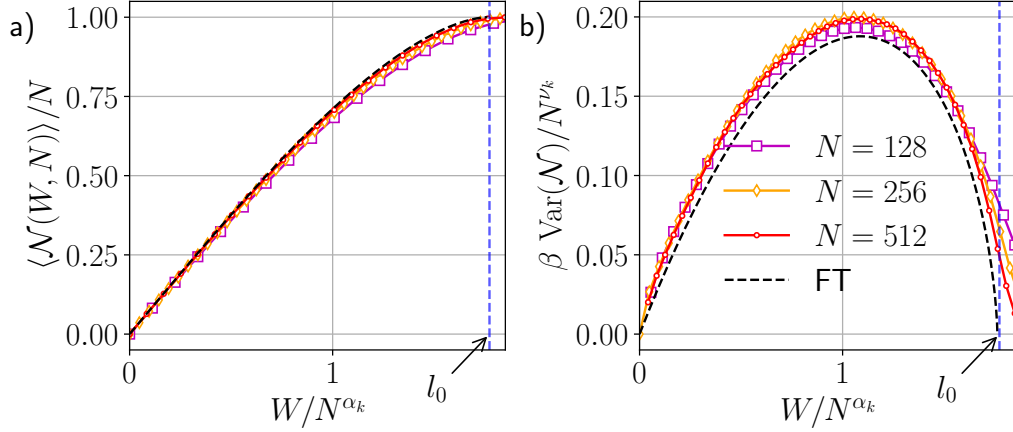


Figure 5.5: Numerical verification of the mean and variance of the number distribution problem. The plot displays the W dependence of (a) the mean fraction of particles and (b) the scaled variance of the number of particles in the box $[-W, W]$ for $N = 128, 256, 512$ with parameters $k = 1.5$, $T = 10$ and $J = 1$. The vertical blue dashed line represents the box with $W = l_{\text{uc}} N^{\alpha_k}$. The symbols indicate the results obtained from the Monte Carlo simulations and they are compared with our theoretical predictions (solid lines) given by Eqs. (5.2) and (5.34) for the mean and the variance, respectively.

around $c = \bar{c}(w)$. Expanding the LDF $\Phi(\bar{c}(w)(1 + \epsilon), w)$ for small ϵ we find [see Appendix A.5.1]:

$$\Phi(\bar{c}(w)(1 + \epsilon), w) - \Phi(\bar{c}(w), w) = \begin{cases} \tilde{\mathbb{A}} \epsilon + \tilde{\mathbb{B}} \epsilon^2 + \tilde{\mathbb{C}}_+ \epsilon^{2+\frac{1}{k}} + o(\epsilon^{2+\frac{1}{k}}), & \text{for } \epsilon > 0 \\ \tilde{\mathbb{A}} \epsilon + \tilde{\mathbb{B}} \epsilon^2 + \tilde{\mathbb{C}}_- \epsilon^3 + O(\epsilon^4), & \text{for } \epsilon < 0 \end{cases}, \quad (5.36)$$

where the constants $\tilde{\mathbb{A}}, \tilde{\mathbb{B}}$ etc. are given in the Eqs. (A.82)-(A.84) of the Appendix A.5.1. Note that $o(\epsilon^{2+\frac{1}{k}}) = O(\min[\epsilon^{2+\frac{2}{k}}, \epsilon^3])$. For a fixed w , the third derivative of the LDF $\Phi(c, w)$ w.r.t. c (*i.e.*, ϵ) shows a discontinuity at $c = \bar{c}(w)$ [Eq. (5.23)] as demonstrated in Fig. 5.6a. More precisely, the third derivative is finite for $c \rightarrow \bar{c}^-(w)$ and is diverging for $c \rightarrow \bar{c}^+(w)$. Similar discontinuities in the third derivative of the LDF have been observed previously in various other contexts and have been associated to third order phase transition – such as linear statistics in 1d Coulomb gas [37] and in extreme statistics of Riesz gas [59], of Coulomb gas [128] and random matrix theory [25, 182]. The non-analyticity of the LDF, described above, stems from the structural change of the saddle point density profile from (I) Low to (II) Moderate fraction regime.

By the same mechanism, a similar third-order phase transition is expected to occur

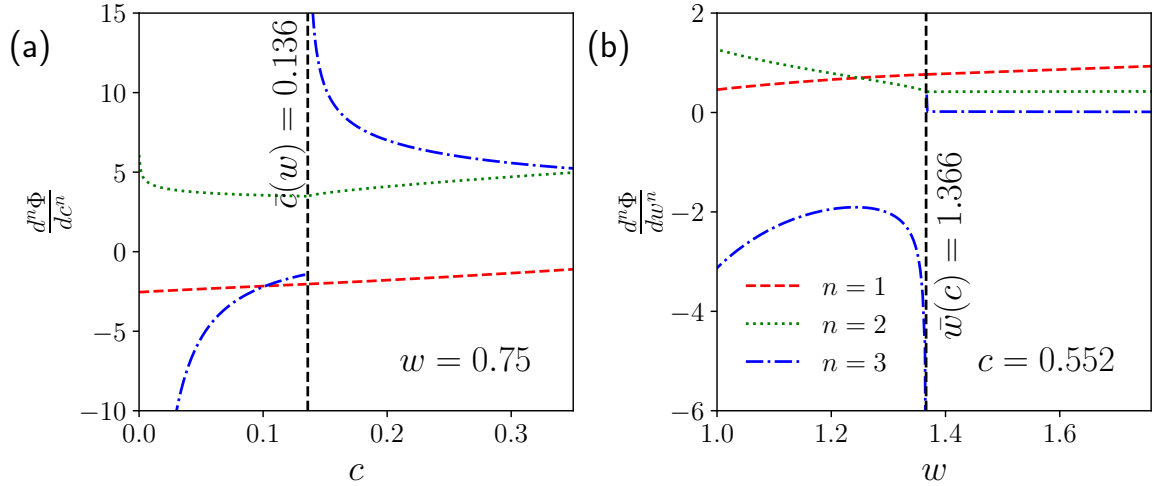


Figure 5.6: The plot displays the derivatives of the LDF $\Phi(c, w)$ [Eq. (5.30)]. Specifically, it shows the first (red dashed line), second (green dotted line) and third (blue dash-dotted line) derivatives: (a) w.r.t. c for $w = 0.75$ and (b) w.r.t. w for $c = 0.552$. Notably, we observe a pronounced discontinuity in the third derivative of $\Phi(c, w)$ in (a) at $c = \bar{c}(w)$ [see Eq. (5.23)] and in (b) at $w = \bar{w}(c) = l_{\text{uc}} c^{\alpha_k}$, establishing the presence of third order phase transitions.

when we cross the line $c = \bar{c}(w)$ horizontally in Fig. (5.2) *i.e.*, by varying w while keeping c fixed as demonstrated in Fig. 5.6b. This phase transition can be shown by analyzing the behavior of $\Phi(c, w)$ near the special box size $\bar{W} = \bar{w}(c)N^{\alpha_k}$ with $\bar{w}(c) = l_{\text{uc}} c^{\alpha_k}$. While reducing the box size starting from a larger value, the hole in the density profile inside the box (containing cN particles) decreases and at a special value $\bar{w}(c)$ of the box size, the droplet touches the boundaries of the box. In Appendix A.5.2 we show that the LDF $\Phi(c, w)$ around $\bar{w}(c)$ also exhibits non-analytic behavior. More elaborately it behaves as

$$\Phi(c, \bar{w}(c)(1 + \epsilon)) - \Phi(c, \bar{w}(c)) = \begin{cases} \tilde{\mathbb{D}} \epsilon + \tilde{\mathbb{E}} \epsilon^2 + \tilde{\mathbb{F}}_+ \epsilon^3 + O(\epsilon^4), & \text{for } \epsilon > 0 \\ \tilde{\mathbb{D}} \epsilon + \tilde{\mathbb{E}} \epsilon^2 + \tilde{\mathbb{F}}_- |\epsilon|^{2+\frac{1}{k}} + o(\epsilon^{2+\frac{1}{k}}), & \text{for } \epsilon < 0 \end{cases}, \quad (5.37)$$

where the constants $\tilde{\mathbb{D}}$, $\tilde{\mathbb{E}}$ etc. are given in the Eqs. (A.86)-(A.87) of the Appendix A.5.2. We find that the third derivative is discontinuous at $w = \bar{w}(c)$. More precisely, $\Phi(c, w)$ is finite for $w \rightarrow \bar{w}(c)_+$ and is diverging for $w \rightarrow \bar{w}(c)_-$.

Behaviour of $\Phi(c, w)$ near $c = 0$ and $c = 1$: In these limits we find the following approx-

imations for a given w ,

$$\Phi(c, w) \approx \Phi(0, w) - \mu^* c, \quad \text{for } c \rightarrow 0, \quad (5.38)$$

$$\Phi(c, w) \approx \Phi(1, w) - \bar{\mu}^*(1 - c) \quad \text{for } c \rightarrow 1. \quad (5.39)$$

Here, $\bar{\mu}^*$ and μ^* represent the chemical potentials [see Eqs. (5.17) and (5.18)] of the gas outside and inside the box for $c = 0$ and $c = 1$, respectively. Here the LDFs $\Phi(0, w)$ and $\Phi(1, w)$ describe the probability of having no particle and all the particles in the box. The linear dependence on c in Eq. (5.38) represents the energy cost for depositing fraction c of particles into the initially empty box. On the other hand, $-\bar{\mu}^*(1 - c)$ represents the energy cost for taking out $(1 - c)$ of particles out of an initially filled box.

Hole formation LDF $\Phi(0, w)$: Taking $c = 0$ in Eq. (5.30), we find that the hole formation LDF $\Phi(0, w)$ is given by

$$\Phi(0, w) = G_{\text{uc}} \times \left(\mathcal{H} \left(\frac{w}{l} \right) - 1 \right), \quad (5.40)$$

where G_{uc} is given in Eq. (5.28), $\mathcal{H}(h)$ is given by Eq. (5.31), and l is the edge of the support of the (scaled) density profile when the box $[-W, W]$ is empty. Numerically, l can be calculated using Eq. (5.25) for $c = 0$.

Complete confinement LDF $\Phi(1, w)$: Taking $c = 1$ in Eq. (5.30), we find the LDF associated to the probability of containing all the particles in the box. This LDF is given by

$$\Phi(1, w) = G_{\text{uc}} \times \left(\mathcal{J} \left(\frac{w}{\bar{l}} \right) - 1 \right), \quad (5.41)$$

where G_{uc} is given in Eq. (5.28), $\mathcal{J}(h)$ is given by Eq. (5.32), and \bar{l} represents the edge of the support of the density profile when the box contains N particles. Numerically, \bar{l} can be calculated using Eq. (5.22) for $c = 1$.

5.4 Index distribution

Another interesting observable is the index for which our calculation presented in Section 5.3 for studying the number distribution can be straightforwardly extended. The

index denoted by $\mathcal{G}(W, N)$, counts the number of particles below a certain position W and it is defined as

$$\mathcal{G}(W, N) = \sum_i^N \Theta(W - x_i), \quad (5.42)$$

where x_i is the position of the i^{th} particle for any $i \in 1, 2, \dots, N$ and $\Theta(x) = 1$ for $x \geq 0$ and zero otherwise. Here we focus on $W > 0$. The case with $W < 0$ can be obtained from the distribution with $W > 0$ using the relation

$$\text{Prob.} [\mathcal{G}(W, N) = I_d] = \text{Prob.} [\mathbb{N}_{[W, \infty)}(N) = N - I_d] = \text{Prob.} [\mathcal{G}(-W, N) = N - I_d], \quad (5.43)$$

where $\mathbb{N}_{[W, \infty)}(N) = \sum_{i=1}^N \Theta(x_i - W)$ represents the number of particles to the right of W . To obtain the second equality we have used the inversion symmetry of the energy function $\tilde{E}_k(\{x_i\}) = \tilde{E}_k(\{-x_i\})$. To find the probability distribution of $\mathcal{G}(W, N)$, we follow the same procedure as done in the previous section. We find that for large N this probability distribution has the following large deviation form

$$\mathcal{P}(\mathcal{G} = c N, W) \asymp \exp \left(-\beta N^{1+2\alpha_k} \Psi(c, W/N^{\alpha_k}) \right), \quad (5.44)$$

where $\Psi(c, w)$ is the LDF and $\alpha_k = k/(k+2)$. We find that the LDF is given by

$$\Psi(c, w) = \begin{cases} \frac{G_{\text{nc}}}{2} \left((2c)^{2\alpha_k+1} + (2(1-c))^{2\alpha_k+1} \mathcal{H}\left(\frac{w}{l}\right) - 2 \right), & \text{for } c \leq \bar{c}(w) \\ \frac{G_{\text{nc}}}{2} \left((2c)^{2\alpha_k+1} \mathcal{J}\left(\frac{w}{l}\right) + (2(1-c))^{2\alpha_k+1} \mathcal{H}\left(\frac{w}{l}\right) - 2 \right), & \text{for } c > \bar{c}(w) \end{cases}, \quad (5.45)$$

where G_{uc} is given in Eq. (5.28), $w = W/N^{\alpha_k}$, $\bar{c}(w) = \left(\frac{w}{l_{\text{uc}}}\right)^{\frac{1}{\alpha_k}}$ and the functions $\mathcal{J}(h)$ and $\mathcal{H}(h)$ are

$$\mathcal{J}(h) = \left(1 + I\left(h^2, \frac{1}{2}, \frac{1}{k} + 1\right)\right)^{-2\alpha_k} - \frac{h(1-h^2)^{\frac{1}{k}+1}}{B\left(\frac{1}{2}, 1 + \frac{1}{k}\right)} \frac{2k^2}{(k+1)(k+2)} \left(1 + I\left(h^2, \frac{1}{2}, \frac{1}{k} + 1\right)\right)^{-2\alpha_k-1}, \quad (5.46)$$

$$\mathcal{H}(h) = \left(1 - I\left(h^2, \frac{1}{2}, \frac{1}{k} + 1\right)\right)^{-2\alpha_k} - \frac{h(1-h^2)^{\frac{1}{k}+1}}{B\left(\frac{1}{2}, 1 + \frac{1}{k}\right)} \frac{2k^2}{(k+1)(k+2)} \left(1 - I\left(h^2, \frac{1}{2}, \frac{1}{k} + 1\right)\right)^{-2\alpha_k-1}. \quad (5.47)$$

The length scales $\bar{l} \equiv \bar{l}(c, w)$ and $l \equiv l(c, w)$ in Eq. (5.45) are functions of c and w . These can be obtained by numerically solving the following transcendental equations

$$\bar{l} = \begin{cases} c^{\alpha_k} l_{\text{uc}} & \text{for } c \leq \bar{c}(w), \\ (2c)^{\alpha_k} l_{\text{uc}} \left(1 + I\left(\left(\frac{w}{\bar{l}}\right)^2, \frac{1}{2}, \frac{1}{k} + 1\right)\right)^{-\alpha_k} & \text{for } c \geq \bar{c}(w) \end{cases}, \quad (5.48)$$

$$l = (2(1-c))^{\alpha_k} l_{\text{uc}} \left(1 - I\left(\left(\frac{w}{l}\right)^2, \frac{1}{2}, \frac{1}{k} + 1\right)\right)^{-\alpha_k}, \quad (5.49)$$

where the function $I(h, a, b)$ is defined in Eq. (5.24). We analyze the behavior of the LDF $\Psi(c, w)$ at $c = \bar{c}(w)$ for a fixed w . We find that it shows a third-order phase transition, similar to the ‘number’ problem. In this case also, the distribution of the typical fluctuations of $\mathcal{G}(W, N)$ is Gaussian distribution and the variance scales as N^{ν_k} with $\nu_k = (2 - k)/(k + 2)$.

Pressure and Bulk modulus: Using the LDF for Index distribution, we can compute the thermodynamic pressure and the bulk modulus [see Appendix A.6].

5.5 Linear statistics

In this section, we study linear statistics which is defined as

$$S_N = \sum_{i=1}^N r(y_i), \quad (5.50)$$

where the function $r(y)$ is arbitrary and recall, from Eq. (2.2), that $y_i = x_i/N^{\alpha_k}$ denote the scaled variables. Linear statistics generalizes FCS, for example, by choosing the function $r(y)$ appropriately we can obtain both the number and index distribution problems:

$$r(y) = \begin{cases} \Theta(y+w)\Theta(w-y) & \text{Number statistics} \\ \Theta(w-y) & \text{Index distribution} \end{cases} \quad (5.51)$$

where $\Theta(y)$ is the Heaviside theta function. Linear statistics can be used to study the ground state properties of the system in arbitrary traps. It has been widely studied in both mathematics and physics [118, 119, 147, 148, 150, 151, 153, 181–198]. Interestingly, in the context of quantum transport [117–119, 147, 150, 151, 153, 181, 183, 184, 191, 192, 194, 195] using the random matrix theory approach the conductance ($r(y) = y$ [117]), Wigner time delay ($r(y) = y$ [153]) and shot noise ($r(y) = y(1-y)$ [150]) have also been computed.

In this section, we generalize the results to any arbitrary functions of $r(y)$. Clearly, the average value of $\langle s \rangle = \langle S_N \rangle / N$, in the large N limit, is given by

$$\langle s \rangle = \int_{-l_{\text{uc}}}^{l_{\text{uc}}} r(y) \rho_{\text{uc}}^*(y) dy, \quad (5.52)$$

with $\rho_{\text{uc}}^*(y)$ given explicitly in Eq. (2.18). Here, we would like to go beyond the mean $\langle s \rangle$ and compute the variance of s for all $k > 1$, which were recently computed for 1dOCP, $k = -1$ (jellium model) in Ref. [180] (see also Ref. [199]) and then extended to all long-ranged cases $k < 1$ in Ref. [46].

We follow the method used in Ref. [180]. We first compute the full distribution of s in the large N limit. This is done by adding an extra term $\mu_r(s) \left(\int_{-\infty}^{\infty} dy r(y) \rho_r(y) - s \right)$ in the energy function and then minimizing the energy by the saddle point method. Here $\mu_r(s)$ is the new Lagrange multiplier that enforces the value s of the linear statistics and hence $\mu_r(s)$ depends implicitly on s . The subscript ‘ r ’ represents the fact that the density

and the corresponding chemical potential should depend on the choice of the function $r(y)$. Consequently, the new saddle point density $\rho_r^*(y)$ satisfies the saddle point condition

$$\frac{y^2}{2} + \mu_r^*(s) r(y) + J\zeta(k)(k+1) (\rho_r^*(y))^k = \mu_k(s) \quad (5.53)$$

where $\mu_k^*(s)$ is the s -dependent Lagrange multiplier that enforces the normalization. For the sake of brevity, we omit the s dependence of μ_r^* and μ_k^* . Thus, the modified density is given by

$$\rho_r^*(y) = A_k \left(\mu_k^* - \frac{y^2}{2} - \mu_r^* r(y) \right)^{\frac{1}{k}}. \quad (5.54)$$

Consequently, the edges of the support, $-l_1(s)$ and $l_2(s)$, where the density vanishes, are determined by the two real roots of

$$\frac{l^2}{2} + \mu_r^* r(l) - \mu_k^* = 0. \quad (5.55)$$

The two Lagrange multipliers μ_r^* and μ_k^* are then fixed by the two conditions

$$\int_{-l_1(s)}^{l_2(s)} dy \rho_r^*(y) = 1, \quad \int_{-l_1(s)}^{l_2(s)} dy r(y) \rho_r^*(y) = s. \quad (5.56)$$

Clearly, when $s \rightarrow \langle s \rangle$, we have $\mu_r^* \rightarrow 0$ and $\mu_k^*(s) \rightarrow \mu_k^*(\langle s \rangle) = \mu_0 = l_{\text{uc}}^2/2$ and the density $\rho_r^*(y) \rightarrow \rho_0(y)$. We expect the distribution $\mathbb{P}(S_N = sN, N)$ in the large N limit to have a large deviation form

$$\mathbb{P}(S_N = sN, N) \asymp \exp[-N^{1+2\alpha_k} \Lambda(s)], \quad (5.57)$$

with the large deviation function given by

$$\Lambda(s) = G_r[\rho_r^*(y)] - G_{\text{uc}}, \quad (5.58)$$

where G_{uc} is given in Eq. (5.28) and the action $G_r[\rho_r^*(y)] = \mathcal{E}_k[\rho_r^*(y)]$ with $\mathcal{E}_k[\rho_r^*(y)]$ given in Eq. (2.16). The s dependence of $\rho_r^*(y)$ is implicit and comes from the second constraint in Eq. (5.56).

To compute the explicit expression for the LDF $\Lambda(s)$ [in Eq. (5.58)], we need to specify

the function $r(y)$. However, we can compute an approximate expression for $\Lambda(s)$ for a general function $r(y)$, when s is around its mean value $\langle s \rangle$ [Eq. (5.52)]. When we expand $\Lambda(s)$ [Eq. (5.58)] for $s = \langle s \rangle + \kappa$ with small κ , we find that

$$\Lambda(\langle s \rangle + \kappa) \approx \frac{\kappa^2}{2\sigma_r^2} \text{ with } \sigma_r^2 = \frac{\mathcal{J}_2\mathcal{J}_0 - \mathcal{J}_1^2}{\mathcal{J}_0}, \quad (5.59)$$

where the constants are

$$\mathcal{J}_0 = 2\frac{A_k}{k} \int_{-l_{\text{uc}}}^{l_{\text{uc}}} dy (l_{\text{uc}}^2 - y^2)^{\frac{1}{k}-1}, \quad \mathcal{J}_1 = 2\frac{A_k}{k} \int_{-l_{\text{uc}}}^{l_{\text{uc}}} dy r(y) (l_{\text{uc}}^2 - y^2)^{\frac{1}{k}-1} \quad (5.60)$$

$$\mathcal{J}_2 = 2\frac{A_k}{k} \int_{-l_{\text{uc}}}^{l_{\text{uc}}} dy r(y)^2 (l_{\text{uc}}^2 - y^2)^{\frac{1}{k}-1}. \quad (5.61)$$

The quadratic behavior of the LDF in Eq. (5.59) suggests that the typical fluctuations of S_N around its mean value behave like a Gaussian distribution given by [see Appendix A.7]

$$\mathbb{P}(S_N = (\langle s \rangle + \kappa)N, N) \asymp \exp\left(-\frac{N^2\kappa^2}{2\text{Var}_S}\right). \quad (5.62)$$

where the variance is given by

$$\text{Var}_S = \frac{N^{\nu_k}\sigma_r^2}{\beta}, \quad \text{with } \nu_k = \frac{2-k}{k+2}. \quad (5.63)$$

Note that the N dependence of the variance of the linear statistics is universal for any function $r(y)$. As mentioned previously, by construction, the linear statistic captures the behavior of number and index distribution. Using $r(y) = \Theta(y+w)\Theta(w-y)$ in Eq. (5.59), one can reproduce the variance of the ‘number’ problem as given in Eq. (5.34). Interestingly, unlike the short-range case, for the long-range case of Dyson’s log-gas ($k \rightarrow 0$) and the 1dOCP ($k = -1$), the behavior of the linear statistics for the smooth and non-smooth function $r(y)$ differ [40–42, 180, 181].

5.6 Conclusions

In summary, this study provides a detailed analysis of FCS of a confined short-range Riesz gas ($k > 1$) in equilibrium at temperatures $T \sim O(1)$ (where the entropy may be neglected). We focused on the number and the index distribution, which characterize the

fluctuations of the number of particles $\mathcal{N}(W, N)$ and $\mathcal{G}(W, N)$, respectively, in two distinct domains, namely $[-W, W]$ and $(-\infty, W]$. We found that the variance of the number of particles in a given domain scales with the system size as $\sim N^{\nu_k}$ with $\nu_k = (2-k)/(k+2)$. Our study is a major step forward in generalizing results of Dyson’s log-gas and the 1dOCP to a broader class of interacting particles *i.e.*, Riesz gas systems with $k > 1$. We also found that the distribution of the typical fluctuations of both quantities $\mathcal{N}(W, N)$ and $\mathcal{G}(W, N)$ around their mean values are Gaussian. These results are obtained by computing the large deviation function (LDF) associated with the distribution of these quantities.

We have employed a field theory method similar to the Coulomb gas method to compute the LDFs for two quantities $\mathcal{N}(W, N)$ and $\mathcal{G}(W, N)$. The method involves determining the saddle point density profiles conditioned on a given fraction of particles inside the specified domain. We found that for both cases (‘number’ and ‘index’), the saddle point density profiles possess discontinuities at the location of the boundary of the specified domain and exhibit three different kinds of profiles as either c or w is changed, such that it crosses the transition lines indicated in Fig. 5.2. These three types of configurations display interesting features – such as discontinuities and emergence of void regions. Our analytical results for the density profiles are in perfect agreement with numerical computations.

These density profiles are then utilized to calculate the LDFs $\Phi(c, w)$ and $\Psi(c, w)$ analytically for the number and index distributions, respectively. The density profiles determine the values of the LDFs in the respective parameter ranges. In particular, one finds that there exists an interesting regime of the parameter ($c \leq \bar{c}(w)$ for fixed w or $w > \bar{w}(c)$ for fixed c) in which the saddle point density profile contains a hole (devoid of particles) at the place of the discontinuity. The LDF corresponding to such density profiles undergoes a discontinuous change in the third-order derivative leading to a third-order phase transition. This transition is similar to the third-order transition observed in random matrix theory [25] and the 1dOCP [37]. Apart from exploring the non-analytic properties of the LDFs we have also discussed the various asymptotic forms of the LDF which allowed us to study well-known problems like hole formation probability or complete confinement probability. Additionally, the index problem provided a natural setting for studying the physical properties like the thermodynamic pressure and bulk

modulus.

Our analysis can be easily adapted to other traps of the form $U(x) = \frac{|x|^\delta}{\delta}$. The results obtained for these generic traps closely resemble those obtained for the harmonic trap with $\delta = 2$. Specifically, it is observed that the fluctuations of the number of particles in the domain $[-W, W]$ or $(-\infty, W]$ are Gaussian and the variance again scales with N as $\sim N^{\nu_k}$. However, now the exponent gets interestingly modified to $\nu_k = 1 - \alpha_k \delta = (\delta + k - k\delta)/(k + \delta)$. Moreover, we found that for any $\delta > 0$ the non-analytic properties of the LDF remain the same, still displaying the third-order phase transition.

This chapter describes the study from the following published work, Ref. [61]: **J. Kethepalli**, M. Kulkarni, A. Kundu, S. N. Majumdar, D. Mukamel, G. Schehr, “Full counting statistics of 1d short range Riesz gases in confinement” [Journal of Statistical Mechanics: Theory and Experiment \(2024\) 083206](#)

In the last three chapters 3, 4 and 5, we studied the equilibrium properties of the Riesz gas at low temperatures $T \lesssim O(L_N^2)$, where L_N is given in Eq. (2.6). In the next chapter, we will study the equilibrium properties at high temperatures for the hard rod gas and the Hyperbolic Calogero model. The hard rod model corresponds to the Riesz gas with $k \rightarrow \infty$, as the interaction between the i -th and j -th particle in the $k \rightarrow \infty$ limit becomes

$$\lim_{k \rightarrow \infty} \left(\frac{|x_i - x_j|}{J^{\frac{1}{k}}} \right)^{-k} = \Theta(|x_i - x_j| - 1) \quad \text{where} \quad \Theta(r - 1) = \begin{cases} \infty, & \text{if } r < 1 \\ 0, & \text{otherwise} \end{cases}.$$

This is a model for hard rods of unit length which is an integrable model in the absence of confinement. On the other hand, the particles of the Hyperbolic Calogero model interact via a repulsive potential of the form $\sinh(r)^{-2}$, where r is the interparticle distance. At very high densities when $r \ll 1$ the interaction $\sinh(r)^{-2} \sim r^{-2}$, which corresponds to the Riesz gas with $k = 2$. Consequently, the field theory for the Hyperbolic Calogero model is the same as the Riesz gas with $k = 2$. Both these models are integrable in the absence of any confinement. However, generic confinement like $U(x) = x^\delta$ breaks the integrability of both models. So it raises a natural question: what are the equilibrium properties of integrable systems in integrability-breaking confinement? In the next chapters, we will study the density profile of the hard rod gas and the Hyperbolic Calogero model in a harmonic and quartic trap when the system is assumed to be in Gibbs equilibrium.

Chapter 6

Finite temperature equilibrium density profiles of integrable systems in confining potentials

6.1 Introduction

Integrable classical systems [200–202] have a macroscopic number of constants of motion that are in involution with each other. In phase space, these systems (i) have regular periodic orbits (invariant torus), (ii) are characterized by zero Lyapunov exponents, and (iii) generally resist thermalization to a Gibbs state. However, many-body integrable systems are also believed to be extremely fragile in the presence of external perturbations and become nonintegrable, ergodic, and chaotic, retaining only a few constants of motion [203]. Consequently, integrable systems are rare, and nonintegrability arising due to imperfections dominates the natural world. For example, most experiments [78, 204, 205] are performed in confining potentials where we expect that integrability will be lost and thermalization to occur. Recent theoretical studies have addressed thermalization and transport in such trapped integrable models [84, 85, 206–211]. To study thermalization, one needs to have a clear understanding of the thermal equilibrium state. One simple characterization is to look at the equilibrium density profile of the particles in the trap which is the most commonly measured quantity in experiments [96, 212, 213].

In this work, we focus on the equilibrium density profile of two one-dimensional short-range integrable classical models in the presence of integrability-breaking external po-

tentials. The integrable models considered here are the gas of hard rods [33] and the hyperbolic Calogero model [14, 214, 215]. The external trap potential keeps the particles spatially confined and breaks integrability. Such systems have been studied recently and many surprising results have been reported. For example, the gas of hard rods [84] and the Lieb-Liniger model [85] in the harmonic trap were investigated. It was found that these systems do not thermalize even in the presence of the harmonic trap. Under out-of-equilibrium conditions, drastically slow relaxations to a non-equilibrium steady state and large finite size effects have also been observed for the Toda model with harmonic (harmonic) pinning potential [206, 209]. In another recent work [216], a similar observation was made for the nonlinearly perturbed Toda model and a universal scaling of the thermalization time has been reported. Studies of the integrable Calogero model in the presence of external confining potentials have also been undertaken in recent times, see for example, Refs. [208, 211, 217–219].

The equilibrium properties of trapped interacting particles have recently been studied where field theoretic techniques are used to compute the equilibrium density profiles and fluctuations [22, 25, 45, 59, 60, 92, 220]. Here we adapt these field theoretic procedures to study the equilibrium properties of hard rods and the hyperbolic Calogero system in the presence of external trapping potentials. The field theory presented here predicts quite accurately the equilibrium density profile of these two models, and their scaling with system size and temperature, as obtained from Monte-Carlo (MC) simulations.

The paper is organized as follows. We describe the models and definitions in Sec. 6.2. Thereafter, in Sec. 6.3, we present the field theory for the hard rod gas and the hyperbolic Calogero model in both harmonic and quartic traps. In Sec. 6.4 we compute the densities and extract their scaling with system size and temperature for (i) hard rods gas in Sec. 6.4.1 and (ii) hyperbolic Calogero model in Sec. 6.4.2. We verify the analytical results using Monte Carlo (MC) simulations. We summarize the main results in Sec. 6.5 and end with a discussion of open questions in such integrability broken classical systems. The Appendix is organized as follows. In Appendix A.8, we derive the field theory for (i) hard rod gas and (ii) hyperbolic Calogero model in external confining traps. In Appendix A.9, we compute the analytical form of the densities for low and high values of the temperature.

6.2 Models and definitions

We study two short-range models given by a Hamiltonian of the form

$$H(\{x_i, p_i\}) = \sum_{i=1}^N \left[\frac{p_i^2}{2m} + U_\delta(x_i) \right] + \frac{1}{2} \sum_{i=1}^N \sum_{\substack{j=1 \\ j \neq i}}^N V(x_i - x_j), \quad (6.1)$$

where $\{x_i, p_i\}$ are the position and momentum of the i^{th} particle ($1 \leq i \leq N$), each of mass m which we set to unity. The second term on the right-hand side of Eq. (6.1) is the external potential

$$U_\delta(x) = \frac{x^\delta}{\delta}, \quad (6.2)$$

which we take to be of harmonic ($\delta = 2$) or quartic ($\delta = 4$) form. The third term in Eq. (6.1) is the interaction term, which for hard rods (HR) of length a is

$$V_R(r) = \begin{cases} 0 & \text{for } r > a \\ \infty & \text{for } r \leq a. \end{cases} \quad (6.3)$$

Note that in Eq. (6.3) the subscript ‘ R ’ in $V_R(r)$ stands for the hard rods gas. For the hyperbolic Calogero (HC) model each particle is coupled to every other particle in the system with the interaction potential

$$V_C(r) = \frac{J}{\sinh^2 |r|}. \quad (6.4)$$

In Eq. (6.4), the subscript ‘ C ’ in $V_C(r)$ stand for the hyperbolic Calogero model and $J > 0$ is the strength of the repulsive interaction.

We consider these systems to be in their respective thermal equilibrium states described by the canonical Gibbs distribution

$$P(\{x_i, p_i\}) = \frac{e^{-\beta H(\{x_i, p_i\})}}{Z_\beta(N)}, \quad (6.5)$$

where $\beta = 1/T$ is the inverse temperature and $Z_\beta(N)$ is the partition function. We are

interested in the spatial density profile

$$\rho(x) = \sum_{i=1}^N \langle \delta(x - x_i) \rangle_{\beta}, \quad (6.6)$$

where $\langle \dots \rangle_{\beta}$ denotes the average over the thermal distribution given in Eq. (6.5). In particular, we will examine the dependence of the density profile $\rho(x)$ on system parameters, such as the number of particles N and the temperature T . In the following sections, we address these questions using field theory and MC simulations.

6.3 Field theory formalism

To obtain the thermal properties one needs to compute the partition function $Z_{\beta}(N)$ which is generally a hard task in microscopic variables. Therefore often one resorts to a field theoretic (macroscopic) approach to compute $Z_{\beta}(N)$. In this method, the partition function is written as a functional integral over density fields. This procedure has been commonly used in several contexts such as Landau theory [221], random matrix theory [22], general Coulomb gas [128], and long-range interacting particles [45, 50]. Despite this progress, there have been only a few rigorous comparisons between densities and other equilibrium properties obtained from microscopic and macroscopic (field theory) computation [45, 59, 60, 92, 220, 222].

In this section, we describe a macroscopic procedure and construct a field theory adapted appropriately for our models. We start with the partition function

$$Z_{\beta}(N) = \int_{-\infty}^{\infty} \prod_{i=1}^N dp_i \int_{-\infty}^{\infty} \mathbf{d}\mathbf{x}_N \exp(-\beta H(\{x_i, p_i\})), \text{ where} \\ \int_w^z \mathbf{d}\mathbf{x}_N \equiv \int_w^z dx_1 \int_{x_1}^z dx_2 \dots \int_{x_{N-1}}^z dx_N. \quad (6.7)$$

Since the position and momentum variables are uncoupled, the partition function reduces to

$$Z_{\beta}(N) = Z_{\beta}^{(\mathcal{K})}(N) Z_{\beta}^{(C)}(N), \quad (6.8)$$

where the configurational contribution to the partition function is given by

$$Z_{\beta}^{(c)}(N) = \int_{-\infty}^{\infty} \mathbf{d}\mathbf{x}_N \exp\left(-\beta \left[\sum_{i=1}^N U_{\delta}(x_i) + \frac{1}{2} \sum_{i=1}^N \sum_{\substack{j=1 \\ j \neq i}}^N V(x_i - x_j) \right]\right), \quad (6.9)$$

and contribution due to kinetic terms is

$$Z_{\beta}^{(K)}(N) = \left(\frac{2\pi}{\beta}\right)^{N/2}. \quad (6.10)$$

Performing the multiple integrals in Eq. (6.9) is a hard problem. However, for (i) short-range repulsive interactions that diverge at vanishing separation, and (ii) slowly varying confining potentials, one can approximate the full partition function as follows.

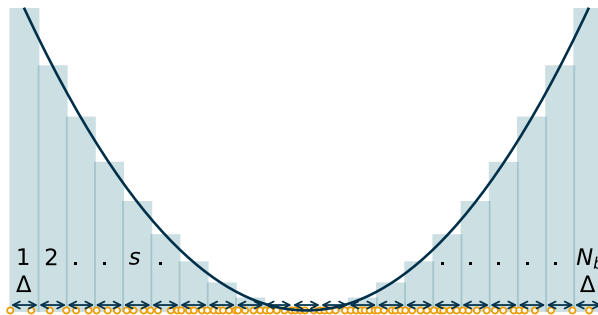


Figure 6.1: A schematic representation for partitioning the system into N_b subsystems, each of size Δ . Here $s = 1, 2, \dots, N_b$ denotes the subsystem index. Note that the particles are represented by orange circles. In the s^{th} subsystem there are n_s particles. The double arrow indicates the extent of each subsystem. While analyzing each subsystem we take large- n_s and then for the complete system, we finally take the small- Δ limit.

We divide the system into N_b subsystems, as shown in Fig. 6.1, where each subsystem s contains a large number of particles n_s . Note that the size of each subsystem, denoted by Δ , is small enough compared to the actual size of the gas and large enough to contain many particles such that the change in potential energy between two successive boxes is smaller than thermal energy T i.e., $|V_{\text{ext}}(x_{s+1}) - V_{\text{ext}}(x_s)| < T$. The particles in each subsystem experience an effective constant potential that depends on the location of the subsystem x_s inside the trap. The partition function $Z_{\beta}^{(c)}(N)$ in Eq. (6.9) can be approximated (in the thermodynamic limit) as the product of the partition functions of

these boxes,

$$Z_\beta^{(c)}(N) \approx \exp \left(\sum_{s=1}^{N_b} \log [Z_\beta(n_s, x_s, \Delta)] \right), \quad (6.11)$$

where the partition function of the s^{th} subsystem of size Δ , centered around x_s containing n_s particles is given by

$$Z_\beta(n_s, x_s, \Delta) = \int_{x_s - \frac{\Delta}{2}}^{x_s + \frac{\Delta}{2}} \mathbf{d}\mathbf{x}_{n_s} \prod_{i=1}^{n_s} \exp \left(-\beta U_\delta(x_i) \right) \prod_{\substack{i,j=1 \\ j \neq i}}^{n_s} \exp \left(-\beta \left[\frac{1}{2} V(x_i - x_j) \right] \right) \quad (6.12)$$

The free energy per particle in the s^{th} box is given by

$$f(x_s, \beta) = -\frac{1}{\beta n_s} \log [Z_\beta(n_s, x_s, \Delta)]. \quad (6.13)$$

We convert the summation in Eq. (6.11) over subsystem index s to an integral over x and get [see Appendix A.8]

$$\mathcal{F}[\rho(x), \beta] = \int_{-\infty}^{\infty} dx \rho(x) f(x, \beta). \quad (6.14)$$

where $\rho(x)$ is the density of particles at position x . The free energy per particle $f(x_s, \beta)$ defined in Eq. (6.13) can be computed from the partition function of the subsystem. As mentioned earlier, we assume that the subsystem size Δ is small enough such that all the n_s particles with position x_i (where $i = 1, 2, \dots, n_s$), experience a constant potential $U_\delta(x_i) \approx U_\delta(x_s)$. The subsystem partition function can then be approximated as

$$Z_\beta(n_s, x_s, \Delta) \approx \exp \left(-\beta n_s U_\delta(x_s) \right) \left[\int_{x_s - \frac{\Delta}{2}}^{x_s + \frac{\Delta}{2}} \mathbf{d}\mathbf{x}_{n_s} \prod_{\substack{i,j=1 \\ j \neq i}}^{n_s} \exp \left(-\beta \left[\frac{1}{2} V(x_i - x_j) \right] \right) \right]. \quad (6.15)$$

Note that, in Eq. (6.15), the x_i is a running integration variable not to be confused with the position of the center of the subsystem x_s . The contribution to the free energy per

particle from the s^{th} box is written as

$$f(x_s, \beta) = U_\delta(x_s) + f_{\text{int}}(x_s, \beta), \quad (6.16)$$

where

$$f_{\text{int}}(x_s, \beta) = -\frac{1}{\beta n_s} \log \left(\int_0^\Delta \mathbf{d}\mathbf{x}_{n_s} \prod_{\substack{i,j=1 \\ j \neq i}}^{n_s} \exp \left[-\frac{\beta}{2} V(x_i - x_j) \right] \right). \quad (6.17)$$

From Eq. (6.17) one can further rewrite $f_{\text{int}}(x_s, \beta) \equiv f_{\text{int}}(\rho(x_s), \beta)$. Furthermore, using Eq. (6.17) we can rewrite Eq. (6.14) as [see Appendix A.8]

$$\mathcal{F}[\rho, \beta] = \int_{-\infty}^{\infty} dx \rho(x) \left\{ U_\delta(x) + f_{\text{int}}(\rho(x), \beta) \right\}. \quad (6.18)$$

For the HR and the HC models the explicit forms of the free energy are derived in Appendix A.8.1 and Appendix A.8.2 respectively.

The average thermal density can then be computed by extremizing the free energy in Eq. (6.18) with the constraint that the density is normalized

$$\int_{-\infty}^{\infty} dx \rho(x) = N. \quad (6.19)$$

In the next section, we compute these densities for both HR and HC models and compare them with MC simulations.

6.4 Results from field theory and comparison with Monte-Carlo simulations

In this section, we adapt the field theory formalism discussed in Sec. 6.3 for the case of hard rods (HR) and hyperbolic Calogero (HC) model to compute the free energy. We extremize the obtained free energy along with the constraint that the density is normalized and this yields the average density profile.

6.4.1 Hard rods model

For the HR model, the contribution due to interaction to the free energy per particle at position x is given by (see Appendix A.8.1)

$$f_{\text{int}}(\rho(x), \beta) = -\frac{1}{\beta} \log \left(\frac{1 - a \rho(x)}{\rho(x)} \right) + \frac{1}{\beta}. \quad (6.20)$$

Using Eq. (6.20) in Eq. (6.18) we get the free energy for the HR model [ignoring the density-independent term $1/\beta$ in Eq. (6.20)]

$$\mathcal{F}_R[\rho(x), \beta] = \int_{-\infty}^{\infty} dx \rho(x) \left[U_\delta(x) - \frac{1}{\beta} \log \left(\frac{1 - a \rho(x)}{\rho(x)} \right) \right]. \quad (6.21)$$

The free energy in Eq. (6.21) is super-extensive i.e., $\mathcal{F}_R[\rho(x), \beta] \sim O(N^{\delta+1})$ since the ground state energy of N hard rods in a confining potential $U_\delta(x) \sim x^\delta$ scales as $N^{\delta+1}$. Therefore, the average thermal density $\rho^*(x, T)$ can be computed via saddle point approximation [45]. This amounts to extremizing the free energy along with the normalization constraint

$$\left. \frac{\delta}{\delta \rho(x)} \mathcal{F}_R[\rho(x), \beta] \right|_{\rho(x)=\rho^*(x, T)} = \mu_N(\beta), \quad (6.22)$$

where the chemical potential $\mu_N(\beta)$ is temperature dependent and can be extracted from the normalization condition given in Eq. (6.19). Using Eq. (6.21) in Eq. (6.22) we get

$$\mu_N(\beta) = U_\delta(x) - T \left[\log \left(\frac{1 - a \rho^*(x, T)}{\rho^*(x, T)} \right) - \frac{1}{1 - a \rho^*(x, T)} \right]. \quad (6.23)$$

To obtain the system size dependence of the density profile, we define

$$\rho_N(x, T) = \frac{1}{N} \rho^*(x, T), \quad (6.24)$$

such that

$$\int_{-\infty}^{\infty} dx \rho_N(x, T) = 1. \quad (6.25)$$

Using Eq. (6.24), Eq. (6.23) can then be expressed as

$$\mu_N(\beta) = U_\delta(x) - T \left[\log \left(\frac{1 - a N \rho_N(x, T)}{N \rho_N(x, T)} \right) - \frac{1}{1 - a N \rho_N(x, T)} \right]. \quad (6.26)$$

To extract the system size (N) and temperature (T) dependence of the density $\rho_N(x, T)$ we substitute the following scaling form ansatz

$$\rho_N(x, T) = N^{-\alpha_R} \rho_R(y, c), \quad \mu_N(\beta) = N^{\lambda_R} \mu_R(c), \quad (6.27)$$

with the scaled variables given by

$$y = \frac{x}{N^{\alpha_R}}, \quad c = \frac{T}{N^{\gamma_R}}, \quad (6.28)$$

in Eq. (6.26). Here α_R and γ_R are scaling exponents which are determined by requiring that Eq. (6.26) is N independent in the scaled variables. Doing so we get

$$\alpha_R = 1, \quad \gamma_R = \delta \quad \text{and} \quad \lambda_R = \delta. \quad (6.29)$$

The value $\alpha_R = 1$ can be understood from the $O(N)$ extent of the density profile at zero temperature. This leads to $O(N^{\delta+1})$ energy of the system in the ground state. For the entropy term to contribute to the free energy one needs to scale the temperature by N^δ implying $\gamma_R = \delta$. Eq. (6.26) finally becomes

$$\mu_R(c) = \frac{y^\delta}{\delta} - c \left[\log \left(\frac{1 - a \rho_R(y, c)}{\rho_R(y, c)} \right) - \frac{1}{1 - a \rho_R(y, c)} \right]. \quad (6.30)$$

It is worth noting that the thermal equilibrium properties of hard rods in an external potential were studied in Ref. [223]. Eq. (6.30) can be obtained from Eq. [13] of Ref. [223] when the density is assumed to vary slowly on the rod length scale a . Since Eq. (6.30) is a transcendental equation, it is difficult to obtain an exact solution. We solve Eq. (6.30) numerically by fixing $\mu_R(c)$ such that the normalization constraint,

$$\int_{-\infty}^{\infty} dy \rho_R(y, c) = 1, \quad (6.31)$$

is satisfied. In Fig. 6.2 we show the comparison between the scaled density profile [obtained by solving Eq. (6.30)] and data from MC simulations (using the standard Metropolis algorithm) for three rescaled temperatures $c = 0.1, 1.0, 10.0$ and three system sizes $N = 32, 64, 128$. We find quite remarkable scaling collapse of the MC data with system size which also agrees with the field theory results for both the harmonic ($\delta = 2$) and quartic ($\delta = 4$) traps.

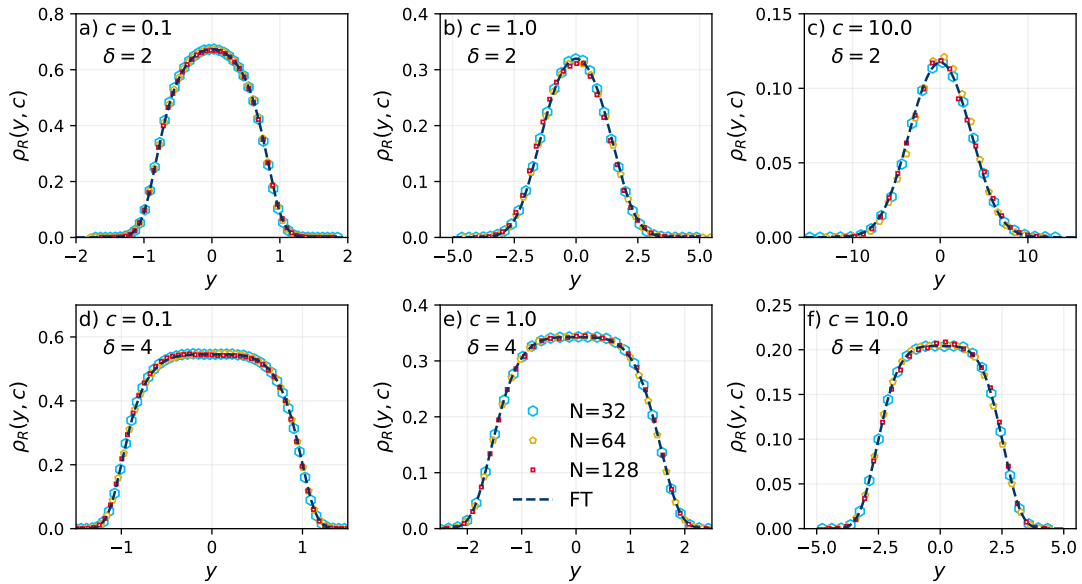


Figure 6.2: Comparison of scaled equilibrium density profiles $\rho_R(y, c)$, obtained from Monte-Carlo simulations with field theory [Eq. (6.30)] denoted by ‘FT’, for the HR model with [(a)-(c)] harmonic trap ($\delta = 2$) and [(d)-(f)] quartic trap ($\delta = 4$). We show Monte-Carlo data for three values of c : $c = 0.1$, $c = 1.0$ and $c = 10.0$, for $N = 32, 64, 128$. Here the scaled variables are related to the unscaled variables as $y = x/N$ and $c = T/N^\delta$ as given in Eq. (6.28).

Although the explicit analytical solution of the saddle point given in Eq. (6.30) is highly nontrivial to obtain, one can study the behavior of the density for low $c \ll 1$ and high $c \gg 1$ analytically using asymptotic analysis (see Appendix A.9.1). At zero temperature the hard rods have a density profile given by

$$\rho_R(y, 0) = \begin{cases} \frac{1}{a} & \text{for } y \leq \left| \frac{a}{2} \right| \\ 0 & \text{for } y > \left| \frac{a}{2} \right|. \end{cases} \quad (6.32)$$

The density profile at low temperatures can then be approximated as

$$\rho_R(y, c) \stackrel{c \ll 1}{\approx} \rho_R(y, 0) + \rho_1(y, c), \quad (6.33)$$

where the deviation from the zero temperature density up to the first iteration (see Appendix A.9.1 for more details) is given by

$$\rho_1(y, c) \approx \begin{cases} -\frac{1}{a} \frac{c \delta}{(y_c^\delta - y^\delta)} & \text{for } |y| < y_c - O(c) \\ \rho_R^* (1 - a \rho_R^*)^2 \times \\ \quad \left(1 - \exp \left[-\frac{y_c^\delta - y^\delta}{c \delta} \right] \right) & \text{for } |y - y_c| < O(c) \\ \frac{1}{e} \exp \left(\frac{y_c^\delta - y^\delta}{c \delta} \right) & \text{for } |y| > y_c + O(c). \end{cases} \quad (6.34)$$

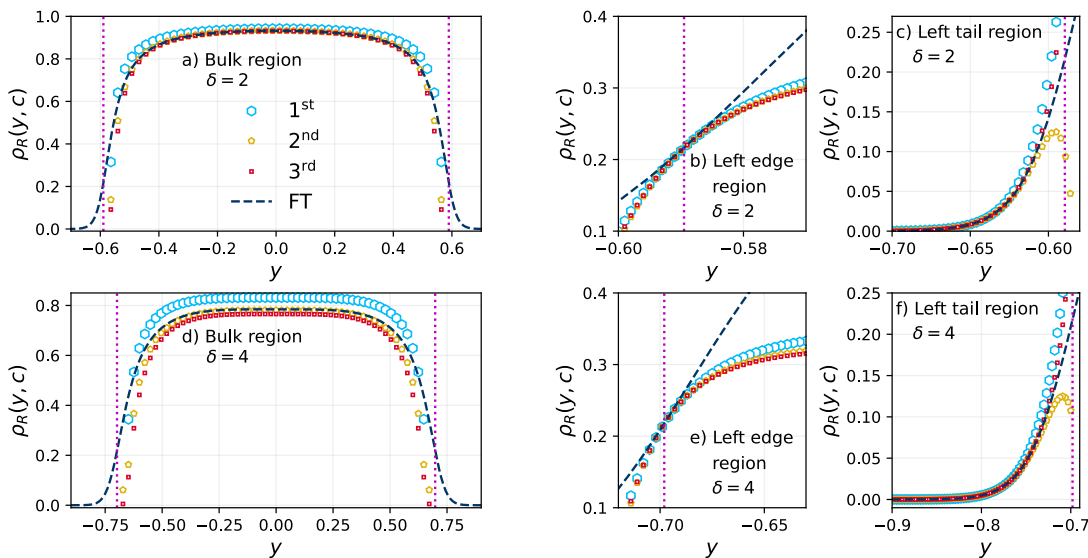


Figure 6.3: A comparison of the asymptotic densities up to the third iteration (see Appendix A.9.1) with the densities obtained from the numerical solution of Eq. (6.30), denoted by ‘FT’, at low temperature $c = 0.01$ for the HR model in [(a)-(c)] harmonic trap ($\delta = 2$) and [(d)-(f)] quartic trap ($\delta = 4$) shows the densities for hard rods confined to harmonic trap ($\delta = 2$). Here [(a),(d)] show the bulk ($|y| < y_c - O(c)$), [(b),(e)] edge ($|y - y_c| \lesssim O(c)$) and [(c),(f)] tail ($|y| > y_c + O(c)$) regions. The vertical dotted line represents the position $y = y_c$ given in Eq. (6.35) and this determines these three regions.

Here y_c is the position at which the term in the parenthesis of Eq. (6.30) changes sign and is given by

$$y_c = (\mu_R \delta)^{\frac{1}{\delta}}. \quad (6.35)$$

The density at $y = y_c$ is denoted by

$$\rho_R^* = \rho_R(y_c, c). \quad (6.36)$$

Note that y_c given in Eq. (6.35) determines the three regions (see Appendix A.9.1) (i) bulk region where $|y| < y_c - O(c)$, (ii) edge region where $|y - y_c| \lesssim O(c)$, and (iii) tail region where $|y| > y_c + O(c)$, which are displayed in Eq. (6.34). The higher-order corrections have also been computed and are presented in Appendix A.9.1. The expression Eq. (6.33) is verified with the numerical solution of Eq. (6.30) for $c = 0.01$ in Fig. 6.3 showing the three regions. For this comparison, the value of the chemical potential $\mu_R(c)$ is taken from Fig. 6.4. Note that in Fig. 6.4 the behavior of $\mu_R(c)$ is non-monotonic: it increases initially as c is increased from zero and thereafter decreases. This nonmonotonicity can be explained by noting that at smaller c , particles can only be added to the edges of the system which requires more energy (owing to the confining potential), without a large increase in entropy. Hence $\mu_R(c)$ increases initially. However, for larger c , the gas expands and this opens up gaps, larger than the size of the rods, between the particles in the bulk of the system. Consequently, one can easily add an extra rod with a small energy cost and a large entropy gain, essentially lowering the free energy change. Hence $\mu_R(c)$ decreases with c for larger c .

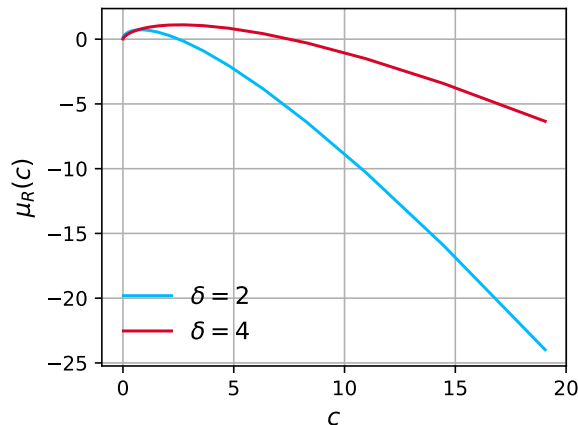


Figure 6.4: Chemical potential, $\mu_R(c)$, for the HR model obtained using Eq. (6.30) and Eq. (6.31), plotted as a function of the rescaled temperature c for harmonic trap with $\delta = 2$ (blue) and quartic trap with $\delta = 4$ (red). At large values of c the chemical potential is negative and diverges.

In the high temperature regime ($c \gg 1$) the spread of the gas increases which in turn dilutes the gas i.e., $\rho_R(y, c) \ll 1$. Using this low-density approximation in Eq. (6.30),

we obtain the approximate analytical expression of the density profile (up to the first iteration), given by (see Appendix A.9.1)

$$\rho_R(y, c) \stackrel{c \gg 1}{\approx} \frac{1}{e} \exp\left(\frac{\mu_R(c)}{c} - \frac{y^\delta}{c\delta}\right), \quad (6.37)$$

where the chemical potential $\mu_R(c)$ is obtained numerically by solving Eq. (6.30) along with the normalization condition [Eq. (6.31)] as shown in Fig. 6.4 and $e = 2.71828$ is the Euler's number. We can obtain higher order terms of the density by also considering subdominant corrections originating due to the presence of interaction as shown in Appendix A.9.1. The expression Eq. (6.37) and the subdominant corrections (up to third order) are verified with the numerical solution of Eq. (6.30) for both traps in Fig. 6.5 for $c = 10.0$.

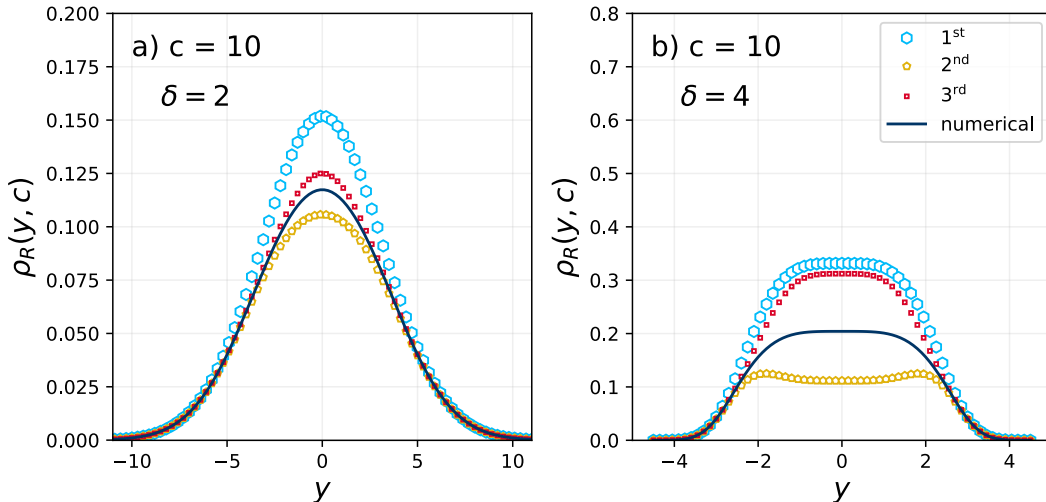


Figure 6.5: Comparison of the asymptotic densities up to third order (see Appendix A.9.1) with the numerical solution of Eq. (6.30), denoted by ‘FT’, at high temperature $c = 10.0$ for the HR model confined to (a) harmonic trap ($\delta = 2$) and (b) quartic trap ($\delta = 4$).

6.4.2 Hyperbolic Calogero model

Unlike the hard rods (HR) model, for the hyperbolic Calogero (HC) model, each particle is coupled to all the other particles. The field theoretic formulation of the hyperbolic Calogero model has been studied [219]. However, the average thermal density profiles at finite temperatures have not been computed yet. Based on the approximate scheme outlined in Sec. 6.3 and the approach described in Refs. [45, 92, 224], we compute the

finite temperature density profiles for the hyperbolic Calogero model below. The free energy in this case is given by (see Appendix A.8.2)

$$\mathcal{F}_C[\rho(x), \beta] = \int_{-\infty}^{\infty} dx \rho(x) \left[U_\delta(x) + J\zeta(2)\rho(x)^2 + \frac{1}{\beta} \log[\rho(x)] \right], \quad (6.38)$$

where $\zeta(k) = \sum_{n=1}^{\infty} n^{-k}$ is the Riemann Zeta function. Note that, despite the all-to-all coupling, the contribution to the free energy per particle due to interactions gets renormalized to a local term in the density field, and is given by

$$f_{\text{int}}(\rho(x), \beta) = J\zeta(2)\rho(x)^2 + \frac{1}{\beta} \log \rho(x). \quad (6.39)$$

Here $\beta^{-1} \log \rho(x)$ is the contribution due to the configurational entropy. To compute the average thermal density $\rho^*(x, T)$, we extremize the free energy functional given in Eq. (6.38) along with the normalization condition [Eq. (6.19)] which gives the chemical potential

$$\mu_N(\beta) = U_\delta(x) + 3\zeta(2)\rho^*(x, T)^2 + T \left(1 + \log[\rho^*(x, T)] \right). \quad (6.40)$$

As in the case of the HR model, to obtain a scaling form for the density profile, we use the density normalized to unity $\rho_N(x, T) = \rho^*(x, T)/N$ in Eq. (6.40) and get

$$\mu_N(\beta) = U_\delta(x) + 3\zeta(2)N^2\rho_N(x, T)^2 + T \left(1 + \log[N\rho_N(x, T)] \right). \quad (6.41)$$

We can extract the system size (N) and temperature (T) dependence of the density $\rho_N(x, T)$ by substituting the scaling form ansatz

$$\rho_N(x, T) = N^{-\alpha_C} \rho_C(y, c), \quad \mu_N(\beta) = \mu_C(c)N^{\lambda_C}, \quad (6.42)$$

with the scaled variables

$$y = \frac{x}{N^{\alpha_C}}, \quad c = \frac{T}{N^{\gamma_C}}, \quad (6.43)$$

in Eq. (6.41). Here α_C and γ_C are scaling exponents which are determined by requiring that Eq. (6.41) is N independent for large- N and depends only on the scaling variables.

Doing so, we get

$$\alpha_C = \frac{2}{2 + \delta}, \quad \gamma_C = \frac{2\delta}{2 + \delta} \quad \text{and} \quad \lambda_C = \frac{2\delta}{2 + \delta}. \quad (6.44)$$

The value $\alpha_C = 2/(2 + \delta)$ can be understood from the $O(N^{\frac{2}{2+\delta}})$ extent of the gas at zero temperature [45]. This leads to $O(N^{\alpha_C\delta+1})$ energy of the system in the ground state. For the entropy term to contribute to the free energy one needs to scale the temperature by $N^{\alpha_C\delta}$ implying $\gamma_C = \alpha_C\delta$. Eq. (6.41) finally becomes

$$\mu_C(c) = \frac{y^\delta}{\delta} + 3\zeta(2)\rho_C(y, c)^2 + c \log \rho_C(y, c). \quad (6.45)$$

We solve Eq. (6.45) numerically by fixing $\mu_C(c)$ such that the normalization constraint,

$$\int_{-\infty}^{\infty} dy \rho_C(y, c) = 1, \quad (6.46)$$

is satisfied. In Fig. 6.6, we show the comparison between the scaled density profile obtained by solving Eq. (6.45) and data from MC simulations for $c = 0.1, 1.0, 10.0$. We observe good agreement albeit with some small discrepancies, the origin of which is not understood clearly at present. The value of the chemical potential $\mu_C(c)$ is obtained as a function of c by numerically solving Eq. (6.45) subject to the normalization condition Eq. (6.46), which is shown in Fig. 6.7. Unlike the HR model, we find that $\mu_C(c)$ decreases monotonically in this case.

Similar to the HR case, obtaining the exact solution of Eq. (6.45) is highly nontrivial for an arbitrary c . However, we can study the average thermal density profiles using asymptotic analysis for small $c \ll 1$ and large $c \gg 1$ (see Appendix A.9.2). At zero temperature, $c = 0$, the density is exactly known and is governed by the interaction term only, since the contribution to the free energy from the entropy is zero. The zero temperature density is given by [45, 92]

$$\rho_C(y, 0) = \begin{cases} A_\delta (l^\delta - y^\delta)^{\frac{1}{2}} & \text{for } |y| < l \\ 0 & \text{for } |y| > l, \end{cases} \quad (6.47)$$

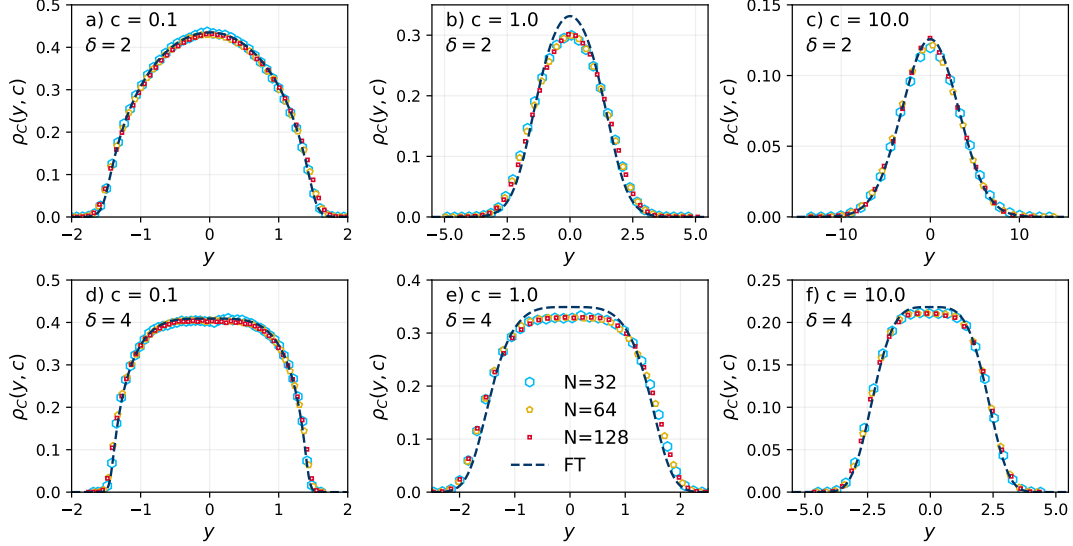


Figure 6.6: Comparison of scaled equilibrium density profiles $\rho_C(y, c)$, obtained from Monte-Carlo simulations with field theory [Eq. (6.45)], denoted by ‘FT’, for the HC model with [(a)-(c)] harmonic trap ($\delta = 2$) and [(d)-(f)] quartic trap ($\delta = 4$). We show MC data for three values of c : $c = 0.1$, $c = 1.0$ and $c = 10.0$, for $N = 32, 64, 128$. Here the scaled variables are related to the unscaled variables as $y = x/N^{\alpha_C}$ and $c = T/N^{\gamma_C}$, where α_C and γ_C are given in Eq. (6.44).

where

$$A_\delta = [3\delta\zeta(2)]^{-\frac{1}{2}} \quad (6.48)$$

and the edge of the support of the density is given by

$$l = \left(\mu_C(0)\delta\right)^{\frac{1}{\delta}} = \left(\frac{\delta}{2A_\delta\text{B}\left(\frac{1}{\delta}, \frac{3}{2}\right)}\right)^{\frac{2}{2+\delta}}, \quad (6.49)$$

with

$$\text{B}(x, y) = \int_0^1 dr r^{x-1}(1-r)^{y-1}, \quad (6.50)$$

being the Beta function. $\mu_C(0)$ in Eq. (6.49) is the scaled chemical potential at zero temperature, obtained by imposing the normalization condition [Eq. (6.46)], and is given by

$$\mu_C(0) = \frac{l^\delta}{\delta} = \left(\frac{\pi}{2}\right)^{\frac{\delta}{\delta+2}} \left(\frac{\delta^{-1/\delta}\Gamma\left(\frac{3}{2} + \frac{1}{\delta}\right)}{\Gamma\left(1 + \frac{1}{\delta}\right)}\right)^{\frac{2\delta}{\delta+2}}, \quad (6.51)$$

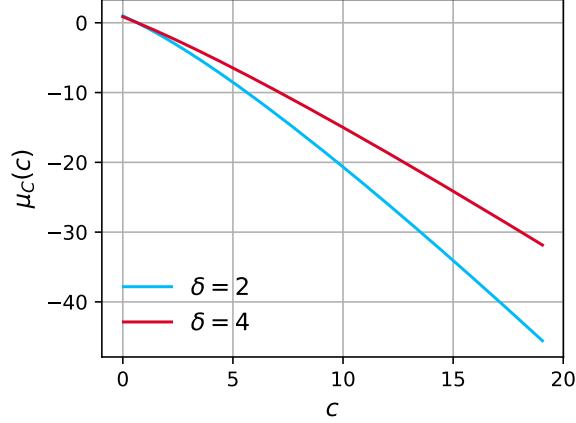


Figure 6.7: Chemical potential $\mu_C(c)$ for HC model, computed by using Eq. (6.45) along with the normalization condition Eq. (6.46), plotted as a function of the rescaled temperature c for harmonic trap with $\delta = 2$ (blue) and quartic trap with $\delta = 4$ (red). At large values of c the chemical potential is negative and diverges.

where

$$\Gamma[n] = \int_0^{\infty} dx x^{n-1} e^{-x}, \quad (6.52)$$

is the Gamma function.

For $c \neq 0$, the entropy starts contributing to the density. As the rescaled temperature is increased from zero, i.e., $c \ll 1$, we can obtain the approximate analytical form of the density profile, as shown in the Appendix A.9.2, which is given by

$$\rho_C(y, c) \stackrel{c \ll 1}{\approx} \rho_C(y, 0) + \rho_1(y, c). \quad (6.53)$$

Here the deviation from zero temperature density (up to the first iteration) is given by

$$\rho_1(y, c) \approx \begin{cases} \rho_C(y, 0) \times \\ \frac{\mu_C(c) - \mu_C(0) - c \log \rho_C(y, 0)}{c + 6\zeta(2)\rho_C(y, 0)^2}, & \text{for } |y| < y_c - O(c), \\ \frac{\rho_C^*(y_c^\delta - y^\delta)}{\delta(c + 6\zeta(2)\rho_C^{*2})} & \text{for } |y - y_c| < O(c), \\ \exp\left(\frac{y_c^\delta - y^\delta}{c^\delta}\right) & \text{for } |y| > y_c + O(c), \end{cases} \quad (6.54)$$

and the higher order corrections are provided in Appendix A.9.2. Similar to the HR model, here $y_c = (\mu_C(c)\delta)^{\frac{1}{\delta}}$ and $\rho_C^* = \rho_C(y_c, c)$ is the value of the density at $y = y_c$. In Fig. 6.8, we find a good agreement between the expression Eq. (6.53) and the numerical

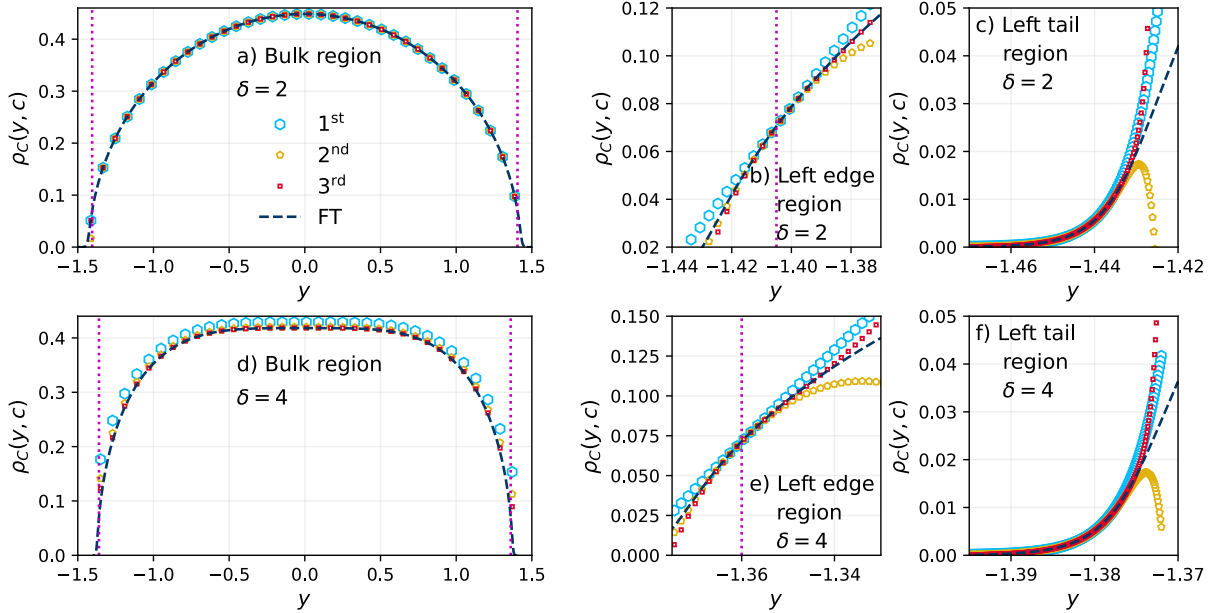


Figure 6.8: A comparison of the asymptotic densities up to third order (see Appendix A.9.2) with the densities obtained from the numerical solution of Eq. (6.45), denoted by ‘FT’, at low temperature $c = 0.01$ for the HC model. Here we show the densities for HC model confined to [(a)-(c)] harmonic trap ($\delta = 2$) and [(d)-(f)] quartic trap ($\delta = 4$). Here [(a),(d)] show the bulk ($|y| < y_c$), [(b),(e)] edge ($|y - y_c| \lesssim O(c)$) and [(c),(f)] tail ($|y| > y_c$) regions. The dotted vertical line represents the position $y = y_c$ which determines the three regions. In (c) and (f), as $y = y_c$ falls outside of the domain of the x -axis, for the sake of presentation, we do not show the dotted line.

solution of Eq. (6.45) for $c = 0.01$. Note that, for this comparison the value of the chemical potential $\mu_C(c)$ is taken from Fig. 6.7, where we recall that $\mu_C(c)$ is obtained by solving Eq. (6.45) along with the normalization condition [Eq. (6.46)].

As temperature increases the particles spread spatially over a wider region. Therefore, at high temperatures, $c \gg 1$, the gas becomes dilute i.e. $\rho_C(y, c) \ll 1$. Using this low density approximation in Eq. (6.45) yields (see Appendix A.9.2)

$$\rho_C(y, c) \stackrel{c \gg 1}{\approx} \exp\left(\frac{\mu_C(c)}{c} - \frac{y^\delta}{c\delta}\right), \quad (6.55)$$

where $\mu_C(c)$ is obtained numerically from Fig. 6.7. The form of the density in Eq. (6.55) comes from the entropy which provides the dominant contribution to the density for $c \gg 1$. In Fig. 6.9, for $c = 10$, we find a good agreement between the approximate expression of the density profile given in Eq. (6.55) (see Appendix A.9.2 for higher correction) and the numerical solution of the Eq. (6.45).

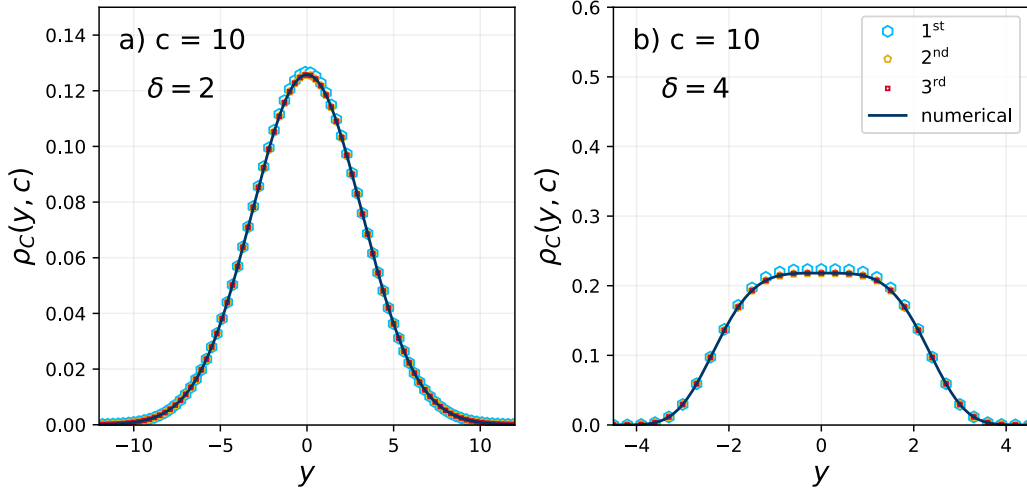


Figure 6.9: Comparison of the asymptotic densities up to third order (see Appendix. A.9.2) with the numerical solution of Eq. (6.45), denoted by ‘FT’, at high temperature $c = 10.0$ for the HC model confined to (a) harmonic trap ($\delta = 2$) and (b) quartic trap ($\delta = 4$).

6.5 Conclusion

To summarize, we have presented the equilibrium density profiles at finite temperatures of two integrable models, the hard rods and the hyperbolic Calogero model, in harmonic and quartic traps. For these models, inter-particle repulsion is strong enough to prevent particle trajectories from crossing. The trap confines these systems spatially and breaks integrability. For these two models, we studied equilibrium density profiles using a field theory approach and Monte Carlo (MC) simulations.

Model \ Trap	Harmonic ($\delta = 2$)	Quartic ($\delta = 4$)
Hard rods	Eq. (6.27), $\alpha_R = 1, \gamma_R = 2,$ $\lambda_R = 2$ Figs. 6.2a, 6.2b, 6.2c	Eq. (6.27), $\alpha_R = 1, \gamma_R = 4,$ $\lambda_R = 4$ Figs. 6.2d, 6.2e, 6.2f
Hyperbolic Calogero	Eq. (6.42), $\alpha_C = \frac{1}{2}, \gamma_C = 1,$ $\lambda_C = 1$ Figs. 6.6a, 6.6b, 6.6c	Eq. (6.42), $\alpha_C = \frac{1}{3}, \gamma_C = \frac{4}{3},$ $\lambda_C = \frac{4}{3}$ Figs. 6.6d, 6.6e, 6.6f

Table 6.1: A summary of the scaling behavior of the densities for the hard rods (HR) and the hyperbolic Calogero (HC) model in harmonic and quartic traps.

We developed appropriate field theory for these two models by extending the approaches

used in Ref. [45]. From the field theory we computed the equilibrium density profiles, and their dependence on system size N and temperature T . The field theory calculations predict precise scaling forms for the equilibrium density profiles as functions of N and T . A summary of the scaling forms is given in Table 6.1. We find that the predictions from field theory for hard rods agree remarkably well with MC simulations (Fig. 6.2). For the hyperbolic Calogero model, the agreement is also reasonably good (Fig. 6.6).

Our work provides a framework for investigating the non-equilibrium dynamics, thermalization and transport in integrable models confined in external potentials. More precisely, one can ask whether these systems under Hamiltonian dynamics are ergodic and chaotic, and whether or not they equilibrate/thermalize when placed in different confining traps. This is an area of active current research both theoretically [211] and experimentally [78]. In the next chapter, we will study the dynamics of the hard rod model in a harmonic and quartic trap and investigate the thermalization properties of the system.

This chapter describes the study from the following published work, Ref. [225]:

J. Kethepalli, D. Bagchi, A. Dhar, M. Kulkarni, A. Kundu, “Finite temperature equilibrium density profiles of integrable systems in confining potentials”, *Phys. Rev. E* **107**, 044101 (2023)

Chapter 7

Unusual ergodic and chaotic properties of trapped hard rods

7.1 Introduction

The question of how isolated many body systems thermalize is of long-standing interest; a canonical study is that of Fermi, Pasta, Ulam and Tsingou (FPUT) [65]. The surprising finding of FPUT was that a one-dimensional anharmonic chain of oscillators did not exhibit equipartition of energy even at very long times, with the system showing quasi-periodic behavior and near-perfect recurrences. Various mechanisms have been proposed to explain the results of FPUT [66–69], e.g, proximity to integrable models such as the Korteweg-De Vries equation [74] or the Toda model [75–77] as formalized by KAM theory [70], the stochasticity threshold [71], the presence of discrete breathers [226] and most recently the formalism of wave turbulence [73].

One striking feature of this system is a separation between the timescales for equilibration and chaos. From numerical simulations of the α -FPUT model [75, 227, 228], it was shown that for generic initial conditions [75], the timescale for the system to thermalize (defined as the time to reach equipartition of energy) was much longer than the timescale needed to observe chaos (defined as the time for the system to escape from regular regions in phase space to chaotic ones), with both timescales increasing as the energy per particle decreased and appearing to diverge at some critical value. (However, recent studies based on wave turbulence seem to indicate the absence of any such threshold [73].) Some subtleties in defining thermalization times and their possible relation to Lyapunov exponents

were investigated recently in Ref. [229]. Despite a vast body of literature on the topic, a definitive theory of thermalization in the FPUT chain still eludes the community and there appears to be no consensus.

More recently, another family of clean many-body systems that fail to thermalize under their dynamics has been scrutinized. These systems consist of particles with integrable two-body interactions, which are placed in an external trapping potential that breaks both translation symmetry and integrability of their interactions. Given that the trap breaks integrability, such systems are naïvely expected to thermalize to the Gibbs ensemble, but a prominent experiment realizing a trapped Lieb-Liniger gas with ultracold rubidium atoms showed that this expectation was not warranted [78]. A detailed theory of the resulting Newton’s-cradle-like dynamics had to await the development of generalized hydrodynamics [80,81] (GHD). While the latter theory appears to be more than adequate for modeling short-time dynamics of such trapped integrable systems [83–86,211,230,231], the fate of these systems at long times and in the absence of experimental imperfections remains somewhat unclear.

For example, previous work on one-dimensional classical hard rods in an integrability-breaking harmonic potential [84] found numerically that despite the dynamics exhibiting positive Lyapunov exponents, the system did not thermalize to a Gibbs state at the longest accessible simulation times (on the order of ten thousand periods of the trapping potential). Moreover, the long-time steady state was found to be a stationary state of the ballistic-scale (i.e. non-dissipative) GHD equations (as suggested previously [83]). This observation, together with further numerical findings reported below, appears to be incompatible with a subsequent proposal [86] that diffusive corrections [232,233] to generalized hydrodynamics inevitably lead to thermalization in integrability-breaking traps. Even if thermalization does occur for harmonically trapped hard rods at numerically inaccessible long times, it remains to be explained why this timescale is so long. Systems of rational Calogero particles have also been found not to thermalize on accessible timescales in traps that are expected to break integrability [211] (though this is not in tension with theory [86] insofar as diffusive corrections to the rational Calogero GHD vanish [211]). Finally, we note that the effect of integrability-breaking by traps has been studied for the classical Toda system [206,209]. In this case, it was found that the harmonically trapped system was weakly chaotic while the quartically trapped system displayed strong chaos

and thermalization.

Thus despite much recent progress, several fundamental questions concerning the thermalization of trapped integrable particles remain unresolved, including whether or not these systems are truly ergodic, whether they can support additional microscopic conservation laws, and how far these properties coexist with chaos. Another open question, in answer to which there is conflicting evidence in the literature, is whether the stationary state in a generic trap is the Gibbs state [86] or one of infinitely many non-thermal stationary solutions to ballistic-scale GHD [83, 84]. We will address some of these questions below.

In this paper, we study the effects of integrability breaking in one-dimensional systems of hard rods of length a that are confined to external potentials of the form $U(x) = kx^\delta/\delta$ with strength $k > 0$, where $\delta = 2$ for harmonic trap and $\delta = 4$ for the quartic trap. We diagnose chaos, ergodicity and thermalization in these systems through probes such as the maximal Lyapunov exponent (LE), the equipartition of energy between rods, and the position and velocity distributions of the rods. We find that while quartically trapped rods behave like a typical non-integrable many-body system, harmonically trapped rods exhibit many drastically different and unexpected properties. The only additional microscopic conservation law for harmonically trapped rods beyond the total energy, E , appears to be the energy of the center of mass, $E_{\text{cm}} = \frac{1}{2N^2} [(\sum_i x_i)^2 + (\sum_i v_i)^2]$. Nevertheless, we find that the system appears to be non-ergodic, has unconventional chaos properties, and fails to thermalize to the Gibbs state even at extremely long times.

Below we summarize our main findings (see Table. 7.1):

1. We find that in a harmonic trap, a system of $N = 3$ hard rods shows a strong signature of integrability in the form of a vanishing maximal Lyapunov exponent (Fig. 7.1a) and a regular Poincaré section (Fig. 7.1b). This is in striking contrast to the case of two rods confined to a quartic trap, which has both finite (positive) and vanishing Lyapunov exponents (Fig. 7.1c) and a mixed phase space with both chaotic and regular regions (Fig. 7.1d). Our findings hint at the existence of more conserved quantities for three rods in a harmonic confining potential (see also [84]).
2. For any finite number of rods $N > 3$ in a harmonic potential, we find that the LE is positive. Nevertheless, we find compelling evidence that the system is highly

non-ergodic. This is demonstrated by the strong initial-condition dependence of the LE and the time-averaged kinetic temperature (Fig. 7.2). Such non-ergodicity is further suggested by the broad distributions of Lyapunov exponents and rescaled temperatures (Fig. 7.3). These distributions are obtained by time-evolving initial conditions that are sampled uniformly from the constant E , E_{cm} microcanonical surface (see Sec. 7.3 for details). Remarkably, hard rods confined to a quartic trap exhibit qualitatively completely different behavior, and we find evidence of conventional chaotic thermalizing dynamics expected for generic, non-integrable, classical many-body systems (Fig. 7.4).

3. The system is described completely by two dimensionless parameters: the rescaled energy, $e = E/(N^{\delta+1}ka^\delta)$ and the number of rods, N . For the harmonic case with fixed e , the average maximal Lyapunov exponent $\langle\lambda\rangle$ converges to a finite value with increasing N . This converged value shows an $\sim e^{-1/2}$ scaling over a wide range of e values (Fig. 7.5a). In sharp contrast, for the quartic case the average LE ($\langle\lambda\rangle$) for a given N grows as $\sim e^{1/2}$ and the proportionality constant increases with N (Fig. 7.5b).
4. We find intriguing behavior in the approach to thermalization of macroscopic observables, such as density profiles and velocity distributions, for macroscopic systems of trapped hard rods. For both trap shapes, we study thermalization starting from four different types of initial conditions, each of which is determined by choosing either a spatially uniform or bimodal (Newton’s-cradle-like) position distribution and choosing either a uniform or a Maxwellian velocity distribution. For each of these four initial conditions, we find that harmonically trapped rods approach different stationary states at large times, none of which corresponds to the conventional Gibbs state (Fig. 7.8). On the other hand, we find that quartically trapped rods thermalize, eventually reaching the stationary Gibbs state for different initial conditions (Fig. 7.9).

The paper is organized as follows. In Sec. 7.2 we describe the model in detail and define the diagnostics that we will be using to characterize its dynamics. In Sec. 7.3, we discuss the numerical methods employed. In Sec. 7.4, we present the results of extensive molecular dynamics simulations of trapped hard rods. We conclude and discuss some

open questions in Sec. 7.5.

7.2 Models and definitions

We consider one-dimensional hard rods of length a and unit mass in a confining potential, given by the Hamiltonian

$$H(\{x_i, v_i\}) = \sum_{i=1}^N \left[\frac{v_i^2}{2} + U(x_i) \right] + \sum_{i=1}^{N-1} V(|x_{i+1} - x_i|), \quad (7.1)$$

where $\{x_i, v_i\}$ denote the position and the momentum of the i^{th} rod such that $x_{i+1} \geq x_i + a$ for $1 \leq i \leq N - 1$. We consider a confining potential of the form

$$U(x) = k \frac{x^\delta}{\delta} \quad (7.2)$$

with two values of δ

$$\delta = \begin{cases} 2 & \text{for a harmonic trap} \\ 4 & \text{for a quartic trap} \end{cases} \quad (7.3)$$

The interaction term for hard rods is of the form

$$V(r) = \begin{cases} 0 & \text{for } r > a \\ \infty & \text{for } r \leq a. \end{cases} \quad (7.4)$$

Under the resulting Hamiltonian dynamics, the rods collide elastically with their neighbors, upon which they exchange momenta instantaneously. In between collisions, the rods move independently in the trap potential. Scaling distances and time by the natural length and time scales, a and $\tau = 1/\sqrt{ka^{\delta-2}}$, respectively, one finds the total energy of the system is given by

$$E = ka^\delta \sum_{i=1}^N \left[\frac{\dot{x}_i^2}{2} + \frac{x_i^\delta}{\delta} \right]. \quad (7.5)$$

The minimum energy, E_m , of the system is attained by a close-packed configuration centered at the origin, with all particles at rest. It is clear that $E_m \sim ka^\delta N^{\delta+1}$. We are interested in observing thermalization at high enough temperatures such that the central

density of the gas is reduced from this close-packed density by a factor of order one or more. This requires excitation energy $E_{\text{ex}} = E - E_{\text{m}}$ of the same order as E_{m} or larger. From Eq. (7.5), we see that the only relevant parameters in the system are the rescaled energy [225]

$$e = \frac{E}{N^{\delta+1} k a^\delta} \quad (7.6)$$

and N . In the following, without loss of generality, we can set $a = 1, k = 1$ and compute various physical quantities for different values of the parameters e and N . We further note that for the harmonic case, there is a second conserved quantity

$$E_{\text{cm}} = \frac{1}{2N^2} \left[\left(\sum_i x_i \right)^2 + \left(\sum_i v_i \right)^2 \right], \quad (7.7)$$

beyond the total energy, which is the energy of the center of mass [84]. The center of mass moves autonomously, and the relative motion of the rods is independent of that of the center of mass, so without loss of generality for the harmonic trap we can restrict to $E_{\text{cm}} = 0$. Note that this also implies that $X_{\text{cm}} = \sum_i x_i = 0$ and $P_{\text{cm}} = \sum_i v_i = 0$ are separately conserved.

For these systems, we compute the finite time Lyapunov exponent, $\lambda(t)$, and its infinite time limit, λ , defined respectively as

$$\lambda(t) = \lim_{\epsilon \rightarrow 0} \frac{1}{t} \ln \left| \frac{d_t}{\epsilon} \right|, \quad (7.8)$$

$$\lambda = \lim_{t \rightarrow \infty} \lambda(t),$$

where $d_0 = \epsilon$ is the separation between the two initial phase-space points, and d_t is their separation at time t . For chaotic systems $\lambda > 0$, which represents the exponential divergence of phase-space trajectories for an infinitesimally small initial separation. It is possible to write a linearised dynamics for the variable $z_t = d_t/\epsilon$ in the $\epsilon \rightarrow 0$ limit, which provides an accurate method for computing λ . We use this method for computing Lyapunov in the harmonic case, whereas for the quartic case, we compute it directly from the evolution of two different initial conditions. In both cases, we use the widely used numerically efficient method due to Benettin, Galgani and Strelcyn [234]. To probe thermalization, we compute the (running) time average of the scaled kinetic temperature

of the individual hard rods defined as

$$c_i = \frac{T_i}{N^\delta}, \quad \text{where} \quad T_i(t) = \frac{1}{t} \int_0^t dt' v_i^2(t'), \quad (7.9)$$

and check for equipartition.

To study the relaxation dynamics and equilibration to a Gibbs state, we compute the spatial density profile $\rho(x, t)$ and the velocity distribution $P(v, t)$ defined as:

$$\rho(x, t) = \sum_{i=1}^N \langle \delta(x - x_i(t)) \rangle, \quad (7.10)$$

$$P(v, t) = \sum_{i=1}^N \langle \delta(v - v_i(t)) \rangle. \quad (7.11)$$

where $\langle \dots \rangle$ denotes an average over many initial microscopic states with the same initial density profiles and velocity distributions, drawn from a microcanonical ensemble with constant energy e and $E_{\text{cm}} = 0$. Details of the preparation of these initial states are given below in Sec. 7.3. If the system thermalizes to a Gibbs state, then one expects that $\rho(x)$ will be the same as the equilibrium distribution obtained from Monte-Carlo simulations whose temperature is fixed so that the average energy (appropriately scaled) equals e . The corresponding velocity distribution $P(v)$ will be Gaussian at the same temperature.

7.3 Numerical methods

In this section, we outline the various numerical methods and conventions that we will use both in and out of equilibrium.

Time evolution: For the harmonic case ($\delta = 2$), one can evolve the equations of motion using exact and numerically efficient event-driven molecular dynamics (EDMD). For the quartic trap ($\delta = 4$) case, we employ standard molecular dynamics (MD) simulations using a symplectic velocity-Verlet integration scheme. During collision events, we exchange the velocities of the particles at the first instant that any two adjacent rods overlap, defined as $x_{i+1} - x_i < a$. To ensure the accuracy of this approximation, we use a very small time increment $dt = 10^{-6}$.

Stochastic momentum exchange dynamics (SMED): To sample initial conditions uni-

formly over the phase space from a microcanonical ensemble with e fixed and $E_{\text{cm}} = 0$, we allow momentum exchange of randomly chosen pairs of neighboring particles at random times in addition to the usual Hamiltonian dynamics. This stochastic process conserves the total momentum and energy of the system. For the harmonic trap case, this stochastic momentum exchange dynamics (SMED) also conserves the center of mass energy E_{cm} . The SMED exhibits the expected equipartition of energy (flat temperature profiles) and insensitivity to initial conditions, both of which are consistent with ergodicity.

Initial state preparation: To check the initial condition dependence of the maximal Lyapunov exponent λ and its distribution we used microcanonical initial conditions generated by the SMED.

To check thermalization, we prepare the system with specified nonequilibrium spatial density profiles $\rho(x)$ and velocity distributions $P(v)$ consistent with given values of e and $E_{\text{cm}} = 0$. This is achieved via the following protocol. First, we distribute the rods spatially by the required density profile $\rho(x)$, imposing the hard-rod constraint and fixing the center of mass at $x = 0$. We then compute the total potential energy E_p for this configuration and subtract it from the total energy E to obtain the total kinetic energy E_k . The velocities are drawn from the distribution $P(v)$ and then shifted and rescaled by appropriate factors so that the center of mass velocity vanishes and the total kinetic energy is exactly E_k . In this work, we consider two non-thermal choices of $\rho(x)$: either uniform over a finite width (denoted U), or a Newton's-cradle-like profile consisting of two uniform blobs, each of finite width and separated by an $O(N)$ distance (denoted Nc). For the velocities, we consider two choices of $P(v)$: either uniform (denoted U) or Maxwellian (denoted Mx). This leads to four possible choices of non-equilibrium initial conditions: (i) U-U, (ii) U-Mx, (iii) Nc-U, and (iv) Nc-Mx.

7.4 Results on Chaos, ergodicity and thermalization

As mentioned earlier, one naïvely expects that the presence of the trap makes the system chaotic ($\lambda > 0$), ergodic (no long-time dependence on the details of the initial condition), and non-integrable (strictly fewer than N independent integrals of motion). In the following, we investigate these properties in detail by computing the Lyapunov exponent and kinetic temperatures for different N in harmonic ($\delta = 2$) and quartic ($\delta = 4$) trapping

potentials.

7.4.1 Chaos and ergodicity

It is easy to see that the dynamics of 2 hard rods ($N = 2$) is integrable for the harmonic trap because of the presence of the second conserved quantity E_{cm} . This is however not the case in a quartic trap, as will be elaborated below.

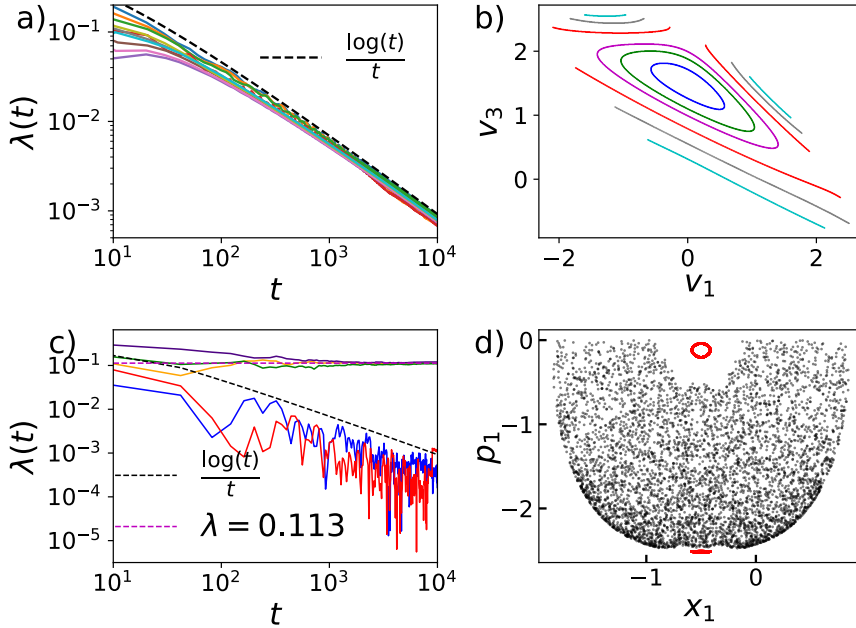


Figure 7.1: Plots of (a) time-dependent Lyapunov exponent $\lambda(t)$, and (b) Poincaré section for $N = 3$ rods in the harmonic trap for 10 and 6 different initial conditions, respectively, with $E = 6$ and $E_{\text{cm}} = 0$. Figures (c,d) show plots of $\lambda(t)$ and the Poincaré section for $N = 2$ rods in the quartic potential for 5 and 2 initial conditions, respectively, with energy $E = 3.2$. To compute $\lambda(t)$, we used linearized dynamics for (a) and two trajectories with $\epsilon = 10^{-10}$ for (c). The $\log t/t$ behavior in (a) and the regular sections in (b) are consistent with the integrability of $N = 3$ rods in the harmonic trap. Interestingly, figure (c) reveals the existence of both chaotic and non-chaotic trajectories for the quartic case. This is also reflected in (d) where we observe two types of patterns, namely scattered (black) and regular (red).

$N = 3$ rods (harmonic trap): We first consider the case of $N = 3$ rods in the harmonic trap with $E_{\text{cm}} = 0$. We find that the systems display features akin to integrable systems as exhibited by the existence of non-chaotic trajectories with Lyapunov exponents decaying as $\lambda(t) \sim \log(t)/t$ (Fig. 7.1a). This is similar to integrable models such as the Toda

chain [229]. The Poincaré sections are shown in Fig. 7.1b where we observe regular patterns consistent with Fig. 7.1a.

$N = 2$ rods (quartic trap): In striking contrast to the above case, the behavior of even $N = 2$ rods in a quartic trap shows both chaotic and regular trajectories, as depicted in Fig. 7.1c. This observation is consistent with the Poincaré sections shown in Fig. 7.1d, where we observe that the phase space of two hard rods can have disjoint chaotic regions (scattered) and non-chaotic (regular) islands. However, our observations indicate that the phase space volume of the regular island is much smaller than that of the chaotic region even for $N = 2$.

$N \geq 4$ rods (harmonic trap): We find that many trajectories for $N = 4$ rods in a harmonic trap are chaotic, although still non-thermalizing. We compute $\lambda(t)$ and $c_1(t)$ for different initial conditions (IC) obtained from SMED simulations (see Section 7.3) for two values of the rescaled energy, $e = 0.5$ and $e = 5.0$. The results are shown in Figs. 7.2a,c and Figs. 7.2b,d, respectively. We find that the values of $\lambda(t)$ and $c_1(t)$ at late times are sensitive to the choice of initial condition. Interestingly, we observe that even for $N = 4$ there is a fraction of trajectories for which $\lambda(t)$ decays in time for all numerically accessible times, as for the case of $N = 3$ rods (see Figs. 7.2a,b). To investigate equipartition we plot $c_i(t)$ for $i = 1, 2, 3, 4$ for a single initial condition in Fig. 7.2e for $e = 0.5$, and observe that $c_1(t) = c_4(t)$ and $c_2(t) = c_3(t) \neq c_1(t)$ at late times. This is also observed for $e = 5.0$ in Fig. 7.2f. These observations suggest that the $N = 4$ system is chaotic but not ergodic for most choices of initial condition.

To quantify and further investigate the IC dependence and non-ergodicity in systems with different numbers of rods N , we compute the probability distributions $P(\lambda)$ and $P(c_1)$ of the late time values of $\lambda(t)$ and $c_1(t)$, obtained from an ensemble of ICs (once again generated using SMED) for $e = 0.5$ (Figs. 7.3a,c) and $e = 5.0$ (Figs. 7.3b,d). Interestingly, for the distribution $P(\lambda)$, we see a peak near $\lambda = 0$ for $N = 4$ arising from the non-chaotic trajectories observed in Figs. 7.2a,b. This peak, however, decreases sharply with increasing N . Further, we observe that the mean of the distribution $P(\lambda)$ behaves non-monotonically with increasing N . On the other hand, the width of the distribution seems to decrease with increasing N . The fact that the distributions of both λ and c_1 are still quite broad even at the largest system size $N = 32$ studied is

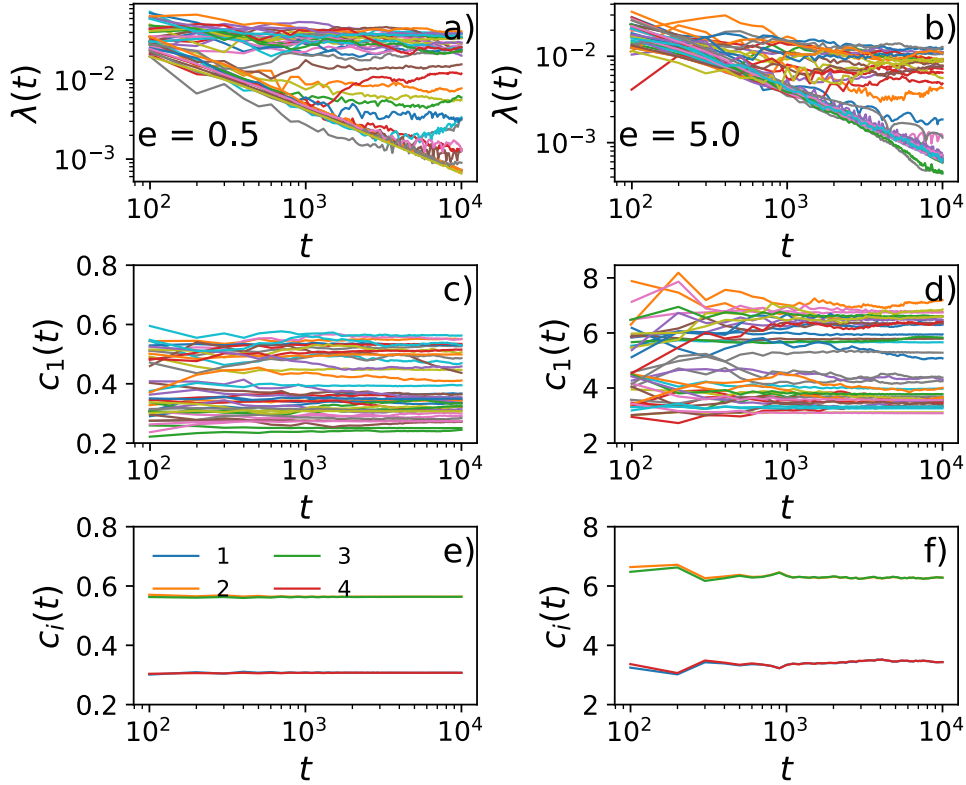


Figure 7.2: Time evolution of $\lambda(t)$ and $c_1(t)$ for $N = 4$, starting from 40 different initial conditions (each color denotes one initial condition) generated using the SMED protocol, for (a,c,e) $e = 0.5$ and (b,d,f) $e = 5.0$. This shows the strong dependence on initial conditions of the late-time values of $\lambda(t)$ and $c_1(t)$ for $N = 4$ hard rods in a harmonic trap. In (e) and (f) we show the evolution of the time-averaged values of $c_i = T_i/N^2$ of $N = 4$ hard-rods for $e = 0.5$ and $e = 5.0$ respectively, for one realization. In the long time limit, c_1 and c_4 are equal but have a value that is significantly different from c_2 and c_3 , indicating a lack of energy equipartition.

strong evidence for a lack of ergodicity in the system. To demonstrate that $t = 10^5$ is a sufficiently long time for computing the distributions $P(\lambda)$ in Figs. 7.2a,b, we, in Figs. 7.3e,f plot the distribution of $\lambda(t)$ at different times for $N = 8$. We observe that these distributions initially display some narrowing, but seem to converge to a limiting form of finite width at long times. This suggests that the system is genuinely non-ergodic and that the identification of λ with $\lambda(t)$ at $t = 10^5$ in Fig. 7.3a,b is justified.

These numerical results are consistent with the following possible scenarios for the harmonic trap:

- The disappearance of the peak in $P(\lambda)$ at $\lambda = 0$ with increasing N indicates that any possible KAM-like non-chaotic islands occupy negligible phase-space volume in the limit of large system size.

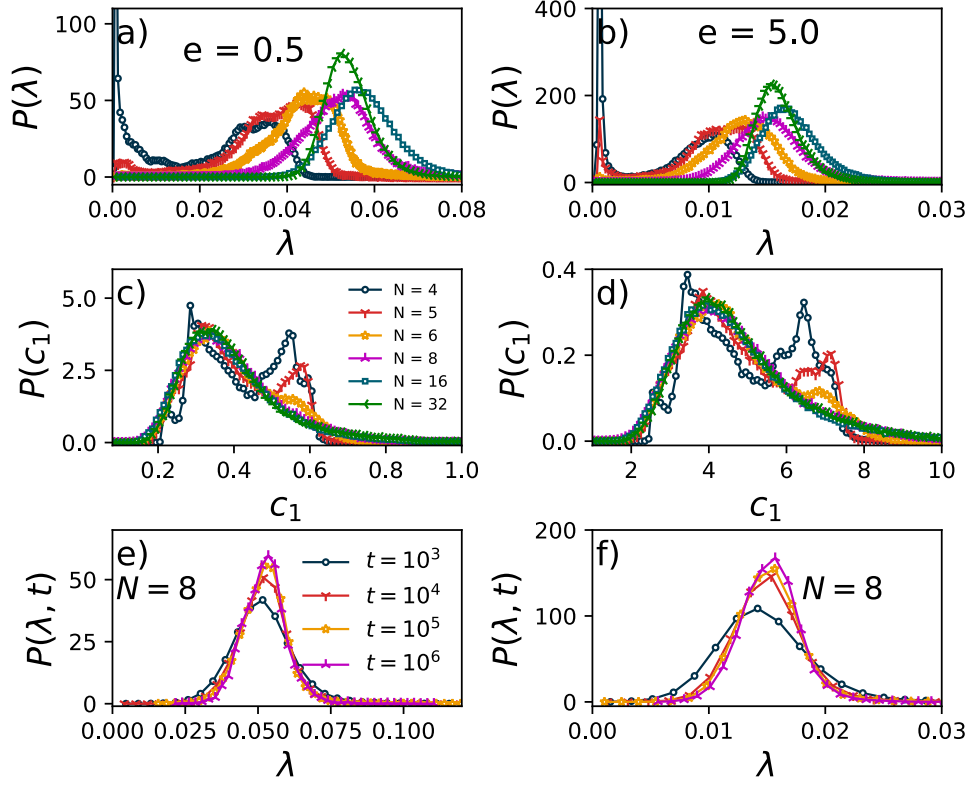


Figure 7.3: (a,b,c,d) Distribution of the maximal Lyapunov exponent λ and rescaled temperature c_1 of the left-most rod, for $4 \leq N \leq 32$, computed at time $t = 10^5$. The system sizes corresponding to different plots are provided in sub-plot (c). We find a significant breakdown of ergodicity for hard rods in this harmonic trap. (e,f) Distribution of λ for $N = 8$ at different times, $10^3 \leq t \leq 10^6$, which shows that $P(\lambda, t)$ approaches a steady limiting distribution at late times. The initial conditions for all the plots are generated using the SMED: (a,c,e) for $e = 0.5$ and (b,d,f) for $e = 5.0$.

- The non-vanishing width of $P(\lambda)$ and $P(c_1)$ for the simulated values of N suggests the existence of multiple chaotic islands with distinct values of λ and c_1 in a given microcanonical shell.
- These chaotic islands could arise either from extra conserved quantities or from strong kinetic constraints (e.g. high entropy barriers) that prevent movement between different islands. In the former case, we expect that the width of the distributions $P(\lambda)$ and $P(c_1)$ will not go to zero even for long times and large N . In the latter case, these distributions will eventually become sharp at sufficiently long times, yielding unique values of λ and c_1 for any N . Our numerical results in Fig. 7.3(e,f) are in closer agreement with the former scenario.

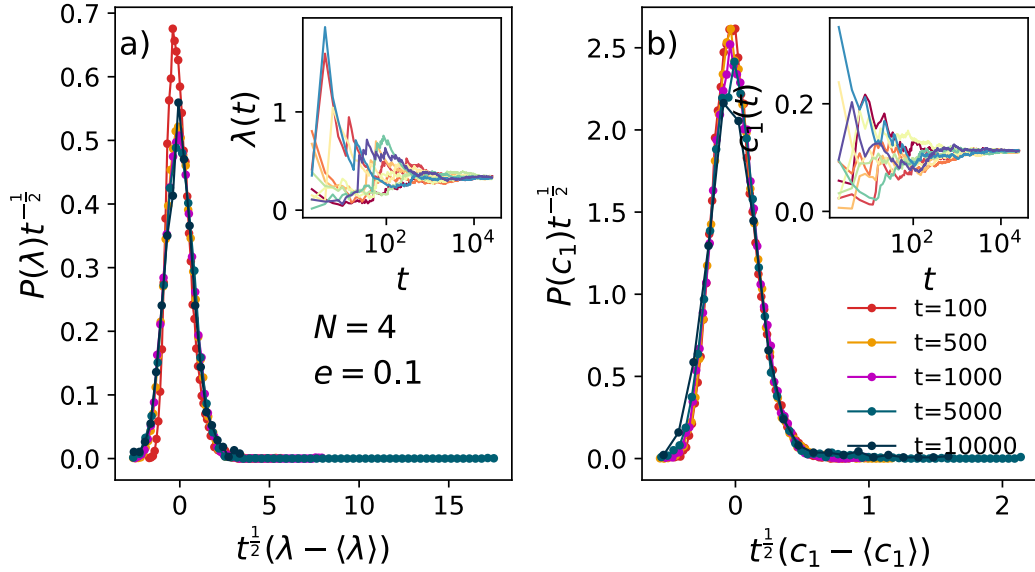


Figure 7.4: Probability distribution of (a) maximum Lyapunov exponents λ and (b) c_1 for $N = 4$ rods in a quartic trap. We observe that both distributions collapse at different times after shifting by their respective means and scaling by \sqrt{t} . This indicates that the width of these two distributions decreases with time and becomes increasingly sharp, in contrast to our findings for the harmonic trap depicted in Fig. 7.3. In the insets, we show the time evolution of λ and c_1 for 20 different realizations (each color denotes one initial condition), all of which converge to a unique value at late times, regardless of the initial conditions.

$N \geq 4$ rods (quartic): For the quartic trap, numerically obtained distributions for $P(\lambda(t))$ and $P(c_1(t))$ are shown in Figs. 7.4a and 7.4b respectively, for different times from $t = 100$ to $t = 10^4$. In contrast to the harmonic trap, we find that both these distributions are sharply peaked and that their width decreases with time as $\sim t^{-1/2}$ (see the scaling in Fig. 7.4). This suggests that hard rods in a quartic trap thermalize. This conclusion is supported by the insets of these figures, which demonstrate that $\lambda(t)$ and $c_1(t)$ converge to unique values (within statistical fluctuations) for different initial conditions. Thus our numerical simulations find negligible dependence of the late-time dynamics on initial conditions, which is evidence for thermalization, and consistent with ergodicity (testing the latter directly would require a more detailed analysis of individual phase-space trajectories).

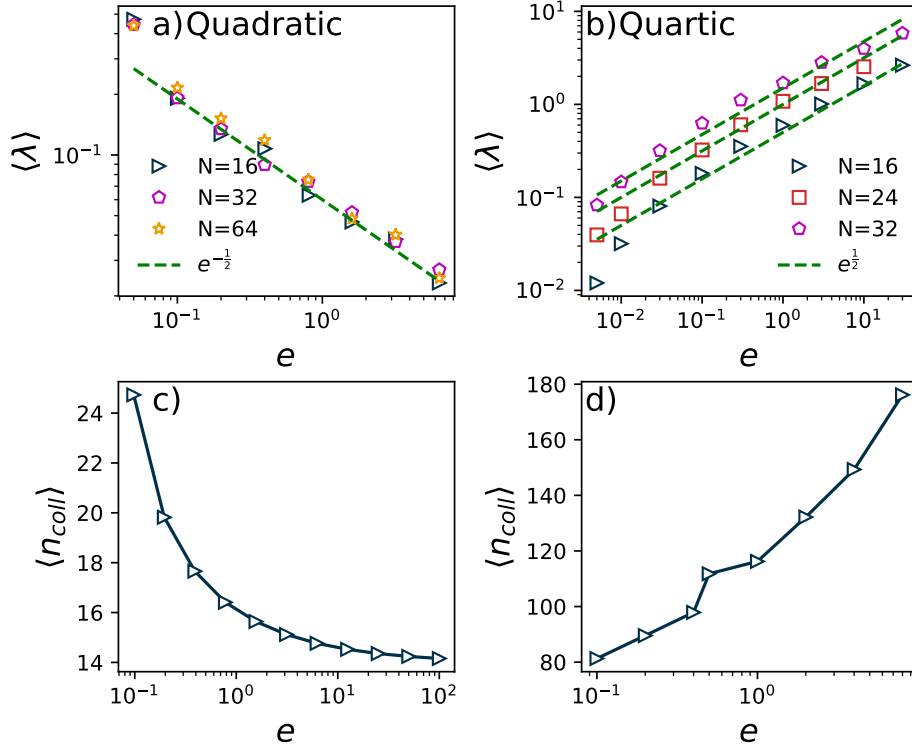


Figure 7.5: Plot of average maximal Lyapunov exponent ($\langle \lambda \rangle$) with rescaled energy e for (a) harmonic and (b) quartic trap. The average number of collisions per unit time $\langle n_{coll} \rangle$ as a function of total energy e for $N = 8$ for (c) harmonic trap and (d) quartic trap.

7.4.2 Energy dependence of chaos

In this section, we investigate how the mean maximal Lyapunov exponent $\langle \lambda \rangle$ (obtained from the distributions in Figs. 7.3a and 7.3b) depends on the rescaled energy e and N for both traps. We observe that in the case of the harmonic trap, $\langle \lambda \rangle$ roughly saturates to a non-zero value at large N for a fixed value of e . In Fig. 7.5a, we plot these saturation values as a function of e where one observes that $\langle \lambda \rangle$ decreases with e as $\sim 1/\sqrt{e}$ at large e . A similar decrease of $\langle \lambda \rangle$ with increasing energy has been reported earlier for soft rods in a harmonic trap [235]. For the quartic trap, in contrast to the harmonic case, $\langle \lambda \rangle$ does not appear to converge with increasing N for the range of N values studied here. For fixed N , $\langle \lambda \rangle$ grows with increasing e as $\sim \sqrt{e}$ for large e as can be seen from Fig. 7.5b. This square-root dependence of λ on temperature is also observed in other non-integrable systems [236, 237].

To understand this intriguing dependence of λ on e better, we compute the average number of collisions per unit time $\langle n_{coll} \rangle$ in both traps, for a fixed $N = 8$ and for different values of the energy e . These are shown in Figs. 7.5c and 7.5d for the harmonic and the

quartic trap respectively. From Fig. 7.5c we find that $\langle n_{coll} \rangle$ decreases in the harmonic trap as e is increased. Thus, as the energy is increased the hard rod gas expands and collisions become rarer. We expect that this reduced rate of collisions is responsible for the decrease in $\langle \lambda \rangle$ with increasing e for the harmonic trap. In contrast, we find for the quartic trap that $\langle n_{coll} \rangle$ increases as e is increased (see Fig. 7.5d), which may cause the increase of $\langle \lambda \rangle$ with e .

7.4.3 Thermalization in macroscopic systems

In previous sections, we studied the chaos and ergodicity properties of hard rods in harmonic and quartic traps. For harmonic traps, we found numerical evidence that for large N the system is chaotic but not ergodic, while for quartic traps we found that the system was both chaotic and thermalizing (and most likely ergodic). A notable feature of the harmonic trap is that the dynamics become *less* chaotic as the rescaled energy is increased.

Whether these results have any bearing on thermalization in macroscopic systems is a nontrivial question, which we now address. We will study this question by looking at the time evolution of non-equilibrium density profiles and velocity distributions of trapped hard rods (evolving under Hamiltonian dynamics) and checking whether these relax to the Gibbs state.

To this end, we compute $\rho(x, t)$ and $P(v, t)$, as defined in Eqs. (7.10) and (7.11), as a function of time for four choices of initial condition (see Sec. 7.3) with fixed values of e and $E_{cm} = 0$. In Figs. 7.6a and b we show $\rho(x)$ and $P(v)$ for small times $0 < t \lesssim \tau = 2\pi$, with $N = 128$ hard rods in the harmonic trap, starting from IC Nc-M, *i.e.*, from Newton’s cradle initial condition in space (two spatially separated blobs of rods) with velocities chosen from a Maxwell distribution. It is clear that the rods, starting from a two-blob initial condition (at $t = 0$), go through “breathing” dynamics and exhibit large oscillations in their density profiles and velocity distributions. As the system “breathes”, the density profile goes through different intriguing shapes that are shown in Fig. 7.6a. Such transients in the finite-time dynamics of trapped integrable systems are well documented by now [78, 84, 85, 203].

After these initial transients, the position and velocity distributions begin to approach a stationary state. We plot the single-particle distributions for $N = 128$ hard rods in a

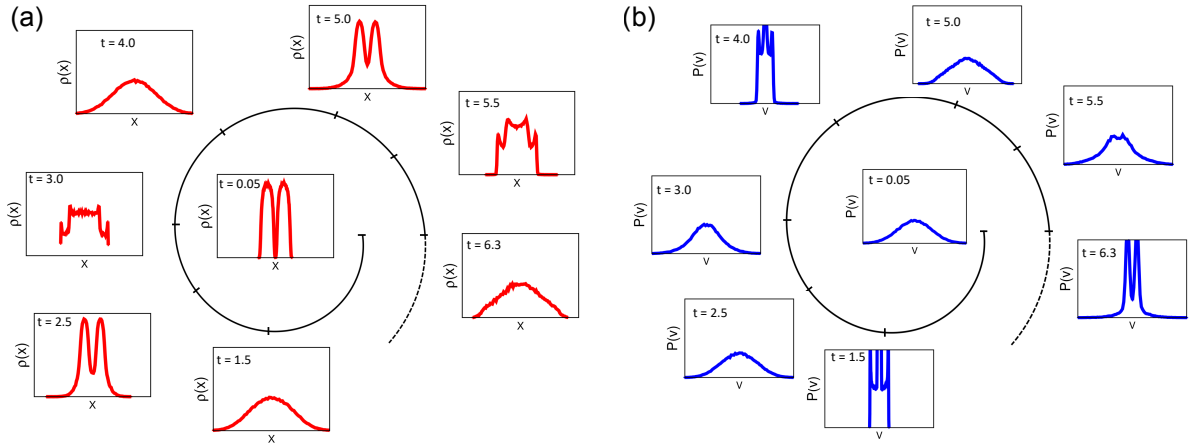


Figure 7.6: (a) Density profiles $\rho(x)$ and (b) velocity distributions $P(v)$ in the harmonic trap, with $e = 0.5$ and $N = 128$, that appear at different times within one time-cycle of the trap, $0 < t \lesssim \tau = 2\pi$. These profiles are obtained starting at $t = 0$ from a two-blob density profile and Gaussian velocity distribution (*i.e.* Nc-Mx) of the hard rods. For all the figures in (a) and (b), the abscissa runs from -400 to 400 . For (a) and (b), the ordinate scale ranges are $0 - 0.007$ and $0 - 0.01$ respectively. As can be observed, the hard-rod system in a harmonic trap has an initial ‘breathing-mode’ dynamics and exhibits oscillations in the distributions, somewhat resembling Newton’s cradle. For our parameters, these oscillations damp out in $O(20)$ cycles.

harmonic trap at late times $t = 500, 10^3, 10^4$. These distributions are shown in Figs. 7.7a-d for $e = 0.5$ and $e = 5.0$. To check whether or not the rods thermalize in the long-time limit, we also plot the corresponding single-particle distributions obtained from SMED, which are expected to recover the microcanonical ensemble.

Strikingly, in the harmonic trap, we find that the density profile obtained from the microscopic dynamics even at the longest accessible times, $t = 10^4\tau$, (where $\tau = \frac{2\pi}{\omega}$ is the time period of the trap) is very different from the SMED prediction. The velocity distribution is also found to differ from the SMED prediction, for both $e = 0.5$ and $e = 5.0$. Thus the hard rod gas does not thermalize in a harmonic trap even at the very longest accessible times. This is consistent with earlier work, which found that the long-time steady state of harmonically trapped hard rods was a non-thermal stationary solution to ballistic-scale GHD on comparable timescales [84]. It appears that for smaller e , the density and velocity profiles are closer to the equilibrium forms obtained from SMED. Thus, quite intriguingly, we find that harmonically trapped hard rods at a higher rescaled energy e are less chaotic, retain the memory of their initial conditions for longer, and show greater reluctance to thermalize than systems at lower e .

To argue convincingly against thermalization, we must further check that the late-

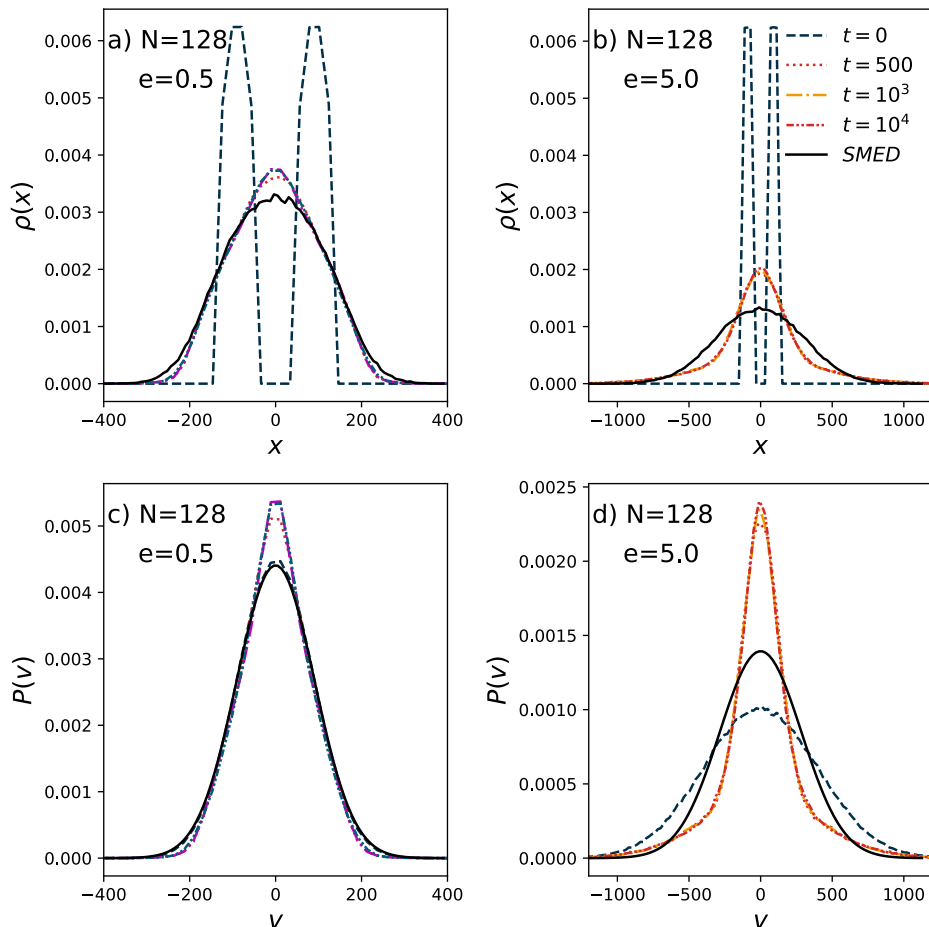


Figure 7.7: Time evolution of density and velocity profiles: (a,c) for $e = 0.5$ and (b,d) $e = 5.0$ for $N = 128$ hard rods in a harmonic trap, starting from Newton’s cradle initial condition (i.e. two spatially separated blobs of rods) with Maxwellian velocities (Nc-Mx, in the notation of Sec. 7.3). The times simulated are indicated by the legend in (b). These plots illustrate that at late times ($t = 10^4\tau$) the density profiles and velocity distributions obtained from EDMD converge to forms that differ from those obtained from SMED.

time behavior of the system is sensitive to the choice of initial condition. In Fig. 7.8, we investigate the late-time behavior of hard rods in a harmonic potential for several initial conditions and compare them with the corresponding thermal predictions from SMED. The four different initial conditions (see Sec. 7.3) considered are (i) uniform density and uniform velocity distribution (U-U), (ii) uniform density and Maxwell velocity distribution (U-Mx), (iii) Newton’s cradle density and uniform velocity distribution (Nc-U), and (iv) Newton’s cradle density and Maxwell velocity distribution (Nc-Mx). We find that neither the density profiles nor the velocity distributions of the late-time microscopic dynamics are consistent with SMED. Remarkably, even the late-time distributions obtained by evolving different initial conditions under the microscopic dynamics are distinct from

one another, implying non-ergodicity.

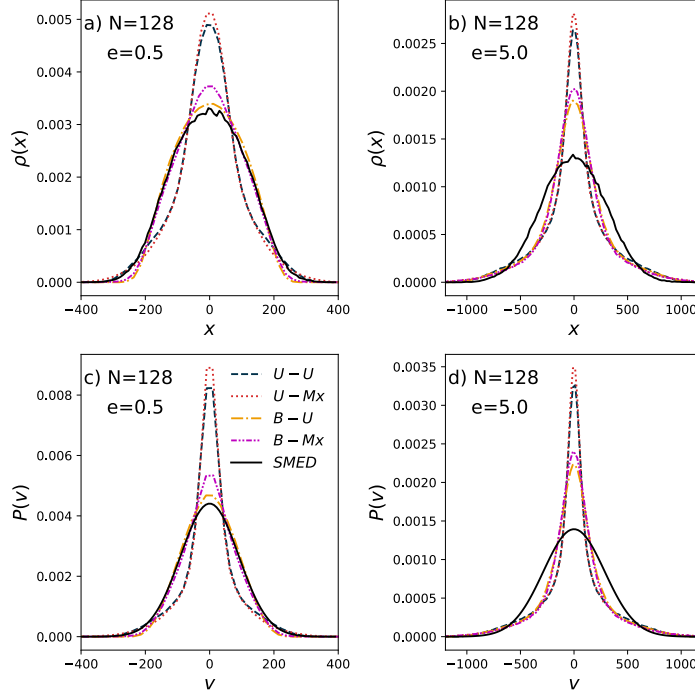


Figure 7.8: In this figure, we investigate the initial condition dependence of the late time ($t = 10^4\tau$) distributions obtained from EDMD of hard rods in a harmonic potential. These are compared with thermal predictions obtained from SMED. We compare the density and velocity profiles of 128 rods at two energies (and : (a-c) $e = 0.5$ and (b-d) $e = 5.0$). We use four different initial conditions: (i) uniform density and uniform velocity distribution (blue dashed line), (ii) uniform density and Gaussian velocity distribution (red dotted line), (iii) Newton’s cradle density and uniform velocity distribution (yellow dashed-dotted line), and (iv) Newton’s cradle density and Gaussian velocity distribution (magenta dashed-double-dotted line). We find that neither the density profile nor the velocity distribution agrees between EDMD and SMED (black solid line), even at long times $t = 10^4\tau$. We also observe that late-time density profiles depend on the choice of initial condition for both temperatures.

In sharp contrast, hard rods in a quartic trap thermalize rapidly to a Gibbs state, regardless of the choice of initial condition. This is shown for two macroscopically distinct initial conditions in Figs. 7.9a and b (for the NC-Mx initial condition) and Figs. 7.9c and d (for the U-Mx initial condition), where long-time density and velocity distributions obtained from the microscopic dynamics are compared with the expected equilibrium distributions. We observe excellent agreement for both choices of initial condition.

To characterize the lack of thermalization of the hard rods in a harmonic trap in a more quantitative manner, we characterize the ‘distance’ of the EDMD density profiles $\rho(x)$, from the expected equilibrium distributions $\rho_{SMED}(x)$ (obtained from SMED), using the

absolute value norm, defined as

$$D_{L1}(\rho, \rho_{SMED}) = \int_{-\infty}^{\infty} dx |\rho(x) - \rho_{SMED}(x)|. \quad (7.12)$$

The absolute value norm as a function of time, for two different e values, is shown in Fig. 7.10. As anticipated, D_{L1} for $e = 5.0$ is clearly larger than D_{L1} for $e = 0.5$. Furthermore, $D_{L1}(t)$ at long times ($t \sim 10^4\tau$) seems to saturate to a non-zero value, implying a lack of thermalization.

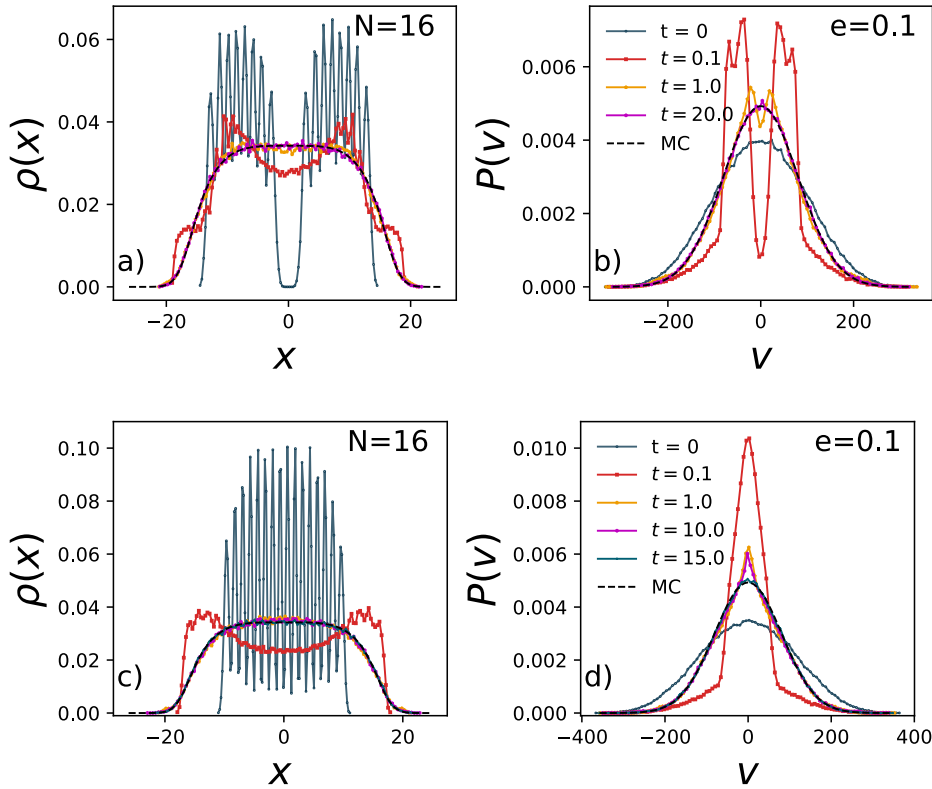


Figure 7.9: Time evolution of (a-c) MD density and (b-d) velocity distribution for hard rods in a quartic trap, starting from (a-b) Nc-Mx and (c-d) U-MX initial condition, compared with Monte-Carlo profiles for $N = 16$ and $e = 0.10$. In this case, the MD profile converges to the Monte Carlo (MC) result appreciably fast, and the velocity distribution approaches a Gaussian at late times, as expected for a non-integrable system.

7.5 Conclusions

In this paper, we have investigated chaos, ergodicity and thermalization for one-dimensional gases of classical hard rods in harmonic and quartic traps. Our work demonstrates that

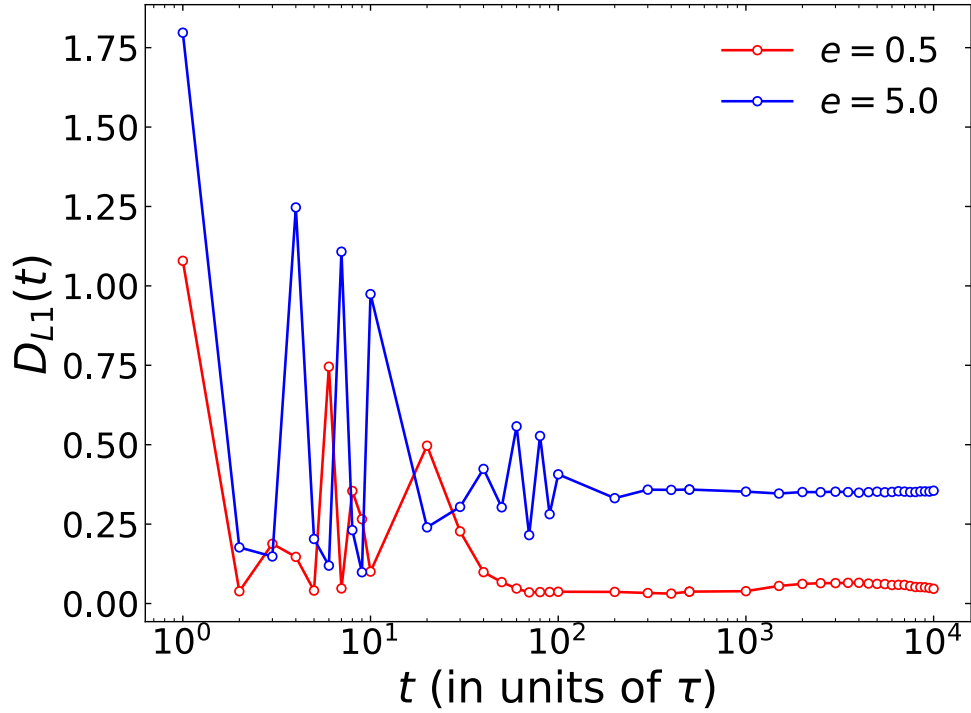


Figure 7.10: Time evolution of the distance measure, D_{L1} [defined in Eq. (7.12)], between $\rho(x)$ and $\rho_{\text{SMED}}(x)$ for $e = 0.5$ and $e = 5.0$ in a harmonic trap. For both EDMD and SMED, the system is initially prepared in the Nc-Mx initial condition. The oscillations at small times are consistent with the oscillations observed in Fig. 7.6. The saturation of D_{L1} to non-zero values at large times indicates a lack of thermalization to a Gibbs state.

thermalization properties are radically different between harmonic traps ($\delta = 2$) and quartic traps ($\delta = 4$). In the harmonic case, even though the system has a positive Lyapunov exponent confirming that integrability is broken, the dynamics nevertheless appear to be non-ergodic and fail to thermalize on the accessible timescale. This is markedly different from expectations for conventional non-integrable classical many-body systems. Our main findings for the case of $N > 3$ hard rods are summarised in Table. 7.1.

Our results hint at the existence of additional microscopic conserved (or quasi-conserved) quantities that give rise to non-ergodic behavior in a harmonic trap even when the Lyapunov exponents are positive. The special case of $N = 3$ displays non-chaotic (zero Lyapunov exponent) behavior. On the other hand, hard rods confined to quartic traps exhibit conventional non-integrable behavior, namely positive Lyapunov exponents and thermalization to the expected Gibbs state.

Our work suggests several interesting open questions for hard rods in a harmonic trap

$N > 3$	Harmonic	Quartic
Chaos	Yes (Fig. 7.2 and 7.5)	Yes (Fig. 7.4 and 7.5)
Ergodicity	No (Fig. 7.3)	Consistent with yes (Fig. 7.4)
Thermalization	No (Fig. 7.7 and 7.8)	Yes (Fig. 7.9)

Table 7.1: The table provides a summary of our findings for $N > 3$ hard rods confined to harmonic and quartic traps. The case of $N = 3$ rods in a harmonic trap is special (Fig. 7.1a,b) because it is characterized by vanishing Lyapunov exponents although its quartic counterpart, even for $N = 2$, has non-zero Lyapunov exponents (Fig. 7.1c,d).

such as: (i) finding the extra conservation law for $N = 3$, assuming this exists (it was previously argued that any such conservation law must be non-analytic in the dynamical variables [84]); (ii) understanding the dependence of λ on energy e and N (see Fig. 7.5); (iii) understanding whether hydrodynamics can capture the regime of intermediate times between the initial and late-time dynamics [84]; (iv) exploring whether this lack of ergodicity for large N has any relation to the known additional, “entropic” conservation laws of ballistic-scale GHD [83–85, 238], or some hitherto undiscovered conservation laws of the full dissipative hydrodynamics.

We expect that some of our findings will be valid more generally for systems of classical or quantum particles confined to a trap that breaks the integrability of their interactions. We note that studies of the Toda chain [206, 209] have also indicated drastic differences in transport properties in a harmonic trap compared to quartic traps. As a more extreme example of such unusual behavior, the rational Calogero model remains integrable in both harmonic and quartic traps [239], and its ballistic scale hydrodynamics is integrable in any trap [211]. A complete theory of this rich phenomenology of integrability breaking by traps remains elusive for now.

This chapter describes the study from the following published work:

D. Bagchi, **J. Kethepalli**, V.B. Bulchandani, A. Dhar, D.A. Huse, M. Kulkarni, A. Kundu, “Unusual ergodic and chaotic properties of trapped hard rods”, [Phys. Rev. E](#) **108**, 064130 (2023)

Chapter 8

Conclusions and Outlook

In this thesis, we study the classical 1d Riesz gas confined to an external potential. This system consists of N number of particles that repel each other through an all-to-all pairwise interaction, that follows a power-law behavior of the form $|x_i - x_j|^{-k}$, where x_i represents the position of the i^{th} particle. The exponent k determines the interaction range, with $k > 1$ corresponding to short-range interactions and $k < 1$ to long-range interactions. We study the Riesz gas in Gibbs equilibrium to understand how the equilibrium properties of the system change as the interactions are modified from short-range to long-range by tuning k . Furthermore, we study the equilibrium and non-equilibrium properties of the hard rods confined to an external trap at high temperatures. The hard rod model is $k \rightarrow \infty$ limit of the Riesz gas.

In our study, we focus on $k > -2$, as for smaller values of k , the repulsive potential, $|x_i - x_j|^{-k}$, becomes dominant when the particles are confined in a harmonic trap $U(x) \sim x^2$. Due to competition between the repulsive interaction and confinement, a typical configuration of this system possesses a characteristic length scale L_N which depends on the exponent k and the number of particles N . The explicit expression for L_N is provided in Eq. (2.6) and is $L_N \gtrsim O(1)$. Consequently, the total energy of the system is super extensive. To examine the equilibrium properties of the Riesz gas, we consider the system to be in Gibbs equilibrium at temperatures $T \sim O(1)$. At this temperature regime, the entropy term in the free energy is negligible in comparison to the energy term. Hence, the physical properties are dominated only by the energy term. In Ref. [45], a coarse-grained description of the system was developed in the form of field-theoretic energy. Using this field theory and the saddle point method the average density profile was computed. We

extend this method to study the equilibrium properties of various coarse-grained physical quantities of the harmonically confined Riesz gas at $T \sim O(1)$.

In chapter 3, we study the average density of a harmonically confined Riesz gas [see Eq. (2.1)] in the presence of a hard wall located at W . This density can be classified into three different regimes of k (i) short-range ($k \geq 1$), (ii) weakly long-range ($-1 < k < 1$) and (iii) strongly long-ranged ($-2 < k \leq -1$) as depicted in Figs. 2.3 and 3.1. Furthermore, we discovered a first-order phase transition for the strongly long-range system as the scaled wall position ($w = W/L_N$) is shifted to the left of a critical value $w = w^*(k)$. Below this, the wall essentially absorbs all the particles making a supercharge, and no extended part is left. The strength of the supercharge $M_k(w)$ plays the role of an order parameter that undergoes a jump to a value 1 as w is decreased through $w^*(k)$. This constrained density profile is important for the computation of the distribution of the position of the right-most particle x_{\max} in the thermodynamic limit [see Eq. (3.1)].

In chapter 4, we study the distribution of the position of the rightmost particle x_{\max} of the harmonically confined Riesz gas. We numerically observe that the typical fluctuation of $y_{\max} = x_{\max}/L_N$ around its mean is of $O(N^{-\eta_k})$. We show that the exponent η_k obtained from the Hessian theory predicts the scale of typical fluctuations remarkably well. The distribution of atypical fluctuations to the left and right of the mean $\langle y_{\max} \rangle$ are governed by the left and right large deviation functions, respectively. We compute these large deviation functions explicitly $\forall k > -2$ and numerically verify them. We also find that these large deviation functions describe a pulled-to-pushed type phase transition as observed in Dyson's log-gas ($k \rightarrow 0$) and $1d$ one component plasma ($k = -1$). Remarkably, we find that the phase transition remains 3rd order for the $-2 < k$. Our results demonstrate the striking universality of the 3rd order transition even in models that fall outside the paradigm of Coulomb systems and the random matrix theory. Furthermore, our study is an important step forward in improving our understanding of extreme value statistics in strongly correlated systems.

The study in chapter 5 provides a detailed analysis of FCS of a confined short-range Riesz gas ($k > 1$). We focused on the number and the index distribution, which characterize the fluctuations of the number of particles $\mathcal{N}(W, N)$ and $\mathcal{I}(W, N)$, respectively, in two distinct domains, namely $[-W, W]$ and $(-\infty, W]$. We analyze the probability distributions of $\mathcal{N}(W, N)$, $\mathcal{I}(W, N)$ and show that they individually exhibits a large deviation

forms for large N characterized by a speed $N^{\frac{3k+2}{k+2}}$ and by a large deviation function of the fraction of the particles (c) inside the respective domain and W . We show in Fig. 5.2, that the density profiles that create the large deviations display interesting shape transitions as one varies c and W . This shape change gets manifested by a third-order phase transition exhibited by the large deviation function that has discontinuous third derivatives. We find that the typical fluctuations of $\mathcal{N}(W, N)$ and $\mathcal{G}(W, N)$, obtained from the field theoretic calculations are Gaussian distributed with a variance that scales as N^{ν_k} , with $\nu_k = (2 - k)/(2 + k)$. Furthermore, we adapt our formalism to study the linear statistics (the variance), thermodynamic pressure and bulk modulus. Our study is a major step forward in generalizing results of Dyson's log-gas and the 1dOCP to a broader class of interacting particles *i.e.*, Riesz gas systems with $k > 1$.

In chapter 6, we study the high-temperature equilibrium properties of the hard rods and the hyperbolic Calogero model, in harmonic and quartic traps. These two models effectively correspond to special values of k of the Riesz gas, $k \rightarrow \infty$ and $k = 2$, respectively. Furthermore, they are integrable in the absence of confinement but the confinement breaks the integrability of the Hamiltonian dynamics. We study the average density profile of these two models at $T \sim O(L_N^2)$. We use field theoretic techniques to compute the density profile and their scaling with system size and temperature and compare them with results from MC simulations. A summary of the scaling forms is given in Table 6.1. In both cases, we find reasonably good agreement between the field theory and simulations (Figs. 6.2 and 6.6). Our work provides an analytical approach for understanding the equilibrium properties of interacting integrable systems in confining traps. This work provides the foundation to study the thermalization properties of integrable systems in integrability-breaking traps. We can use these density profiles to understand whether the system thermalizes to the expected Gibbs state.

In chapter 7, we shift our focus and study the dynamics of the 1d gases of classical hard rods in harmonic and quartic traps, which breaks microscopic integrability. We investigate its chaos, ergodicity and thermalization properties. To quantify the strength of chaos in this system, we compute its maximal Lyapunov exponent numerically. The approach to thermal equilibrium is studied by considering the time evolution of single particle position and velocity distributions and observe that at late time these distributions become time stationary. We compare these stationary profiles with the Gibbs state studied in the

previous chapter 6. Our work demonstrates that thermalization properties are radically different between harmonic and quartic traps. In the harmonic case, even though the system has a positive Lyapunov exponent confirming that integrability is broken, the dynamics nevertheless appear to be non-ergodic and fail to thermalize on the accessible timescale. Our results hint at the existence of additional microscopic conserved (or quasi-conserved) quantities that give rise to non-ergodic behavior in a harmonic trap even when the Lyapunov exponents are positive. The special case of $N = 3$ displays non-chaotic (zero Lyapunov exponent) behavior. On the other hand, our numerical results reveal that hard rods in a quartic trap exhibit both chaos and thermalization and equilibrate to a Gibbs state as expected for a nonintegrable many-body system. Our main findings for the case of $N > 3$ hard rods are summarised in Table. 7.1.

In this thesis we studied the Riesz gas, initially focusing on its low-temperature properties and later examining its high-temperature behaviour, particularly in cases where $k = 2$ and $k \rightarrow \infty$. We further study the unusual thermalization properties of the $k \rightarrow \infty$ case. Interesting future prospects include the study of the equilibrium properties of the Riesz gas for general k in various external traps, at high temperatures where entropy and energy have comparable contributions to free energy. Another interesting direction is to investigate the Riesz gas in higher dimensions $d > 1$, focusing on the behaviour of equilibrium density profiles. Additionally, constructing a field-theoretic free energy functional for the short-range case when $k \geq d$ remains an open problem.

The Riesz gas encompasses diverse models and exhibits complex behaviours, making its thermalization properties an intriguing area of study. Such studies could clarify the role of the range of interaction (short and long) in thermalization. While the dynamics of the Riesz gas have attracted significant interest for systems connected to a heat bath [47, 240, 241], the thermalization of an isolated Riesz gas remains an open question. One promising approach to studying this is hydrodynamics, which emphasizes the evolution of the densities of conserved quantities like mass, momentum, and energy over the microscopic observables. However, hydrodynamics assumes local equilibrium, and whether it can effectively describe long-range systems with non-local interactions is still uncertain and warrants further investigation. Similarly, in a kinetic theory approach when the interaction is weak and Kac-rescaled, one would obtain the appropriately modified Vlasov equation (see Ref. [242]). Solving the Vlasov equation could give insights

into how such systems relax.

Appendix A

Appendix

A.1 Constrained density profiles

In this Appendix, we detail our derivation of the constrained scaled density for $-1 < k < 1$ in Eq. (3.34), and for and for $-2 < k \leq -1$ in Eq. (3.48).

A.1.1 Regime 2 : $-1 < k < 1$

We start with the solution of the Sonin equation (3.31), as given in Eqs. (3.32) and (3.33). For convenience we rewrite here the particular solution $u_k(z)$ in Eq. (3.33)

$$u_k(z) = \frac{2A_k|k|z^{\frac{k-1}{2}}}{B\left(\frac{k+1}{2}, \frac{k+1}{2}\right)} \frac{\partial}{\partial z} \left(\int_z^1 t^{-k}(t-z)^{\frac{k+1}{2}} \frac{\partial}{\partial t} \int_0^t h_k(y)y^{\frac{k+1}{2}}(t-y)^{\frac{k-1}{2}} dy dt \right), \quad (\text{A.1})$$

where $h_k(z) = \mathcal{A}_k(z - q_k(w))$. This Eq. (A.1) can be written as

$$u_k(z) = \frac{2A_k|k|}{B\left(\frac{k+1}{2}, \frac{k+1}{2}\right)} z^{\frac{k-1}{2}} \frac{\partial}{\partial z} I_2(z, k) \quad (\text{A.2})$$

where

$$I_2(z, k) = \int_z^1 dt t^{-k}(t-z)^{\frac{k+1}{2}} \frac{\partial}{\partial t} I_1(t, k) \quad (\text{A.3})$$

$$I_1(t, k) = \int_0^t dy h_k(y)y^{\frac{k+1}{2}}(t-y)^{\frac{k-1}{2}}. \quad (\text{A.4})$$

The integral $I_1(t, k)$ in Eq. (A.4) can be computed explicitly and we get

$$I_1(t, k) = \frac{\mathcal{A}_k t^{1+k}}{2} B\left(\frac{k+1}{2}, \frac{k+1}{2}\right) \left(t \left(\frac{k+3}{2(k+2)} \right) - q_k(w) \right). \quad (\text{A.5})$$

Taking a derivative of the Eq. (A.5) with respect to t , we get

$$\frac{\partial}{\partial t} I_1(t, k) = B \left(\frac{k+1}{2}, \frac{k+1}{2} \right) \left(\mathcal{A}_k t^{k+1} \left(\frac{k+3}{4} \right) - \frac{\mathcal{A}_k q_k(w)(k+1)}{2} t^k \right). \quad (\text{A.6})$$

Substituting this result in Eq. (A.3), the integral $I_2(z, k)$ reads

$$I_2(z, k) = B \left(\frac{k+1}{2}, \frac{k+1}{2} \right) \left(\int_z^1 dt (t-z)^{\frac{k+1}{2}} \frac{\mathcal{A}_k(k+3)}{4} t - \int_z^1 dt (t-z)^{\frac{k+1}{2}} \frac{\mathcal{A}_k q_k(w)(k+1)}{2} \right). \quad (\text{A.7})$$

Now taking a derivative with respect to z gives

$$\frac{\partial}{\partial z} I_2(z, k) = B \left(\frac{k+1}{2}, \frac{k+1}{2} \right) \mathcal{A}_k (1-z)^{\frac{k+1}{2}} \left(\frac{q_k(w)(k+1)}{2} - \frac{(1+k+2z)}{4} \right). \quad (\text{A.8})$$

We then finally get from Eq. (A.2)

$$u_k(z) = A_k |k| z^{\frac{k-1}{2}} (1-z)^{\frac{k+1}{2}} \mathcal{A}_k \left(q_k(w)(k+1) - \frac{1+k+2z}{2} \right). \quad (\text{A.9})$$

In terms of $\gamma_k = \frac{k+1}{2}$ it reads

$$u_k(z) = -A_k |k| \mathcal{A}_k z^{\gamma_k-1} (1-z)^{\gamma_k} (z - \gamma_k(2q_k(w) - 1)). \quad (\text{A.10})$$

Substituting this in Eq. (3.32) gives

$$\phi_k(z, w) = (z(1-z))^{\gamma_k-1} \left(C_0 - A_k |k| \mathcal{A}_k (1-z) (z - \gamma_k(2q_k(w) - 1)) \right), \quad (\text{A.11})$$

which is indeed Eq. (3.34) in the main text.

A.1.2 Regime 3 : $-2 < k \leq -1$

Equation (3.46) in the main text reads explicitly

$$\int_0^1 dz' \frac{\text{sgn}(z' - z)}{|z' - z|^{k+1}} \phi_k(z', w) = \mathcal{A}_k(z - q_k(w)) + \mathcal{B}_k(g_k(w) - z)^{-(k+1)} \quad (\text{A.12})$$

where $\mathcal{A}_k = -\frac{\tilde{L}_k(w)^{k+2}}{|k|}$, $g_k(w) = \frac{w+l_w}{l_w+l_w}$, $q_k(w) = \frac{l_k(w)}{\tilde{L}_k(w)}$ and $\mathcal{B}_k = -D_k^*(w)$. The solution of the Sonin equation (A.12) is given by

$$\phi_k(z, w) = C_0(z(1-z))^{\frac{k-1}{2}} + u_k(z) \quad (\text{A.13})$$

with the particular solution $u_k(z)$ given by

$$u_k(z) = \frac{2A_k|k|z^{\frac{k-1}{2}}}{B\left(\frac{k+1}{2}, \frac{k+1}{2}\right)} \frac{\partial}{\partial z} \left(\int_z^1 dt t^{-k}(t-z)^{\frac{k+1}{2}} \frac{\partial}{\partial t} \int_0^t dy h_k(y) y^{\frac{k+1}{2}} (t-y)^{\frac{k-1}{2}} \right) \quad (\text{A.14})$$

where $h_k(z) = \mathcal{A}_k(z - q_k(w)) + \mathcal{B}_k(g_k(w) - z)^{-(k+1)}$. This can be written as

$$u_k(z) = \frac{2A_k|k|}{B\left(\frac{k+1}{2}, \frac{k+1}{2}\right)} z^{\frac{k-1}{2}} \frac{\partial}{\partial z} I_2(z, k) \quad (\text{A.15})$$

where

$$I_2(z, k) = \left(\int_z^1 dt t^{-k}(t-z)^{\frac{k+1}{2}} \frac{\partial}{\partial t} I_1(t, k) \right) \quad (\text{A.16})$$

$$I_1(t, k) = \int_0^t dy h_k(y) y^{\frac{k+1}{2}} (t-y)^{\frac{k-1}{2}}. \quad (\text{A.17})$$

The integral $I_1(t, k)$ in Eq. (A.17) becomes

$$\begin{aligned} I_1(t, k) &= \frac{\mathcal{A}_k t^{1+k}}{2} B\left(\frac{k+1}{2}, \frac{k+1}{2}\right) \left(t \left(\frac{k+3}{2(k+2)} \right) - q_k(w) \right) \\ &\quad + \mathcal{B}_k \int_0^1 dr \frac{r^{\frac{k+1}{2}} (1-r)^{\frac{k-1}{2}}}{\left(\frac{g_k(w)}{t} - r \right)^{k+1}}. \end{aligned} \quad (\text{A.18})$$

We take the derivative with respect to t to get

$$\begin{aligned} \frac{\partial}{\partial t} I_1(t, k) &= B\left(\frac{k+1}{2}, \frac{k+1}{2}\right) \left(\mathcal{A}_k t^{k+1} \left(\frac{k+3}{4} \right) - \frac{\mathcal{A}_k q_k(w)(k+1)}{2} t^k \right) \\ &\quad + \mathcal{B}_k \frac{(k+1)g}{t^2} \int_0^1 dr \frac{r^{\frac{k+1}{2}} (1-r)^{\frac{k-1}{2}}}{\left(\frac{g_k(w)}{t} - r \right)^{k+2}}. \end{aligned} \quad (\text{A.19})$$

The integral in the second term in Eq. (A.19) can be done by a change of variable

$$s = \frac{r(a-1)}{a-r} \text{ with } a = \frac{g_k(w)}{t}, \quad (\text{A.20})$$

where we have assumed that $\frac{g_k(w)}{t} \geq 1$ (which can be verified a posteriori). Doing the above variable transformation and performing the integral in Eq. (A.19) we get

$$\int_0^1 dr \frac{r^{\frac{k+1}{2}} (1-r)^{\frac{k-1}{2}}}{\left(\frac{g_k(w)}{t} - r\right)^{k+2}} = \frac{1}{2} \left(\frac{t}{g_k(w)}\right)^{k+2} B\left(\frac{k+1}{2}, \frac{k+1}{2}\right) \left(1 - \frac{t}{g_k(w)}\right)^{-\frac{k+3}{2}}. \quad (\text{A.21})$$

Using Eq. (A.21) in Eq. (A.19) we write

$$\begin{aligned} \frac{\partial}{\partial t} I_1(t, k) = B\left(\frac{k+1}{2}, \frac{k+1}{2}\right) & \left(\mathcal{A}_k t^{k+1} \left(\frac{k+3}{4}\right) - \frac{\mathcal{A}_k q_k(w)(k+1)}{2} t^k \right. \\ & \left. + \frac{\mathcal{B}_k(k+1)}{2g_k(w)} \left(\frac{t}{g_k(w)}\right)^k \left(1 - \frac{t}{g_k(w)}\right)^{-\frac{k+3}{2}} \right) \end{aligned} \quad (\text{A.22})$$

Substituting this in Eq. (A.16) we get

$$\begin{aligned} I_2(z, k) = B\left(\frac{k+1}{2}, \frac{k+1}{2}\right) & \int_z^1 dt (t-z)^{\frac{k+1}{2}} \frac{\mathcal{A}_k(k+3)}{4} t \\ & - B\left(\frac{k+1}{2}, \frac{k+1}{2}\right) \int_z^1 dt (t-z)^{\frac{k+1}{2}} \frac{\mathcal{A}_k q_k(w)(k+1)}{2} \\ & + B\left(\frac{k+1}{2}, \frac{k+1}{2}\right) \int_z^1 dt (t-z)^{\frac{k+1}{2}} \frac{\mathcal{B}_k(k+1)}{2g_k(w)^{k+1}} \left(1 - \frac{t}{g_k(w)}\right)^{-\frac{k+3}{2}}. \end{aligned} \quad (\text{A.23})$$

The first two integrals in the above equation can be straightforwardly reduced to Beta functions. For the third integral, we first transform $t \rightarrow r = (t-z)/(1-z)$ and then take a derivative with respect to z . The resulting expression for the integral is now amenable for analytical calculation once we make the transformation given in Eq. (A.20) but now with $a = (g_k(w) - z)/(1-z)$. We finally get

$$\begin{aligned} \frac{\partial}{\partial z} I_2(z, k) = B\left(\frac{k+1}{2}, \frac{k+1}{2}\right) & \mathcal{A}_k \frac{(1-z)^{\frac{k+1}{2}}}{g_k(w) - z} \left(\left(\frac{(k+1)(g_k(w) - z)q_k(w)}{2} \right) \right. \\ & \left. - \left(\frac{(1+k+2z)(g_k(w) - z)}{4} + \frac{\mathcal{B}_k g_k(w)(k+1)}{2\mathcal{A}_k(g_k(w)(g_k(w) - 1))^{\frac{k+1}{2}}} \right) \right). \end{aligned} \quad (\text{A.24})$$

Using this expression in Eq. (A.15), we get

$$u_k(z) = A_k |k| \frac{z^{\frac{k-1}{2}} (1-z)^{\frac{k+1}{2}}}{g_k(w) - z} \mathcal{A}_k \left(\left(q_k(w)(k+1) - \frac{1+k+2z}{2} \right) (g_k(w) - z) - \frac{\mathcal{B}_k}{\mathcal{A}_k} \frac{g_k(w)(k+1)}{(g_k(w)(g_k(w)-1))^{\frac{k+1}{2}}} \right). \quad (\text{A.25})$$

In terms of $\gamma_k = \frac{k+1}{2}$ it reads

$$u_k(z) = -A_k |k| \frac{z^{\gamma_k-1} (1-z)^{\gamma_k}}{g_k(w) - z} \mathcal{A}_k \left((\gamma_k(1-2q_k(w)) + z)(g_k(w) - z) + \frac{\mathcal{B}_k}{\mathcal{A}_k} \frac{2\gamma_k g_k(w)}{(g_k(w)(g_k(w)-1))^{\gamma_k}} \right). \quad (\text{A.26})$$

Substituting the above expression in Eq. (A.13) gives

$$\phi_k(z, w) = (z(1-z))^{\gamma_k-1} \left[C_o - A_k |k| (1-z) \mathcal{A}_k (\gamma_k(1-2q_k(w)) + z) - A_k |k| \frac{1-z}{g_k(w) - z} \mathcal{B}_k \frac{2\gamma_k g_k(w)}{(g_k(w)(g_k(w)-1))^{\gamma_k}} \right], \quad (\text{A.27})$$

which is indeed Eq. (3.48) in the main text.

A.2 System size dependence of $\sigma_{y_{\max}}$

Here, we provide plots of the numerical data for $\log_2 \sigma_{y_{\max}}^2$ vs $\log_2 N$ (symbols) in Fig. A.1 (for confined Riesz gas [Eq. (2.1)]) and Fig. A.2 (for the Hessian Hamiltonian [Eq. (4.24)]) for different values of k . For each k the slope of the linear fit (solid lines) of this data provides the exponent $(\eta_k, \eta_k^{\text{(hMC)})}$ which we plot in Fig. 4.3.

A.3 Large deviation functions

In this appendix, we present the details of the derivation of the LDF ($\Phi_{\pm}(w, k)$) which characterizes the distribution of the atypical fluctuations. To obtain the LDF $\Phi_{\pm}(w, k)$, we use the energy functional Eq. (3.17) in the formal expression of the LDF given in Eq. (4.43). We study all the three regimes of k separately and compute $\Phi_{\pm}(w, k)$, for (a)

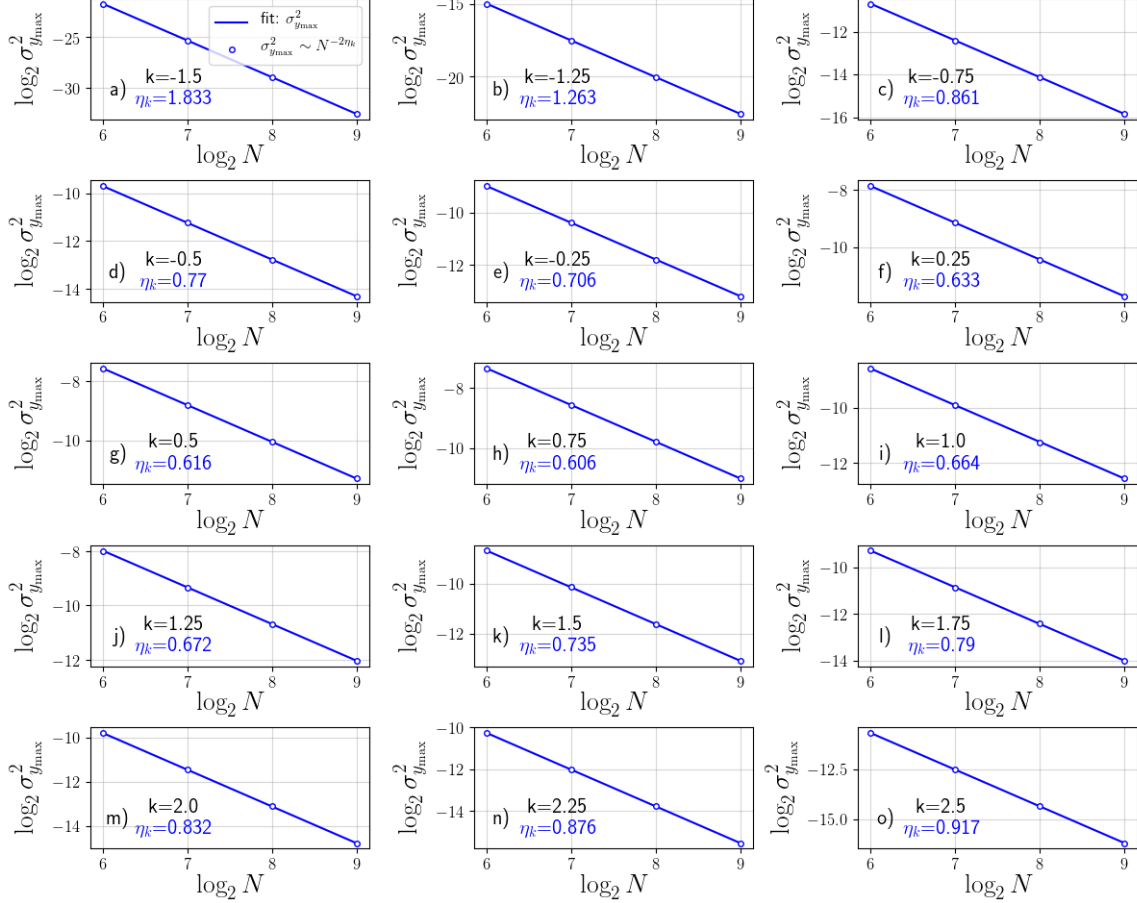


Figure A.1: Plots of the logarithm of the variance of the position of the rightmost particle obtained using the MC simulations of the confined Riesz gas Hamiltonian [Eq. (2.1)] versus the logarithm (base-2) of system size N (disks) for (a) $k = -1.5$, (b) $k = -1.25$, (c) $k = -0.75$, (d) $k = -0.5$, (e) $k = -0.25$, (f) $k \rightarrow 0$, (g) $k = 0.25$, (h) $k = 0.5$, (i) $k = 0.75$, (j) $k = 1.0$, (l) $k = 1.25$, (n) $k = 1.5$, (m) $k = 1.75$, (n) $k = 2.25$, (o) $k = 2.5$. Here we use a linear fit (solid lines) of the data to extract the slope $-2\eta_k$.

$k > 1$ given in Eq. (4.47) and (4.48), (b) $-1 < k < 1$ given in Eq. (4.55) and (4.56) and (c) $-2 < k \leq -1$ given in Eq. (4.69) and (4.71).

A.3.1 Regime 1 : $k > 1$

Left large deviation function: We start by rewriting the expression of the left LDF $\Phi_-(w, k)$ given in Eq. (4.43) as

$$\Phi_-(w, k) = \frac{1}{2(k+1)} \left(l_k(w)^2 - (l_{\text{uc}})^2 + k \int_{-l_k(w)}^w dy y^2 \rho_k^*(y, w) - k \int_{-l_{\text{uc}}}^{l_{\text{uc}}} dy y^2 \rho_{\text{uc}}(y) \right). \quad (\text{A.28})$$

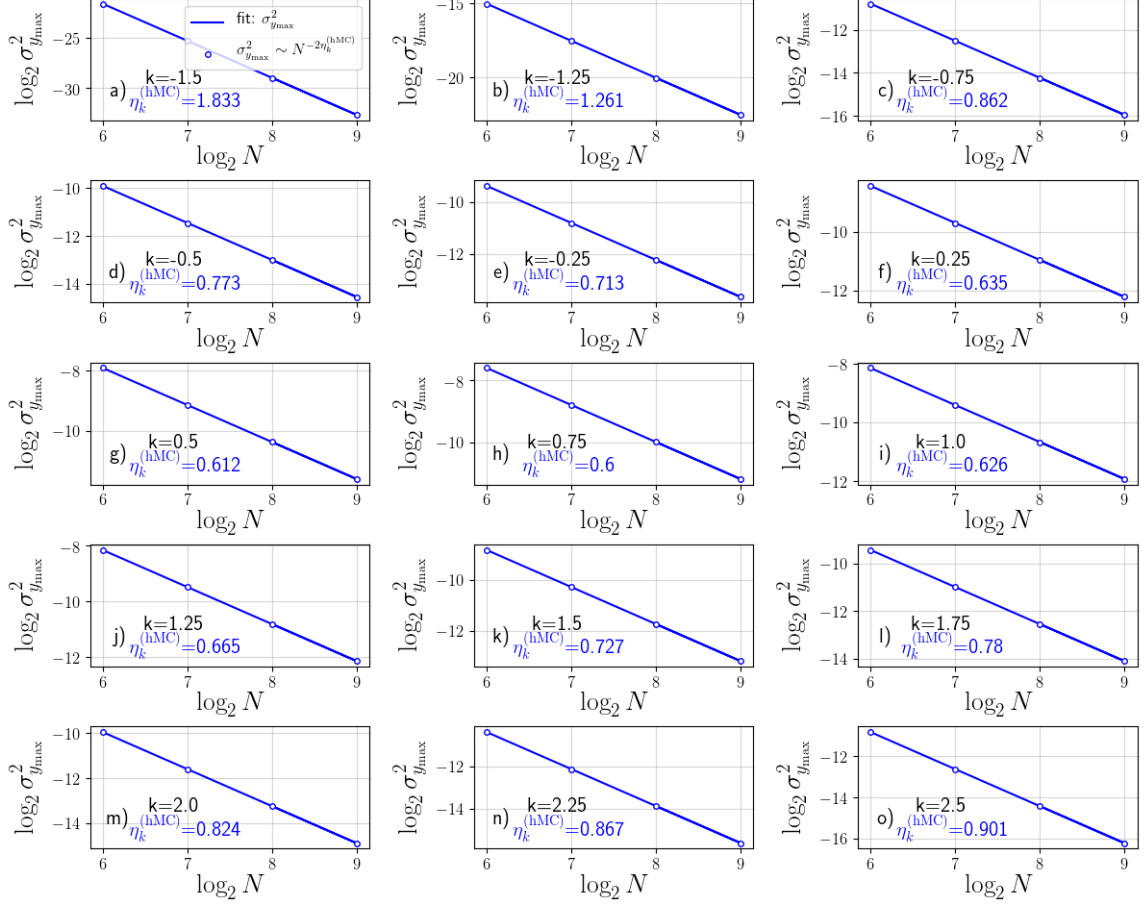


Figure A.2: Plots of the logarithm of the variance of the position of the rightmost particle obtained using the MC simulations for the Hessian Hamiltonian [Eq. (4.24)] versus the logarithm (base-2) of system size N (disks) for (a) $k = -1.5$, (b) $k = -1.25$, (c) $k = -0.75$, (d) $k = -0.5$, (e) $k = -0.25$, (f) $k \rightarrow 0$, (g) $k = 0.25$, (h) $k = 0.5$, (i) $k = 0.75$, (j) $k = 1.0$, (l) $k = 1.25$, (n) $k = 1.5$, (m) $k = 1.75$, (n) $k = 2.25$, (o) $k = 2.5$. Here we use a linear fit (solid lines) of the data to extract the slope $-2\eta_k^{(\text{hMC})}$.

Substituting the expression of the constrained density from Eq. (4.44), unconstrained density from Eq. (2.18) in Eq. (A.28), and using a variable transformation

$$z = \frac{y + l_k(w)}{2l_k(w)}, \quad (\text{A.29})$$

the left LDF can be expressed in terms of an auxiliary variable, $m_k(w) = \frac{w+l_k(w)}{2l_k(w)}$ [see Eq. (4.45)] as

$$\begin{aligned} \Phi_-(w, k) = & \frac{1}{2(k+1)} \left[l_k(w)^2 - (l_{\text{uc}})^2 + kA_k(l_k(w))^{2\gamma_k+3} \int_0^{m_k(w)} dz \left(z - \frac{1}{2} \right)^2 (z(1-z))^{\gamma_k} \right. \\ & \left. - kA_k(l_{\text{uc}})^{2\gamma_k+3} \int_0^1 dz \left(z - \frac{1}{2} \right)^2 (z(1-z))^{\gamma_k} \right]. \end{aligned} \quad (\text{A.30})$$

Using Eq. (4.46) in Eq. (A.28) we can further simplify the expression in terms of incomplete Beta function as given in Eq. (4.47), i.e.,

$$\begin{aligned} \Phi_-(w, k) = & \frac{l_k(w)^2}{2(k+1)} \left[1 + \frac{4k}{B(m_k(w), \gamma_k+1, \gamma_k+1)} \left(B(m_k(w), \gamma_k+3, \gamma_k+1) \right. \right. \\ & \left. \left. - B(m_k(w), \gamma_k+2, \gamma_k+1) + \frac{B(m_k(w), \gamma_k+1, \gamma_k+1)}{4} \right) \right] - \frac{(l_{\text{uc}})^2(k+2)}{2(3k+2)}. \end{aligned} \quad (\text{A.31})$$

Right large deviation function: The formal expression for the PDF of the atypical fluctuation to the right of the mean is given in Eq. (4.41) from which the right LDF can be written as

$$\Phi_+(w, k) = \left(\frac{w^2 - l_{\text{uc}}^2}{2} + \frac{JN}{L_N^{k+2}} \int dy \rho_{\text{uc}}^*(y) \left(\frac{1}{|w-y|^k} - \frac{1}{|l_{\text{uc}}-y|^k} \right) \right). \quad (\text{A.32})$$

Note that the right LDF has two parts: (1) an external potential term and (2) an interaction term. In the large- N limit, the interaction term becomes negligible, since $N \rightarrow \infty$ implies $N/L_N^{k+2} \rightarrow 0$, compared to the external potential term, which is a consequence of the short-ranged nature of the force. Hence, we obtain Eq. (4.48) which is given by

$$\Phi_+(w, k) = \frac{w^2 - (l_{\text{uc}})^2}{2}. \quad (\text{A.33})$$

A.3.2 Regime 2 : $-1 < k < 1$

Left large deviation function: The expression for left LDF given in Eq. (4.43) is simplified using the formal equation for the chemical potential Eq. (3.28) which gives

$$\Phi_-(w, k) = \int_{-l_k(w)}^w dy \frac{y^2}{4} \rho_k^*(y, w) - \int_{-l_{uc}}^{l_{uc}} dy \frac{y^2}{4} \rho_{k,uc}^*(y) + \frac{2\mu_k^*(w) - (l_{uc})^2}{4}. \quad (\text{A.34})$$

We substitute the expression for the constrained density profile $[\rho_k^*(y, w)]$ from Eq. (3.38) and the unconstrained density profile $[\rho_{k,uc}^*(y)]$ from Eq. (2.18) in the above simplified expression Eq. (A.34). Using the change of variable

$$z = \frac{y + l_k(w)}{L_k(w)} \text{ with } L_k(w) = w + l_k(w), \quad (\text{A.35})$$

where $L_k(w)$ is the total size of the support, one can express Eq. (A.34) in terms of auxiliary variables

$$g_k(w) = \frac{\tilde{l}_k(w) + l_k(w)}{L_k(w)} \text{ and } q_k(w) = \frac{l_k(w)}{L_k(w)} = \frac{1}{2} + \frac{g_k(w) - 1}{k + 1}. \quad (\text{A.36})$$

In terms of these auxiliary variables, the left LDF takes the form

$$\begin{aligned} \Phi_-(w, k) &= A_k (L_k(w))^{2\gamma_k+3} \int_0^1 dz \frac{(z - q_k(w))^2}{4} (g_k(w) - z) z^{\frac{k+1}{2}} (1 - z)^{\frac{k-1}{2}} \\ &\quad - A_k (2l_{uc})^{2\gamma_k+3} \int_0^1 dz \frac{(z - \frac{1}{2})^2}{4} (z(1 - z))^{\frac{k+1}{2}} + \frac{2\mu_k^*(w) - (l_{uc})^2}{4}. \end{aligned} \quad (\text{A.37})$$

To proceed further we now need to compute the chemical potential $\mu_k^*(w)$.

The chemical potential in Eq. (3.28) can be simplified by a variable transformation given in Eq. (A.35) which gives

$$\mu_k^*(w) = L_k(w)^2 \left[\frac{(z - q_k(w))^2}{2} + A_k \text{sgn}(k) \int_0^1 dr \frac{r^{\frac{k+1}{2}} (1 - r)^{\frac{k-1}{2}}}{|z - r|^k} (g_k(w) - r) \right]. \quad (\text{A.38})$$

The integral in the square bracket can be split into two integrals as

$$\begin{aligned} \int_0^1 dr \frac{r^{\frac{k+1}{2}} (1 - r)^{\frac{k-1}{2}}}{|z - r|^k} (g_k(w) - r) &= \int_0^z dr \frac{r^{\frac{k+1}{2}} (1 - r)^{\frac{k-1}{2}}}{(z - r)^k} (g_k(w) - r) \\ &\quad + \int_z^1 dr \frac{r^{\frac{k+1}{2}} (1 - r)^{\frac{k-1}{2}}}{(r - z)^k} (g_k(w) - r). \end{aligned} \quad (\text{A.39})$$

The first integral in Eq. (A.39) can be further simplified by using the following variable transformation

$$s_1 = \frac{z-r}{z}, \quad (\text{A.40})$$

which gives

$$\begin{aligned} & \int_0^z dr \frac{r^{\frac{k+1}{2}} (1-r)^{\frac{k-1}{2}}}{(z-r)^k} (g_k(w) - r) \\ &= z^2 \int_0^1 ds_1 \frac{s_1^{-k} (1-s_1)^{\frac{k+1}{2}}}{\left(s_1 + \frac{1-z}{z}\right)^{\frac{1-k}{2}}} \left(s_1 + \frac{g_k(w) - z}{z}\right) \\ &= \left(\frac{1-z}{z}\right)^{\frac{k-1}{2}} \left[z^2 B\left(2-k, \frac{k+3}{2}\right) {}_2F_1\left[\frac{1-k}{2}, 2-k, \frac{7-k}{2}, \frac{z}{z-1}\right] \right. \\ & \quad \left. + z(g_k(w) - z) B\left(1-k, \frac{k+3}{2}\right) {}_2F_1\left[\frac{1-k}{2}, 1-k, \frac{5-k}{2}, \frac{z}{z-1}\right] \right]. \end{aligned} \quad (\text{A.41})$$

Similarly, the second integral in Eq. (A.39) can be further simplified by using the following variable transformation

$$s_2 = \frac{r-z}{1-z}, \quad (\text{A.42})$$

which gives

$$\begin{aligned} & \int_z^1 dr \frac{r^{\frac{k+1}{2}} (1-r)^{\frac{k-1}{2}}}{(r-z)^k} (g - r) \\ &= (1-z)^2 \int_0^1 ds_2 \frac{s_2^{-k} (1-s_2)^{\frac{k-1}{2}}}{\left(s_2 + \frac{z}{1-z}\right)^{-\frac{1+k}{2}}} \left(\frac{g-z}{1-z} - s_2\right) \\ &= \left(\frac{z}{1-z}\right)^{\frac{k+1}{2}} \left[(1-z)(g-z) B\left(1-k, \frac{k+1}{2}\right) {}_2F_1\left[-\frac{k+1}{2}, 1-k, \frac{3-k}{2}, \frac{z-1}{z}\right] \right. \\ & \quad \left. - (1-z)^2 B\left(2-k, \frac{k+1}{2}\right) {}_2F_1\left[-\frac{k+1}{2}, 2-k, \frac{5-k}{2}, \frac{z-1}{z}\right] \right]. \end{aligned} \quad (\text{A.43})$$

Note that the argument of the hypergeometric function in Eq. (A.41) is $\frac{z}{z-1}$ whereas in Eq. (A.43) it is $\frac{z-1}{z}$. Hence to simplify this further we use the following hypergeometric

function identity [243]

$$\begin{aligned}
B(b+1, a+1) {}_2F_1 \left[a+1, c, a+b+2, -\frac{1}{u} \right] \\
= u^{a+1} B(-a+c-1, a+1) {}_2F_1 [a+1, -b, a-c+2, -u] \\
+ u^c B(b+1, a-c+1) {}_2F_1 [c, -a-b+c-1, c-a, -u].
\end{aligned} \tag{A.44}$$

Substituting the above identity in Eq. (A.41), we can express the Eq. (A.41) as a function of $\frac{z-1}{z}$ instead of $\frac{z}{z-1}$. Then using the new expression in terms of $\frac{z-1}{z}$ and Eq. (A.43) in Eq. (A.38), we can simplify the expression of $\mu_k^*(w)$ which after a tedious calculation gives

$$\mu_k^*(w) = L_k(w)^2 \left(\frac{1}{8k} + \frac{(g_k(w) - 1)^2}{2(k+1)^2} + \frac{g_k(w) - 1}{2k(k+1)} \right). \tag{A.45}$$

Since the chemical potential is a constant, we can independently find the value of $\mu_k^*(w)$ by substituting $z = 0$ or $z = 1$ in Eq. (A.38). This expression is verified by numerically evaluating the integrals in Eq. (A.38) directly and comparing with Eq. (A.45). This comparison is shown in Fig. A.3. The remaining integrals in the left LDF given in

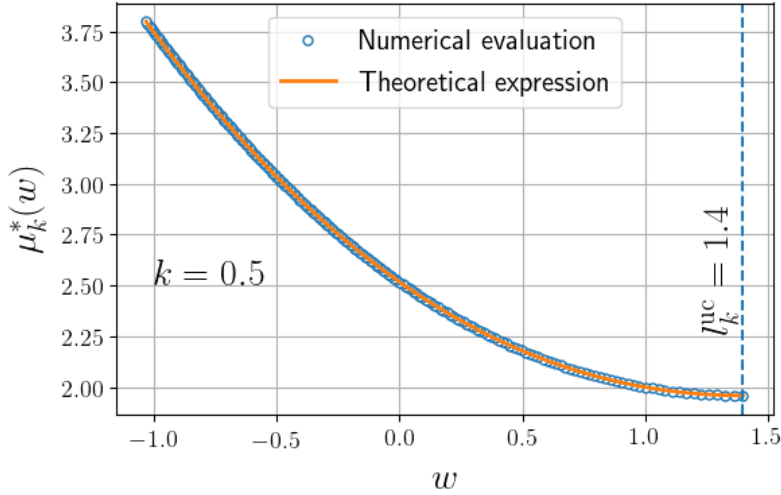


Figure A.3: *Regime 2* ($-1 < k < 1$): For $k = 0.5$, the plot of chemical potential as a function of the wall position, computed from numerical integration (circles) of Eq. (A.38) for $z = 0$. This evaluation is compared with the simplified expression given in Eq. (A.45) (solid lines). The parameter used for the computations is $J = 1$.

Eq. (A.37) can be expressed as beta functions. Now using the expression of the chemical

potential from Eq. (A.45) in Eq. (A.37) we get

$$\begin{aligned} \Phi_-(w, k) = & (k+2)(l_{\text{uc}})^2 \left[\left(1 + \frac{2(k+2)}{k+1}(g_k(w) - 1) \right)^{-\frac{k+4}{k+2}} \left[\frac{1}{2k(k+4)} \right. \right. \\ & \left. \left. + \frac{(g_k(w) - 1)}{k(k+1)} + \frac{2(g_k(w) - 1)^2}{k(k+1)^2} + \frac{4(g_k(w) - 1)^3}{(1+k)^3} \right] - \frac{1}{2k(k+4)} \right], \end{aligned} \quad (\text{A.46})$$

as announced in Eq. (4.55). Here, the length of the constrained support $L_k(w) = w/(1 - g_k(w))$ was expressed in terms of the auxiliary variable $g_k(w)$ which was obtained using Eq. (3.39).

Right large deviation function: In this regime both the external potential term and the interaction term contribute equally to the right LDF in Eq. (A.32) since $N \rightarrow \infty$ implies $N/L_N^{k+2} \rightarrow 1$. Hence the right LDF is given by

$$\Phi_+(w, k) = A_k \text{sgn}(k) \left(\int_{-l_{\text{uc}}}^{l_{\text{uc}}} dy \frac{((l_{\text{uc}})^2 - y^2)^{\frac{k+1}{2}}}{(w - y)^k} \right) + \frac{w^2}{2} - \frac{(l_{\text{uc}})^2}{2k}. \quad (\text{A.47})$$

Using the following variable transformation

$$z = \frac{l_{\text{uc}} - y}{2l_{\text{uc}}} \quad \text{and} \quad g_{\text{uc}}(w)^{-1} = \frac{w + l_{\text{uc}}}{2l_{\text{uc}}}, \quad (\text{A.48})$$

Eq. (A.47) can be expressed as

$$\Phi_+(w, k) = (2l_{\text{uc}})^2 \left(A_k \text{sgn}(k) \int_0^1 dz \frac{(z(1-z))^{\frac{k+1}{2}}}{(z + g_{\text{uc}}(w)^{-1} - 1)^k} + \frac{(2g_{\text{uc}}(w)^{-1} - 1)^2}{8} - \frac{1}{8k} \right). \quad (\text{A.49})$$

This can be further simplified to

$$\begin{aligned} \Phi_+(w, k) = & (l_{\text{uc}})^2 \frac{32(g_{\text{uc}}(w)^{-1} - 1)^{\frac{3-k}{2}} B(2+k, \frac{5-k}{2})}{(k+3)(k+5)(k+7)} \times \\ & {}_2F_1\left[-\frac{k+1}{2}, \frac{k+3}{2}, \frac{5-k}{2}, 1 - g_{\text{uc}}(w)^{-1}\right]. \end{aligned} \quad (\text{A.50})$$

which is Eq. (4.56) of the main text.

A.3.3 Regime 3 : $-2 < k \leq -1$

We start by expressing the normalization condition $\int_{-l_k(w)}^w dy \rho_k^*(y, w) = 1$ in terms of the auxiliary variable $h_k(w)$ given in Eq. (4.67). Using the expression of the constrained density given in Eq. (4.63) and the variable transformation

$$z = \frac{\bar{l}_k(w) - y}{\tilde{L}_k(w)} \text{ with } \tilde{L}_k(w) = \bar{l}_k(w) + l_k(w), \quad (\text{A.51})$$

we get

$$\begin{aligned} \int_{-l_k(w)}^w \rho_k^*(y, w) &= \left(\tilde{L}_k(w) \right)^{2\gamma_k+1} \left(A_k \int_0^1 dz \frac{z^{\frac{k+3}{2}} (1-z)^{\frac{k+1}{2}}}{z + h_k(w) - 1} + \frac{h_k(w)^{\frac{k+1}{2}} (h_k(w) - 1)^{\frac{k+3}{2}}}{k(k+1)} \right) \\ &= \left(\tilde{L}_k(w) \right)^{2\gamma_k+1} \left(A_k \left((h_k(w) - 1)^{\frac{k+3}{2}} h_k(w)^{\frac{k+1}{2}} B \left(-\frac{k+3}{2}, \frac{k+5}{2} \right) \right. \right. \\ &\quad \left. \left. + B \left(\frac{k+3}{2}, \frac{k+3}{2} \right) {}_2F_1 \left[1, -(k+2), -\frac{k+1}{2}, 1 - h_k(w) \right] \right) \right. \\ &\quad \left. + \frac{h_k(w)^{\frac{k+1}{2}} (h_k(w) - 1)^{\frac{k+3}{2}}}{k(k+1)} \right), \end{aligned} \quad (\text{A.52})$$

where $\tilde{L}_k(w)$ is the size of the support of the extended part of the density profile. This equation can be further simplified by using the fact that

$$A_k B \left(-\frac{k+3}{2}, \frac{k+5}{2} \right) = \frac{1}{|k|(k+1)}, \quad (\text{A.53})$$

which then gives

$$\left(\frac{\tilde{L}_k(w)}{2l_{uc}} \right)^{2\gamma_k+1} {}_2F_1 \left[1, -(k+2), -\frac{k+1}{2}, 1 - h_k(w) \right] = 1. \quad (\text{A.54})$$

The position of the wall can be expressed as $w = \tilde{L}_k(w)(h_k(w) - n_k(w))$ where

$$n_k(w) = \frac{l_k(w)}{\tilde{L}_k(w)} = \frac{1}{2} + \frac{1 - h_k(w)}{k+1}. \quad (\text{A.55})$$

The relation between $n_k(w)$ and $h_k(w)$ is obtained using Eq. (4.65). This finally gives Eq. (4.68).

Left Large deviation function: Since the structure of the field theory is the same, the formal expression of the left LDF in this regime is similar to the previous regime given in Eq. (A.34). However, the density profiles here are different, as in this regime the constrained density given in Eq. (4.63) has a delta function of strength $D_k^*(w)$ and a disjoint extended part denoted as $\rho_b^*(y, w)$. For convenience we here write the explicit expression of $\rho_b^*(y, w)$ from Eq. (4.63) as

$$\rho_b^*(y, w) = A_k \frac{(l_k(w) + y)^{\frac{k+1}{2}} (\bar{l}_k(w) - y)^{\frac{k+3}{2}}}{(w - y)}. \quad (\text{A.56})$$

We use $\rho_k^*(y, w) = \rho_b^*(y, w)\mathbb{I}[-l_k(w) < y \leq \bar{l}_k(w)] + D_k^*(w)\delta(y - w)$ in Eq. (A.34) which gives

$$\begin{aligned} \Phi_-(w, k) &= \frac{2\mu_k^*(w) + D_k(w)w^2}{4} + \int_{-l_k(w)}^{\bar{l}_k(w)} dy \frac{y^2}{4} \rho_b^*(y, w) \\ &\quad - \frac{(l_{\text{uc}})^2}{4} - \int_{-l_{\text{uc}}}^{l_{\text{uc}}} dy \frac{y^2}{4} \rho_{k,\text{uc}}^*(y). \end{aligned} \quad (\text{A.57})$$

We substitute the expressions of $\rho_b^*(y, w)$ from Eq. (A.56), $D_k^*(w)$ from Eq. (3.52) and $\rho_{k,\text{uc}}^*(y)$ from Eq. (2.18) in the above equation. Using the variable change given in Eq. (A.51), we can now express the left LDF in terms of auxiliary variables $h_k(w)$ and $n_k(w)$ given in Eq. (4.67) and Eq. (A.55), respectively. The left LDF then becomes

$$\begin{aligned} \Phi_-(w, k) &= A_k \left(\tilde{L}_k(w) \right)^{2\gamma_k+3} \int_0^1 dz \frac{(1 - q_k(w) - z)^2}{4} \frac{z^{\frac{k+3}{2}} (1 - z)^{\frac{k+1}{2}}}{z + h_k(w) - 1} \\ &\quad - A_k (2l_{\text{uc}})^{2\gamma_k+3} \int_0^1 dz \frac{(z - \frac{1}{2})^2}{4} (z(1 - z))^{\frac{k+1}{2}} + \frac{2\mu_k^*(w) + w^2 D_k^*(w) - (l_{\text{uc}})^2}{4}. \end{aligned} \quad (\text{A.58})$$

To simplify this expression further we evaluate the chemical potential $\mu_k^*(w)$ first by substituting the expression of the constrained density Eq. (4.63) in Eq. (4.62) and we get

$$\begin{aligned} \mu_k^*(w) &= \frac{y^2}{2} - \int_{-l_k(w)}^w dy' \frac{\rho_k^*(y', w)}{|y' - y|^k} \\ &= \frac{y^2}{2} - A_k \int_{-l_k(w)}^{\bar{l}_k(w)} dy' \frac{(l_k(w) + y')^{\frac{k+1}{2}} (\bar{l}_k(w) - y')^{\frac{k+3}{2}}}{(w - y')|y' - y|^k} - \frac{D_k^*(w)}{(w - y)^k}. \end{aligned} \quad (\text{A.59})$$

It turns out to be non-trivial to compute it for an arbitrary value of y . However, it can

be calculated for specific values $y = -l_k(w)$ and $y = \bar{l}_k(w)$. Here we compute it for $y = \bar{l}_k(w)$, which formally gives

$$\begin{aligned} \mu_k^*(w) &= \frac{\bar{l}_k(w)^2}{2} - A_k \int_{-l_k(w)}^{\bar{l}_k(w)} dy' \frac{(l_k(w) + y')^{\frac{k+1}{2}} (\bar{l}_k(w) - y')^{\frac{3-k}{2}}}{(w - y')} \\ &\quad - \frac{D_k^*(w)}{(w - \bar{l}_k(w))^k}. \end{aligned} \quad (\text{A.60})$$

To perform the above integral, we use the variable transformation given in Eq. (A.51) which simplifies the equation to

$$\begin{aligned} \mu_k^*(w) &= \tilde{L}_k(w)^2 \left[\frac{(1 - n_k(w))^2}{2} - A_k \int_0^1 dz \frac{(1 - z)^{\frac{k+1}{2}} z^{\frac{3-k}{2}}}{(z + h_k(w) - 1)} \right. \\ &\quad \left. - \frac{h_k(w)^{\frac{k+1}{2}} (h_k(w) - 1)^{\frac{3-k}{2}}}{k(k+1)} \right] \\ &= \tilde{L}_k(w)^2 \left[\frac{(1 - n_k(w))^2}{2} - A_k \frac{B\left(\frac{5-k}{2}, \frac{k+3}{2}\right) {}_2F_1\left(\frac{5-k}{2}, 1, 4, \frac{1}{1-h_k(w)}\right)}{h_k(w) - 1} \right. \\ &\quad \left. - \frac{h_k(w)^{\frac{k+1}{2}} (h_k(w) - 1)^{\frac{3-k}{2}}}{k(k+1)} \right]. \end{aligned} \quad (\text{A.61})$$

Further using the hypergeometric identity in Eq. (A.44) and Eq. (A.55), one gets the following simplified equation

$$\mu_k^*(w) = \tilde{L}_k(w)^2 \left(\frac{1}{8k} - \frac{h_k(w) - 1}{2k(k+1)} - \frac{(h_k(w) - 1)^2(k+2)}{2k(k+1)^2} \right). \quad (\text{A.62})$$

To verify the validity of this expression we numerically perform the integral in Eq. (A.59) and compare it with Eq. (A.62) in Fig. A.4. The left LDF given in Eq. (A.58), can be further simplified by using the expression of the chemical potential from Eq. (A.62) and

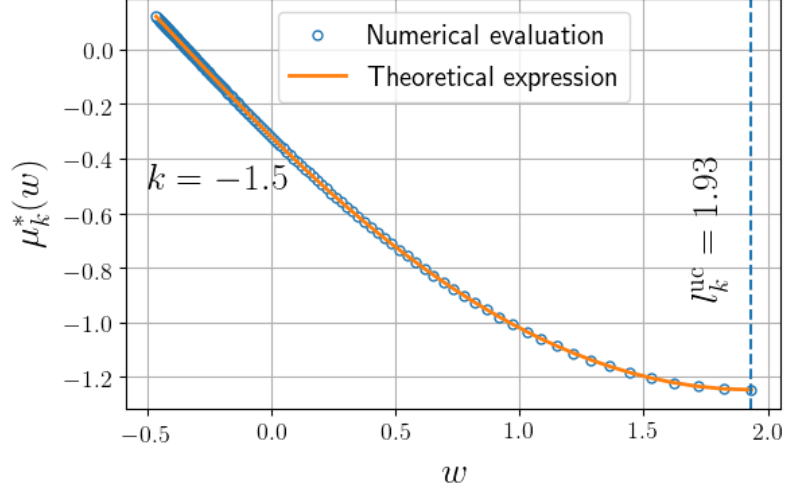


Figure A.4: *Regime 3* ($-2 < k < -1$): For $k = -1.5$, the plot of chemical potential as a function of wall position, computed from numerical integration (circle) given in Eq. (4.62) and the simplified expression (solid lines) given in Eq. (A.62). Here we considered $J = 1$.

representing the integrals in terms of hypergeometric functions,

$$\begin{aligned}
& A_k \int_0^1 dz \frac{(1 - n_k(w) - z)^2}{4} \frac{z^{\frac{k+3}{2}} (1-z)^{\frac{k+1}{2}}}{z + h_k(w) - 1} \\
&= \frac{A_k}{4} \left[n_k(w)^2 \int_0^1 dz \frac{z^{\frac{k+3}{2}} (1-z)^{\frac{k+1}{2}}}{z + h_k(w) - 1} - 2n_k(w) \int_0^1 dz \frac{z^{\frac{k+3}{2}} (1-z)^{\frac{k+3}{2}}}{z + h_k(w) - 1} \right. \\
&\quad \left. + \int_0^1 dz \frac{z^{\frac{k+3}{2}} (1-z)^{\frac{k+5}{2}}}{z + h_k(w) - 1} \right] \\
&= \frac{A_k}{4(h_k(w) - 1)} \left[n_k(w)^2 B\left(\frac{k+3}{2}, \frac{k+5}{2}\right) {}_2F_1\left[\frac{k+5}{2}, 1, k+4, \frac{1}{1-h_k(w)}\right] \right. \\
&\quad - 2n_k(w) B\left(\frac{k+5}{2}, \frac{k+5}{2}\right) {}_2F_1\left[\frac{k+5}{2}, 1, k+5, \frac{1}{1-h_k(w)}\right] \\
&\quad \left. + B\left(\frac{k+5}{2}, \frac{k+7}{2}\right) {}_2F_1\left[\frac{k+5}{2}, 1, k+6, \frac{1}{1-h_k(w)}\right] \right].
\end{aligned} \tag{A.63}$$

Using the hypergeometric identity given in Eq. (A.44) in Eq. (A.63) and simplifying, we

get

$$\begin{aligned}
A_k \int_0^1 dz & \frac{(1 - n_k(w) - z)^2 z^{\frac{k+3}{2}} (1 - z)^{\frac{k+1}{2}}}{4(z + h_k(w) - 1)} \\
& = \frac{A_k}{4} B\left(\frac{3+k}{2}, \frac{3+k}{2}\right) \\
& \times {}_2F_1\left[1, -(k+2), -\frac{k+1}{2}, 1 - h_k(w)\right] \left[n_k(w)^2 \right. \\
& - n_k(w) \frac{{}_2F_1\left[1, -(k+3), -\frac{k+1}{2}, 1 - h_k(w)\right]}{{}_2F_1\left[1, -(k+2), -\frac{k+1}{2}, 1 - h_k(w)\right]} \\
& \left. + \frac{k+5}{4(k+4)} \frac{{}_2F_1\left[1, -(k+4), -\frac{k+1}{2}, 1 - h_k(w)\right]}{{}_2F_1\left[1, -(k+2), -\frac{k+1}{2}, 1 - h_k(w)\right]} \right] \\
& - \frac{h_k(w)^{\frac{k+1}{2}} (h_k(w) - 1)^{\frac{k+3}{2}}}{4k(k+1)} \left(\frac{2(k+2)h_k(w) - (k+3)}{2(k+1)} \right)^2.
\end{aligned} \tag{A.64}$$

This Eq. (A.64) can be expressed further as

$$\begin{aligned}
A_k \int_0^1 dz & \frac{(1 - n_k(w) - z)^2 z^{\frac{k+3}{2}} (1 - z)^{\frac{k+1}{2}}}{4(z + h_k(w) - 1)} \\
& = \frac{1}{4 \left(\tilde{L}_k(w) \right)^{k+2}} \left[n_k(w)^2 - n_k(w) \frac{{}_2F_1\left[1, -(k+3), -\frac{k+1}{2}, 1 - h_k(w)\right]}{{}_2F_1\left[1, -(k+2), -\frac{k+1}{2}, 1 - h_k(w)\right]} \right. \\
& \left. + \frac{k+5}{4(k+4)} \frac{{}_2F_1\left[1, -(k+4), -\frac{k+1}{2}, 1 - h_k(w)\right]}{{}_2F_1\left[1, -(k+2), -\frac{k+1}{2}, 1 - h_k(w)\right]} \right] \\
& - \frac{h_k(w)^{\frac{k+1}{2}} (h_k(w) - 1)^{\frac{k+3}{2}}}{4k(k+1)} \left(\frac{2(k+2)h_k(w) - (k+3)}{2(k+1)} \right)^2.
\end{aligned} \tag{A.65}$$

where we used Eq. (A.54). We then use this expression along with the simplified expression of the chemical potential given in Eq. (A.62) and the normalization condition from Eq. (A.54) to get the final expression for left LDF given in Eq. (4.69).

A.4 Importance sampling method

Using a conventional Markov chain Monte-Carlo simulation using the Metropolis-Hashting algorithm, we can explore the probabilities of the order n_{mc}^{-1} , where $n_{mc} \equiv$ number of data points. However, to compute the probability of the extremely rare events say of order 10^{-20} is not feasible to use this algorithm. Hence, we use the importance sampling method [141, 142, 244] which is described here.

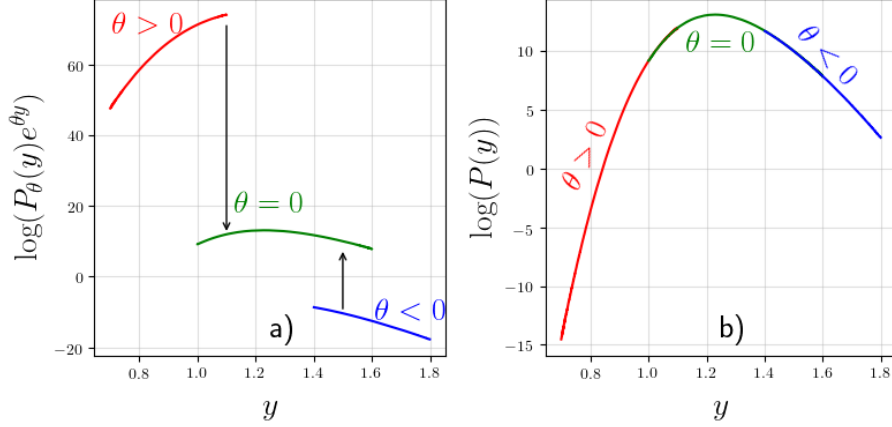


Figure A.5: (a) We join the $P_\theta(y_{\max})e^{\theta y_{\max}}$ for different values of θ by multiplying them by the appropriate normalization constant considering there is a small overlap in the argument of the distribution for two successive values of θ . (b) This stitching procedure gives the distribution of y_{\max} in the unbiased problem for rare fluctuations.

Probability of the position of the edge particle for a given ensemble is

$$P(y) = \sum_{\{y_i\}} Q[\{y_i\}] \delta(y - y_{\max}), \quad (\text{A.66})$$

where $Q[\{y_i\}]$ is the probability of a configuration $\{y_i\}$ and y_{\max} is the position of the rightmost particle. To sample atypical values of y_{\max} one needs to bias the sampling procedure in the simulation. We run a Markov chain Monte-Carlo simulation using a biased Metropolis-Hastings Algorithm given by the following weight for the jump from configuration $\{y_i\}$ to $\{y'_i\}$:

$$A(\{y_i\}, \{y'_i\}) = \min \left(1, \frac{Q[\{y'_i\}]}{Q[\{y_i\}]} e^{(-\theta(y'_{\max} - y_{\max}))} \right). \quad (\text{A.67})$$

More precisely $A(\{y_i\}, \{y'_i\})$ is the probability of acceptance of the new configuration ($\{y'_i\}$) given a configuration ($\{y_i\}$). Note that $\theta > 0$ biases the ensemble to have smaller y_{\max} and $\theta < 0$ does the opposite. The stationary distribution of this Markov chain is given by $Q_\theta[\{y_i\}] = Q[\{y_i\}]e^{-\theta y_{\max}}$.

Now using this algorithm one can numerically compute the PDF of y_{\max} in the biased

simulation which we denote by $P_\theta(y)$. We have

$$\begin{aligned}
P_\theta(y) &= \sum_{\{y_i\}} Q_\theta[\{y_i\}] \delta(y - y_{\max}), \\
&= \sum_{\{y_i\}} Q[\{y_i\}] e^{-\theta y_{\max}} \delta(y - y_{\max}), \\
&= e^{-\theta y} \sum_{\{y_i\}} Q[\{y_i\}] \delta(y - y_{\max}),
\end{aligned} \tag{A.68}$$

which from Eq. (A.66) gives

$$P(y) = \sum_{\{y_i\}} Q[\{y_i\}] \delta(y - y_{\max}) = P_\theta(y) e^{\theta y}. \tag{A.69}$$

Using this relation Eq. (A.69), we can compute the PDF $[P(y_{\max} = y)]$ of extremely large fluctuations of y_{\max} which can be obtained by considering larger absolute values of θ . However for any θ the width of the distribution obtained numerically is finite. Hence to compute the PDF which also includes the rare fluctuations one has to simulate $P_\theta(y)$ for many values of θ and these different biased PDFs are glued together by multiplying by the appropriate normalization prefactor to $P_\theta(y)$ such that $\theta \neq 0$ connects smoothly with $\theta = 0$. A schematic cartoon of this procedure is shown in Fig. A.5.

A.5 Non-analytic properties of LDF $\Phi(c, w)$

In this appendix, we investigate the non-analytic properties of the LDFs $\Phi(c, w)$ as given in Eqs. (5.36) and (5.37). We study the series expansions of the LDF $\Phi(c, w)$ around $c = \bar{c}(w)$ for a fixed value of w , where $\bar{c}(w) = (w/l_0)^{\frac{1}{\alpha_k}}$ and around $w = \bar{w}(c)$ for a fixed value of c , where $\bar{w}(c) = c^{\alpha_k} l_0$. For this analysis, we take advantage of the separable nature of the LDF *i.e.* $\Phi(c, w) = \mathcal{E}_{\text{in}} + \mathcal{E}_{\text{out}} - G_{\text{uc}}$ for the number distribution problem [see Eq. (5.30)]. The energy \mathcal{E}_{in} and \mathcal{E}_{out} for the particles inside and outside the box

$[-w, w]$ is given by

$$\mathcal{E}_{\text{in}} = \begin{cases} G_{\text{uc}} \times c^{2\alpha_k+1} & \text{for } c \leq \bar{c}(w) \\ G_{\text{uc}} \times c^{2\alpha_k+1} \mathcal{J}\left(\frac{w}{\bar{l}}\right) & \text{for } c > \bar{c}(w) \end{cases} \quad \text{and,} \quad (\text{A.70})$$

$$\mathcal{E}_{\text{out}} = G_{\text{uc}} \times (1-c)^{2\alpha_k+1} \mathcal{H}\left(\frac{w}{\bar{l}}\right), \quad (\text{A.71})$$

where the constant G_{uc} is given in Eq. (5.28) and, the functions $\mathcal{J}(h)$ and $\mathcal{H}(h)$ are given in Eq. (5.32) and Eq. (5.31), respectively. Here the length scales l and \bar{l} are given in Eqs. (5.22) and (5.25).

A.5.1 $\Phi(c, w)$ for $c \sim \bar{c}(w)$ for a fixed w

We first present the series expansion of the \mathcal{E}_{in} and \mathcal{E}_{out} separately as follows:

Energy within the box (\mathcal{E}_{in}): When the fraction of particles c within the box $[-w, w]$ is slightly greater than the $\bar{c}(w)$, i.e., $c = (1 + \epsilon)\bar{c}(w)$ with $0 < \epsilon \ll 1$, we can find the free energy of particles inside the box by expanding the expression in Eq. (A.70) in terms of ϵ . This expansion yields the following series:

$$\mathcal{E}_{\text{in}} = G_{\text{uc}} (\bar{c}(w))^{1+2\alpha_k} \left[1 + \mathbb{A}_{\text{in}} \epsilon + \mathbb{B}_{\text{in}} \epsilon^2 + \mathbb{C}_{\text{in}+} (\epsilon)^{2+\frac{1}{k}} + o(\epsilon^{2+\frac{1}{k}}) \right], \quad \text{where,} \quad (\text{A.72})$$

$$\mathbb{A}_{\text{in}} = 1 + 2\alpha_k, \quad \mathbb{B}_{\text{in}} = \frac{(1 + 2\alpha_k)2\alpha_k}{2}, \quad \mathbb{C}_{\text{in}+} = \frac{k^2(1 + 2\alpha_k)(2\alpha_k)^{2+\frac{1}{k}}}{(k+1)(2k+1) B\left(\frac{1}{2}, \frac{1}{k} + 1\right)}. \quad (\text{A.73})$$

To obtain Eq. (A.72) we use the expressions of \bar{l} and l which are functions of c and w and are given in Eqs. (5.22) and (5.25). The notation small ‘ o ’ specifically $o(\epsilon^a)$ indicates corrections smaller than ϵ^a as $\epsilon \rightarrow 0$.

Conversely, when the fraction of particles within the box is smaller than $\bar{c}(w)$ and satisfies $c = (1 + \epsilon)\bar{c}(w)$, with $\epsilon < 0$ and $|\epsilon| \ll 1$, we find that the energy of the particles inside the box is given by:

$$\mathcal{E}_{\text{in}} = G_{\text{uc}} (\bar{c}(w))^{1+2\alpha_k} \left[1 + \mathbb{A}_{\text{in}} \epsilon + \mathbb{B}_{\text{in}} \epsilon^2 + \mathbb{C}_{\text{in}-} \epsilon^3 + O(\epsilon^4) \right], \quad (\text{A.74})$$

where the constants \mathbb{A}_{in} and \mathbb{B}_{in} are given in Eq. (A.73), and

$$\mathbb{C}_{\text{in-}} = \frac{(1 - 4\alpha_k^2)2\alpha_k}{6}. \quad (\text{A.75})$$

Energy outside the box (\mathcal{E}_{out}): Similarly, we examine the energy of particles outside the box given in Eq. (A.71). We find the following expansion in powers of ϵ

$$\mathcal{E}_{\text{out}} = G_{\text{uc}} (1 - \bar{c}(w))^{1+2\alpha_k} \left[\mathcal{H}^{(0)}(\tilde{h}) + \mathbb{A}_{\text{out}} \epsilon + \mathbb{B}_{\text{out}} \epsilon^2 + \mathbb{C}_{\text{out}} \epsilon^3 + O(\epsilon^4) \right], \quad (\text{A.76})$$

$$\mathbb{A}_{\text{out}} = \tilde{h} \gamma_{\text{out}} \mathcal{H}^{(1)}(\tilde{h}) - \frac{\bar{c}(w)(1 + 2\alpha_k)}{1 - \bar{c}(w)}, \quad (\text{A.77})$$

$$\mathbb{B}_{\text{out}} = \frac{(\bar{c}(w))^2 2\alpha_k(1 + 2\alpha_k)}{2(1 - \bar{c}(w))^2} + \frac{\tilde{h}^2 \gamma_{\text{out}}^2 \mathcal{H}^{(2)}(\tilde{h})}{2} - \frac{\bar{c}(w) h \gamma_{\text{out}} \mathcal{H}^{(1)}(\tilde{h})(1 + 2\alpha_k)}{1 - \bar{c}(w)}, \quad (\text{A.78})$$

$$\begin{aligned} \mathbb{C}_{\text{out}} = & -\frac{(\bar{c}(w))^3 2\alpha_k(4\alpha_k^2 - 1)}{6(1 - \bar{c}(w))^3} + \frac{(\bar{c}(w))^2 \tilde{h} \gamma_{\text{out}} \mathcal{H}^{(1)}(\tilde{h}) 2\alpha_k(1 + 2\alpha_k)}{2(1 - \bar{c}(w))^2} + \frac{h^3 \gamma_{\text{out}}^3 \mathcal{H}^{(3)}(\tilde{h})}{6} \\ & - \frac{\bar{c}(w) \tilde{h}^2 \gamma_{\text{out}}^2 \mathcal{H}^{(2)}(\tilde{h})(1 + 2\alpha_k)}{2(1 - \bar{c}(w))}, \end{aligned} \quad (\text{A.79})$$

where $\tilde{h} = w/l(\bar{c}(w), w)$ and $\mathcal{H}^{(n)}(\tilde{h})$ is the n^{th} derivative of $\mathcal{H}(\tilde{h})$ given in Eq. (5.31).

The constant γ_{out} is given by

$$\gamma_{\text{out}} = \frac{\bar{c}(w)\alpha_k}{1 - \bar{c}(w)} \left[\frac{1 - I\left(\tilde{h}^2, \frac{1}{2}, 1 + \frac{1}{k}\right)}{1 - I\left(\tilde{h}^2, \frac{1}{2}, 1 + \frac{1}{k}\right) + 2\alpha_k \frac{\tilde{h}(1 - \tilde{h}^2)^{\frac{1}{k}}}{B\left(\frac{1}{2}, \frac{1}{k} + 1\right)}} \right], \quad (\text{A.80})$$

where the function $I(g, a, b)$ is given in Eq. (5.24).

We can now calculate the LDF $\Phi(\bar{c}(w)(1 + \epsilon), w)$ for small $|\epsilon| \ll 1$ by substituting the expressions of the energies from Eqs. (A.72), (A.74) and (A.76) in the expression of the LDF $\Phi(c, w)$ given in Eq. (5.27). This yields:

$$\Phi(\bar{c}(w)(1 + \epsilon), w) - \Phi(\bar{c}(w), w) = \begin{cases} \tilde{\mathbb{A}} \epsilon + \tilde{\mathbb{B}} \epsilon^2 + \tilde{\mathbb{C}}_+ \epsilon^{2+\frac{1}{k}} + o(\epsilon^{2+\frac{1}{k}}), & \text{for } \epsilon > 0 \\ \tilde{\mathbb{A}} \epsilon + \tilde{\mathbb{B}} \epsilon^2 + \tilde{\mathbb{C}}_- \epsilon^3 + O(\epsilon^4), & \text{for } \epsilon < 0 \end{cases}, \quad (\text{A.81})$$

where the constants are given by

$$\tilde{\mathbb{A}} = G_{\text{uc}} \left((\bar{c}(w))^{1+2\alpha_k} \mathbb{A}_{\text{in}} + (1 - \bar{c}(w))^{1+2\alpha_k} \mathbb{A}_{\text{out}} \right), \quad (\text{A.82})$$

$$\tilde{\mathbb{B}} = G_{\text{uc}} \left((\bar{c}(w))^{1+2\alpha_k} \mathbb{B}_{\text{in}} + (1 - \bar{c}(w))^{1+2\alpha_k} \mathbb{B}_{\text{out}} \right), \quad (\text{A.83})$$

$$\tilde{\mathbb{C}}_+ = G_{\text{uc}} (\bar{c}(w))^{1+2\alpha_k} \mathbb{C}_{\text{in}+}, \quad \tilde{\mathbb{C}}_- = G_{\text{uc}} \left((\bar{c}(w))^{1+2\alpha_k} \mathbb{C}_{\text{in}-} + (1 - \bar{c}(w))^{1+2\alpha_k} \mathbb{C}_{\text{out}} \right). \quad (\text{A.84})$$

The values of \mathbb{A}_{in} , \mathbb{B}_{in} , \mathbb{C}_{in} , \mathbb{A}_{out} , \mathbb{B}_{out} and \mathbb{C}_{out} are provided in Eqs. (A.73), (A.77), (A.78) and (A.79). From Eq. (A.81), we find that the third derivative of the LDF $\Phi(c, w)$ w.r.t. c shows a discontinuity at $c = \bar{c}(w)$, which is a signature of a third order phase transition.

A.5.2 $\Phi(c, w)$ for $w \sim \bar{w}(c)$ for a fixed c

By following the same procedure as in the previous subsection A.5.1, we can expand the LDFs $\Phi(c, (1 + \epsilon)\bar{w}(c))$ in powers of ϵ , for small $|\epsilon| \ll 1$ at a fixed c . We find:

$$\Phi(c, \bar{w}(c)(1 + \epsilon)) - \Phi(c, \bar{w}(c)) = \begin{cases} \tilde{\mathbb{D}} \epsilon + \tilde{\mathbb{E}} \epsilon^2 + \tilde{\mathbb{F}}_+ \epsilon^3 + O(\epsilon^4), & \text{for } \epsilon > 0 \\ \tilde{\mathbb{D}} \epsilon + \tilde{\mathbb{E}} \epsilon^2 + \tilde{\mathbb{F}}_- |\epsilon|^{2+\frac{1}{k}} + o(|\epsilon|^{2+\frac{1}{k}}), & \text{for } \epsilon < 0 \end{cases}, \quad (\text{A.85})$$

where the constants are given by

$$\tilde{\mathbb{D}} = G_{\text{uc}} (1 - \bar{c}(w))^{1+2\alpha_k} \tilde{h} \Gamma_{\text{out}} \mathcal{H}^{(1)}(\tilde{h}), \quad \tilde{\mathbb{E}} = G_{\text{uc}} (1 - \bar{c}(w))^{1+2\alpha_k} \frac{\Gamma_{\text{out}}^2 \tilde{h}^2}{2} \mathcal{H}^{(2)}(\tilde{h}), \quad (\text{A.86})$$

$$\tilde{\mathbb{F}}_+ = G_{\text{uc}} (1 - \bar{c}(w))^{1+2\alpha_k} \frac{\Gamma_{\text{out}}^3 \tilde{h}^3}{6} \mathcal{H}^{(3)}(\tilde{h}), \quad \tilde{\mathbb{F}}_- = G_{\text{uc}} \frac{(\bar{c}(w))^{1+2\alpha_k} k^2 (1 + 2\alpha_k) (2)^{2+\frac{1}{k}}}{(k+1)(2k+1) B\left(\frac{1}{2}, \frac{1}{k} + 1\right)}, \quad (\text{A.87})$$

where in this case $\tilde{h} = \bar{w}(c)/l(c, \bar{w}(c))$ and the function $\mathcal{H}^{(n)}(h)$ is the n^{th} derivative of $\mathcal{H}(h)$ given in Eq. (5.31). The constant Γ_{out} is given by

$$\Gamma_{\text{out}} = \left[\frac{1 - I\left(\tilde{h}^2, \frac{1}{2}, 1 + \frac{1}{k}\right)}{1 - I\left(\tilde{h}^2, \frac{1}{2}, 1 + \frac{1}{k}\right) + 2\alpha_k \frac{\tilde{h}(1-\tilde{h}^2)^{\frac{1}{k}}}{B\left(\frac{1}{2}, \frac{1}{k}+1\right)}} \right]. \quad (\text{A.88})$$

Here the function $I(g, a, b)$ is given in Eq. (5.24). From Eq. (A.85), we find that the third derivative of the LDF $\Phi(c, w)$ w.r.t. w shows a discontinuity at $w = \bar{w}(c)$ which is a signature of a third order phase transition.

A.6 Pressure and Bulk modulus

For the short-range Riesz gas, we find that the index problem provides a natural setup to compute the pressure in the bulk of the gas. Consider the unconstrained Riesz gas in thermal equilibrium characterized by the density profile $\rho_0(y)$ from Eq. (2.18). The thermodynamic pressure of this gas at a location W can be thought of as the free energy change of the particles to the left of W when they are pushed by moving a wall from W by an infinitesimal amount ϵ_N . Using the separable (additive) nature of free energy in Eq. (5.45), one can easily identify the free energy of the left partition which is given by

$$\Psi^{(L)}(c^*(w), w) = N^{1+2\alpha_k} \frac{G_{\text{uc}}}{2} \left((2c^*(w))^{\frac{3k+2}{k+2}} \mathcal{J}\left(\frac{w}{\bar{l}}\right) \right), \quad (\text{A.89})$$

where $w = W/N^{\alpha_k}$, \bar{l} is given in the Eq. (5.48) and $c^*(w) = \int_{-l_0}^w dy \rho_0(y)$, represents the fraction of particles below W when the gas is at equilibrium (without any constraint). Also, the function $\mathcal{J}(h)$ in Eq. (A.89) is given in Eq. (5.46). When the particles on the left are pushed by moving a wall from W to $W - \epsilon_N$ the free energy on the left changes to $\Psi^{(L)}(c^*(w), w - \epsilon)$ where $\epsilon = \epsilon_N/N^{\alpha_k}$. Note the fraction of particle on the left of $W - \epsilon_N$ remains the same. The pressure is then obtained by taking a derivative of the free energy of the left partition and can be written as

$$\begin{aligned} \mathbb{P}(W, N) &= N^{1+\alpha_k} \frac{d}{d\epsilon} \Psi^{(L)}(c^*(w), w - \epsilon) \Big|_{\epsilon=0} \\ &= N^{\frac{2(k+1)}{k+2}} \mathbf{P} \left(\frac{W}{N^{\alpha_k}} \right), \end{aligned} \quad (\text{A.90})$$

where the scaling function $\mathbf{P}(w)$ is given by

$$\mathbf{P}(w) = J\zeta(k)k(\rho_0(w))^{k+1}. \quad (\text{A.91})$$

One can also define a mechanical pressure $\mathbb{P}_M(W, N)$ locally at W as the average force exerted by the particles above W on the particles below W and can be expressed as

$$\mathbb{P}_M(W, N) = \left\langle \sum_{i=1}^s \sum_{j=s+1}^N \frac{1}{|x_j - x_i|^{k+1}} \right\rangle, \quad (\text{A.92})$$

where $x_s \leq W < x_{s+1}$ and x_i 's are the unscaled positions of the particles. We remark that the definition of the local mechanical pressure does not involve the external potential explicitly, but only implicitly through the average over the equilibrium measure in Eq. (A.92).

We observe that in our model the mechanical pressure $\mathbb{P}_M(W, N)$ [see Eq. (A.92)] and the thermodynamic pressure $\mathbb{P}(W, N)$ [see Eq. (A.90)] yield the same result as shown in Fig. A.6a. Since the gas is confined to a harmonic trap the pressure is not uniform as expected. It is maximum at the center of the trap and decreases as we go further from the center of the trap and becomes zero at the edge of the support of the scaled density profile at $y = l_0$ because the value of the density decreases to zero.

Bulk modulus: As usually done in statistical mechanics, to define the bulk modulus we here consider the change of the mean position $\langle x_m \rangle$ of a particle inside the bulk (say the m^{th}) due to an external force F applied only on that particle. The bulk modulus is defined as

$$\frac{1}{\mathbb{K}_m} = -\frac{1}{\beta} \frac{\partial \langle x_m \rangle}{\partial F} \Big|_{F=0} = \frac{1}{\beta^2} \partial_F^2 \ln Z(\beta, F) \Big|_{F=0}, \quad (\text{A.93})$$

where $Z(\beta, F)$ is the partition function of the system in the presence of an external force F on the m^{th} particle *i.e.* with the energy function $\tilde{E}_F(\{x_i\}) = \tilde{E}_k(\{x_i\}) + Fx_m$ that appears in the Gibbs-Boltzmann distribution. A straightforward calculation shows the following fluctuation-response relation

$$\frac{1}{\mathbb{K}_m} = \langle x_m^2 \rangle - \langle x_m \rangle^2 = N^{2\alpha_k} (\langle y_m^2 \rangle - \langle y_m \rangle^2), \quad (\text{A.94})$$

where we have used the scaled position $y_m = x_m/N^{\alpha_k}$.

To obtain the bulk modulus at position W , denoted by $\mathbb{K}(W, N)$, we need to compute the variance of the position y_m of the m^{th} particle such that $m = c^*(w)N$ with $w = W/N^{\alpha_k}$ and $c^*(w) = \int_{-l_0}^w dy \rho_0(y)$. In other words

$$\mathbb{K}(W, N) = \mathbb{K}_{m=c^*(w)N} \text{ with } w = \frac{W}{N^{\alpha_k}}. \quad (\text{A.95})$$

To proceed, we first note that

$$\text{Prob.}[y_m \leq w] = \mathcal{P}(\mathcal{G} = m, N), \quad (\text{A.96})$$

where from Section 5.4 we have

$$\mathcal{P}(\mathcal{G} = m, N) \asymp \exp\left(-\beta N^{1+2\alpha_k} \Psi\left(\frac{m}{N}, w\right)\right). \quad (\text{A.97})$$

From this probability distribution, it is straightforward to see that

$$\langle y_m^2 \rangle - \langle y_m \rangle^2 = \left(\beta N^{1+2\alpha_k} \frac{d^2}{d\epsilon^2} \Psi(c^*(w), w - \epsilon) \Big|_{\epsilon=0} \right)^{-1}. \quad (\text{A.98})$$

Inserting Eq. (A.98) in Eq. (A.94), we get

$$\mathbb{K}(W, N) = N \mathbf{K}\left(\frac{W}{N^{\alpha_k}}\right), \text{ where,} \quad (\text{A.99})$$

$$\mathbf{K}(w) = \frac{k}{(k+2)} \left[\frac{l_0^2 (\rho_0(w))^2}{\left(c^*(w) - \frac{k}{k+2} w \rho_0(w)\right) \left(1 - \left(c^*(w) - \frac{k}{k+2} w \rho_0(w)\right)\right)} \right]. \quad (\text{A.100})$$

In Fig. A.6b, $\mathbf{K}(w)$ given in Eq. (A.100) is plotted and compared with \mathbb{K}_m , obtained from MC simulations. We observe a good agreement as stated in Eq. (A.95) which improves as N is increased. In this figure, we observe that the bulk modulus monotonically decreases starting from a finite value at the center of the trap and approaches zero at the edge of support of the scaled density profile $\rho_0(y)$ at l_0 . Near the edge of the scaled density profile, l_0 , the bulk modulus $\mathbf{K}(w \rightarrow l_0) \sim (l_0 - w)^{\frac{1}{k}}$ and its derivative exhibits a discontinuity.

This reflects a third-order phase transition, interpreting the bulk modulus as an order parameter.

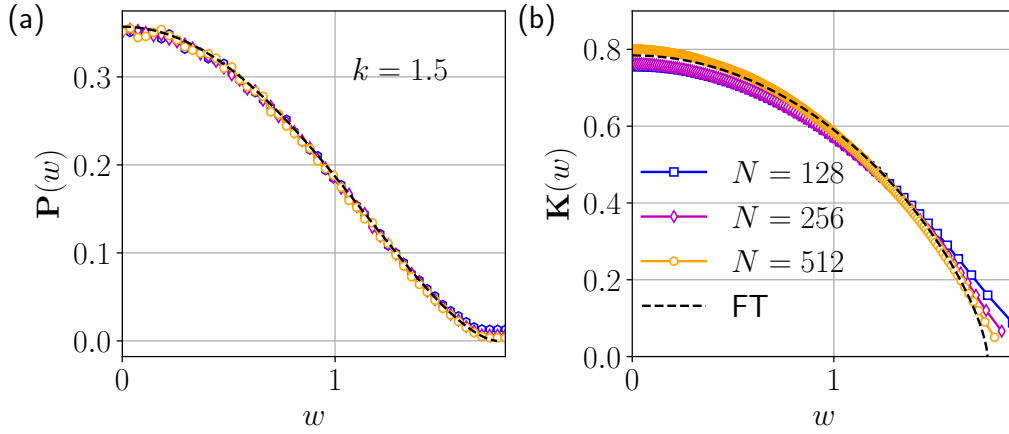


Figure A.6: In (a) we plot the scaling function of the thermodynamic pressure [Eq. (A.91)], $\mathbf{P}(w)$, as depicted by the dashed line and the scaled average mechanical pressure [Eq. (A.92)], $\mathbf{P}_M(wN^{\alpha_k}, N)/N^{\frac{2(k+1)}{k+2}}$, as indicated by symbols. The average in Eq. (A.92) is computed using the MC simulations. In plot (b), the scaling function of the bulk modulus [Eq. (A.100)], $\mathbf{K}(w)$, as depicted by the dashed line is compared with \mathbb{K}_m/N [Eq. (A.94)] where $m = c^*(w)N$ and is shown by symbols. In Eq. (A.94), the variance of the position of the m^{th} particle is computed using the MC simulations. We use $k = 1.5$, $T = 1$, and $J = 1$ for performing the MC simulations of the unconstrained gas consisting of $N = 128, 256$ and 512 particles and the averages are computed using 10^6 samples.

A.7 Variance of linear statistics

In this section, we study the variance of linear statistics $S_N = \sum_{i=1}^N r(y_i)$ [Eq. (5.50)] for arbitrary function $r(y)$. Note that $r(y) = \Theta(w - y)\Theta(w + y)$ and $r(y) = \Theta(w - y)$ correspond the number problem and index problem, respectively. To compute the variance we adapt the method of the field theory described in Ref. [220]. We are computing the typical fluctuations of S_N around its mean $\langle S_N \rangle = \langle s \rangle N$ where $\langle s \rangle$ is given in Eq. (5.52). We express S_N as $S_N = N(\langle s \rangle + \kappa)$ where $N\kappa$ is the fluctuation. To compute the variance, we consider the small deviations, $\Delta\rho_r \ll 1$, of the density profile from the unconstrained density profile as

$$\rho_r(y) = \rho_0(y) + \Delta\rho_r(y). \quad (\text{A.101})$$

Note that the deviation in density profile satisfies the constraints in Eq. (5.56), which becomes

$$\int_{-l_0}^{l_0} dy \Delta\rho_r(y) = 0, \quad \int_{-l_0}^{l_0} dy r(y)\Delta\rho_r(y) = \kappa, \quad (\text{A.102})$$

where the limits of the integrals have been approximated to leading order. Using the Eq. (A.101) in the saddle point equation Eq. (5.53) and assuming the contribution due to the higher order terms $O((\Delta\rho_r^*)^3)$ are negligible, gives

$$\Delta\rho_r^*(y) = \frac{\Delta\mu_k^* + r(y)\Delta\mu_r^*}{J\zeta(k)(k+1)(k)} (\rho_0(y))^{1-k}, \quad (\text{A.103})$$

where ‘*’ represents the saddle point value. Here $\Delta\mu_k^* = \mu_k^* - \mu_0$ and $\Delta\mu_r^* = \mu_r^*$. Inserting the expression of the perturbed density from Eq. (A.103) in the constraints in Eq. (A.102) we get

$$\Delta\mu_k^*J_0 + \Delta\mu_r^*J_1 = 0, \quad \Delta\mu_k^*J_1 + \Delta\mu_r^*J_2 = \kappa, \quad (\text{A.104})$$

with the constants J_0, J_1, J_2 given explicitly in Eq. (5.60) and (5.61) which we recall to be

$$J_0 = 2\frac{A_k}{k} \int_{-l_0}^{l_0} dy (l_0^2 - y^2)^{\frac{1}{k}-1}, \quad J_1 = 2\frac{A_k}{k} \int_{-l_0}^{l_0} dy r(y) (l_0^2 - y^2)^{\frac{1}{k}-1}, \quad (\text{A.105})$$

$$J_2 = 2\frac{A_k}{k} \int_{-l_0}^{l_0} dy r(y)^2 (l_0^2 - y^2)^{\frac{1}{k}-1}. \quad (\text{A.106})$$

Solving for $\Delta\mu_k^*$ and $\Delta\mu_r^*$ in Eq. (A.104) one finds

$$\mu_k^* = \mu_0 - \frac{\kappa J_1}{J_2 J_0 - J_1^2}, \quad \mu_r^* = \frac{\kappa J_0}{J_2 J_0 - J_1^2}. \quad (\text{A.107})$$

Inserting the expression for the perturbed density $\rho_r^*(y) = \rho_0(y) + \Delta\rho_r(y)$ with $\Delta\rho_r(y)$ from Eq. (A.103) and the perturbed chemical potentials from Eq. (A.107), in the expression of the LDF given in Eq. (5.58), we find that $\Lambda(s = \langle s \rangle + \kappa)$ (upto quadratic order in κ) is given by

$$\Lambda(s = \langle s \rangle + \kappa) = \frac{\kappa^2}{2\sigma_r^2} \text{ where } \sigma_r^2 = \frac{J_2 J_0 - J_1^2}{J_0}. \quad (\text{A.108})$$

Here the constants \mathcal{J}_0 , \mathcal{J}_1 and \mathcal{J}_2 are given in Eqs. (A.105) and (A.106). By substituting this LDF [Eq. (A.108)] in large deviation form given in Eq. (5.57), we find that the typical fluctuations of S_N are Gaussian distributed [see Eq. (5.62)] with the variance given by [Eq. (5.63)]

$$\text{Var}_r = \frac{N^{1-2\alpha_k} \sigma_r^2}{\beta}. \quad (\text{A.109})$$

Here σ_r^2 is given in Eq. (A.108) and it depends on the function $r(y)$. By choosing the function $r(y) = \Theta(y+w)\Theta(w-y)$ in Eq. (A.109), we recover the variance for the number problem as given in Eq. (5.8). Similarly, for the index case, when we choose the function $r(y) = \Theta(w-y)$, the variance is given by

$$\text{Var}(\mathcal{G}) = \frac{N^{\nu_k}}{\beta l_0^2 \alpha_k} \mathcal{U} \left(\frac{W}{N^{\alpha_k} l_0} \right), \quad (\text{A.110})$$

where l_0 is given in Eq. (2.20) and the exponent $\nu_k = 1 - 2\alpha_k = (2-k)/(2+k)$. Here the function $\mathcal{U}(h)$ is given by

$$\mathcal{U}(h) = \frac{(1 - I(h^2, \frac{1}{2}, \frac{1}{k})) (1 + I(h^2, \frac{1}{2}, \frac{1}{k}))}{4}, \quad (\text{A.111})$$

where the function $I(h, a, b)$ is defined in Eq. (5.24).

A.8 Derivation of the free energy

To obtain the free energy $\mathcal{F}[\rho, \beta]$ in Eq. (6.18), one first needs to compute $f_{\text{int}}(\rho(x), \beta)$ defined in Eq. (6.17), where we recall that $f_{\text{int}}(\rho(x), \beta)$ is the contribution to the free energy of the subsystem (recall Fig. 6.1) due to interactions (i.e., excluding the external confining potential). In the following, we present the calculation of $f_{\text{int}}(\rho(x), \beta)$ for the hard rods (HR) model in Appendix A.8.1 and the hyperbolic Calogero (HC) model in Appendix A.8.2 separately.

A.8.1 Free energy for hard rods

The free energy per particle for hard rods of length a , $f_{\text{int}}(\rho(x), \beta)$, can be calculated using the partition function [term in the parenthesis (square bracket) of Eq. (6.15)]

$$\begin{aligned}
Z_{\text{int}}(n_s, x_s, \Delta, \beta) &= \int_{x_s - \Delta/2 + \frac{a}{2}}^{x_s + \Delta/2 - (n_s - \frac{1}{2})a} dy_1 \dots \int_{y_{i-1} + a}^{x_s + \Delta/2 - (n_s - i + \frac{1}{2})a} dy_i \dots \times \\
&\quad \int_{y_{n_s-1} + a}^{x_s + \Delta/2 - \frac{a}{2}} dy_{n_s} \\
&= \int_{\frac{a}{2}}^{\Delta - (n_s - \frac{1}{2})a} dy_1 \dots \int_{y_{i-1} + a}^{\Delta - (n_s - i + \frac{1}{2})a} dy_i \dots \int_{y_{n_s-1} + a}^{\Delta - \frac{a}{2}} dy_{n_s}, \tag{A.112}
\end{aligned}$$

where y_i is the position of the i^{th} rod of the subsystem which is centered at x_s and has a size Δ . In each subsystem, there are n_s hard rods. Note that, since the integrand in the second line of Eq. (A.112) is constant and translationally invariant, we have shifted the limits of the integrals from $y_i \rightarrow y_i - (x_s - \Delta/2)$. This shift results in the integrals given in the third line of Eq. (A.112). These integrals can be computed using the variable transformation $z_i = y_i - (i - \frac{1}{2})a$, which gives

$$Z_{\text{int}}(n_s, x_s, \Delta, \beta) = \exp \left[n_s \log \left(\frac{1 - \rho(x_s)a}{\rho(x_s)} \right) - n_s \right], \tag{A.113}$$

where we introduce the density in the given subsystem

$$\rho(x_s) = \frac{n_s}{\Delta}. \tag{A.114}$$

The free energy per particle in a given subsystem in the large n_s limit is given by [33]

$$\begin{aligned}
f_{\text{int}}(x_s, \beta) &= -\frac{1}{n_s \beta} \log \left[Z_{\text{int}}(n_s, x_s, \Delta, \beta) \right] \\
&= -\frac{1}{\beta} \log \left[\frac{1 - a\rho(x_s)}{\rho(x_s)} \right] + \frac{1}{\beta}. \tag{A.115}
\end{aligned}$$

One can see that, from the partition function in Eq. (A.112), the logarithmic term in Eq. (A.115) is the configurational entropy which includes the effect of hard rod exclusion. Note that the free energy due to interaction is a function of the density field and we

rewrite the arguments of

$$f_{\text{int}}(x_s, \beta) \equiv f_{\text{int}}(\rho(x_s), \beta). \quad (\text{A.116})$$

The total (i.e. including the contribution due to the external potential) free energy of the entire system $\mathcal{F}_R[\rho(x_s), \beta]$ is obtained by summing over the total free energy

$$n_s f(x_s, \beta) = n_s f_{\text{int}}(\rho(x_s), \beta) + n_s U_\delta(x_s), \quad (\text{A.117})$$

associated with each subsystem. We therefore get

$$\begin{aligned} \mathcal{F}_R[\rho(x_s), \beta] &= \sum_{s=1}^{N_b} n_s f(x_s, \beta), \\ &= \sum_{s=1}^{N_b} \rho(x_s) \Delta \left[f_{\text{int}}(\rho(x_s), \beta) + U_\delta(x_s) \right]. \end{aligned} \quad (\text{A.118})$$

Converting the summation to integration i.e., $\sum_{s=1}^{N_b} \Delta \rightarrow \int_{-\infty}^{\infty} dx$ we obtain

$$\mathcal{F}_R[\rho(x), \beta] = \int_{-\infty}^{\infty} dx \rho(x) \left[f_{\text{int}}(\rho(x), \beta) + U_\delta(x) \right] \quad (\text{A.119})$$

Using Eq. (A.115) in Eq. (A.119), we obtain

$$\mathcal{F}_R[\rho(x), \beta] = \int_{-\infty}^{\infty} dx \rho(x) \left[U_\delta(x) - \frac{1}{\beta} \log \left(\frac{1 - a\rho(x)}{\rho(x)} \right) \right], \quad (\text{A.120})$$

which is the free energy of the hard rods in an external trap $U_\delta(x)$ given in Eq. (6.21) of the main text. In Eq. (A.120) we have ignored the density-independent term from Eq. (A.115).

A.8.2 Free energy for hyperbolic Calogero model

The field theoretic description of the hyperbolic Calogero model in external traps is well understood [219]. In this section, we present an alternative derivation of the total free energy $\mathcal{F}_C[\rho(x), \beta]$ of the system. Using the approximate scheme described in Refs. [45, 224] we compute the free energy per particle $f_{\text{int}}(\rho(x), \beta)$ of the subsystem due to the interaction which is described below.

The free energy per particle for the HC model, $f_{\text{int}}(\rho(x), \beta)$, can be calculated using the partition function which we recall to be

$$Z_\beta(n_s, x_s, \Delta) \approx \exp(-\beta n_s U_\delta(x_s)) \times \left[\int_{x_s - \frac{\Delta}{2}}^{x_s + \frac{\Delta}{2}} \mathbf{d}\mathbf{x}_{n_s} \prod_{\substack{i,j=1 \\ j \neq i}}^{n_s} \exp\left(-\frac{\beta}{2} [V(x_i - x_j)]\right) \right]. \quad (\text{A.121})$$

For the HC model Eq. (A.121) becomes

$$Z_\beta(n_s, x_s, \Delta) \approx \exp(-\beta n_s U_\delta(x_s)) Z_{\text{int}}(n_s, x_s, \Delta, \beta),$$

where

$$Z_{\text{int}}(n_s, x_s, \Delta, \beta) = \int_0^\Delta \mathbf{d}\mathbf{x}_{n_s} \times \exp\left[-\frac{\beta J}{2} \sum_{i=1}^{n_s} \sum_{\substack{j=1 \\ j \neq i}}^{n_s} \frac{1}{\sinh^2(|x_i - x_j|)}\right], \quad (\text{A.122})$$

where x_i is the position of the i^{th} particle and J is the interaction strength. As mentioned in the main text [Sec. 6.3], the x_i is a running integration variable not to be confused with the position of the center of the subsystem x_s . One can approximate the exponential term in the integrand of Eq. (A.122) as

$$\begin{aligned} & \exp\left(-\frac{\beta J}{2} \sum_{i=1}^{n_s} \sum_{\substack{j=1 \\ j \neq i}}^{n_s} \frac{1}{\sinh^2(|x_i - x_j|)}\right) \\ & \approx \exp\left(-\frac{\beta J}{2} \frac{n_s^2}{\Delta^2} \sum_{i=1}^{n_s} \sum_{\substack{j=1 \\ j \neq i}}^{n_s} \frac{1}{(|i - j|)^2}\right), \\ & \approx \exp\left(-\beta J \frac{n_s^3}{\Delta^3} \zeta(2) \Delta\right), \end{aligned} \quad (\text{A.123})$$

where in the second line of Eq. (A.123) we approximated $x_i \approx i\Delta/n_s$ for all i since Δ is assumed to be small enough to ensure uniform density over the subsystem. We have also used $\zeta(2) = \sum_{i=1}^{\infty} 1/i^2$, where $\zeta(k) = \sum_{i=1}^{\infty} 1/i^k$ represents the Riemann zeta function.

Using Eq. (A.123) the partition function in Eq. (A.122) takes the form

$$\begin{aligned} Z_{\text{int}}(n_s, x_s, \Delta, \beta) &\approx \exp\left(-\beta J \frac{n_s^3}{\Delta^3} \zeta(2) \Delta\right) \int_0^\Delta \mathbf{d}\mathbf{x}_{n_s}, \\ &= \exp\left(-\beta J \frac{n_s^3}{\Delta^3} \zeta(2) \Delta\right) \frac{\Delta^{n_s}}{n_s!}, \end{aligned} \quad (\text{A.124})$$

which can be rewritten using Stirling's approximation $\log[n!] \approx n \log[n] - n$ as

$$\begin{aligned} Z_{\text{int}}(n_s, x_s, \Delta, \beta) \\ \asymp \exp\left(-n_s \left[\log[\rho(x_s)] + \zeta(2) \beta J \rho(x_s)^2\right]\right), \end{aligned} \quad (\text{A.125})$$

where we recall that $\rho(x_s) = n_s/\Delta$. Hence, using the first line in Eq. (A.115), the free energy per particle of the subsystem becomes

$$f_{\text{int}}(\rho(x_s), \beta) = J\zeta(2)\rho(x_s)^2 + \frac{1}{\beta} \log[\rho(x_s)]. \quad (\text{A.126})$$

Similar to the procedure detailed in Appendix A.8.1, using the above expression Eq. (A.126) we can compute the total free energy of the system as

$$\begin{aligned} \mathcal{F}_C[\rho(x), \beta] = \int_{-\infty}^{\infty} dx \rho(x) \left(U_\delta(x) + J\zeta(2)\rho(x)^2 \right. \\ \left. + \frac{1}{\beta} \log \rho(x) \right), \end{aligned} \quad (\text{A.127})$$

which is the expression for the free energy [see Eq. (6.38) of the main text] of the HC model in an external trap $U_\delta(x)$.

A.9 Analytical forms of density profiles for hard rods and hyperbolic Calogero model at low and high rescaled temperatures c

To obtain the exact analytical expression for the equilibrium density profiles by solving the transcendental equations, Eq. (6.30) for the HR model and Eq. (6.45) for the HC

model, is a highly non-trivial. However, we can obtain approximate expressions for the densities at low ($c \ll 1$) and high ($c \gg 1$) rescaled temperatures c . For $c \ll 1$, this is done by approximating the equilibrium density profile to be a small deviation around the zero temperature density profile. On the other hand, for $c \gg 1$, the particles are expected to spread far apart, thereby diluting the gas. Thus in this regime ($c \gg 1$), it is reasonable to assume the density to be very small. In this section, using the above-mentioned assumptions for the saddle point equations i.e., Eq. (6.30) for the HR model and Eq. (6.45) for the HC model, we discuss the analytical forms of the density profiles.

A.9.1 Analytical forms of the density profiles for hard rods

In this subsection, we discuss the case of hard rods, recall that the saddle point equation for the hard rods is

$$\mu_R(c) = \frac{y^\delta}{\delta} - c \left[\log \left(\frac{1 - a \rho_R(y, c)}{\rho_R(y, c)} \right) - \frac{1}{1 - a \rho_R(y, c)} \right]. \quad (\text{A.128})$$

We now analyze Eq. (A.128) for both small and large rescaled temperatures c . In the following, we use the value of chemical potential $\mu_R(c)$ which is obtained by numerical solving Eq. (A.128) with the constraint that the density is normalized to unity.

Small rescaled temperature $c \ll 1$

At zero temperature i.e., $c = 0$, all the hard rods arrange themselves leaving no gaps. In other words, the center-to-center distance between the rods is a , thereby making the density $\rho_N(x, 0) = N/a$ where we recall that N is the number of hard rods. In the rescaled density variables this corresponds to a scaled density profile

$$\rho_R(y, 0) = \begin{cases} \frac{1}{a} & \text{for } y \leq \left| \frac{a}{2} \right| \\ 0 & \text{for } y > \left| \frac{a}{2} \right|. \end{cases} \quad (\text{A.129})$$

We now study the effects of turning on a small temperature. More precisely we address how the zero temperature profile given in Eq. (A.129) gets smeared. Note that at

$$y = y_c = (\mu_c \delta)^{\frac{1}{\delta}}. \quad (\text{A.130})$$

the square bracket in Eq. (A.128) changes sign. This in turn determines the following three distinct regions

- (i) Bulk region ($|y| < y_c$): The density profile deviates from the value $1/a$.
- (ii) Edge region (a zone where $|y - y_c| \lesssim O(c)$): The density profile deviates from a value $\rho_R(y_c, c) = \rho_R^*$ which is the density at $y = y_c$. At this value of ρ_R^* the square bracket in Eq. (A.128) becomes zero.
- (iii) Tail region ($|y| > y_c$): The density profile for finite temperature in this region deviates from its zero temperature value $\rho_R(y, 0) = 0$.

We now compute the density profile at low temperatures of these three regions separately.

(i) *Bulk region* $|y| < y_c$: In this region, we assume that the density takes the form

$$\rho_R(y, c) = \frac{1}{a} + \rho_1(y, c), \quad (\text{A.131})$$

where $\rho_1(y, c)$ denotes the deviation about the zero temperature density. For the sake of brevity, we henceforth omit the arguments of $\rho_1(y, c)$. Using Eq. (A.131) in Eq. (A.128) we get

$$\mu_c - \frac{y^\delta}{\delta} = -c \left[\log \left(\frac{-a^2 \rho_1}{1 + a \rho_1} \right) + \frac{1}{a \rho_1} \right]. \quad (\text{A.132})$$

It turns out that a convenient perturbation parameter is the following

$$\nu(y) = \frac{c\delta}{(y_c^\delta - y^\delta)}, \quad (\text{A.133})$$

where we have used Eq. (A.130). Using Eq. (A.133) in Eq. (A.132) we obtain

$$-\frac{1}{\nu(y)} = \log \left(\frac{-a^2 \rho_1}{1 + a \rho_1} \right) + \frac{1}{a \rho_1}. \quad (\text{A.134})$$

To solve Eq. (A.134) we first perform a Taylor expansion

$$-\frac{1}{\nu(y)} = \log(-a^2 \rho_1) - a \rho_1 - \frac{a^2}{2} \rho_1^2 + \frac{1}{a \rho_1}, \quad (\text{A.135})$$

which can be again rearranged to give

$$a \rho_1 = -\nu(y) \frac{1}{1 + \nu(y) \left(\log [-a^2 \rho_1] - a \rho_1 - \frac{a^2}{2} \rho_1^2 \right)}. \quad (\text{A.136})$$

We perform a Taylor series expansion [up to second order in $\nu(y)$] of the fraction on the right-hand side of Eq. (A.136), since $\nu(y) \ll 1$. This gives

$$\begin{aligned} \rho_1 \approx & -\frac{\nu(y)}{a} \left[1 - \nu(y) \left(\log [-a^2 \rho_1] - a \rho_1 - \frac{a^2}{2} \rho_1^2 \right) \right. \\ & \left. + \nu(y)^2 \left(\log [-a^2 \rho_1] - a \rho_1 - \frac{a^2}{2} \rho_1^2 \right)^2 \right]. \end{aligned} \quad (\text{A.137})$$

Since the correction to the zero temperature density $\rho_1 \ll 1$ and $\nu(y) \ll 1$, we can invert Eq. (A.137) to express ρ_1 as a function of $\nu(y)$ order by order. This gives

$$\rho_1^{(0)} = -\frac{\nu(y)}{a}, \quad (\text{A.138})$$

$$\rho_1^{(1)} = -\frac{\nu(y)}{a} + \frac{\nu(y)^2}{a} \log [a\nu(y)], \quad (\text{A.139})$$

$$\rho_1^{(2)} = -\frac{\nu(y)}{a} + \frac{\nu(y)^2}{a} \log [a\nu(y)] - \frac{\nu(y)^3}{a} \log [a\nu(y)]^2, \quad (\text{A.140})$$

where recall that $\nu(y)$ is defined in Eq. (A.133). The superscript associated with ρ_1 in Eqs. (A.138)-(A.140) represents their respective orders. In Figs. 6.3a and 6.3d using Eqs. (A.138)-(A.140), we find a good agreement between the analytically obtained series solutions and the numerical solution of Eq. (A.128).

(ii) *Edge region* $|y - y_c| \lesssim O(c)$: Recall that this region is a zone defined by $|y - y_c| \lesssim O(c)$. Here $\nu(y) \gtrsim O(1)$, and therefore, the above expressions Eqs. (A.138)-(A.140) fail. Hence, in this zone [$|y_c - y| \lesssim O(c)$], we assume that the density takes the form

$$\rho_R(y, c) = \rho_R^* + \phi(y), \quad (\text{A.141})$$

where ρ_R^* is the value of the density at $y = y_c$ and the correction $\phi(y) \ll 1$. The value of ρ_R^* can be obtained by numerically solving Eq. (A.128) at $y = y_c$ which gives

$$\log \left(\frac{1 - a\rho_R^*}{\rho_R^*} \right) - \frac{1}{1 - a\rho_R^*} = 0. \quad (\text{A.142})$$

In this region, we define the perturbation parameter

$$b(y) = 1 - \exp \left[-\frac{y_c^\delta - y^\delta}{c\delta} \right] \ll 1. \quad (\text{A.143})$$

Using Eq. (A.143) in Eq. (A.128) we get

$$\log [1 - b(y)] = \log \left[\frac{1 - a\rho_R^* - a\phi(y)}{\rho_R^* + \phi(y)} \right] - \frac{1}{1 - a\rho_R^* - a\phi(y)}, \quad (\text{A.144})$$

which upon Taylor series expansion, up to third order in $\phi(y)$, yields

$$\begin{aligned} b(y) \approx & \phi(y) \left(\frac{1}{\rho_R^* (1 - a\rho_R^*)^2} \right) - \phi(y)^2 \left(\frac{-1 + 3a\rho_R^*}{2\rho_R^{*2} (1 - a\rho_R^*)^3} \right) \\ & - \phi(y)^3 \left(\frac{-1 + 4a\rho_R^* - 6(a\rho_R^*)^2}{3\rho_R^{*3} (1 - a\rho_R^*)^4} \right). \end{aligned} \quad (\text{A.145})$$

We can represent the correction to density $\phi(y)$ as a function of $b(y)$ by inverting Eq. (A.145) order by order which gives

$$\phi^{(0)}(y) = b(y)\rho_R^*(1 - a\rho_R^*)^2, \quad (\text{A.146})$$

$$\phi^{(1)}(y) = b(y)\rho_R^*(1 - a\rho_R^*)^2 + \frac{b(y)^2}{2}\rho_R^*(1 - a\rho_R^*)^3(-1 + 3a\rho_R^*), \quad (\text{A.147})$$

$$\begin{aligned} \phi^{(2)}(y) = & b(y)\rho_R^*(1 - a\rho_R^*)^2 + \frac{b(y)^2}{2}\rho_R^*(1 - a\rho_R^*)^3(-1 + 3a\rho_R^*) \\ & + \frac{b(y)^3}{6}\rho_R^*(1 - a\rho_R^*)^4(1 - 10a\rho_R^* + 15(a\rho_R^*)^2). \end{aligned} \quad (\text{A.148})$$

In Figs. 6.3b and 6.3e, using Eqs. (A.146)-(A.148), we compare the analytically obtained series solutions with the numerical solution of Eq. (A.128) and see reasonable agreement.

(iii) *Tail region* $|y| > y_c$: In this region we assume that the density is very small and takes the form $\rho_R(y, c) = \rho_1$ with $\rho_1 \ll 1$. Using this assumption in Eq. (A.128) we get

$$\mu_c = \frac{y^\delta}{\delta} - c \left[\log \left(\frac{1 - a\rho_1}{\rho_1} \right) - \frac{1}{1 - a\rho_1} \right]. \quad (\text{A.149})$$

We introduce the perturbation parameter

$$\epsilon(y) = \exp \left(\frac{y_c^\delta - y^\delta}{c\delta} \right). \quad (\text{A.150})$$

Since in this region $|y| > y_c$ and $c \ll 1$, it implies $\epsilon(y) \ll 1$. Using Eq. (A.150) in Eq. (A.128) we get

$$\log [\epsilon(y)] = -\log \left(\frac{1 - a \rho_1}{\rho_1} \right) + \frac{1}{1 - a \rho_1}. \quad (\text{A.151})$$

After some algebra and assuming $\rho_1 \ll 1$ in Eq. (A.151), we obtain the transcendental equation

$$\rho_1 \approx \frac{\epsilon(y)}{e} \exp \left(-2a\rho_1 - \frac{(a\rho_1)^2}{2} \right), \quad (\text{A.152})$$

where $e \approx 2.71828$ is the Euler's number. We can now represent the density in terms of $\epsilon(y)/e$ as a series given by

$$\rho_1^{(0)} = \frac{\epsilon(y)}{e}, \quad (\text{A.153})$$

$$\rho_1^{(1)} = \frac{\epsilon(y)}{e} - 2a \left(\frac{\epsilon(y)}{e} \right)^2, \quad (\text{A.154})$$

$$\rho_1^{(2)} = \frac{\epsilon(y)}{e} - 2a \left(\frac{\epsilon(y)}{e} \right)^2 + \frac{11}{2} a^2 \left(\frac{\epsilon(y)}{e} \right)^3. \quad (\text{A.155})$$

In Figs. 6.3c and 6.3f, using Eqs. (A.153)-(A.155), we show a good agreement between the analytically obtained series solutions with the numerical solution of Eq. (A.128). Recall that the chemical potential $\mu_R(c)$ in the perturbation parameter $\epsilon(y)$ given in Eq. (A.150) is obtained from the numerical solution of Eq. (A.128) along with the constraint of unit normalized density.

Large rescaled temperatures: $c \gg 1$

When the temperature is high the particles explore a larger region in space thereby diluting the system as a consequence of which we get $\rho_R(y, c) \ll 1$. We introduce a convenient perturbation parameter

$$\eta(y) = \exp \left(\frac{\mu_c \delta - y^\delta}{c\delta} \right), \quad (\text{A.156})$$

where $\eta(y) \ll 1$, since the chemical potential [see Fig. 6.4 in the main text], obtained by numerically solving Eq. (A.128), is negative and diverges for $c \gg 1$.

We use the approximation $\rho_R(y, c) \ll 1$ in Eq. (A.128), and use a procedure mathematically similar to the low-temperature tail region (Appendix A.9.1), to obtain the expressions

$$\rho_R^{(0)}(y, c) = \frac{\eta(y)}{e}, \quad (\text{A.157})$$

$$\rho_R^{(1)}(y, c) = \frac{\eta(y)}{e} - 2a \left(\frac{\eta(y)}{e} \right)^2, \quad (\text{A.158})$$

$$\rho_R^{(2)}(y, c) = \frac{\eta(y)}{e} - 2a \left(\frac{\eta(y)}{e} \right)^2 + \frac{11}{2} a^2 \left(\frac{\eta(y)}{e} \right)^3. \quad (\text{A.159})$$

Note that the superscript in Eqs. (A.157)-(A.159) represents the order in $\eta(y)$. In Fig. 6.5, we see a decent agreement of the analytically obtained series solutions with the numerical solution of Eq. (A.128).

A.9.2 Asymptotic densities for hyperbolic Calogero model

In the following subsections, we compute the asymptotic densities for the hyperbolic Calogero model at low and high rescaled temperature c using a similar approach as described above for the HR model in Appendix A.9.1. Here we recall that the saddle point equation for the HC model is

$$\mu_C(c) = \frac{y^\delta}{\delta} + 3\zeta(2)\rho_C(y, c)^2 + c \log \rho_C(y, c). \quad (\text{A.160})$$

As before we analyze Eq. (A.160) for small and large c . In the following, we use the value of chemical potential $\mu_C(c)$ which is obtained by numerically solving Eq. (A.160) with the constraint that the density is normalized to unity.

Small rescaled temperatures $c \ll 1$

For $c \ll 1$ the densities $\rho_C(y, c)$ are assumed to be a small deviation from the zero temperature which is obtained by solving Eq. (A.160) for $c = 0$. The density profile is then given by

$$\rho_C(y, 0) = \begin{cases} A_\delta (l^\delta - y^\delta)^{\frac{1}{2}} & \text{for } |y| < l \\ 0 & \text{for } |y| > l, \end{cases} \quad (\text{A.161})$$

where

$$A_\delta = (3\delta\zeta(2))^{-\frac{1}{2}} \quad (\text{A.162})$$

and the edge of the support of the density is given by

$$l = \left(\frac{\delta}{2A_\delta \text{Beta}\left(\frac{1}{\delta}, \frac{3}{2}\right)} \right)^{\frac{2}{2+\delta}}. \quad (\text{A.163})$$

Here

$$\text{Beta}(x, y) = \int_0^1 dr r^{x-1} (1-r)^{y-1}, \quad (\text{A.164})$$

is the Beta function. The zero temperature chemical potential is given by [Eq. (6.51) of main text]

$$\mu_C(0) = \left(\frac{\pi}{2}\right)^{\frac{\delta}{\delta+2}} \left(\frac{\delta^{-1/\delta} \Gamma\left(\frac{3}{2} + \frac{1}{\delta}\right)}{\Gamma\left(1 + \frac{1}{\delta}\right)} \right)^{\frac{2\delta}{\delta+2}}. \quad (\text{A.165})$$

Similar to the HR model [Appendix A.9.1], at low temperatures the value of chemical potential $\mu_C(c)$ [in Eq. (A.160)], determines the (i) bulk $|y| < y_c$, (ii) edge $|y - y_c| \lesssim O(c)$ and the (iii) tail regions $|y| > y_c$, where

$$y_c = (\mu_C(c)\delta)^{\frac{1}{\delta}}. \quad (\text{A.166})$$

We compute the density profile at low temperatures separately for the three regions.

(i) *Bulk region* $|y| < y_c$: In this region we assume that the density takes the form

$$\rho_C(y, c) = \rho_C(y, 0) + \rho_1(y, c), \quad (\text{A.167})$$

where $\rho_1(y, c)$ is the correction to the zero temperature density. We use the following notations in the rest of the calculations

$$\begin{aligned} \rho_1(y, c) &\equiv \rho_1, & \rho_C(y, 0) &\equiv \rho_0 \\ \mu_C(c) &\equiv \mu_c, & \mu_C(0) &\equiv \mu_0. \end{aligned} \quad (\text{A.168})$$

Using Eq. (A.168) in Eq. (A.160) gives

$$\begin{aligned}\mu_c &= \frac{y^\delta}{\delta} + c \log \rho_0 + c \log \left[1 + \frac{\rho_1}{\rho_0} \right] \\ &\quad + 3\zeta(2) (\rho_0 + \rho_1)^2.\end{aligned}\tag{A.169}$$

Since the temperature is low ($c \ll 1$), the correction to the zero temperature density $\rho_1 \ll \rho_0$. Furthermore, we introduce the perturbation parameter in the bulk region

$$\nu(y) = \frac{\mu_0 + c \log \rho_0 - \mu_c}{c + 6\zeta(2)\rho_0^2} \ll 1.\tag{A.170}$$

For $c \ll 1$, it turns out that μ_c and μ_0 are very close, which implies $\nu(y) \ll 1$ and therefore a suitable perturbative parameter. Using Eq. (A.170) in Eq. (A.169) and expanding Logarithmic term up to $(\rho_1/\rho_0)^3$ gives

$$\frac{\rho_1}{\rho_0} \approx -\nu(y) - \frac{1}{2} \left(\frac{\rho_1}{\rho_0} \right)^2 - \frac{1}{3} \left(\frac{\rho_1}{\rho_0} \right)^3 \frac{c}{c + 6\zeta(2)\rho_0^2}.\tag{A.171}$$

We can solve Eq. (A.171) iteratively which gives

$$\frac{\rho_1^{(0)}}{\rho_0} = -\nu(y),\tag{A.172}$$

$$\frac{\rho_1^{(1)}}{\rho_0} = -\nu(y) - \frac{\nu(y)^2}{2},\tag{A.173}$$

$$\frac{\rho_1^{(2)}}{\rho_0} = -\nu(y) - \frac{\nu(y)^2}{2} - \nu(y)^3 \left(\frac{1}{2} - \frac{1}{3} \frac{c}{c + 6\zeta(2)\rho_0^2} \right),\tag{A.174}$$

where the superscript represents their respective orders. In Fig. 6.8a and 6.8d using the Eqs. (A.172)-(A.174) we find a good agreement between the analytically obtained series solution and the numerical solution of Eq. (A.160).

(ii) *Edge region* $|y - y_c| \lesssim O(c)$: Recall that this region is a zone defined by $|y - y_c| \lesssim O(c)$. Here $\nu(y)$ defined in Eq. (A.170) is no longer a small parameter and therefore ill-suited to be a perturbation parameter. Hence as in the case of the HR model, we assume the density to take the form

$$\rho_C(y, c) = \rho_C^* + \phi(y),\tag{A.175}$$

where ρ_C^* is the value of the density at $y = y_c$ and the deviation $\phi(y) \ll \rho_C^*$. The value of ρ_C^* can be obtained by numerically solving Eq. (A.160) at $y = y_c$ where y_c is given in Eq. (A.166). This gives

$$3\zeta(2)\rho_C^{*2} + c \log \rho_C^* = 0. \quad (\text{A.176})$$

We now introduce a perturbative parameter

$$b(y) = \frac{y_c^\delta - y^\delta}{\delta(c + 6\zeta(2)\rho_C^{*2})} \ll 1, \quad (\text{A.177})$$

since in this region $|y - y_c| \lesssim O(c)$ and $c \ll 1$. Substituting Eq. (A.175) and using Eq. (A.177) in Eq. (A.160) and expanding, we get

$$\frac{\phi(y)}{\rho_C^*} = b(y) - \frac{1}{2} \left(\frac{\phi(y)}{\rho_C^*} \right)^2 - \frac{1}{3} \left(\frac{\phi(y)}{\rho_C^*} \right)^3 \frac{c}{c + 6\zeta(2)\rho_C^{*2}}. \quad (\text{A.178})$$

Using a similar iterative approach as before we can represent the correction to the zero temperature density $\phi(y)$ as

$$\frac{\phi^{(0)}(y)}{\rho_C^*} = b(y), \quad (\text{A.179})$$

$$\frac{\phi^{(1)}(y)}{\rho_C^*} = b(y) - \frac{b(y)^2}{2}, \quad (\text{A.180})$$

$$\frac{\phi^{(2)}(y)}{\rho_C^*} = b(y) - \frac{b(y)^2}{2} + b(y)^3 \left(\frac{1}{2} - \frac{1}{3} \frac{c}{c + 6\zeta(2)\rho_C^{*2}} \right). \quad (\text{A.181})$$

In Figs. 6.8b. and 6.8e, using Eqs. (A.179)-(A.181), we find a good agreement between the analytically obtained series solution and the numerical solution of Eq. (A.160).

(iii) *Tail region* $|y| > y_c$: Unlike the bulk and the edge regions, in the tail region, we assume that the density is small and takes the form $\rho_C(y, c) = \rho_1$ where $\rho_1 \ll 1$. Using this assumption in Eq. (A.160) we obtain

$$\mu_c = \frac{y^\delta}{\delta} + c \log \rho_1 + 3\zeta(2)\rho_1^2. \quad (\text{A.182})$$

We now introduce a suitable perturbation parameter

$$\epsilon(y) = \exp\left(\frac{y_c^\delta - y^\delta}{c\delta}\right). \quad (\text{A.183})$$

In the tail region, since $|y| > y_c$ and $c \ll 1$, the perturbation parameter $\epsilon(y) \ll 1$. Using Eq. (A.183) in Eq. (A.182) and rearranging the terms gives

$$\rho_1 = \epsilon(y) \exp\left(-\frac{3\zeta(2)\rho_1^2}{c}\right). \quad (\text{A.184})$$

We can now represent the density in terms of $\epsilon(y)$ by using the iterative scheme, similar to bulk and edge regions, on Eq. (A.184). This then gives

$$\rho_1^{(0)} = \epsilon(y), \quad (\text{A.185})$$

$$\rho_1^{(1)} = \epsilon(y) \left[1 - \frac{3\zeta(2)}{c} \epsilon(y)^2\right], \quad (\text{A.186})$$

$$\rho_1^{(2)} = \epsilon(y) \left[1 - \frac{3\zeta(2)}{c} \epsilon(y)^2 + \frac{5}{2} \left(\frac{3\zeta(2)}{c}\right)^2 \epsilon(y)^4\right]. \quad (\text{A.187})$$

In Fig. 6.8c and 6.8f, using Eqs. (A.185)-(A.187), we show the analytically obtained asymptotic densities of the matches well with the numerical solution of Eq. (A.160).

Large rescaled temperature: $c \gg 1$

Similar to the HR model (Appendix A.9.1), when the temperature is high the particles are spread out over a larger region of space hence diluting the system as a consequence of which we get $\rho_C(y, c) \ll 1$. We again introduce a convenient perturbation parameter

$$\eta(y) = \exp\left(\frac{\mu_c \delta - y^\delta}{\delta c}\right). \quad (\text{A.188})$$

Since the chemical potential (see Fig. 6.7 in the main text), obtained by numerically solving Eq. (A.160), is negative and diverges for $c \gg 1$, the perturbation parameter becomes small i.e., $\eta(y) \ll 1$. Using Eq. (A.188) along with the low-density approximation in Eq. (A.160) and following a procedure mathematically similar to low-temperature tail

region (Appendix A.9.2) we obtain the expressions

$$\rho_C^{(0)}(y, c) = \eta(y), \quad (\text{A.189})$$

$$\rho_C^{(1)}(y, c) = \eta(y) \left[1 - \frac{3\zeta(2)}{c} \eta(y)^2 \right], \quad (\text{A.190})$$

$$\rho_C^{(2)}(y, c) = \eta(y) \left[1 - \frac{3\zeta(2)}{c} \eta(y)^2 + \frac{5}{2} \left(\frac{3\zeta(2)}{c} \right)^2 \eta(y)^4 \right]. \quad (\text{A.191})$$

In Fig. 6.9, using Eqs. (A.189)-(A.191), we see a good agreement of the analytically obtained series solutions with the numerical solution of Eq. (A.160).

Bibliography

- [1] A. Campa, T. Dauxois, and S. Ruffo, “Statistical mechanics and dynamics of solvable models with long-range interactions,” *Physics Reports*, vol. 480, p. 57, 2009. [Online]. Available: <https://doi.org/10.1016/j.physrep.2009.07.001>
- [2] M. Kac, G. Uhlenbeck, and P. Hemmer, “On the van der waals theory of the vapor-liquid equilibrium. i. discussion of a one-dimensional model,” *Journal of Mathematical Physics*, vol. 4, no. 2, pp. 216–228, 1963. [Online]. Available: <https://doi.org/10.1063/1.1703946>
- [3] T. Padmanabhan, “Statistical mechanics of gravitating systems,” *Physics Reports*, vol. 188, p. 285, 1990. [Online]. Available: [https://doi.org/10.1016/0370-1573\(90\)90051-3](https://doi.org/10.1016/0370-1573(90)90051-3)
- [4] P. H. Chavanis and L. Delfini, “Phase transitions in self-gravitating systems and bacterial populations with a screened attractive potential,” *Physical Review E*, vol. 81, p. 051103, 2010. [Online]. Available: <https://doi.org/10.1103/PhysRevE.109.014118>
- [5] B. Marcos, “Collisional relaxation of two-dimensional self-gravitating systems,” *Physical Review E*, vol. 88, p. 032112, 2013. [Online]. Available: <https://doi.org/10.1103/PhysRevE.88.032112>
- [6] D. F. Escande and Y. Elskens, “Microscopic dynamics of plasmas and chaos: the wave–particle interaction paradigm,” *Plasma physics and controlled fusion*, vol. 45, p. A115, 2003. [Online]. Available: <https://doi.org/10.1088/0741-3335/45/12A/008>
- [7] A. Antoniazzi, D. Fanelli, S. Ruffo, J. Barré, T. Dauxois, and G. De Ninno, “Free electron laser as a paradigmatic example of systems with long-range

- interactions,” *28th International Free Electron Laser Conference*, vol. 87, 2006. [Online]. Available: <https://accelconf.web.cern.ch/f06/papers/mopph025.pdf>
- [8] J. Miller, “Statistical mechanics of euler equations in two dimensions,” *Physical Review Letters*, vol. 65, p. 2137, 1990. [Online]. Available: <https://doi.org/10.1103/PhysRevLett.65.2137>
- [9] R. Robert and J. Sommeria, “Statistical equilibrium states for two-dimensional flows,” *Journal of Fluid Mechanics*, vol. 229, p. 291, 1991. [Online]. Available: <https://doi.org/10.1017/S0022112091003038>
- [10] M. Kulkarni and A. G. Abanov, “Hydrodynamics of cold atomic gases in the limit of weak nonlinearity, dispersion, and dissipation,” *Physical Review A*, vol. 86, p. 033614, 2012. [Online]. Available: <https://doi.org/10.1103/PhysRevA.86.033614>
- [11] J. M. Brown and A. Carrington, *Rotational spectroscopy of diatomic molecules*. Cambridge university press, 2003. [Online]. Available: <https://doi.org/10.1017/CBO9780511814808>
- [12] M. Chalony, J. Barré, B. M., A. Olivetti, and D. Wilkowski, “Long-range one-dimensional gravitational-like interaction in a neutral atomic cold gas,” *Physical Review A*, vol. 87, p. 013401, 2013. [Online]. Available: <https://doi.org/10.1103/PhysRevA.87.013401>
- [13] J. Zhang, G. Pagano, P. W. Hess, A. Kyprianidis, P. Becker, H. Kaplan, A. V. Gorshkov, Z.-X. Gong, and C. Monroe, “Observation of a many-body dynamical phase transition with a 53-qubit quantum simulator,” *Nature*, vol. 551, p. 601, 2017. [Online]. Available: <https://doi.org/10.1038/nature24654>
- [14] M. A. Olshanetsky and A. M. Perelomov, “Classical integrable finite-dimensional systems related to lie algebras,” *Physics Reports*, vol. 71, p. 313, 1981. [Online]. Available: [https://doi.org/10.1016/0370-1573\(81\)90023-5](https://doi.org/10.1016/0370-1573(81)90023-5)
- [15] A. P. Polychronakos, “Physics and mathematics of calogero particles,” *Journal of Physics A: Mathematics and General*, vol. 39, p. 12793, 2006. [Online]. Available: <https://doi.org/10.1088/0305-4470/39/41/S07>

- [16] M. Rigol, V. Dunjko, V. Yurovsky, and M. Olshanii, “Relaxation in a completely integrable many-body quantum system: an ab initio study of the dynamics of the highly excited states of 1d lattice hard-core bosons,” *Physical review letters*, vol. 98, no. 5, p. 050405, 2007. [Online]. Available: <https://doi.org/10.1103/PhysRevLett.98.050405>
- [17] M. Riesz, “Intégrales de riemann-liouville et potentiels,” *Acta Scientiarum Mathematicarum University Szged*, vol. 9, p. 1, 1938. [Online]. Available: https://doi.org/10.1007/978-3-642-37535-4_38
- [18] F. J. Dyson, “Statistical theory of the energy levels of complex systems. i,” *Journal of Mathematical Physics*, vol. 3, p. 140, 1962. [Online]. Available: <https://doi.org/10.1063/1.1703773>
- [19] M. L. Mehta, “Random matrices,” *Elsevier*, 2004.
- [20] P. J. Forrester, *Log-gases and random matrices*. Princeton, 2010. [Online]. Available: <https://www.jstor.org/stable/j.ctt7t5vq>
- [21] F. J. Dyson, “Statistical theory of the energy levels of complex systems. ii,” *Journal of Mathematical Physics*, vol. 3, p. 157, 1962. [Online]. Available: <https://doi.org/10.1063/1.1703774>
- [22] D. S. Dean and S. N. Majumdar, “Large deviations of extreme eigenvalues of random matrices,” *Physical Review Letters*, vol. 97, p. 160201, 2006. [Online]. Available: <https://doi.org/10.1103/PhysRevLett.97.160201>
- [23] —, “Extreme value statistics of eigenvalues of gaussian random matrices,” *Physical Review E*, vol. 77, p. 041108, 2008. [Online]. Available: <https://doi.org/10.1103/PhysRevE.77.041108>
- [24] E. B. Saff and V. Totik, *Logarithmic potentials with external fields*. Springer Science & Business Media, 2013, vol. 316. [Online]. Available: <https://doi.org/10.1007/978-3-662-03329-6>
- [25] S. N. Majumdar and G. Schehr, “Top eigenvalue of a random matrix: large deviations and third order phase transition,” *Journal of Statistical Mechanics*:

- Theory and Experiment*, vol. 2014, p. P01012, 2014. [Online]. Available: <https://doi.org/10.1088/1742-5468/2014/01/P01012>
- [26] F. Calogero, “Solution of the one-dimensional n-body problems with quadratic and/or inversely quadratic pair potentials,” *Journal of Mathematical Physics*, vol. 12, p. 419, 1971. [Online]. Available: <https://doi.org/10.1063/1.1665604>
- [27] —, “Exactly solvable one-dimensional many-body problems,” *Lettere al Nuovo Cimento*, vol. 13, p. 411, 1975. [Online]. Available: <https://doi.org/10.1007/BF02790495>
- [28] A. Lenard, “Exact statistical mechanics of a one-dimensional system with coulomb forces,” *Journal of Mathematical Physics*, vol. 2, p. 682, 1961. [Online]. Available: <https://doi.org/10.1063/1.1703757>
- [29] S. Prager, “The one-dimensional plasma,” *Advances in Chemical Physics*, vol. 4, p. 201, 1962. [Online]. Available: <https://doi.org/10.1002/9780470143506.ch5>
- [30] R. J. Baxter, “Statistical mechanics of a one-dimensional coulomb system with a uniform charge background,” *Mathematical Proceedings of the Cambridge Philosophical Society*, vol. 59, p. 779, 1963. [Online]. Available: <https://doi.org/10.1017/S0305004100003790>
- [31] A. Dhar, A. Kundu, S. N. Majumdar, S. Sabhapandit, and G. Schehr, “Exact extremal statistics in the classical 1d coulomb gas,” *Physical Review Letters*, vol. 119, p. 060601, 2017. [Online]. Available: <https://doi.org/10.1103/PhysRevLett.119.060601>
- [32] —, “Extreme statistics and index distribution in the classical 1d coulomb gas,” *Journal of Physics A: Mathematical and Theoretical*, vol. 51, p. 295001, 2018. [Online]. Available: <https://doi.org/10.1088/1751-8121/aac75f>
- [33] L. Tonks, “The complete equation of state of one, two and three-dimensional gases of hard elastic spheres,” *Physics Review*, vol. 50, p. 955, 1936. [Online]. Available: <https://doi.org/10.1103/PhysRev.50.955>
- [34] A. Krajenbrink and P. Le Doussal, “Linear statistics and pushed coulomb gas at the edge of β -random matrices: Four paths to large deviations,”

- Europhysics Letters*, vol. 125, p. 20009, 2019. [Online]. Available: <https://doi.org/10.1209/0295-5075/125/20009>
- [35] A. Flack, S. N. Majumdar, and G. Schehr, “An exact formula for the variance of linear statistics in the one-dimensional jellium model,” *Journal of Physics A: Mathematical and Theoretical*, vol. 56, p. 105002, 2023. [Online]. Available: <https://doi.org/10.1088/1751-8121/acb86a>
- [36] A. Grabsch, “General truncated linear statistics for the top eigenvalues of random matrices,” *Journal of Physics A: Mathematical and Theoretical*, vol. 55, p. 124001, 2021. [Online]. Available: <https://doi.org/10.1088/1751-8121/ac52e3>
- [37] A. Flack, S. N. Majumdar, and G. Schehr, “Truncated linear statistics in the one dimensional one-component plasma,” *Journal of Physics A: Mathematical and Theoretical*, vol. 54, p. 435002, 2021. [Online]. Available: <https://doi.org/10.1088/1751-8121/ac2599>
- [38] S. N. Majumdar, C. Nadal, A. Scardicchio, and P. Vivo, “Index distribution of gaussian random matrices,” *Physical Review Letters*, vol. 103, p. 220603, 2009. [Online]. Available: <https://doi.org/10.1103/PhysRevLett.103.220603>
- [39] —, “How many eigenvalues of a gaussian random matrix are positive?” *Physical Review E*, vol. 83, p. 041105, 2011. [Online]. Available: <https://doi.org/10.1103/PhysRevE.83.041105>
- [40] R. Marino, S. N. Majumdar, G. Schehr, and P. Vivo, “Phase transitions and edge scaling of number variance in gaussian random matrices,” *Physical Review Letters*, vol. 112, p. 254101, 2014. [Online]. Available: <https://doi.org/10.1103/PhysRevLett.112.254101>
- [41] —, “Number statistics for β -ensembles of random matrices: applications to trapped fermions at zero temperature,” *Physical Review E*, vol. 94, p. 032115, 2016. [Online]. Available: <https://doi.org/10.1103/PhysRevE.94.032115>
- [42] A. Flack, S. N. Majumdar, and G. Schehr, “Gap probability and full counting statistics in the one-dimensional one-component plasma,” *Journal of Statistical*

- Mechanics: Theory and Experiment*, vol. 5, p. 053211, 2022. [Online]. Available: <https://iopscience.iop.org/article/10.1088/1742-5468/ac6a59/meta>
- [43] E. P. Wigner, “On the statistical distribution of the widths and spacings of nuclear resonance levels,” *Mathematical Proceedings of the Cambridge Philosophical Society*, vol. 47, p. 790, 1951. [Online]. Available: <https://doi.org/10.1017/S0305004100027237>
- [44] P. Choquard, H. Kunz, P. A. Martin, and M. Navet, “One-dimensional coulomb systems,” in *Physics in One Dimension: Proceedings of an International Conference Fribourg*. Springer, 1981, p. 335. [Online]. Available: https://doi.org/10.1007/978-3-642-81592-8_39
- [45] S. Agarwal, A. Dhar, M. Kulkarni, A. Kundu, S. N. Majumdar, D. Mukamel, and G. Schehr, “Harmonically confined particles with long-range repulsive interactions,” *Physical Review Letters*, vol. 123, p. 100603, 2019. [Online]. Available: <https://doi.org/10.1103/PhysRevLett.123.100603>
- [46] C. W. J. Beenakker, “Pair correlation function of the one-dimensional riesz gas,” *Physical Review Research*, vol. 5, p. 013152, 2023. [Online]. Available: <https://doi.org/10.1103/PhysRevResearch.5.013152>
- [47] R. Dandekar, P. L. Krapivsky, and K. Mallick, “Dynamical fluctuations in the riesz gas,” *Physical Review E*, vol. 107, p. 044129, 2023. [Online]. Available: <https://journals.aps.org/pre/abstract/10.1103/PhysRevE.107.044129>
- [48] K. S. Bhanu, D. A. Huse, and M. Kulkarni, “Spatiotemporal spread of perturbations in power-law models at low temperatures: Exact results for classical out-of-time-order correlators,” *Physical review. E*, vol. 104, p. 044117, 2021. [Online]. Available: <https://doi.org/10.1103/PhysRevE.104.044117>
- [49] R. Lelotte, “Phase transitions in one-dimensional riesz gases with long-range interaction,” *arXiv:2309.08951v1 [cond-mat.stat-mech]*, 2023. [Online]. Available: <https://doi.org/10.48550/arXiv.2309.08951>

- [50] D. P. Hardin, T. Leblé, E. B. Saff, and S. Serfaty, “Large deviation principles for hypersingular riesz gases,” *Constructive Approximation*, vol. 48, p. 61, 2018. [Online]. Available: <https://doi.org/10.1007/s00365-018-9431-9>
- [51] T. Leblé and S. Serfaty, “Large deviation principle for empirical fields of log and riesz gases,” *Inventiones Mathematicae*, vol. 210, p. 645, 2017. [Online]. Available: <https://link.springer.com/article/10.1007/s00222-017-0738-0>
- [52] M. Lewin, “Coulomb and riesz gases: The known and the unknown,” *Journal of Mathematical Physics*, vol. 63, p. 061101, 2022. [Online]. Available: <https://doi.org/10.1063/5.0086835>
- [53] D. Dereudre and T. Vasseur, “Number-rigidity and beta-circular riesz gas,” *arXiv:2104.09408v1 [math.PR]*, 2021. [Online]. Available: <https://doi.org/10.48550/arXiv.2104.09408>
- [54] J. Boursier, “Decay of correlations and thermodynamic limit for the circular riesz gas,” *arXiv preprint arXiv:2209.00396*, 2022. [Online]. Available: <https://arxiv.org/abs/2209.00396>
- [55] P. Jurcevic, B. P. Lanyon, P. Hauke, C. Hempel, P. Zoller, R. Blatt, and C. F. Roos, “Quasiparticle engineering and entanglement propagation in a quantum many-body system,” *Nature*, vol. 511, no. 7508, pp. 202–205, 2014. [Online]. Available: <https://doi.org/10.1038/nature13461>
- [56] W. S. Bakr, J. I. Gillen, A. Peng, S. Fölling, and M. Greiner, “A quantum gas microscope for detecting single atoms in a hubbard-regime optical lattice,” *Nature*, vol. 462, p. 74, 2009. [Online]. Available: <https://doi.org/10.1038/nature08482>
- [57] L. W. Cheuk, M. A. Nichols, M. Okan, T. Gersdorf, V. V. Ramasesh, W. S. Bakr, T. Lompe, and M. W. Martin, “Quantum-gas microscope for fermionic atoms,” *Physical Review Letters*, vol. 114, p. 193001, 2015. [Online]. Available: <https://doi.org/10.1103/PhysRevLett.114.193001>
- [58] M. F. Parsons, F. Huber, A. Mazurenko, C. S. Chiu, W. Setiawan, K. Brown-Wooley, S. Blatt, and M. Greiner, “Site-resolved imaging of fermionic li 6 in

- an optical lattice,” *Physical Review Letters*, vol. 114, p. 213002, 2015. [Online]. Available: <https://doi.org/10.1103/PhysRevLett.114.213002>
- [59] J. Kethepalli, M. Kulkarni, A. Kundu, S. N. Majumdar, D. Mukamel, and G. Schehr, “Edge fluctuations and third-order phase transition in harmonically confined long-range systems,” *Journal of Statistical Mechanics: Theory and Experiment*, vol. 2022, p. 033203, 2022. [Online]. Available: <https://doi.org/10.1088/1742-5468/ac52b2>
- [60] —, “Harmonically confined long-ranged interacting gas in the presence of a hard wall,” *J. Stat. Mech.: Theory and Experiment*, vol. 2021, p. 103209, 2021. [Online]. Available: <https://doi.org/10.1088/1742-5468/ac2896>
- [61] —, “Full counting statistics of 1d short range riesz gases in confinement,” *Journal of Statistical Mechanics: Theory and Experiment*, vol. 2024, p. 083206, 2024. [Online]. Available: <https://doi.org/10.1088/1742-5468/ad66c5>
- [62] J. W. Gibbs, “Elementary principles in statistical mechanics,” *C. Scribner’s sons*, 1902. [Online]. Available: <https://doi.org/10.1017/CBO9780511686948>
- [63] E. T. Jaynes, “Information theory and statistical mechanics,” *Physical Review*, vol. 106, p. 620, 1957. [Online]. Available: <https://doi.org/10.1103/PhysRev.106.620>
- [64] F. Reif, *Fundamentals of statistical and thermal physics*. McGraw-Hill, 1965. [Online]. Available: <https://archive.org/details/fundamentalsofst00reif/page/n679/mode/2up>
- [65] E. Fermi, P. Pasta, S. Ulam, and M. Tsingou, “Studies of the nonlinear problems,” Los Alamos National Lab.(LANL), Los Alamos, NM (United States), Tech. Rep., 1955.
- [66] J. Ford, “The fermi-pasta-ulam problem: paradox turns discovery,” *Physics Reports*, vol. 213, p. 271, 1992. [Online]. Available: [https://doi.org/10.1016/0370-1573\(92\)90116-H](https://doi.org/10.1016/0370-1573(92)90116-H)
- [67] G. P. Berman and F. M. Izrailev, “The Fermi–Pasta–Ulam problem: fifty years of progress,” *Chaos: An Interdisciplinary Journal of Nonlinear Science*, vol. 15, p. 015104, 2005. [Online]. Available: <https://doi.org/10.1063/1.1855036>

- [68] T. Dauxois, M. Peyrard, and S. Ruffo, “The Fermi–Pasta–Ulam ‘numerical experiment’: history and pedagogical perspectives,” *European Journal of Physics*, vol. 26, p. S3, 2005. [Online]. Available: <https://iopscience.iop.org/article/10.1088/0143-0807/26/5/S01/pdf>
- [69] G. Gallavotti, *The Fermi-Pasta-Ulam problem: a status report*. Springer, 2007, vol. 728. [Online]. Available: <https://link.springer.com/book/10.1007/978-3-540-72995-2>
- [70] A. Henrici and T. Kappeler, “Results on normal forms for FPU chains,” *Communications in mathematical physics*, vol. 278, p. 145, 2008. [Online]. Available: <https://link.springer.com/article/10.1007/s00220-007-0387-z>
- [71] F. M. Israiljev and B. v. Chirikov, “The statistical properties of a non-linear string,” 1965. [Online]. Available: <https://cds.cern.ch/record/395891/files/the%20statistical.pdf>
- [72] A. V. G. S. Flach, “Discrete breathers-advances in theory and applications,” *Physics Reports*, vol. 467, p. 1, 2008. [Online]. Available: <https://doi.org/10.1016/j.physrep.2008.05.002>
- [73] M. Onorato, L. Vozella, D. Proment, and Y. V. Lvov, “Route to thermalization in the α -fermi–pasta–ulam system,” *Proceedings of the National Academy of Sciences*, vol. 112, p. 4208, 2015. [Online]. Available: <https://doi.org/10.1073/pnas.1404397112>
- [74] N. J. Zabusky and M. D. Kruskal, “Interaction of ”solitons” in a collisionless plasma and the recurrence of initial states,” *Physical review letters*, vol. 15, p. 240, 1965. [Online]. Available: <https://journals.aps.org/prl/pdf/10.1103/PhysRevLett.15.240>
- [75] L. Casetti, M. Cerruti-Sola, M. Pettini, and E. G. D. Cohen, “The Fermi-Pasta-Ulam problem revisited: Stochasticity thresholds in nonlinear Hamiltonian systems,” *Physical Review E*, vol. 55, p. 6566, 1997. [Online]. Available: <https://journals.aps.org/pre/pdf/10.1103/PhysRevE.55.6566>
- [76] G. Benettin, H. Christodoulidi, and A. Ponno, “The Fermi-Pasta-Ulam problem and its underlying integrable dynamics,” *Journal of Statistical Physics*, vol.

- 152, p. 195, 2013. [Online]. Available: <https://link.springer.com/article/10.1007/s10955-013-0760-6>
- [77] T. Goldfriend and J. Kurchan, “Equilibration of quasi-integrable systems,” *Physical Review E*, vol. 99, p. 022146, 2019. [Online]. Available: <https://doi.org/10.1103/PhysRevE.99.022146>
- [78] T. Kinoshita, T. Wenger, and D. S. Weiss, “A quantum newton’s cradle,” *Nature*, vol. 440, p. 900, 2006. [Online]. Available: <https://doi.org/10.1038/nature04693>
- [79] M. Olshanii, “Atomic scattering in the presence of an external confinement and a gas of impenetrable bosons,” *Physical review letters*, vol. 81, no. 5, p. 938, 1998. [Online]. Available: <https://doi.org/10.1103/PhysRevLett.81.938>
- [80] O. A. Castro-Alvaredo, B. Doyon, and T. Yoshimura, “Emergent hydrodynamics in integrable quantum systems out of equilibrium,” *Physical Review X*, vol. 6, p. 041065, 2016. [Online]. Available: <https://doi.org/10.1103/PhysRevX.6.041065>
- [81] B. Bertini, M. Collura, J. De Nardis, and M. Fagotti, “Transport in out-of-equilibrium XXZ chains: Exact profiles of charges and currents,” *Physical review letters*, vol. 117, p. 207201, 2016. [Online]. Available: <https://doi.org/10.1103/PhysRevLett.117.207201>
- [82] H. Spohn, *Large scale dynamics of interacting particles*. Springer Science & Business Media, 2012.
- [83] B. Doyon and T. Yoshimura, “A note on generalized hydrodynamics: inhomogeneous fields and other concepts,” *SciPost Physics*, vol. 2, p. 014, 2017. [Online]. Available: <https://scipost.org/SciPostPhys.2.2.014/pdf>
- [84] X. Cao, V. B. Bulchandani, and J. E. Moore, “Incomplete thermalization from trap-induced integrability breaking: Lessons from classical hard rods,” *Phys. Rev. Lett.*, vol. 120, p. 164101, 2018. [Online]. Available: <https://doi.org/10.1103/PhysRevLett.120.164101>
- [85] J. S. Caux, B. Doyon, J. Dubail, R. Konik, and T. Yoshimura, “Hydrodynamics of the interacting Bose gas in the Quantum Newton Cradle setup,” *SciPost*

- Phys.*, vol. 6, p. 070, 2019. [Online]. Available: <https://scipost.org/10.21468/SciPostPhys.6.6.070>
- [86] A. Bastianello, A. De Luca, B. Doyon, and J. De Nardis, “Thermalization of a trapped one-dimensional bose gas via diffusion,” *Physical Review Letters*, vol. 125, p. 240604, 2020. [Online]. Available: <https://journals.aps.org/prl/pdf/10.1103/PhysRevLett.125.240604>
- [87] H. T. Stoof, “Equilibrium on hold,” *Nature*, vol. 440, no. 7086, pp. 877–878, 2006. [Online]. Available: <https://doi.org/10.1038/440877a>
- [88] J. De Nardis, D. Bernard, and B. Doyon, “Hydrodynamic diffusion in integrable systems,” *Physical review letters*, vol. 121, no. 16, p. 160603, 2018. [Online]. Available: <https://doi.org/10.1103/PhysRevLett.121.160603>
- [89] C. A. Tracy and H. Widom, “Fredholm determinants, differential equations and matrix models,” *Communications in mathematical physics*, vol. 163, p. 33, 1994. [Online]. Available: <https://doi.org/10.1007/BF02101734>
- [90] —, “On orthogonal and symplectic matrix ensembles,” *Communications in mathematical physics*, vol. 177, p. 727, 1996. [Online]. Available: <https://doi.org/10.1007/BF02099545>
- [91] F. Bouchet, S. Gupta, and D. Mukamel, “Thermodynamics and dynamics of systems with long-range interactions,” *Physica A: Statistical Mechanics and its Applications*, vol. 389, p. 4389, 2010. [Online]. Available: <https://doi.org/10.1016/j.physa.2010.02.024>
- [92] A. Kumar, M. Kulkarni, and A. Kundu, “Particles confined in arbitrary potentials with a class of finite-range repulsive interactions,” *Physical Review E*, vol. 102, p. 032128, 2020. [Online]. Available: <https://doi.org/10.1103/PhysRevE.102.032128>
- [93] S. Santra and A. Kundu, “Crossover in density profiles of confined particles in power-law models with finite range of interaction,” *Journal of Physics A: Mathematical and Theoretical*, vol. 57, p. 245003, 2023. [Online]. Available: <https://doi.org/10.1088/1751-8121/ad4c30>

- [94] M. R. Andrews, C. G. Townsend, H. J. Miesner, D. S. Durfee, D. M. Kurn, and W. Ketterle, “Observation of interference between two bose condensates,” *Science*, vol. 275, p. 637, 1997. [Online]. Available: <https://doi.org/10.1126/science.275.5300.637>
- [95] K. M. O’Hara, S. L. Hemmer, M. E. Gehm, S. R. Granade, and J. E. Thomas, “Observation of a strongly interacting degenerate fermi gas of atoms,” *Science*, vol. 298, p. 2179, 2002. [Online]. Available: <https://doi.org/10.1126/science.1079107>
- [96] J. A. Joseph, J. E. Thomas, M. Kulkarni, and A. G. Abanov, “Observation of shock waves in a strongly interacting fermi gas,” *Physical Review Letters*, vol. 106, p. 150401, 2011. [Online]. Available: <https://doi.org/10.1103/PhysRevLett.106.150401>
- [97] A. L. Gaunt, T. F. Schmidutz, I. Gotlibovych, R. P. Smith, and Z. Hadzibabic, “Bose-einstein condensation of atoms in a uniform potential,” *Physical Review Letters*, vol. 110, p. 200406, 2013. [Online]. Available: <https://doi.org/10.1103/PhysRevLett.110.200406>
- [98] S. N. Majumdar, A. Pal, and G. Schehr, “Extreme value statistics of correlated random variables: a pedagogical review,” *Physics Reports*, vol. 840, p. 1, 2020. [Online]. Available: <https://doi.org/10.1016/j.physrep.2019.10.005>
- [99] G. Livan, M. Novaes, and P. Vivo, “Introduction to random matrices theory and practice,” *SpringerBriefs in Mathematical Physics*, 2018. [Online]. Available: <https://doi.org/10.1007/978-3-319-70885-0>
- [100] S. V. Buldyrev, M. Gitterman, S. Havlin, A. Y. Kazakov, M. Da Luz, E. P. Raposo, H. E. Stanley, and G. M. Viswanathan, “Properties of lévy flights on an interval with absorbing boundaries,” *Physica A: Statistical Mechanics and its Applications*, vol. 302, p. 148, 2001. [Online]. Available: [https://doi.org/10.1016/S0378-4371\(01\)00461-7](https://doi.org/10.1016/S0378-4371(01)00461-7)
- [101] D. Dhar, “The abelian sandpile and related models,” *Physica A: Statistical Mechanics and its Applications*, vol. 263, p. 4, 1999. [Online]. Available: [https://doi.org/10.1016/S0378-4371\(98\)00493-2](https://doi.org/10.1016/S0378-4371(98)00493-2)

- [102] G. Rotskoff and E. Vanden-Eijnden, “Trainability and accuracy of artificial neural networks: An interacting particle system approach,” *Communications on Pure and Applied Mathematics*, vol. 75, p. 1889, 2022. [Online]. Available: <https://doi.org/10.1002/cpa.22074>
- [103] G. D. Mahan, *Many-Particle Systems*. Princeton University Press, 2008.
- [104] G. Akemann, J. Baik, and P. Francesco, *The Oxford Handbook of Random Matrix Theory*. Oxford University Press, 2011.
- [105] X. He, Q. Ai, R. C. Qiu, W. Huang, L. Piao, and H. Liu, “A big data architecture design for smart grids based on random matrix theory,” *IEEE transactions on smart Grid*, vol. 8, p. 674, 2015. [Online]. Available: <https://doi.org/10.1109/TSG.2015.2445828>
- [106] C. Nadal and S. N. Majumdar, “A simple derivation of the tracy-widom distribution of the maximal eigenvalue of a gaussian unitary random matrix,” *Journal of Statistical Mechanics: Theory and Experiment*, p. 04001, 2011. [Online]. Available: <https://doi.org/10.1088/1742-5468/2011/04/P04001>
- [107] S. Giorgini, L. P. Pitaevskii, and S. Stringari, “Theory of ultracold atomic fermi gases,” *Rev. Mod. Phys.*, vol. 80, p. 1215, 2008. [Online]. Available: <https://doi.org/10.1103/RevModPhys.80.1215>
- [108] P. Le Doussal and C. Monthus, “Exact solutions for the statistics of extrema of some random 1d landscapes, application to the equilibrium and the dynamics of the toy model,” *Physica A: Statistical Mechanics and its Applications*, vol. 317, p. 140, 2003. [Online]. Available: [https://doi.org/10.1016/S0378-4371\(02\)01317-1](https://doi.org/10.1016/S0378-4371(02)01317-1)
- [109] S. N. Majumdar and A. Comtet, “Exact maximal height distribution of the fluctuating interfaces,” *Physical Review Letters*, vol. 92, p. 225501, 2004. [Online]. Available: <https://doi.org/10.1103/PhysRevLett.92.225501>
- [110] G. Schehr and S. N. Majumdar, “Universal asymptotic statistics of maximal relative height in one-dimensional solid-on-solid models,” *Physical Review E*, vol. 73, p. 056101, 2006. [Online]. Available: <https://doi.org/10.1103/PhysRevE.73.056101>

- [111] S. Raychaudhuri, M. Cranston, C. Przybyla, and Y. Shapir, “Maximal height scaling of kinetically growing surfaces,” *Physical Review Letters*, vol. 87, p. 136101, 2001. [Online]. Available: <https://doi.org/10.1103/PhysRevLett.87.136101>
- [112] P. L. Krapivsky and S. N. Majumdar, “Traveling waves, front selection, and exact nontrivial exponents in a random fragmentation problem,” *Physical Review Letters*, vol. 85, p. 5492, 2000. [Online]. Available: <https://doi.org/10.1103/PhysRevLett.85.5492>
- [113] S. N. Majumdar and M. Vergassola, “Large deviations of the maximum eigenvalue for wishart and gaussian random matrices,” *Physical Review Letters*, vol. 102, p. 060601, 2009. [Online]. Available: <https://doi.org/10.1103/PhysRevLett.102.060601>
- [114] R. D. H. Rojas, C. S. H. Calva, and I. Perez-Castillo, “Universal behaviour of the full particle statistics of one-dimensional coulomb gases with an arbitrary external potential,” *Physical Review E*, vol. 98, p. 020104, 2018. [Online]. Available: <https://journals.aps.org/pre/abstract/10.1103/PhysRevE.98.020104>
- [115] V. Y. Fyodorov and C. Nadal, “Critical behavior of the number of minima of a random landscape at the glass transition point and the tracy-widom distribution,” *Physical Review Letters*, vol. 109, p. 167203, 2012. [Online]. Available: <https://doi.org/10.1103/PhysRevLett.109.167203>
- [116] P. Kazakopoulos, P. Mertikopoulos, A. L. Moustakas, and G. Caire, “Living at the edge: A large deviations approach to the outage mimo capacity,” *IEEE Transactions on Information Theory*, vol. 57, p. 1984, 2011. [Online]. Available: <https://doi.org/10.1109/TIT.2011.2112050>
- [117] P. Vivo, S. N. Majumdar, and O. Bohigas, “Distributions of conductance and shot noise and associated phase transitions,” *Physical review letters*, vol. 101, p. 216809, 2008. [Online]. Available: <https://doi.org/10.1103/PhysRevLett.101.216809>
- [118] —, “Probability distributions of linear statistics in chaotic cavities and associated phase transitions,” *Physical Review B*, vol. 81, p. 104202, 2010. [Online]. Available: <https://doi.org/10.1103/PhysRevB.81.104202>

- [119] K. Damle, S. N. Majumdar, V. Tripathi, and P. Vivo, “Phase transitions in the distribution of the andreev conductance of superconductor-metal junctions with multiple transverse modes,” *Physical Review Letters*, vol. 107, p. 177206, 2011. [Online]. Available: <https://doi.org/10.1103/PhysRevLett.107.177206>
- [120] F. D. Cunden, P. Facchi, and P. Vivo, “Joint statistics of quantum transport in chaotic cavities,” *Europhysics Letters*, vol. 110, p. 50002, 2015. [Online]. Available: <https://doi.org/10.1209/0295-5075/110/50002>
- [121] A. De Pasquale, P. Facchi, G. Parisi, S. Pascazio, and A. Scardicchio, “Phase transitions and metastability in the distribution of the bipartite entanglement of a large quantum system,” *Physical Review A*, vol. 81, p. 052324, 2010. [Online]. Available: <https://doi.org/10.1103/PhysRevA.81.052324>
- [122] P. Facchi, U. Marzolino, G. Parisi, and S. Pascazio, “Phase transitions of bipartite entanglement,” *Physical Review Letters*, vol. 101, p. 050502, 2008. [Online]. Available: <https://doi.org/10.1103/PhysRevLett.101.050502>
- [123] C. Nadal, S. N. Majumdar, and M. Vergassola, “Phase transitions in the distribution of bipartite entanglement of a random pure state,” *Physical Review Letters*, vol. 104, p. 110501, 2010. [Online]. Available: <https://doi.org/10.1103/PhysRevLett.104.110501>
- [124] F. Colomo and A. G. Pronko, “Third-order phase transition in random tilings,” *Physical Review E*, vol. 88, p. 042125, 2013. [Online]. Available: <https://doi.org/10.1103/PhysRevE.88.042125>
- [125] G. Schehr, S. N. Majumdar, A. Comtet, and P. J. Forrester, “Reunion probability of n vicious walkers: typical and large fluctuations for large n ,” *Journal of Statistical Physics*, vol. 150, p. 3, 2013. [Online]. Available: <https://doi.org/10.1007/s10955-012-0614-7>
- [126] P. J. Forrester, S. N. Majumdar, and G. Schehr, “Non-intersecting brownian walkers and yang-mills theory on the sphere,” *Nuclear Physics B*, vol. 844, p. 3, 2011. [Online]. Available: <https://doi.org/10.1016/j.nuclphysb.2010.11.013>

- [127] F. D. Cunden, P. Facchi, M. Ligabò, and P. Vivo, “Universality of the third-order phase transition in the constrained coulomb gas,” *Journal of Statistical Mechanics: Theory and Experiment*, p. 053303, 2017. [Online]. Available: <https://doi.org/10.1088/1742-5468/aa690c>
- [128] F. D. Cunden, P. Facchi, M. Ligabó, and P. Vivo, “Universality of the weak pushed-to-pulled transition in systems with repulsive interactions,” *Journal of Physics A: Mathematical and Theoretical*, vol. 51, p. 35LT01, 2018. [Online]. Available: <https://doi.org/10.1088/1751-8121/aad147>
- [129] F. D. Cunden, P. Facchi, M. Ligabò, and P. Vivo, “Third-order phase transition: random matrices and screened coulomb gas with hard walls,” *Journal of statistical physics*, vol. 175, p. 1262, 2019. [Online]. Available: <https://doi.org/10.1007/s10955-019-02281-9>
- [130] D. J. Gross and E. Witten, “Possible third-order phase transition in the large- n lattice gauge theory,” *Phys. Rev. D*, vol. 21, p. 446, 1980. [Online]. Available: <https://doi.org/10.1103/PhysRevD.21.446>
- [131] S. R. Wadia, “ $N = \infty$ phase transition in a class of exactly soluble model lattice gauge theories,” *Physics Letters B*, vol. 93, p. 403, 1980. [Online]. Available: [https://doi.org/10.1016/0370-2693\(80\)90353-6](https://doi.org/10.1016/0370-2693(80)90353-6)
- [132] M. R. Douglas and V. A. Kazakov, “Large n phase transition in continuum qcd²,” *Physics Letters B*, vol. 319, p. 219, 1993. [Online]. Available: [https://doi.org/10.1016/0370-2693\(93\)90726-6](https://doi.org/10.1016/0370-2693(93)90726-6)
- [133] S. Agarwal, M. Kulkarni, and A. Dhar, “Some connections between the classical calogero–moser model and the log-gas,” *Journal of Statistical Physics*, vol. 176, p. 1463, 2019. [Online]. Available: <https://doi.org/10.1007/s10955-019-02394-6>
- [134] N. Goldenfeld, *Lectures on phase transitions and the renormalization group*. CRC press, 2018.
- [135] S. Sachdev, *Quantum Phase Transitions*. Cambridge University Press, 2011.

- [136] M. S. Ma, “Fractional-order phase transition of charged ads black holes,” *Physics Letters B*, vol. 795, p. 490, 2019. [Online]. Available: <https://doi.org/10.1016/j.physletb.2019.06.054>
- [137] R. Hilfer, *Applications of fractional calculus in physics*. World scientific, 2000. [Online]. Available: <https://doi.org/10.1142/3779>
- [138] —, “Multiscaling and the classification of continuous phase transitions,” *Phys. Rev. Letts.*, vol. 68, p. 190, 1992. [Online]. Available: <https://doi.org/10.1103/PhysRevLett.68.190>
- [139] R. Fletcher, “A new approach to variable metric algorithms,” *The Computer Journal*, vol. 13, p. 317, 1970. [Online]. Available: <https://doi.org/10.1093/comjnl/13.3.317>
- [140] C. G. Broyden, “The convergence of a class of double-rank minimization algorithms 1. general considerations,” *IMA Journal of Applied Mathematics*, vol. 6, p. 76, 1970. [Online]. Available: <https://doi.org/10.1093/imamat/6.1.76>
- [141] A. K. Hartmann, “Large-deviation properties of largest component for random graphs,” *The European Physical Journal B*, vol. 84, p. 627, 2011. [Online]. Available: <https://doi.org/10.1140/epjb/e2011-10836-4>
- [142] A. K. Hartmann and M. Mézard, “Distribution of diameters for erdős-rényi random graphs,” *Physical Review E*, vol. 97, p. 032128, 2018. [Online]. Available: <https://doi.org/10.1103/PhysRevE.97.032128>
- [143] J. Esteve, J.-B. Trebbia, T. Schumm, A. Aspect, C. I. Westbrook, and I. Bouchoule, “Observations of density fluctuations in an elongated bose gas: Ideal gas and quasicondensate regimes,” *Physical Review Letters*, vol. 96, p. 130403, 2006. [Online]. Available: <https://doi.org/10.1103/PhysRevLett.96.130403>
- [144] T. Jacqmin, J. Armijo, T. Berrada, K. V. Kheruntsyan, and I. Bouchoule, “Sub-poissonian fluctuations in a 1d bose gas: from the quantum quasicondensate to the strongly interacting regime,” *Physical Review Letters*, vol. 106, p. 230405, 2011. [Online]. Available: <https://doi.org/10.1103/PhysRevLett.106.230405>

- [145] I. V. Protopopov, D. B. Gutman, and A. D. Mirlin, “Luttinger liquids with multiple fermi edges: Generalized fisher-hartwig conjecture and numerical analysis of toeplitz determinants,” *Journal of Physics*, vol. 52, p. 165, 2012. [Online]. Available: <https://doi.org/10.3952/physics.v52i2.2359>
- [146] L. S. Levitov, H. Lee, and G. B. Lesovik, “Electron counting statistics and coherent states of electric current,” *Journal of Mathematical Physics*, vol. 37, p. 4845, 1996. [Online]. Available: <https://doi.org/10.1063/1.531672>
- [147] C. W. J. Beenakker, “Universality in the random-matrix theory of quantum transport,” *Physical Review Letters*, vol. 70, p. 1155, 1993. [Online]. Available: <https://doi.org/10.1103/PhysRevLett.70.1155>
- [148] V. A. Osipov and E. Kanzieper, “Integrable theory of quantum transport in chaotic cavities,” *Physical Review Letters*, vol. 101, p. 176804, 2008. [Online]. Available: <https://doi.org/10.1103/PhysRevLett.101.176804>
- [149] L. S. Levitov and G. B. Lesovik, “Charge distribution in quantum shot noise,” *JETP Letters*, vol. 58, p. 230, 1993. [Online]. Available: https://www.researchgate.net/profile/Gordey-Lesovik/publication/253694870_Charge_distribution_in_quantum_shot_noise/links/53f5e4230cf2888a7491f4c5/Charge-distribution-in-quantum-shot-noise.pdf
- [150] V. A. Osipov and E. Kanzieper, “Statistics of thermal to shot noise crossover in chaotic cavities,” *Journal of Physics A: Mathematical and Theoretical*, vol. 42, p. 475101, 2009. [Online]. Available: <https://iopscience.iop.org/article/10.1088/1751-8113/42/47/475101/meta>
- [151] H. J. Sommers, W. Wiecek, and D. V. Savin, “Statistics of conductance and shot noise power for chaotic cavities,” *Acta Phys. Pol. A*, vol. 112, p. 691, 2007. [Online]. Available: <https://doi.org/10.48550/arXiv.0710.5370>
- [152] C. W. Groth, B. Michaelis, and C. W. J. Beenakker, “Counting statistics of coherent population trapping in quantum dots,” *Physical Review B*, vol. 74, p. 125315, 2006. [Online]. Available: <https://doi.org/10.1103/PhysRevB.74.125315>

- [153] A. Grabsch, S. N. Majumdar, and C. Texier, “Truncated linear statistics associated with the eigenvalues of random matrices ii. partial sums over proper time delays for chaotic quantum dots,” *Journal of Statistical Physics*, vol. 167, p. 1452, 2017. [Online]. Available: <https://link.springer.com/article/10.1007/s10955-017-1780-4>
- [154] V. Eisler and Z. Rácz, “Full counting statistics in a propagating quantum front and random matrix spectra,” *Physical Review Letters*, vol. 110, p. 060602, 2013. [Online]. Available: <https://doi.org/10.1103/PhysRevLett.110.060602>
- [155] A. D. Ivanov and A. G. Abanov, “Characterizing correlations with full counting statistics: Classical ising and quantum x y spin chains,” *Physical Review E*, vol. 87, p. 022114, 2013. [Online]. Available: <https://doi.org/10.1103/PhysRevE.87.022114>
- [156] I. Klich, “Lower entropy bounds and particle number fluctuations in a fermi sea,” *Journal of Physics A: Mathematical and General*, vol. 39, p. L85, 2006. [Online]. Available: <https://iopscience.iop.org/article/10.1088/0305-4470/39/4/L02/meta>
- [157] I. Klich and L. Levitov, “Quantum noise as an entanglement meter,” *Physical Review Letters*, vol. 102, p. 100502, 2009. [Online]. Available: <https://doi.org/10.1103/PhysRevLett.102.100502>
- [158] H. F. Song, C. Flindt, S. Rachel, I. Klich, and K. Le Hur, “Entanglement entropy from charge statistics: Exact relations for noninteracting many-body systems,” *Physical Review B*, vol. 83, p. 161408, 2011. [Online]. Available: <https://doi.org/10.1103/PhysRevB.83.161408>
- [159] P. Calabrese, P. Le Doussal, and S. N. Majumdar, “Random matrices and entanglement entropy of trapped fermi gases,” *Physical Review A*, vol. 91, p. 012303, 2015. [Online]. Available: <https://doi.org/10.1103/PhysRevA.91.012303>
- [160] B. Lacroix-A-Chez-Toine, S. N. Majumdar, and G. Schehr, “Entanglement entropy and full counting statistics for $2d$ -rotating trapped fermions,” *Physical Review A*, vol. 99, p. 021602, 2019. [Online]. Available: <https://doi.org/10.1103/PhysRevA.99.021602>
- [161] N. R. Smith, P. Le Doussal, S. N. Majumdar, and G. Schehr, “Counting statistics for noninteracting fermions in a d -dimensional potential,” *Physical Review E*, vol.

- 103, p. L030105, 2021. [Online]. Available: <https://journals.aps.org/pre/abstract/10.1103/PhysRevE.103.L030105>
- [162] A. Bastianello and L. Piroli, “From the sinh-gordon field theory to the one-dimensional bose gas: exact local correlations and full counting statistics,” *Journal of Statical Mechanics: Theory and Experiments*, vol. 11, p. 113104, 2018. [Online]. Available: <https://iopscience.iop.org/article/10.1088/1742-5468/aaeb48/meta>
- [163] M. Arzamasovs and D. M. Gangardt, “Full counting statistics and large deviations in a thermal 1d bose gas,” *Physical Review Letters*, vol. 122, p. 120401, 2019. [Online]. Available: <https://doi.org/10.1103/PhysRevLett.122.120401>
- [164] N. R. Smith, P. Le Doussal, S. N. Majumdar, and G. Schehr, “Full counting statistics for interacting trapped fermions,” *SciPost Physics*, vol. 11, p. 110, 2021. [Online]. Available: <https://www.scipost.org/SciPostPhys.11.6.110>
- [165] A. Bastianello, L. Piroli, and P. Calabrese, “Exact local correlations and full counting statistics for arbitrary states of the one-dimensional interacting bose gas,” *Physical Review Letters*, vol. 120, p. 190601, 2018. [Online]. Available: <https://doi.org/10.1103/PhysRevLett.120.190601>
- [166] R. Law, J. Illian, D. F. Burslem, G. Gratzer, C. V. S. Gunatilleke, and I. Gunatilleke, “Ecological information from spatial patterns of plants: insights from point process theory,” *Journal of Ecology*, vol. 97, p. 616, 2009. [Online]. Available: <https://doi.org/10.1111/j.1365-2745.2009.01510.x>
- [167] S. Azaele, S. Suweis, J. Grilli, I. Volkov, J. R. Banavar, and A. Maritan, “Statistical mechanics of ecological systems: Neutral theory and beyond,” *Review of Modern Physics*, vol. 88, p. 035003, 2016. [Online]. Available: <https://doi.org/10.1103/RevModPhys.88.035003>
- [168] G. Akemann, N. Chakarov, O. Krüger, A. Mielke, M. Ottensmann, and P. Päßler, “Interactions between different birds of prey as a random point process,” *arXiv preprint arXiv:2310.20670*, 2023. [Online]. Available: <https://arxiv.org/pdf/2310.20670.pdf>

- [169] T. Shirai and Y. Takahashi, “Random point fields associated with certain fredholm determinants i: fermion, poisson and boson point processes,” *Journal of Functional Analysis*, vol. 205, p. 414, 2003. [Online]. Available: [https://doi.org/10.1016/S0022-1236\(03\)00171-X](https://doi.org/10.1016/S0022-1236(03)00171-X)
- [170] S. Ghosh and A. Nishry, “Point processes, hole events, and large deviations: random complex zeros and coulomb gases,” *Constructive Approximations*, vol. 48, p. 101, 2018. [Online]. Available: <https://link.springer.com/article/10.1007/s00365-018-9418-6>
- [171] S. Torquato, “Hyperuniformity and its generalizations,” *Physical Review E*, vol. 94, p. 022122, 2016. [Online]. Available: <https://doi.org/10.1103/PhysRevE.94.022122>
- [172] —, “Hyperuniform states of matter,” *Physics Reports*, vol. 745, p. 1, 2018. [Online]. Available: <https://doi.org/10.1016/j.physrep.2018.03.001>
- [173] F. J. Dyson and M. L. Mehta, “Statistical theory of the energy levels of complex systems. iv,” *Journal of Mathematical Physics*, vol. 4, no. 5, p. 701, 1963. [Online]. Available: <https://doi.org/10.1063/1.1704008>
- [174] M. M. Fogler and B. I. Shklovskii, “Probability of an eigenvalue number fluctuation in an interval of a random matrix spectrum,” *Physical Review Letters*, vol. 74, p. 3312, 1995. [Online]. Available: <https://doi.org/10.1103/PhysRevLett.74.3312>
- [175] Z. Bai, X. Wang, and W. Zhou, “Clt for linear spectral statistics of wigner matrices,” *Electronic Journal of Probability*, vol. 14, p. 2391, 2009. [Online]. Available: <https://doi.org/10.1214/EJP.v14-705>
- [176] A. Borodin, “Clt for spectra of submatrices of wigner random matrices,” *Moscow Mathematical Journal*, vol. 14, p. 29, 2014. [Online]. Available: <http://www.mathjournals.org/mmj/2014-014-001/2014-014-001-002.html>
- [177] R. M. May, “Will a large complex system be stable?” *Nature*, vol. 238, p. 413, 1972. [Online]. Available: <https://www.nature.com/articles/238413a0>
- [178] D. J. Wales, J. P. K. Doye, M. A. Miller, P. N. Mortenson, and T. R. Walsh, “Energy landscapes: from clusters to biomolecules,” *Advances in Chemical*

- Physics*, vol. 115, 2000. [Online]. Available: <https://onlinelibrary.wiley.com/doi/book/10.1002/9780470141748#page=9>
- [179] I. Perez-Castillo, “Large deviations of the shifted index number in the gaussian ensemble,” *Journal of Statistical Mechanics: Theory and Experiment*, vol. 6, p. 063207, 2016. [Online]. Available: <https://iopscience.iop.org/article/10.1088/1742-5468/2016/06/063207/pdf>
- [180] A. Flack, S. N. Majumdar, and G. Schehr, “An exact formula for the variance of linear statistics in the one-dimensional jellium mode,” *Journal of Physics A: Mathematical and Theoretical*, vol. 56, p. 105002, 2023. [Online]. Available: <https://iopscience.iop.org/article/10.1088/1751-8121/acb86a/meta>
- [181] Y. Chen and S. M. Manning, “Distribution of linear statistics in random matrix models (metallic conductance fluctuations),” *Journal of Physics: Condensed Matter*, vol. 6, p. 3039, 1994. [Online]. Available: <https://iopscience.iop.org/article/10.1088/0953-8984/6/16/009/meta>
- [182] F. D. Cunden, P. Facchi, and P. Vivo, “A shortcut through the coulomb gas method for spectral linear statistics on random matrices,” *Journal of Physics A: Mathematical and Theoretical*, vol. 49, p. 135202, 2016. [Online]. Available: <https://iopscience.iop.org/article/10.1088/1751-8113/49/13/135202/meta>
- [183] H. D. Politzer, “Random-matrix description of the distribution of mesoscopic conductance,” *Physical Review B*, vol. 40, p. 11917, 1989. [Online]. Available: <https://doi.org/10.1103/PhysRevB.40.11917>
- [184] C. W. J. Beenakker, “Random-matrix theory of mesoscopic fluctuations in conductors and superconductors,” *Physical Review B*, vol. 47, p. 15763, 1993. [Online]. Available: <https://doi.org/10.1103/PhysRevB.47.15763>
- [185] E. L. Basor and C. A. Tracy, “Variance calculations and the bessel kernel,” *Journal of Statistical Physics*, vol. 73, p. 415, 1993. [Online]. Available: <https://link.springer.com/article/10.1007/BF01052770>

- [186] T. H. Baker and P. J. Forrester, “Finite- n fluctuation formulas for random matrices,” *Journal of Statistical Physics*, vol. 88, p. 1371, 1997. [Online]. Available: <https://link.springer.com/article/10.1007/BF02732439>
- [187] K. Johansson, “On fluctuations of eigenvalues of random hermitian matrices,” *Duke Mathematical Journal*, vol. 91, p. 151, 1998. [Online]. Available: <https://doi.org/10.1215/S0012-7094-98-09108-6>
- [188] A. Soshnikov, “The central limit theorem for local linear statistics in classical compact groups and related combinatorial identities,” *Annals of Probability*, vol. 28, p. 1353, 2000. [Online]. Available: <https://www.jstor.org/stable/2652991>
- [189] L. Pastur, “Limiting laws of linear eigenvalue statistics for hermitian matrix models,” *Journal of Mathematical Physics*, vol. 47, p. 103303, 2006. [Online]. Available: <https://doi.org/10.1063/1.2356796>
- [190] A. Lytova and L. Pastur, “Central limit theorem for linear eigenvalue statistics of random matrices with independent entries.” *Annals of Probability*, vol. 37, p. 1778, 2009. [Online]. Available: <https://projecteuclid.org/journals/annals-of-probability/volume-37/issue-5/Central-limit-theorem-for-linear-eigenvalue-statistics-of-random-matrices/10.1214/09-AOP452.full>
- [191] B. A. Khoruzhenko, D. V. Savin, and H. J. Sommers, “Systematic approach to statistics of conductance and shot-noise in chaotic cavities,” *Physical Review B*, vol. 80, p. 125301, 2009. [Online]. Available: <https://doi.org/10.1103/PhysRevB.80.125301>
- [192] C. Texier and S. N. Majumdar, “Wigner time-delay distribution in chaotic cavities and freezing transition,” *Physical Review Letters*, vol. 110, p. 250602, 2013. [Online]. Available: <https://doi.org/10.1103/PhysRevLett.110.250602>
- [193] F. D. Cunden and P. Vivo, “Universal covariance formula for linear statistics on random matrices,” *Physical Review Letters*, vol. 113, p. 070202, 2014. [Online]. Available: <https://doi.org/10.1103/PhysRevLett.113.070202>

- [194] A. Grabsch and C. Texier, “Capacitance and charge relaxation resistance of chaotic cavities - joint distribution of two linear statistics in the laguerre ensemble of random matrices,” *Europhys. Lett.*, vol. 109, p. 50004, 2015. [Online]. Available: <https://iopscience.iop.org/article/10.1209/0295-5075/109/50004/meta>
- [195] —, “Distribution of spectral linear statistics on random matrices beyond the large deviation function - wigner time delay in multichannel disordered wires,” *Journal of Physics A: Mathematical and Theoretical*, vol. 49, p. 465002, 2016. [Online]. Available: <https://iopscience.iop.org/article/10.1088/1751-8113/49/46/465002/meta>
- [196] A. Grabsch, S. N. Majumdar, and C. Texier, “Truncated linear statistics associated with the top eigenvalues of random matrices,” *Journal of Statistical Physics*, vol. 167, p. 234, 2017. [Online]. Available: <https://link.springer.com/article/10.1007/s10955-017-1755-5>
- [197] A. Grabsch, “General truncated linear statistics for the top eigenvalues of random matrices,” *Journal of Physics A: Mathematical and Theoretical*, vol. 55, p. 124001, 2021. [Online]. Available: <https://iopscience.iop.org/article/10.1088/1751-8121/ac52e3/meta>
- [198] A. Valov, B. Meerson, and P. V. Sasorov, “Large deviations and phase transitions in spectral linear statistics of gaussian random matrices,” *Journal of Physics A: Mathematical and Theoretical*, vol. 57, p. 065001, 2024. [Online]. Available: <https://iopscience.iop.org/article/10.1088/1751-8121/ad1e1a/meta>
- [199] B. De Bruyne, P. Le Doussal, S. N. Majumdar, and G. Schehr, “Linear statistics for coulomb gases: higher order cumulants,” *Journal of Physics A: Mathematical and Theoretical*, vol. 57, p. 155002, 2024. [Online]. Available: <https://iopscience.iop.org/article/10.1088/1751-8121/ad329f/meta>
- [200] O. Babelon, D. Bernard, and M. Talon, *Introduction to classical integrable systems*. Cambridge University Press, 2003.
- [201] A. Torrielli, “Classical integrability,” *Journal of Physics A: Mathematical and Theoretical*, vol. 49, p. 323001, 2016. [Online]. Available: <https://doi.org/10.1088/1751-8113/49/32/323001>

- [202] C. Cao, “Classical integrable systems,” in *Soliton Theory and Its Applications*. Springer, 1995, p. 152. [Online]. Available: https://doi.org/10.1007/978-3-662-03102-5_4
- [203] A. Bastianello, A. De Luca, and R. Vasseur, “Hydrodynamics of weak integrability breaking,” *Journal of Statistical Mechanics: Theory and Experiment*, vol. 2021, p. 114003, 2021. [Online]. Available: <https://doi.org/10.1088/1742-5468/ac26b2>
- [204] Y. Tang, W. Kao, K. Y. Li, S. Seo, K. Mallayya, M. Rigol, S. Gopalakrishnan, and B. L. Lev, “Thermalization near integrability in a dipolar quantum newton’s cradle,” *Physical Review X*, vol. 8, p. 021030, 2018. [Online]. Available: <https://doi.org/10.1103/PhysRevX.8.021030>
- [205] I. Bouchoule and J. Dubail, “Generalized hydrodynamics in the one-dimensional bose gas: theory and experiments,” *Journal of Statistical Mechanics: Theory and Experiment*, vol. 2022, p. 014003, 2022. [Online]. Available: <https://doi.org/10.1088/1742-5468/ac3659>
- [206] P. Di Cintio, S. Iubini, S. Lepri, and R. Livi, “Transport in perturbed classical integrable systems: The pinned toda chain,” *Chaos, Solitons & Fractals*, vol. 117, p. 249, 2018. [Online]. Available: <https://doi.org/10.1016/j.chaos.2018.11.003>
- [207] K. D. N. T. Lam and J. Kurchan, “Stochastic perturbation of integrable systems: a window to weakly chaotic systems,” *Journal of Statistical Physics*, vol. 156, p. 619, 2014. [Online]. Available: <https://doi.org/10.1007/s10955-014-1030-y>
- [208] M. A. Rajabpour and S. Sotiriadis, “Quantum quench of the trap frequency in the harmonic calogero model,” *Physical Review A*, vol. 89, p. 033620, 2014. [Online]. Available: <https://doi.org/10.1103/PhysRevA.89.033620>
- [209] A. Dhar, A. Kundu, J. L. Lebowitz, and J. A. Scaramazza, “Transport properties of the classical toda chain: effect of a pinning potential,” *Journal of Statistical Physics*, vol. 175, p. 1298, 2019. [Online]. Available: <https://doi.org/10.1007/s10955-019-02284-6>

- [210] J. Durnin, M. J. Bhaseen, and B. Doyon, “Nonequilibrium dynamics and weakly broken integrability,” *Physical Review Letters*, vol. 127, p. 130601, 2021. [Online]. Available: <https://doi.org/10.1103/PhysRevLett.127.130601>
- [211] V. B. Bulchandani, M. Kulkarni, J. E. Moore, and X. Cao, “Quasiparticle kinetic theory for calogero models,” *Journal of Physics A: Mathematical and Theoretical*, vol. 54, p. 474001, 2021. [Online]. Available: <https://doi.org/10.1088/1751-8121/ac2f8e>
- [212] M. Inguscio, W. Ketterle, and C. Salomon, *Ultra-cold Fermi gases*. IOS press, 2008, vol. 164.
- [213] F. Dalfovo, S. Giorgini, L. P. Pitaevskii, and S. Stringari, “Theory of bose-einstein condensation in trapped gases,” *Reviews of Modern Physics*, vol. 71, p. 463, 1999. [Online]. Available: <https://link.aps.org/doi/10.1103/RevModPhys.71.463>
- [214] A. M. Perelomov *et al.*, *Integrable Systems of Classical Mechanics and Lie Algebras: Volume I*. Springer, 1990.
- [215] A. P. Polychronakos, “New integrable systems from unitary matrix models,” *Physical Letters B*, vol. 277, p. 102, 1992. [Online]. Available: [https://doi.org/10.1016/0370-2693\(92\)90964-6](https://doi.org/10.1016/0370-2693(92)90964-6)
- [216] W. Fu, Y. Zhang, and H. Zhao, “Universal law of thermalization for one-dimensional perturbed toda lattices,” *New Journal of Physics*, vol. 21, p. 043009, 2019. [Online]. Available: <https://doi.org/10.1088/1367-2630/ab115a>
- [217] N. Gurappa and P. K. Panigrahi, “Equivalence of the calogero-sutherland model to free harmonic oscillators,” *Physical Review B*, vol. 59, p. R2490, 1999. [Online]. Available: <https://doi.org/10.1103/PhysRevB.59.R2490>
- [218] M. Kulkarni and A. P. Polychronakos, “Emergence of the calogero family of models in external potentials: duality, solitons and hydrodynamics,” *Journal of Physics A: Mathematical and Theoretical*, vol. 50, p. 455202, 2017. [Online]. Available: <https://doi.org/10.1088/1751-8121/aa8c6b>
- [219] A. K. Gon and M. Kulkarni, “Duality in a hyperbolic interaction model integrable even in a strong confinement: multi-soliton solutions and field theory,” *Journal*

- of Physics A: Mathematical and Theoretical*, vol. 52, p. 415201, 2019. [Online]. Available: <https://doi.org/10.1088/1751-8121/ab3f42>
- [220] S. Santra, J. Kethepalli, S. Agarwal, A. Dhar, M. Kulkarni, and A. Kundu, “Gap statistics for confined particles with power-law interactions,” *Physical Review Letters*, vol. 128, p. 170603, 2022. [Online]. Available: <https://doi.org/10.1103/PhysRevLett.128.170603>
- [221] G. Mussardo, *Statistical field theory: an introduction to exactly solved models in statistical physics*. Oxford University Press, 2010.
- [222] R. Allez, J. P. Bouchaud, and A. Guionnet, “Invariant beta ensembles and the gauss-wigner crossover,” *Physical Review Letters*, vol. 109, p. 094102, 2012. [Online]. Available: <https://doi.org/10.1103/PhysRevLett.109.094102>
- [223] J. K. Percus, “Equilibrium state of a classical fluid of hard rods in an external field,” *Journal of Statistical Physics*, vol. 15, p. 505, 1976. [Online]. Available: <https://doi.org/10.1007/BF01020803>
- [224] M. Stone, I. Anduaga, and L. Xing, “The classical hydrodynamics of the calogero–sutherland model,” *Journal of Physics A: Mathematical and Theoretical*, vol. 41, p. 275401, 2008. [Online]. Available: <https://doi.org/10.1088/1751-8113/41/27/275401>
- [225] J. Kethepalli, D. Bagchi, A. Dhar, M. Kulkarni, and A. Kundu, “Finite temperature equilibrium density profiles of integrable systems in confining potentials,” *Physical Review E*, vol. 107, p. 044101, 2023. [Online]. Available: <https://doi.org/10.1103/PhysRevE.107.044101>
- [226] S. Flach and A. V. Gorbach, “Discrete breathers—advances in theory and applications,” *Physics Reports*, vol. 467, p. 1, 2008. [Online]. Available: <https://doi.org/10.1016/j.physrep.2008.05.002>
- [227] J. DeLuca, A. J. Lichtenberg, and S. Ruffo, “Energy transitions and time scales to equipartition in the Fermi-Pasta-Ulam oscillator chain,” *Physical Review E*, vol. 51, p. 2877, 1995. [Online]. Available: <https://journals.aps.org/pre/pdf/10.1103/PhysRevE.51.2877>

- [228] R. Livi, M. Pettini, S. Ruffo, M. Sparpaglione, and A. Vulpiani, “Equipartition threshold in nonlinear large hamiltonian systems: The fermi-pasta-ulam model,” *Physical Review A*, vol. 31, p. 1039, 1985. [Online]. Available: <https://journals.aps.org/pr/a/pdf/10.1103/PhysRevA.31.1039>
- [229] S. Ganapa, A. Apte, and A. Dhar, “Thermalization of local observables in the α -fput chain,” *Journal of Statical Physics*, vol. 180, p. 1010, 2020. [Online]. Available: <https://doi.org/10.1007/s10955-020-02576-2>
- [230] V. B. Bulchandani, R. Vasseur, C. Karrasch, and J. E. Moore, “Solvable hydrodynamics of quantum integrable systems,” *Physical Review letters*, vol. 119, p. 220604, 2017. [Online]. Available: <https://doi.org/10.1103/PhysRevLett.119.220604>
- [231] N. Malvania, Y. Zhang, Y. Le, J. Dubail, M. Rigol, and D. S. Weiss, “Generalized hydrodynamics in strongly interacting 1D Bose gases,” *Science*, vol. 373, p. 1129, 2021. [Online]. Available: <https://www.science.org/doi/pdf/10.1126/science.abf0147>
- [232] J. De Nardis, D. Bernard, and B. Doyon, “Diffusion in generalized hydrodynamics and quasiparticle scattering,” *SciPost Physics*, vol. 6, p. 049, 2019. [Online]. Available: <https://www.scipost.org/SciPostPhys.6.4.049/pdf>
- [233] S. Gopalakrishnan, D. A. Huse, V. Khemani, and R. Vasseur, “Hydrodynamics of operator spreading and quasiparticle diffusion in interacting integrable systems,” *Physical Review B*, vol. 98, p. 220303, 2018. [Online]. Available: <https://doi.org/10.1103/PhysRevB.98.220303>
- [234] G. Benettin, L. Galgani, and J. M. Strelcyn, “Kolmogorov entropy and numerical experiments,” *Physical Review A*, vol. 14, p. 2338, Dec 1976. [Online]. Available: <https://link.aps.org/doi/10.1103/PhysRevA.14.2338>
- [235] Z. Dong, R. Moessner, and M. Haque, “Classical dynamics of harmonically trapped interacting particles,” *Journal of Statistical Mechanics: Theory and Experiment*, vol. 2018, p. 063106, 2018. [Online]. Available: <https://iopscience.iop.org/article/10.1088/1742-5468/aac741/pdf>

- [236] S. D. Murugan, D. Kumar, S. Bhattacharjee, and S. S. Ray, “Many-body chaos in thermalized fluids,” *Physical Review Letters*, vol. 127, p. 124501, 2021. [Online]. Available: <https://journals.aps.org/prl/pdf/10.1103/PhysRevLett.127.124501>
- [237] J. Kurchan, “Quantum bound to chaos and the semiclassical limit,” *Journal of statistical physics*, vol. 171, p. 965, 2018. [Online]. Available: <https://link.springer.com/article/10.1007/s10955-018-2052-7>
- [238] V. B. Bulchandani, “On classical integrability of the hydrodynamics of quantum integrable systems,” *Journal of Physics A: Mathematical and Theoretical*, vol. 50, p. 435203, 2017. [Online]. Available: <https://doi.org/10.1088/1751-8121/aa8c62>
- [239] A. P. Polychronakos, “The physics and mathematics of calogero particles,” *Journal of Physics A: Mathematical and General*, vol. 39, no. 41, p. 12793, 2006. [Online]. Available: <https://dx.doi.org/10.1088/0305-4470/39/41/S07>
- [240] L. Touzo, P. Le Doussal, and G. Schehr, “Fluctuations in the active dyson brownian motion and the overdamped calogero-moser model,” *Physical Review E*, vol. 109, p. 014136, 2024. [Online]. Available: <https://doi.org/10.1103/PhysRevE.109.014136>
- [241] A. Flack, P. Le Doussal, S. N. Majumdar, and G. Schehr, “Out of equilibrium dynamics of repulsive ranked diffusions: the expanding crystal,” *Physical Review E*, vol. 107, p. 064105, 2023. [Online]. Available: <https://doi.org/10.1103/PhysRevE.107.064105>
- [242] A. Campa, T. Dauxois, D. Fanelli, and S. Ruffo, *Physics of long-range interacting systems*. OUP Oxford, 2014. [Online]. Available: <https://doi.org/10.1093/acprof:oso/9780199581931.001.0001>
- [243] “Hypergeometric function.” [Online]. Available: <https://dlmf.nist.gov/15.8.E2>
- [244] A. K. Hartmann, P. Le Doussal, S. N. Majumdar, and G. Schehr, “High-precision simulation of the height distribution for the kpz equation,” *European Physics Letters*, vol. 121, p. 67004, 2018. [Online]. Available: <https://doi.org/10.1209/0295-5075/121/67004>

Publications

List of publications included in the Thesis

1. **J. Kethepalli**, M. Kulkarni, A. Kundu, S. N. Majumdar, D. Mukamel, G. Schehr, “Harmonically confined long-ranged interacting gas in the presence of a hard wall”, [Journal of Statistical Mechanics: Theory and Experiment 2021 \(10\), 103209](#)
2. **J. Kethepalli**, M. Kulkarni, A. Kundu, S. N. Majumdar, D. Mukamel, G. Schehr, “Edge fluctuations and third-order phase transition in harmonically confined long-range systems”, [Journal of Statistical Mechanics: Theory and Experiment 2022 \(3\), 033203](#)
3. **J. Kethepalli**, D. Bagchi, A. Dhar, M. Kulkarni, A. Kundu, “Finite temperature equilibrium density profiles of integrable systems in confining potentials”, [Phys. Rev. E 107, 044101 \(2023\)](#)
4. D. Bagchi, **J. Kethepalli**, V.B. Bulchandani, A. Dhar, D.A. Huse, M. Kulkarni, A. Kundu, “Unusual ergodic and chaotic properties of trapped hard rods”, [Phys. Rev. E 108, 064130 \(2023\)](#)
5. **J. Kethepalli**, M. Kulkarni, A. Kundu, S. N. Majumdar, D. Mukamel, G. Schehr, “Full counting statistics of 1d short range Riesz gases in confinement” [Journal of Statistical Mechanics: Theory and Experiment \(2024\) 083206](#)

Other publications

6. L. P. Dadhichi, **J. Kethapelli**, R. Chajwa, S. Ramaswamy, A. Maitra, “Nonmutual torques and the unimportance of motility for long-range order in two-dimensional flocks”, [Physical Review E 101 \(5\), 052601 \(2020\)](#).

7. S. Santra, **J. Kethepalli**, S. Agarwal, A. Dhar, M. Kulkarni, A. Kundu, “Gap statistics for confined particles with power-law interactions”, [Phys. Rev. Lett.](#) **128**, 170603 (2022)